Graphite as Co-intercalation Host for Sodium Ion Batteries

Dissertation
(kumulativ)

Zur Erlangung des akademischen Grades doctor rerum naturalium
– Dr. rer. nat. –

vorgelegt dem Institut für Technische Chemie und Umweltchemie
dem Rat der Chemisch-Geowissenschaftlichen Fakultät der
Friedrich-Schiller-Universität Jena

von
M.Sc. Mustafa Göktaş
geb. am 08.07.1990
in Ankara, Turkey

1. Reviewer / Gutachter …… Prof. Dr. Philipp Adelhelm (ITUC)……

2. Reviewer / Gutachter …… Prof. Dr. Andrea Balducci (ITUC)……

Tag der Verteidigung …… 11 . September . 2019 ……

Selbständigkeitserklärung

Ich erkläre, dass ich die vorliegende Arbeit selbständig und unter Verwendung der angegebenen Hilfsmittel, persönlichen Mitteilungen und Quellen angefertigt habe.

Ort, Datum Unterschrift der Verfasserin/des Verfassers

Erklärung zu den Eigenanteilen der Promovendin/des Promovenden sowie der weiteren Doktorandinnen/Doktoranden als Co-Autorinnen/-Autoren an den Publikationen und Zweitpublikationsrechten bei einer kumulativen Dissertation

Für alle in dieser kumulativen Dissertation verwendeten Manuskripte liegen die notwendigen Genehmigungen der Verlage („Reprint permissions“) für die Zweitpublikation vor.

Die Co-Autorinnen/-Autoren der in dieser kumulativen Dissertation verwendeten Manuskripte sind sowohl über die Nutzung, als auch über die oben angegebenen Eigenanteile der weiteren Doktorandin-nen/Doktoranden als Co-Autorinnen/-Autoren an den Publikationen und Zweitpublikationsrechten bei einer kumulativen Dissertation informiert und stimmen dem zu.

Die Anteile der Promovendin/des Promovenden sowie der weiteren Doktorandinnen/Doktoranden als Co-Autorinnen/Co-Autoren an den Publikationen und Zweitpublikationsrechten bei einer kumulativen Dissertation sind in der Anlage aufgeführt.

Name der Promovendin/ des Promovenden	Datum	Ort	Unterschrift

Ich bin mit der Abfassung der Dissertation als publikationsbasierte Dissertation, d.h. kumulativ, einver-standen und bestätige die vorstehenden Angaben.

Name Betreuerin/ Betreuer	Datum	Ort	Unterschrift

Declaration on authorship and copyright in a cumulative doctoral thesis

Publication #1
Mustafa Goktas (**1**), Christoph Bolli (**2**), Erik J. Berg (**3**), Petr Novák (**4**), Kilian Pollok (**5**), Falko Langenhorst (**6**), M. v. Roeder (**7**), Olena Lenchuk (**8**), Doreen Mollenhauer (**9**), Philipp Adelhelm (**10**), *Graphite as Cointercalation Electrode for Sodium-Ion Batteries: Electrode Dynamics and the Missing Solid Electrolyte Interphase (SEI), Advanced Energy Materials* **2018**, 1702724.

	1	2	3	4	5	6	7	8	9	10
Research concept and idea	✓									✓
Planning of research activities	✓									
Online electrochemical mass spectrometry (OEMS)		✓	✓	✓						
Computational studies							✓	✓	✓	
TEM analysis					✓	✓				
Electrochemical measurements	✓	✓	✓	✓						
***In situ* Electrochemical Dilatometry (ECD)**	✓									
XRD, SEM, EDX, Elemental analysis and calculations	✓									
Data collection, analyses and overall interpretation	✓									
Comments on Manuscript	✓	✓	✓	✓	✓	✓	✓	✓	✓	✓
Manuscript discussion	✓									✓
Suggested publication equivalence value	1.0									

Publication #2
Mustafa Goktas (**1**), Baris Akduman (**2**), Peihua Huang (**3**), Andrea Balducci (**4**), Philipp Adelhelm (**5**), *Temperature-Induced Activation of Graphite Co-intercalation Reactions for Glymes and Crown Ethers in Sodium-Ion Batteries, The Journal of Physical Chemistry C* **2018**, *122*, 26816−26824.

	1	2	3	4	5
Research concept and idea	✓				✓
Planning of research activities	✓				
Viscosimetry and conductivity measurements			✓	✓	
Electrochemical measurements	✓	✓			
XRD measurements	✓				
Morphological analysis and calculations	✓				
3D model drawing		✓			
Data collection, analyses and overall interpretation	✓				
Manuscript discussion	✓	✓	✓	✓	✓
Manuscript writing	✓				✓
Suggested publication equivalence value	1.0				

Publication #3

Mustafa Goktas (**1**), Christoph Bolli (**2**), Johannes Buchheim (**3**), Erik J. Berg (**4**), Petr Novák (**5**), Francisco Bonilla (**6**), Teófilo Rojo (**7**), Shinichi Komaba (**8**), Kei Kubota (**9**), Philipp Adelhelm (**10**), *Stable and instable diglyme-based electrolytes for batteries with sodium or graphite as electrode, (Submitted Manuscript)*.

	1	2	3	4	5	6	7	8	9	10
Research concept and idea	✓									✓
Planning of research activities	✓									
OEMS measurements		✓		✓	✓					
XRD measurements and analysis	✓		✓							
TEM and EDX analysis						✓	✓			
FTIR measurements	✓							✓	✓	
Electrochemical measurements	✓	✓								
***In situ* Dilatometry**	✓									
XRD, SEM and 3D model drawing	✓									
Data collection, analyses and overall interpretation	✓									
Manuscript discussion	✓	✓	✓	✓	✓	✓	✓	✓	✓	✓
Manuscript writing	✓									✓
Suggested publication equivalence value	1.0									

Publication #4

Thangavelu Palaniselvam (**1*′**), Mustafa Goktas (**1***), Bihag Anothumakkool (**2**), Ya-Nan Sun (**3**), Richard Schmuch (**4**), Li Zhao (**5**), Bao-Hang Han (**6**), Martin Winter (**7**), Philipp Adelhelm (**8**), *Sodium Storage and Electrode Dynamics of Tin–Carbon Composite Electrodes from Bulk Precursors for Sodium-Ion Batteries, Advanced Functional Materials* **2019**, 1900790. (* shared first authorship)

	1*′	1*	2	3	4	5	6	7	8
Research concept and idea	✓								✓
Planning of research activities	✓								
XRD measurements and analysis	✓		✓		✓			✓	
TEM analysis	✓			✓		✓	✓		
XPS analysis			✓						
Electrochemical measurements	✓								
***In situ* Dilatometry**		✓							
Morphological analysis and calculations	✓								
3D model drawing		✓							
Data collection, analyses and overall interpretation	✓	✓							
Manuscript discussion	✓	✓	✓	✓	✓	✓	✓	✓	✓
Manuscript writing	✓								✓
Suggested publication equivalence value		0.5							

Dedication

I dedicate this thesis to my mother, Hafiye Göktaş and to my father, Cahit Göktaş.

Acknowledgement

This thesis ends with a journey of three and a half years. Of course, without pain, there is no gain. Therefore, I have faced some difficulties. But I should accept that by the help of my supervisor, I felt the difficulties so slightly. I would like to give my special thanks to my supervisor, Prof. Philipp ADELHELM, for all their guidance, encouragement and supports during Ph.D. and while writing the thesis. I appreciate the passion and freedom which he provides to me. I always feel that I can gain something else from his wisdom. I admire his stress management skills and how he combines the data into a scientific story.

Many thanks to my dear colleagues in the lab who made my life in Jena enjoyable: Lukas MEDENBACH, Aggunda Lingamurthy SANTHOSHA, Wolfgang BREHM, Liangtao YANG, Ines ESCHER, Zhenggang ZHANG, Jonas GEISLER, Christian LEIBING, Baris AKDUMAN, Dr. Johannes BUCHHEIM and Dr. Palaniselvam THANGAVELU, our institute secretary Saskia THIEME, our technicians; Gisela GOTTSCHALT, Beate FÄHNDRICH and Ronald TROTZKI and other members in Institute for Technical and Environmental Chemistry (ITUC) and Center for Energy and Environmental Chemistry Jena (CEEC). Also, I would like to thank our collaborators for their contributions to my publications. Moreover, I would like to give my thanks to Prof. Shinichi KOMABA and to his students who welcome me to his laboratory for around one month for some experiments in the Department of Applied Chemistry in Tokyo University of Science in Japan.

I feel lucky that I have had friends around me who were supporting me during my Ph.D. I want to give special thanks to G.K. who is so special in my life and will always be. Without her, I wouldn't be able to be myself and wouldn't feel valuable, loved and happy. "Thank you that you made me feel special." Moreover, I would like to thank my family; Göktaş Family, especially to my mother who suffered a lot while missing me. When I was up or down, you are always there, and if I am alive, I am always with you.

Finally, I would like to thank Almighty Allah. "He is Allah, the One and Only." (part of the verse from Al-Ikhlas-112). Thanks that I am in this condition now. My journey of study started with the first word, the first order, the first direction in the verse from the Koran: "Read (Proclaim!) In the Name of your Lord Who created" (parts from Surah Al-'Alaq- 96). With this direction and education of the prophet, I move from country to country, seeking for knowledge.

Contents

List of Figure

List of Tables

List of Abbreviations

C.E. ---- Counter Electrode
CMC ---- Carboxymethyl Cellulose
Crown Ethers ---- Crown Ether 4 (12-Crown-4), Crown Ether 5 (15-crown-5), Crown Ether 6 (18-crown-6)
CV ---- Cyclic voltammetry
EC ---- Ethylene Carbonate
EDLCs ---- Electrical Double-Layer Capacitors
ECD ---- *In situ* electrochemical dilatometer
EDX ---- Energy Dispersive X-Ray Analysis
LIBs ---- Lithium Ion Batteries

Glymes

1G ---- Monoglyme, Dimethoxyethane
2G ---- Diglyme, Bis(2-methoxyethyl) ether
3G ---- Triglyme, Triethylene glycol dimethyl ether
4G ---- Tetraglyme, Tetraethylene glycol dimethyl ether
5G ---- Pentaglyme, Pentaethylene glycol dimethyl ether

GIC

b-GIC ---- Binary Graphite Intercalation Compound
t-GIC ---- Ternary Graphite Intercalation Compound

GNP ---- Graphene Nanoplatelets

MW, GW, TW ----------Megawatt, Gigawatt, Terawatt
MWh, GWh----------Megawatt hour, Gigawatt hour
Ni-Cd ----------Nickel Cadmium
Ni-MH----------Nickel-Metal Hydride
OEMS ----------Online Electrochemical Mass Spectrometry
OME ----------Polyoxymethylene Dimethyl Ethers-POMDME
PC ----------Propylene Carbonate
PEM----------Polymer Electrolyte Membrane
PVDF ----------Polyvinylidene Fluoride

Salts

$LiPF_6$----------Lithium hexafluorophosphate
LiTFSI----------Lithium bis(trifluoromethanesulfonyl)imide
NaOTf ----------Sodium Trifluoromethanesulfonate
$NaPF_6$----------Sodium Hexafluorophosphate
$NaClO_4$ ----------Sodium Perchlorate
NaFSI----------Sodium (I) Bis(fluorosulfonyl)imide
NaTFSI----------Sodium (I) Bis(trifluoromethanesulfonyl)imide

SEI ----------Solid electrolyte interphase
SIBs----------Sodium Ion Batteries
SMES----------Superconducting Magnetic Energy Storage
SnNGnP----------Composite of Tin, Tin Nitrogen and Graphene Nanoplatelets
TEM ----------Transmission Electron Microscopy
TMU ----------Tetramethylharnstoff
W.E.----------Working Electrode
XRD ----------X-ray Diffraction
ZEBRA cells----------Zeolite Battery Research Africa cells, (sodium-nickel chloride)

1. Summary

Nowadays, for human mankind, meeting the global energy demand in a sustainable way is one of the most difficult challenges awaiting to be solved. The intermittent nature of renewable energy sources is an important barrier towards reaching a deep market penetration. Hence, the energy storage systems come to play an important role in the energy industry. The electrical energy can be stored when there is oversupply and used when it is needed. Besides this, for some applications, particularly transport, an efficient storage system in crucial. Various energy storage systems have been developed but lithium ion batteries (LIBs) has taken the lead in rechargeable battery technologies since their introduction in the early 1990s. Excellent electrochemical performance, especially the high energy density, high voltage, and long cycle life can be counted as the most relevant advantages of LIBs. However, the abundance and the price of lithium and some other elements such as cobalt are an issue, as the growing battery market will require more supply chains and resources. Therefore, alternative cell chemistries based on abundant elements are being examined. Especially in case of stationary energy storage applications alternative battery technologies become more important.

Sodium-ion battery (SIB) technology is recently being revisited as such an alternative. The researches on SIBs are motivated by the large abundance of sodium and the hope to realize more cost-effective batteries. Although SIBs often have slightly lower energy densities and cell voltages compared to their lithium analogues, the lower polarization of the sodium-ion might enable cells with peculiar advantages over conventional lithium ion technology.

The anode part of a battery is essential to its function, it stores ions when charged and releases them during discharge at low redox potentials. As an anode material for LIBs, graphite is currently the most preferred choice due to its low cost, safety and good cycling performance. Reversible intercalation of lithium ions happens by forming binary graphite intercalation compounds (*b*-GICs) with the final stoichiometry of LiC_6 ($q_{theoretical} = 372$ mAh g^{-1}). Graphite is also favored in SIBs but storage of sodium-ions is only possible by formation of ternary graphite intercalation compounds (*t*-GICs), i.e. by co-intercalatiing solvent molecules. Related to latest studies, a specific capacity of 110 mAh g^{-1} is reached by forming *t*-GICs, therefore, graphite is now a potential candidate to be used in SIBs. Yet, many fundamental aspects of this type of reaction need to be clarified and explored.

This cumulative Ph.D. thesis summarizes the research progress obtained during the last years on the role of graphite (and related anode materials) in SIBs. The study focus is on better understanding the co-intercalation reaction and to further improve the performance by changing electrochemical parameters, test environment, solvent and salt.

This Ph.D. thesis is divided into two major parts. In the first part, a brief literature overview on the current state of research and the aim of this thesis are presented. In the second part, the summary of the scientific results that have been achieved and published in 3 articles and one submitted manuscript, is stated.

The first part starts with discussing brief fundamentals of energy demand, energy supply by renewables and storage concepts including batteries. The following parts discussed some

basics of lithium-ion and sodium-ion batteries. The beginning is done with a brief historical overview on the use of graphite in LIBs which is followed by the use of graphite in SIBs. Also, a short revision is done by highlighting the works of different groups on this topic. The survey ends by describing the working principle of the co-intercalation reaction.

The second major part summarizes the results of this Ph.D. thesis in 3 peer reviewed publications and 1 submitted manuscript. The majority of the work was done at the Friedrich-Schiller-University Jena within the research group Adelhelm (partly in cooperation with the research groups of Prof. Falko Langenhorst and Prof. Andrea Balducci). Additional cooperations with other institutions were initiated for more specialized measurements and theory. In the first publication, as holding first authorship, "*Graphite as Cointercalation Electrode for Sodium-Ion Batteries: Electrode Dynamics and the Missing Solid Electrolyte Interphase (SEI)*", the electrochemical co-intercalation mechanism, its effect on the change of electrode thickness and the missing SEI layer on graphite are discussed. Insight from theory on the dimensions of the intercalated sodium-ion diglyme complex in the graphite lattice are obtained by collaborating with a group at Justus-Liebig-University Giessen (Research group Mollenhauer). To observe the effect of ion intercalation into the crystal lattice, thickness changes are measured by an *in situ* electrochemical dilatometry set up. The difference between lithium or sodium intercalation principles is clearly observed/measured. Moreover, by collaborating with the Paul Scherrer Institute (Research group of Prof. Petr Novak), gas evolution over several cycles is monitored using online electrochemical mass spectrometry (OEMS) which provide important information on side reactions and (potential) SEI formation. Gas evolution is by and large only observed in the first cycle which can be considered as an electrode activation cycle. Combined with other methods such as TEM, an important conclusion from all measurements is that the reaction is likely the first example of an SEI-free graphite anode.

In the second publication, as being first author, "*Temperature-Induced Activation of Graphite Co-intercalation Reactions for Glymes and Crown Ethers in Sodium-Ion Batteries*", a series of five glymes (mono-, di-, tri-, tetra- and pentaglyme) and three crown ethers (crown ether 4 (12c4), 5 (15c5) and 6 (18c6)) are taken into consideration. For the different glyme-based electrolytes, viscosity and conductivity properties are discussed from room temperature to 80°C. A strong influence of temperature on the electrode reactions is found. As an important finding, it is observed that intercalation of Na^+ pentaglyme complexes into graphite can be achieved above room temperature. In a similar way, the so far only poor performance of triglyme-based electrolytes could be eliminated by rising the temperature. In case of mono-, di- and tetraglyme, only a minor temperature effect is observed. In fact, in these cases, the reaction is thermodynamically controlled and hence the temperature coefficient and the entropy change for the reaction could be determined. On the other hand, out of three crown ether types, only crown ether 6 could create co-intercalation with sodium. This is the first experimental proof for sodium intercalation with a crown ether solvent by an electrochemical method.

The third part of this thesis covers the topics studied in the submitted manuscript, as being first author. While in the previous publication the major focus was on the role of different solvents on the co-intercalation reaction, the submitted manuscript entitled "*Stable and*

Instable Diglyme-based Electrolytes for Batteries with Sodium or Graphite as Electrode" is dedicated to the stability of glyme-based electrolytes with varying inorganic and organic salts. The stability of these electrolytes in contact with sodium and lithium metal and also the graphite electrode is tested using different *in situ* and *ex situ* methods. For some salts, clear side reactions with the sodium metal take place which are further quantified by electrochemical impedance spectroscopy (EIS) and OEMS using Na│Na symmetric cells. Moreover, systematic TEM studies combined with EDX also provide evidence for irreversible trapping of ions inside the graphite, the degree being highly dependent on the type of salt used (TEM and EDX are performed in cooperation with CIC EnergiGUNE, by the research group of Prof. Teófilo Rojo). The choice of electrolyte salt has also a prominent influence on the electrode thickness change as followed *in situ* electrochemical dilatometry. Overall, the numerous studies on the suitability of various electrolyte salts provides a clear ranking in the order NaOTf (best) ≥$NaPF_6$>$NaClO_4$>NaFSI>>NaTFSI (worst).

Finally, the fourth article is published by holding shared first authorship. In this publication entitled "*Sodium Storage and Electrode Dynamics of Tin-Carbon Composite Electrodes from Bulk Precursors for Sodium-ion Batteries*", several anode materials are tested with the aim to improve the storage capacity compared to pure graphite electrodes. For this, the graphite is first converted into graphene nano platelets (GnP) by ball milling. The data taken from galvanostatic cycling and *in situ* dilatometry measurements prove that the solvent co-intercalation mechanism of graphite is largely diminished and replaced by an insertion reaction (providing higher capacity combined with a change in the voltage profile). Also, the thickness change of the GnP anode electrode during cycling is much less compared to graphite electrodes. At the same time, addition of tin into this carbon matrix further improves the specific capacity while at the same time excellent cycle life is gained. Moreover, *in situ* dilatometry results also show that the obstacle related to high volume change of tin during ion insertion is effectively buffered by this porous host on the electrode level.

This thesis ends with a conclusion summarizing the published and some unpublished results. Some final comments about the remaining scientific challenges in the research field are given and some suggestions for further experiments are provided. The results obtained during within this Ph.D. thesis provide a better understanding on the use of *t*-GICs in sodium-ion batteries, on the use of *in situ* electrochemical dilatometry in studying electrode reactions of sodium with graphite and graphene/tin composites and on the (electro-)chemical stability of glyme-based electrolytes against sodium and graphite. While some questions could be clarified and new aspects were discovered, the results obtained are also not exhaustive which should be taken a clear motivation to further study sodium-ion batteries and *t*-GICs in the future.

Zusammenfassung

Die nachhaltige Deckung des globalen Energiebedarfs ist in der heutigen Zeit für die Menschheit eine der schwierigsten Herausforderungen, die es zu lösen gilt. Die fluktuierende Verfügbarkeit von erneuerbaren Energien wie Wind- und Solarstrom stellt ein große Herausforderung für eine weitreichende Verbreitung am Markt dar. Deswegen spielen Energiespeichersysteme eine wichtige Rolle in der Energiewirtschaft. Die elektrische Energie kann bei Überversorgung gespeichert und bei Bedarf genutzt werden. Außerdem ist für einige Anwendungen, insbesondere für den Transport, ein effizientes Speichersystem von entscheidender Bedeutung. Es wurden verschiedene Energiespeichersysteme entwickelt jedoch haben Lithiumionenbatterien (LIBs) seit ihrer Einführung Anfang der 90er Jahre die Führung bei den Technologien für wiederaufladbare Batterien übernommen. Exzellente elektrochemische Eigenschaften, insbesondere die hohe Energiedichte, die hohe Spannung und die lange Lebensdauer, können als die wichtigsten Vorteile von LIBs angesehen werden. Jedoch stellt die Verfügbarkeit und der Preis von Lithium und einiger anderer Elemente wie Kobalt ein Problem dar, da der wachsende Batteriemarkt mehr Lieferketten und Ressourcen benötigen wird. Deswegen wird an alternativen Zellsystemen geforscht, die auf verfügbaren Elementen basieren. Insbesondere bei stationären Energiespeicheranwendungen gewinnen alternative Batterietechnologien an Bedeutung.

Die Natriumionenbatterietechnologie (SIB-Technologie) wird in jüngster Zeit als solche wieder aufgegriffen. Die Forschung an SIBs ist motiviert durch die weite Verbreitung von Natrium und die Hoffnung kosteneffiziente Batterien zu realisieren. Obwohl SIBs im Vergleich zu ihren Lithiumanalogen oft etwas geringere Energiedichten und Zellspannungen aufweisen, könnte die aufgrund des größeren Ionenradius von Na^+ geringere Polarisation der Ionenumgebung (Gitterstruktur, Solvathülle) zu Natriumionenbatterien mit besonderen Eigenschaften gegenüber der herkömmlichen Lithiumionentechnologie führen.

Mit Blick auf das Funktionsprinzip einer LIB oder SIB, speichert die Anode bei niedrigen Redoxpotentialen beim Aufladen (under Reduktion) Ionen und gibt diese bei der Entladung (unter Oxidation) wieder ab. Als Anodenmaterial für LIBs ist Graphit aufgrund seiner niedrigen Kosten, seiner Sicherheit und seines guten Zyklusverhaltens derzeit die bevorzugte Wahl. Die reversible Interkalation von Lithiumionen erfolgt durch Bildung von binären Graphitinterkalationsverbindungen (b-GICs) mit einer finalen Stöchiometrie von LiC_6 ($q_{theoretisch}$ = 372 mAh g^{-1}). Graphit wäre daher auch für SIBs „erste Wahl“, jedoch ist die Speicherung von Natriumionen nur durch die Bildung von ternären Graphitinterkalationsverbindungen (t-GICs) möglich, d.h. durch Kointerkalation von Lösungsmittelmolekülen. Neuste Studien zeigten, dass durch die Bildung von t-GICs eine spezifische Kapazität von 110 mAh g^{-1} erreicht wird, sodass Graphit nun ein potenzieller Kandidat für den Einsatz in SIBs ist. Dennoch müssen viele grundlegende Aspekte dieser Art von Reaktion geklärt und untersucht werden.

Diese kumulative Doktorarbeit fasst die in den letzten Jahren erzielten Forschungsfortschritte zur Rolle von Graphit (und verwandten Anodenmaterialien) in SIBs zusammen. Der Schwerpunkt der Studie liegt auf einem besseren Verständnis der Kointerkalationsreaktion und darauf, die Speichereigenschaften weiter zu verbessern indem elektrochemische Parameter, die Testumgebung, Lösungsmittel und Salze verändert werden.

Diese Dissertation gliedert sich in zwei Hauptteile. Im ersten Teil wird ein kurzer Literaturüberblick über den aktuellen Forschungsstand und das Ziel dieser Arbeit gegeben. Im zweiten Teil wird die Zusammenfassung der wissenschaftlichen Ergebnisse, die in drei wissenschaftlichen Artikeln und einem eingereichten Manuskript erzielt und veröffentlicht wurden, gegeben.

Der erste Teil beginnt mit einer kurzen Diskussion zu den Grundlagen des Energiebedarfs, der Energieversorgung durch erneuerbare Energien und der Speicherkonzepte einschließlich Batterien. In den folgenden Teilen wurden einige Grundlagen von Lithiumionen- und Natriumionenbatterien erläutert. Der Anfang wird mit einem kurzen historischen Überblick über die Verwendung von Graphit in LIBs gemacht, gefolgt von der Verwendung von Graphit in SIBs. Außerdem wird ein kurzer Überblick über die Arbeiten gegeben, welche verschiedene Gruppen zu diesem Thema in den letzten Jahren publiziert haben. Der Überblick endet mit einer Beschreibung des Funktionsprinzips der Kointerkalationsreaktion.

Der zweite Hauptteil fasst die Ergebnisse dieser Doktorarbeit in drei Publikationen, welche einen peer-review Prozesses durchlaufen haben, und einem eingereichten Manuskript zusammen. Der Großteil der Arbeit wurde an der Friedrich-Schiller-Universität Jena in der Arbeitsgruppe Adelhelm (teilweise in Zusammenarbeit mit den Arbeitsgruppen von Prof. Falko Langenhorst und Prof. Andrea Balducci) durchgeführt. Weitere Kooperationen mit anderen Instituten wurden für spezialisierte Messungen und theoretische Untersuchungen eingegangen. In der ersten Publikation, als Erstautor, "*Graphite as Cointercalation Electrode for Sodium-Ion Batteries: Electrode Dynamics and the Missing Solid Electrolyte Interphase (SEI)*" wird der elektrochemische Kointerkalationsmechanismus, sein Einfluss auf die Änderung der Elektrodendicke und die fehlende SEI-Schicht auf Graphit diskutiert. Vorhersagen zur Geometrie des in die Graphitstruktur interkalierten Komplexes aus Natriumionen und Diglyme-Molekülen wurden durch die Zusammenarbeit mit einer Theoriegruppe der Justus-Liebig-Universität Gießen (Forschungsgruppe Mollenhauer) durchgeführt. Um die Ioneneinlagerung in das Kristallgitter zu verfolgen, wurde mittels *in situ* Dilatometrie die Änderung der Elektrodendicke mit Zellbetrieb gemessen. Dabei konnten Unterschiede zwischen den Einlagerungsmechanismen für Lithium und Natrium deutlich beobachtet werden. Darüber hinaus wurde in Zusammenarbeit mit dem Paul Scherrer Institut (Forschungsgruppe von Prof. Petr Novak) die Gasentwicklung über mehrere Zyklen hinweg mittels elektrochemischer Online-Massenspektrometrie (OEMS) überwacht. Diese Methode lieferte wichtige Informationen über Nebenreaktionen und (potenzielle) SEI-Bildung. Es zeigte sich, dass eine Gasbildung fast ausschließlich nur im ersten Zyklus stattfindet, welcher daher als Aktivierungszyklus bezeichnet werden kann. In Kombination mit anderen Methoden wie TEM-Messungen ist die wichtigste Schlussfolgerung aus allen Messungen, dass die Reaktion wahrscheinlich als erstes Beispiel für eine SEI-freie Graphitanode angesehen werden kann.

In der zweiten Publikation als Hauptautor, "*Temperature-Induced Activation of Graphite Co-intercalation Reactions for Glymes and Crown Ethers in Sodium-Ion Batteries*" wurde eine Reihe von fünf Glymen (Mono-, Di-, Tri-, Tetra- und Pentaglyme) und drei Kronenethern (Kronenether 4 ([12]Krone-4), 5 ([15]Krone-5) und 6 ([18]Krone-6)) betrachtet. Für die verschiedenen glymebasierten Elektrolyte wurden die Viskosität und die

Leitfähigkeit von Raumtemperatur bis 80°C verglichen. Mit Blick auf die Elektrodenreaktione wurde ein starker Einfluss der Temperatur festgestellt. Als wichtiges Ergebnis wurde entdeckt, dass die Interkalation von Na^+-Pentaglyme Komplexen in Graphit bei erhöhten Temperaturen stattfindet. In ähnlicher Weise konnte die, im Falle von Triglyme-basierten Elektrolyten bisher nur schlechte Speicherfähigkeit durch Temperaturerhöhung verbessert werden. Bei Mono-, Di- und Tetraglyme wurde hingegen nur ein geringer Temperatureinfluss beobachtet. Tatsächlich war in diesen Fällen die Reaktion thermodynamisch kontrolliert, was eine Bestimmung des Temperaturkoeffizienten und der Entropieänderung für die Reaktion ermöglichte. Andererseits fand von den drei Kronenethertypen nur bei Kronenether 6 eine Kointerkalationsreaktion mit Natrium statt. Gleichzeitig war dies aber der erste experimentelle Nachweis für eine elektrochemische Interkalation von Natriumionen mit Hilfe eines Kronenethers überhaupt.

Der dritte Teil dieser Arbeit behandelt die Themen, die in dem eingereichten Manuskript behandelt wurden (Erstautorautorschaft). Während in der vorangegangenen Publikation der Schwerpunkt auf der Rolle verschiedener Lösungsmittel bei der Kointerkalationsreaktion lag, widmet sich das eingereichte Manuskript "*Stable and Instable Diglyme-based Electrolytes for Batteries with Sodium or Graphite as Electrode*" der Stabilität von glymebasierten Elektrolyten mit unterschiedlichen anorganischen und organischen Salzen. Die Stabilität dieser Elektrolyte in Kontakt mit Natrium- und Lithiummetall sowie der Graphitelektrode wurde mit verschiedenen *in situ*- und *ex situ*-Methoden getestet. Für einige Salze konnten eindeutig erhebliche Nebenreaktionen mit dem Natriummetall nachgewiesen werden, die durch elektrochemische Impedanzspektroskopie (EIS) und OEMS mit Hilfe von Na│Na symmetrischen Zellen weiter quantifiziert wurden. Darüber hinaus lieferten systematische TEM-Untersuchungen in Kombination mit EDX auch Hinweise auf ein irreversibles Einfangen von Ionen im Graphit, wobei das Ausmaß stark von der verwendeten Salzart abhängt. (TEM und EDX wurden in Zusammenarbeit mit dem CIC EnergiGUNE von der Arbeitsgruppe von Prof. Teófilo Rojo durchgeführt). Die Wahl des Elektrolytsalzes hatte auch einen wesentlichen Einfluss auf die Änderung der Elektrodendicke während der Zyklisierung, was wiederum mittels elektrochemischer *in situ* Dilatometrie nachgewiesen werden konnte. Insgesamt lieferten die zahlreichen Studien zur Eignung verschiedener Elektrolytsalze ein klares Ranking für deren Eignung in der Reihenfolge NaOTf (am besten)≥$NaPF_6$>$NaClO_4$>NaFSI>>NaTFSI (am schlechtesten).

Schließlich wurde ein vierter Artikel mit geteilter Erstautorenschaft veröffentlicht. In dieser Publikation mit dem Titel "*Sodium Storage and Electrode Dynamics of Tin-Carbon Composite Electrodes from Bulk Precursors for Sodium-ion Batteries*" werden mehrere Anodenmaterialien getestet, um die Speicherkapazität im Vergleich zu reinen Graphitelektroden zu verbessern. Dazu wurde der Graphit zunächst durch Kugelvermahlung in Graphen-Nanoplättchen (GnP) umgewandelt. Die Daten aus dem galvanostatischen Zyklisieren und *in situ* Dilatometriemessungen belegen, dass der Kointerkalationsmechanismus dadurch weitgehend unterbunden und durch eine Insertionsreaktion ersetzt wird (höhere Kapazität bei gleichzeitiger Änderung des Spannungsprofils). Außerdem ist die Dickenänderung der GnP-Anodenelektrode während des Zyklisierens viel geringer als bei Graphitelektroden. Gleichzeitig erhöht die Zugabe von Zinn in diese Kohlenstoffmatrix die spezifische Kapazität bei gleichzeitig ausgezeichneter

Lebensdauer. Darüber hinaus zeigen die Ergebnisse der *in situ* Dilatometrie auch, dass das Hindernis, dass mit der großen Volumenänderung des Zinns während der Ioneninsertion zusammenhängt, durch diese poröse Wirtsstruktur auf Elektrodenebene effektiv gepuffert wird.

Die Arbeit endet mit einer Übersicht, welche die veröffentlichten und einige unveröffentlichte Ergebnisse zusammenfasst. Einige abschließende Kommentare zu den verbleibenden wissenschaftlichen Herausforderungen im Forschungsbereich werden gegeben und einige Vorschläge für weitere Experimente gemacht. Die Ergebnisse dieser Dissertation verbessern das Verständnis für die Verwendung von t-GICs in Natriumionenbatterien, für den Einsatz der *in situ* elektrochemischen Dilatometrie als Methode zur Charakterisierung von Elektrodenreaktionen zwischen Natrium und Graphit bzw. Graphen/Zinn-Kompositmaterialien und für die (elektro-)chemische Stabilität von Elektrolyten auf Glymebasis gegenüber Natrium und Graphit. Während einige Fragen geklärt und neue Aspekte entdeckt wurden, sind die erzielten Ergebnisse jedoch nicht vollumfassend, was eine klare Motivation sein sollte, Natriumionenbatterien und t-GICs in Zukunft weiter zu untersuchen.

2. Introduction

The increase in the world population combined with a rising living standard significantly rises the energy demand. As a consequence, energy supply has already become a challenge. Related to forecasts, energy rate demand will double from 14 terawatts (TW) (2010) to 28 TW (2050) (**Figure 1**) [1, 2].

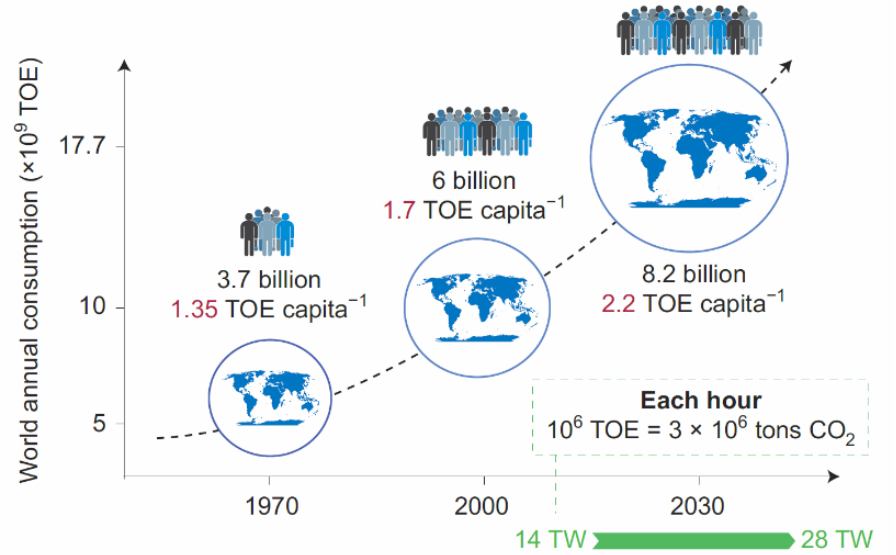

Figure 1. Past, present and forecast of the world's energy needs up to 2050. With the changing lifestyles of an increasing number of inhabitants, our energy rate demand will double from 14 TW (2010) to 28 TW (2050). TOE = ton of oil equivalent. Illustration: © Macmillan Mexico/Haide Ortiz Ortiz, Mario Enrique Ramírez Ruiz. [1]

While a growth in energy demand is likely unavoidable, the major challenge will be to meet this demand while at the same time reducing CO_2 emission and the use of fossil fuel resources which are finite. Unfortunately, the consumption of fossil fuels caused a large increase in CO_2 emission. Therefore, advanced renewable energy technologies are needed to be developed. This also will include developing suitable energy stores that can supply energy on demand for different applications.

2.1. Renewable Energy Supply

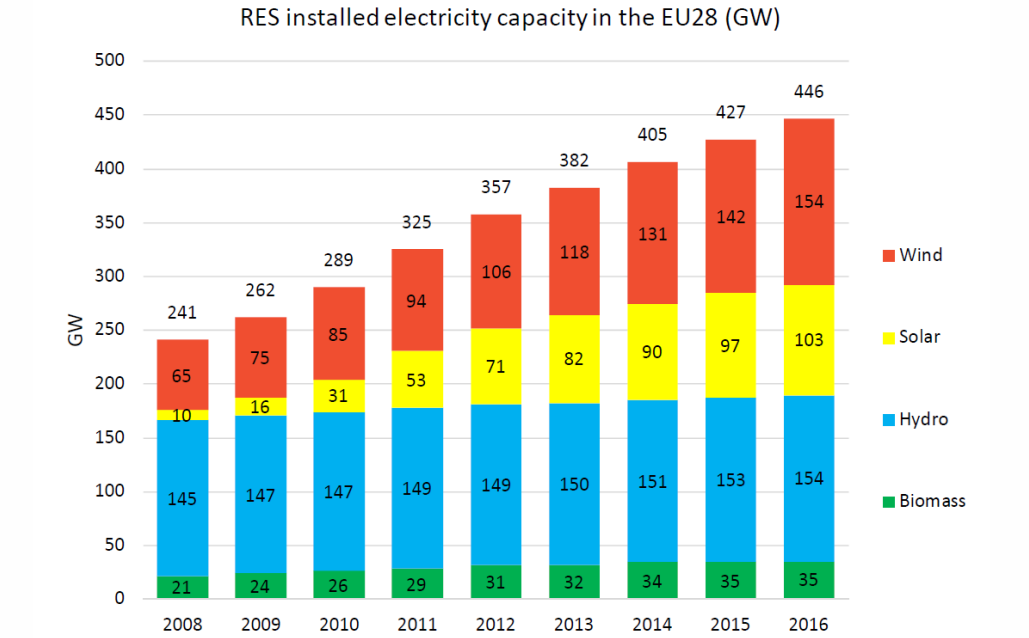

Figure 2. Development of renewable power generation installed capacity (2008-2016, GW), EU28. RES: Renewable Energy Sources [3].

Related to European Commission announcements, in Europe, from 2008 to 2016, the installed capacity of renewable electricity supplies almost doubled, in terms of power from 240 gigawatts (GW) to 450 GW (**Figure 2**) [3]. This growth trend is highly related to the reduction in the cost of renewable energy source technologies. Also, this trend is supported by policies such as reverse-auction mechanisms for large installations, etc.

Currently, wind energy and solar photovoltaics are the two major and fastest growing technologies. More investments are given to these low carbon emission renewable energies and results are seen in the market. To illustrate this, in 2017, the energy delivered by wind turbines in Denmark reached up to 44 % of the electricity consumption of Denmark [4]. Along with this development, the storage of electrical energy has become more and more important.

2.2. Energy Storage Systems

There are different forms of energy such as mechanical, gravitational, magnetic, nuclear, thermal or heat, chemical or electrical, etc. Here, the main interest is to store electrical energy by considering renewable sources. Electrical energy storage refers to a process of electrical energy conversion from a source into a storage form for converting back to electrical energy when needed. Energy storage systems for large scale applications can be split into four main groups by name chemical/electrochemical, mechanical, electrical and thermal energy storage [5-7].

1) **Mechanical storage**: It is accepted as the one having the highest storage capacity with around 95 % share of worldwide storage capacity [8] (**Figure 3**). In 2012, this number was 99 % [9]. Especially, for pumped hydro electrical and compressed air storage technologies, this level can reach up to 1 GW of discharge power [6]. However, the discharge duration can be considered as the drawback as it is at the level of hours, which is much higher compared to other types. Other than the above-mentioned examples, flywheels can be more suitable for intermediate storage which can deliver various power within seconds up to 10 megawatts (MW) [10]. The overall capacity of this technology is quite limited, however. Therefore, pumped hydro electrical energy storage is the most effective and developed technology. Installations have a lifetime of up to 70 years [8].

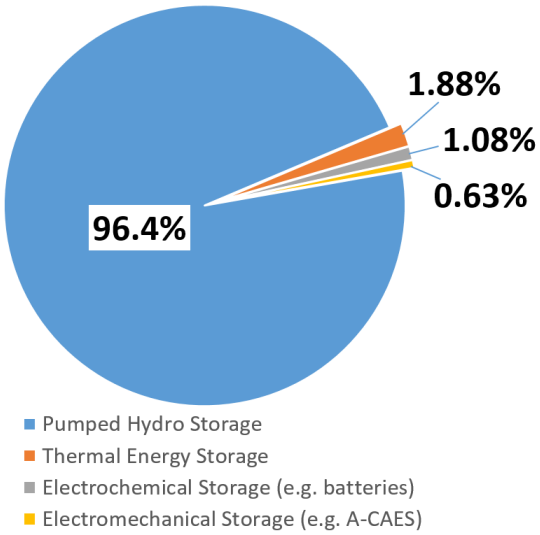

Figure 3. Total installed capacity of storage technology. Adopted from mid-2017 data [8] (Data is modified after the reference). A-CAES : Adiabatic Compressed Air Energy Storage.

2) **Thermal storage**: Heat can be stored as sensible heat, thermochemical and latent heat. In *sensible heat* storage, the energy is stored by increasing the temperature of a solid or liquid. The stored energy depends on the specific heat of the material. In *latent heat* storage based on the energy exchange during the phase change of the material between the solid, liquid and gas phases. In *thermochemical* storage depends on the formation of molecular bonds in complete-reversible chemical reactions [11]. In terms of application, such systems can be classified into low and high temperatures due to their operating temperatures. The thermal battery is an important technology in this group. The invention goes back to World War II and such batteries are even used to absorb energy exhaust heat from the rocket during launching the rockets [12]. Currently, solar thermal energy is very attractive to be stored by this technology. Just as an example, related to the study in 2014, 25 GW is achieved in Spain [13]. As a drawback, the cycle efficiency of such systems is low (30-60 %) [8]

3) **Electrical storage**: The main examples of this group are superconducting magnetic energy storage, capacitors, and supercapacitors which are also called as electrical double-layer capacitors (EDLCs).

   In Superconducting magnetic energy storage (SMES), the energy is stored in direct current (DC) electricity. The current is carried by the conductor operating at cryogenic temperatures. At such low temperatures, the conductor is a superconductor and it has no resistive losses virtually due to its own magnetic field production. This system can supply tens of MW of power in seconds [14]. The high power supply in a short period of time is the main characteristic [10].

   In capacitors technology, electrical energy is stored in an electric field. The effect of a capacitor is represented as capacitance. A capacitor is a component designed to add capacitance to a circuit. A capacitor component has at least two electrical conductors separated by a dielectric medium [15].

   In supercapacitor technology, storage of charge is achieved by adsorbing electrolyte ions onto the surface of electrode materials [16]. By the motion of the ions between electrodes, charging and discharging are performed. "Regular double layer capacitance arises from the potential-dependence of the surface density of charges stored electrostatically (i.e., non-faradaically) at the interfaces of the capacitor electrodes.[17]" Both capacitors and supercapacitors have the same working principle. However, supercapacitors have several orders of magnitude higher energy density than capacitors [18]. Supercapacitors have several types such as electric double layer capacitors, pseudocapacitors, and hybrid capacitors. Pseudocapacitors have a different charge storage mechanism than EDLCs [19]. They are also faradaic in origin, but during the transfer of charge from the electrolyte to electrode, electrosorption, reduction-oxidation reactions and intercalations may take place [20]. On the other hand, hybrid capacitors utilize faradaic and non-faradaic processes to store charge. This type of supercapacitors gained interest as they achieve energy and power densities greater than EDLCs [20]. Related to their storage mechanisms, pseudocapacitors, and hybrid capacitors can be accepted as in the groups of both electrical and chemical storage.

4) **Chemical/Electrochemical storage**: Chemical energy storage makes use of the bonding energy of chemical compounds. The major representatives of this storage type are batteries, which store and release energy by electrochemical reactions in a single device and sustainably synthesized chemicals such as hydrogen gas, which is being produced by electrolysis and converted back on demand to water by a fuel cell, for example. While chemical storage is more suited for storing larger amounts of energy, electrochemical storage is desirable due to its high overall efficiency [21]. Flow batteries can be considered as an intermediate approach.

   In the working principle of flow batteries, the electrolyte types, stored in the tanks, are pumped through a central reaction unit and the current is delivered or applied by redox reactions. The salts in fluid electrolyte media are active materials. The advantage is that the power capability depends on the reaction unit and the amount of energy can be designed by the size of the tank. [21] Up to 10 MW power capacity can be reached [10]. This system has a large cycle life over 10,000 cycles. The most popular example is the vanadium redox flow battery. Unfortunately, the cost of this technology is still too high [21].

   Fuel cells are energy converters and convert the free energy of a chemical reaction into electrical energy [22]. There are several types of fuel cells such as the polymer electrolyte membrane (PEM) fuel cells, direct methanol fuel cells, solid oxide fuel cells, etc. The working principle varies slightly from one to the other. The most prominent example is the PEM fuel cells in which hydrogen gas enters and splits into protons by the help of a catalyst and the electrons are transferred to do work. Once the protons move through the electrolyte and reach the cathode, they react with oxygen and the electrons to create water [22]. In fact, the reaction is the reverse process of electrolysis. and H_2 and O_2, are combusted as the fuel, and electricity is produced instead of heat energy being liberated [23]. Despite the progress over the last decades, fuel cells still are more a niche market [23].

   Finally, batteries as a group can be considered as the most relevant electrochemical energy store and they are widely used in different types of applications from small scale (mobile energy storage) to large scale (stationary energy storage). Up to 10 MW of power can be supplied within minutes related to the type of design [10]. A battery consists of one or more electrochemical cells [24]. They have internal storage capability without the requirement of an external source. By a different way, batteries can be categorized as primary and secondary. If a battery cannot be recharged, it is named as the primary battery. In this category, the electrochemical reaction cannot be reversed. The most popular examples are alkaline batteries. On the other hand, when the electrochemical reaction can be reversed by applying a certain voltage, they are named as a secondary battery which is also referred to as a rechargeable battery.

2.3. Basic Working Principle of Batteries and Type of Batteries

A battery converts the chemical energy within its active materials into electrical energy by spatially separated oxidation/reduction (redox) reactions occurring at two different electrodes. A cell consists of an anode (place of oxidation) and a cathode (place of reduction) which are separated by an ion-conducting electrolyte. In most cases, the electrodes are solid

compounds whereas the electrolyte is a liquid. Once the electrodes are dipped into the electrolyte media and connected to each other via an external load, discharge is expected. Electrons flow through the outer circuit while ion flow within the electrolyte leads to charge compensation. Anions migrate to the anode while cations migrate to the cathode. During the discharge process, oxidation occurs at the negative electrode (anode) while reduction occurs at the positive electrode (cathode). The reason for this electron and ion motion is the potential difference created by the dissimilar electrodes placed into the electrolyte media. Each material has its own reduction/oxidation potential related to its nature [8, 21, 24]. There are many different types of rechargeable batteries. However, only some of them such as lead-acid, nickel cadmium (Ni-Cd), nickel-metal hydride (Ni-MH), sodium-sulfur, zebra, metal-air and lithium-ion batteries (LIBs) are relevant at an industrial level. In fact, the total rechargeable battery market is by and large dominated by lead-acid and lithium-ion batteries.

Lead-Acid

Lead acid batteries are the low price and easy manufacture batteries. It gets its name from the negative electrode, lead (Pb) and the acid ($H_2SO_{4(aq)}$) used as the electrolyte. During discharge, Pb is oxidized at the negative electrode forming solid lead sulfate ($PbSO_4$) with the electrolyte solution. On the positive electrode, lead dioxide (PbO_2) is reduced and forms $PbSO_4$ as well. Although this type of battery has a comparably low energy and power density and shows limited cycle life compared to other competitors, the low cost and the wide operational temperature window are very attractive [24]. Therefore, the market share of lead-acid batteries is the highest one from 1990 to 2016 (**Figure 4a**). Also in terms of investments and sales, in 2016, more than half of the 65 billion dollars of battery market is dominated by this battery technology. In terms of storage capacity, more than 0.35 GWh of energy is stored into lead-acid batteries. Another advantage is that more than 97 % of all battery lead is recycled. Therefore, it is at the top of the list of batteries which can be recycled [24].

Nickel Cadmium (Ni-Cd)

This type of battery consists of cadmium as the negative electrode and a metal grid containing a paste of nickel oxide hydroxide (NiOOH) acting as a positive electrode. And as an electrolyte, an aqueous solution of potassium or sodium hydroxide is used. It is very reliable with long life at high discharge rates and over a wide range of temperature. Although its cost is higher than lead-acid batteries, the energy and power densities are higher [24]. Due to the toxicity of cadmium, however, starting from the early 1990s Ni-Cd batteries started to be replaced by Nickel-Metal Hydride (Ni-MH) batteries. Also, LIB technology was also growing and was a competitor to Ni-Cd batteries [25]. Especially, LIBs had higher voltages as compared to Ni-Cd batteries. In addition, higher energy and power density properties of LIBs were superior to Ni-Cd cells. The costs of lithium-ion batteries in the 1990s were, however, much higher as compared to Ni-Cd batteries [25].

Nickel-Metal Hydride (Ni-MH)

This type of battery was introduced to the market in the late 1980s having higher energy, power and cycle life than lead acid and nickel-cadmium batteries. Nickel hydroxide ($Ni(OH)_2$) as a positive electrode and metal hydride (MH) as a negative electrode are used in this technology [24]. For the negative electrode, $LaNi_5$, $TiMn_2$ or $ZrMn_2$ are preferred electrodes.

Although the studies go back to the 1960s, this type of battery is introduced into the global market in 1989 for the use of portable PCs. Since then, it started to gain a place in the

industry. In 2008, nearly 10 % market share of the total rechargeable battery market was for Ni-based batteries [24]. However, this share is slowly decreasing over the last years due to the rise of Li-ion batteries [8, 26] (**Figure 4a,b**).

Sodium-sulfur

High temperature

The high temperature (> 300 °C) sodium-sulfur battery is developed since the 1960s[27]. This battery is based on molten sodium as an anode, molten sulfur as a cathode and beta alumina as a solid electrolyte. However, the technology also has certain limitations such as the limited utilization of sulfur, maintenance and safety issues arising from the use of liquid sodium at high temperatures [27]. As a safer alternative, the ZEBRA (sodium-nickel-chloride) battery was developed. The battery is assembled in the discharged state. The positive electrode consists of nickel powder and NaCl. During charging, $NiCl_2$ forms while molten sodium forms at the negative electrode. Beta-alumina (β"-Al_2O_3) is used as an ion conducting separator. The positive electrode also contains $NaAlCl_4$ as an additional electrolyte which melts at around 150ºC. The ZEBRA battery operates at temperatures between 270-350 ºC [28]. Despite these advantages, the technology is still awaiting its large scale commercial breakthrough.

Room temperature

Since 1980s metal-sulfur batteries operating at room temperature are also explored. Most research is currently done on lithium-sulfur batteries due to their very high theoretical energy density. During discharging, lithium reacts with sulfur to form lithium sulfide (Li_2S) at the positive electrode. The reaction is, however, very complex and many intermediate polysulfide species form during charging and discharging which lead to limited cycle life. Moreover, the formed sulfides are poor conductors which require to add a lot of additives. Despite the recent improvements, the lithium-sulfur battery still awaits is mass market production. Along with the strong interest in lithium-sulfur batteries, also sodium-sulfur, potassium-sulfur and magnesium-sulfur batteries are being explored. [29, 30]

Metal-air

Metal-air batteries are based on reactions between metals as anode and oxygen (which is taken from the air) at the cathode. Therefore, metal-air systems are capable of releasing an extremely high specific energy. To illustrate this, the theoretical specific energy values for a Li-air battery with Li_2O_2/Li_2O as discharge products are close to the combustion energy of gasoline which is one of the most energy dense liquids [31]. According to the available research, Li-air, Na-air, Zn-air, Mg-air, Al-air, and K-air batteries are proposed [32]. Despite the promises, there are several bottlenecks that hamper the development of any practical rechargeable metal-air battery to date. For example, the intrinsic slow reactions, high overpotentials and poor reversibility of oxygen chemistry are the major obstacles on the cathode side [31].

Lithium-ion (Li-ion)

Due very low reduction potential and low weight, lithium has been attractive for batteries and research into lithium batteries began in the 1950s. Primary lithium batteries were commercialized in the 1970s. The development of secondary battery took longer time. In

1991, Sony Corporation Battery Group introduced a rechargeable lithium-ion battery having excellent cycle life and a higher level of intrinsic safety by using graphite and $LiCoO_2$ [33-35]. Shortly after, this battery was also released by a joint venture of Asahi Kasei and Toshiba in 1992. This was the first example for graphite anode used in LIBs. Previously, there were studies related to lithium intercalation into graphite. However, this is the first commercial application of LIB by using graphite as the anode (further details will be given in ***Section 3.1***.).

During the last decade, invested money into LIB technology increased extremely, therefore, in 2016, LIBs have a large rise in market share (**Figure 4a**). It is due to its high voltage, high energy density, and long cycle life. The total market in GWh is currently still larger for lead-acid technology as compared to LIB technology. This is large because of the wide-spread use of the lead-acid battery in industrial applications as well as for starter batteries in cars (**Figure 4b**).

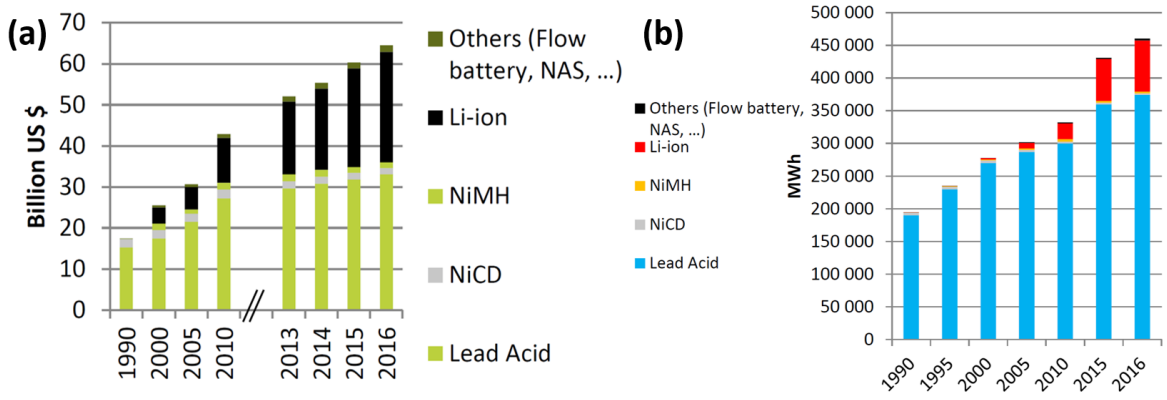

Figure 4. From 1990 to 2016, the worldwide battery market shares in terms of a) money and b)energy capacity [36].

As a footnote to the discussions related to the rechargeable battery market, the energy storage systems are mainly required by industry which prefers lead-acid batteries. Compared to the energy capacity required by industry, the energy requirement of portable devices is much lower and therefore, the market share of portable batteries is low. However, the development of electrical vehicles is currently boosting the demand for LIBs. As a forecast, in 2025, the market share of LIBs is expected to be higher than others in terms of stored energy and the invested money[37]. Parallel with electric vehicles, the industrial use of LIBs will also rise.

3. State of Art

3.1. Graphite and Graphite Intercalation Compounds (GICs)

The discovery of suitable negative electrode materials for lithium-ion batteries was more complicated than the positive electrode materials. As being low-cost, easily accessible and highly conductive, carbon-based materials were initially taken into consideration.

Considering the carbon allotropes, graphite is certainly the technologically most important one. Within this structure, graphene layers are stacked with ABAB sequence in c axis by forming weak van der Waals bonds (π-π interactions) [38, 39]. Under suitable conditions, molecules, atoms or ions can easily penetrate into this host material forming the very diverse family of graphite intercalation compounds (GICs) [38, 40].

GICs, especially for the preparation of expanded graphite, can be prepared in different methods. These methods depend on the hosted components such as Brønsted acids (e.g., sulfuric acid, nitric acid, and acetic acid), metal chlorides ($FeCl_3$, $CuCl_3$, and $ZnCl_2$) and alkali metals in a solvent [38]. The first examples of GICs are from C. Schafhaeutl in 1840 [41] and B. Brodie in 1851 [42]. They tried to describe graphite bisulfate synthesis. The reported GICs consisted of graphite layers intercalated by HSO_4^- and H_2SO_4 molecules [38]. Later on, the ability of graphite to store alkali ions was realized but it took many years to introduce them into lithium-ion batteries. In fact, the development for cathode electrode materials was earlier than for anode materials. Some important cathodes were $LiMn_2O_4$, $LiCoO_2$ and $LiNiO_2$ [35]. The first report related to $LiCoO_2$ was given by Goodenough and co-workers in 1979, for example [43, 44]. However, electrochemically, the first trial of graphite as anode material for lithium intercalation and release was in 1982-1983 by Yazami and Touzain [40]. Although they have used a solid electrolyte based on polyethylene oxide and lithium perchlorate (formula $P(OE)_8$-$LiClO_4$), this study provided the scientific basis for the use of graphite in such an application. Actually, in the early 1960s lithium-based batteries are tested by using metal halides and the majority of these works are performed by using propylene carbonate (PC) [45-47]. This progress is due to the findings from the thesis of Harris (under the supervision of Tobias) [45] that can be accepted as a milestone. He tried several different solvents for Li-electrodeposition. After a long time, in 1967, a study from Rao and Hill represented the very first report solvent co-intercalation which is causing graphite exfoliation by gassing of PC [48].

On the other hand, Akira Yoshino made the first prototype of a secondary battery by using $LiCoO_2$ as positive electrode and polyacetylene as the negative electrode in 1983 [49]. He tried several carbonaceous materials as the negative electrode. He found that carbonaceous material with a certain crystalline structure provides greater capacity without causing the decomposition of PC. Therefore, in 1985, Yoshino patented a battery with $LiCoO_2$ as the cathode and carbonaceous material with certain crystallinity as the anode material [50, 51].

It was shown in some studies that the intercalation of lithium ions was complicated due to solvent reduction and disruption of the carbon structure [52]. Earlier studies related to electrochemical lithium intercalation into graphite showed that by the use of PC based electrolytes, decomposition products of PC were observed on the surface of graphite [53]. PC was preferred at that time, as it was used highly in primary lithium cells. In the study of Fong *et al*., this problem of irreversible behavior is associated with the use of PC as a single solvent [54]. Therefore, as a co-solvent, ethylene carbonate (EC) is added into the electrolyte. The reversibility of lithium intercalation into graphite is improved. The tests are performed for graphite and also for petroleum coke cells. In both of the cases, the cycling performance of

the electrode is improved by the use of PC/EC as compared to PC. It was found that EC as a co-solvent creates a protective lithium ion conducting surface film. The surface layer is named solid electrolyte interphase (SEI) after a concept introduced by Peled [55-57]. The SEI forms during the first lithiation of the graphite electrode before the actual ion intercalation takes place. The SEI is ionically conducting and mechanically robust and hinders further electrolyte decomposition. The formation of an efficient SEI on the graphite surface was essential for enabling reversible intercalation of lithium ions [54].

3.2. Use of Graphite in Lithium Ion Batteries – binary GICs

In the first commercial Li-ion batteries, hard carbon had been used as a negative electrode. Reversible intercalation of ions into hard carbon is possible. Due to being disordered, cycling is done without a staging transition [58]. On the other hand, the electrolyte decomposition during cycling was a great obstacle for using graphite. After this problem was overcome; in today's LIBs, graphite is chosen as the active material for the negative electrode. As the crystallinity is useful for long term cycling with good performance, graphite is preferred as compared to hard carbon. Therefore, the battery containing graphite can have a high cycle life with high retention. Moreover, by the intercalation of lithium ions into graphite, high capacity is gained ($q_{\text{theoretical}} = 372$ mAh g^{-1}) [54, 59, 60]. In fact, the practical reversible capacity of such batteries is 360 mAh g^{-1}. This is close to the theoretical value with low and flat operational plateaus at 0.1-0.2V vs. Li^+/Li [58, 61]. The electrode reaction based on intercalating naked lithium ions can be generalized as follows:

$$\mathrm{Li}^+\left(solv\right)_n + x\cdot\mathrm{C} + e^- \underset{\text{intercalation}}{\overset{}{\rightleftharpoons}} \mathrm{LiC}_x + n\cdot solv \qquad (1)$$

By electrochemical reduction, Li^+ ions are intercalated in between graphene layers and a binary graphite intercalation compound (*b*-GIC) with the final stoichiometry of LiC_6 is formed (reaction 1) [58, 62 63, 64]. There are several intermediate stages formed during lithiation which can be followed by XRD. The order from the highest lithiated form to the lowest is; the first stage (LiC_6), the second stage (LiC_{12}), the third stage (LiC_{27}), the fourth stage (LiC_{36}) and the eighth stage (LiC_{72}).

3.3. Rise of Sodium Ion Batteries

Obviously, there is a rapid growth of the battery market and the demand for lithium and other elements such as Co that are relevant for LIB technology will put pressure on the supply chains and resources. Low-cost alternative cell chemistries based on abundant elements are therefore required, especially considering grid storage or the rising market for short-range/low-speed electric vehicles such as e-scooters. Sodium-ion batteries (SIBs) appear as an attractive alternative for the future. Motivated by the large abundance of sodium, research efforts on SIBs increased significantly [58, 65-73] with the aim to develop high energy batteries with fewer resource constraints. This also includes the substitution of other expensive components of LIBs, most importantly using Mn- and Fe-rich instead of Ni- and Co-rich cathode materials or by using aluminum as anode current collector. Although the energy density of SIBs is lower compared to LIBs, it is higher compared to other rechargeable battery technologies. There are also some specifics related to size effects *(compare ion radii)* which can lead to advantages over LIBs[70].

Similar to Li-ion batteries, hard carbons are also applied to Na-ion batteries and success was obtained before graphite could be used in SIBs. Electrochemical reversible

insertion/extraction of sodium-ions into hard carbon was reported by Stevens and Dahn in 2000, for example [74]. A reversible capacity of 300 mAh g^{-1} is typically gained.

As reversible intercalation of lithium ions by forming *b*-GICs with the stoichiometry of LiC_6 is possible, one could easily imagine using graphite in SIBs as well. Unfortunately, the formation of sodium-rich *b*-GICs does not take place and experimental values for the capacity are in the range of 20-40 mAh g^{-1} (or lower) [65, 75-78]. This was often explained with the larger ion size of sodium. On the other hand, the even larger alkali metals can form *b*-GICs (KC_8, RbC_8, CsC_8) which raises questions on the special behavior in case of sodium.

In theoretical studies, it is suggested that the formation of sodium-rich *b*-GICs is thermodynamically not favorable [64, 79, 80]. Nobuhura *et al.* [64] links this behavior of instability to the stretching of the C-C bond within the graphene. Liu *et al.* [79] systematically compared the energy balance between ionization energies and ion-substrate interactions for a series of alkaline and alkaline earth elements. Within the alkali metals (A), only sodium represents the positive formation energy while forming AC_6 and AC_8 [64]. Moreover, Na, as well as Mg, show the weakest binding energy to many substrates in general [79]. Based on DFT calculations, Moriwake *et al*. interestingly suggested Li (rather than Na) should be seen as an exception within the series of alkali metal b-GICs [80].

3.4. Use of graphite in sodium-ion batteries – ternary GICs

As the use of graphite in SIBs showed only disappointing results, other strategies had to be employed. In 2014, Jache *et al.* demonstrated that the reversible intercalation of sodium ions into graphite can be achieved using diglyme as electrolyte solvent [81]. The main conceptual difference is that for this solvent, sodium-ions can intercalate as "solvated ions" into the graphite structure. This process is called a co-intercalation reaction and can be generalized as follows

$$\mathrm{Na}^+\left(solv\right)_n + x\cdot\mathrm{C} + e^- \underset{}{\overset{\text{intercalation}}{\rightleftarrows}} \mathrm{Na}\left(solv\right)_n \mathrm{C}_x \qquad (2)$$

This reaction is different from reaction (1) where the solvation shell is completely stripped from the ion during charge transfer. Co-intercalation of solvent molecules along with the ions leads to so-called ternary graphite intercalation compounds (*t*-GICs) with the formula of $Na(solv)_nC_x$. It is important to remember that t-GICs have been known for decades and were mostly prepared by chemical methods with the aim to explore out the structural variety of this material class [82-84]. The electrochemical formation over many cycles by electrochemical methods was, however, only realized quite recently. The reaction including diglyme as a co-intercalating solvent is

$$\mathrm{Na}^+\left(diglyme\right)_n + x\cdot\mathrm{C} + e^- \underset{}{\overset{\text{intercalation}}{\rightleftarrows}} \mathrm{Na}\left(diglyme\right)_n \mathrm{C}_x \quad n = 1 \text{ or } 2,\ x = 16\text{-}26 \qquad (3)$$

After this initial finding, a number of experimental and theoretical studies have been published in the last years as shown in detail in **Table 1**. Although the reaction is found to work very well over many cycles, many questions related to the exact structure, compositions and the dynamics of the reaction still remain under debate. Experimental and theoretical studies suggest values for n=1 or 2 and x=16-26 [81, 85-90]. For x = 20, the above reaction gives a theoretical specific capacity of 111.7 mAh $g^{-1}_{(graphite)}$. As in the case of b-GICs, the reaction for t-GICs proceeds over several intermediate phases (stages). At around 0.6V, a constant potential plateau contributing to about 25-30 % of the total capacity. A plateau represents

the two-phase region during this electrochemical reaction. Intercalation of solvated sodium ions starts below 1 V vs Na^+/Na finally ending with a stage 1 compound. During intercalation, a significant increase of graphene layer spacing occurs. The layer spacing of graphite increases from 3.35 Å up to about 11.3-11.9 Å during stage 1 formation. The volume expansion is in the range of 240 to 250 % [91, 78, 86, 88]. Although lattice expansion is too high, interestingly, this co-intercalation reaction does not destroy the graphite electrode. The crystal structure is preserved during cycling [91].

In many studies, $NaPF_6$ dissolved in diglyme is the preferred electrolyte. It is shown that the cyclability of this reaction is extraordinary up to 8000 cycles and also high current densities up to 30 A g^{-1} can be applied onto this reaction [92]. Other than diglyme, other types of linear ethers can be applied to this reaction such as mono- di- tri- or tetraglymes [78, 93]. Unfortunately, none of carbonate-based electrolytes could reveal any useful capacity for graphite in SIBs [78].

Table 1. Overview on different experimental studies on solvent co-intercalations with graphite by using sodium ion. Their used electrolyte solutions and main findings.

Cell type	Salt and Solvent	Cycle Number	Comments / Main findings	Ref.
Na/Graphite	NaOTf or LiOTf in Diglyme, $NaPF_6$ or $LiPF_6$ in EC/DMC	1000 cycles	Jache *et al*.; The first time, in 2014; Graphite can have 110 mAh g^{-1} of capacity	81
Na/Graphite	NaOTf or LiOTf in Monoglyme, Diglyme, Triglyme, Tetraglyme, Bis(methoxypropyl)ether (DPGDME), Bis(2-butoxyethyl)ether (Butyl-2G), 1,5-Dimethoxy-pentane (1,5-DMP), tetrahydrofuran (THF). $NaPF_6$ or $LiPF_6$ in EC/DMC.	50 cycles	Jache *et al*.; Some electrochemical properties such as capacity, retention, efficiency and over potential are compared. It is found that diglyme is electrochemically performing well within glyme series.	78
Na/Graphite	$NaClO_4$ in Monoglyme, Diglyme, Triglyme, Tetraglyme. $NaClO_4$ in EC/DMC	20 cycles	Seidl *et al*; Crystal structure changes and phase formations of graphite during cycling with glyme series. The crystal structure change of graphite depends on the type of glymes used during sodiation. But overpotential is slightly increasing during these cycles.	91
Na/Graphite	$NaPF_6$ in Monoglyme, Diglyme and Tetraglyme	200 cycles	Kim *et al*. A comparative study of several glymes by experimental and computational methods in order to understand the intercalation mechanisms. There are two layers of ions together with glymes going in between graphene layers while forming stage 1 compound.	94
Na/Graphite	NaOTf in Monoglyme, Diglyme, Triglyme, Tetraglyme, Pentaglyme, Crown Ether 4, Crown Ether 5, Crown Ether 6.	50 cycles	Goktas *et al*. The electrochemical properties of glymes from monoglyme to pentaglyme are examined. The kinetic and thermodynamic properties of the reaction are discussed as a function of temperature. The first time, crown ethers are used for electrochemical co-intercalation of sodium ions into graphite by giving 75 mAh g^{-1} capacity.	93
Na/Graphite	$NaPF_6$ in Diglyme	8000 cycles	Cohn *et al*. The superior performances of graphite in SIBs are tried to be underlined. High rate capabilities up to 30 A g^{-1} and high cycle life of 8000 cycles are gained.	92
Na/Graphite	$NaCF_3SO_3$ in Tetraglyme	6000 cycles	Zhu *et al.* A study was done by using $NaCF_3SO_3$ in tetraglyme and they reached up to 10 A g^{-1} for 6000 cycles. For the first time, graphite in used in full cell in SIBs	95
Na/Graphite	$NaClO_4$ in Tetraglyme, EC/DMC, EC/DEC	500 cycles for half cell	Hasa *et al*.	96

		and 100 cycles for full cell.	Trial of graphite with a cathode to make a full cell. High rate as high as 10 C is applied to the full cell.	
Na/Graphite	Sodium−diglyme-d_{14}−GIC was prepared by a solution-phase reaction.	-	Gotoh *et al.* NMR study to prove t-GICs. The formation of t-GICs with a stoichiometry $C_{22-26}(diglyme)_{1.8-2.2}Na_{1.0}$ is proven by NMR studies.	[97]
Na/Graphite	-	-	Jung *et al*. Study for modeling Due to the co-intercalation mechanism, diglyme can easily create Van Der Waals interactions and diffuses fast through the graphite lattice. Diffusion is faster compared to the case of lithium.	[98]
Na/Graphite	$NaPF_6$ in tetraglyme, diglyme, monoglyme, THF, DOL, DMC, DEC, EC, PC.	-	Yoon *et al*. The computational studies are performed for the electrolytes of $NaPF_6$ salt in carbonate solvents such as EC/DMC, DMC, DEC, PC, and ethers such as THF, DOL, DME, DEGDME, TEGDME. And they concluded that for the reversible co-intercalation the high solvation energy of Na and the chemical stability of Na-solvent complexes are important parameters.	[89]
Na, Li, K / Graphite	MCF_3SO_3 M= Na, Li or K in tetraglyme	60 cycles	Kim *et al.* Comparisons of Li, K and Na are done by using tetraglyme based electrolyte. Current density is applied up to 3 A g^{-1}.	[99]
Na/Graphite	NaOTf in diglyme	100 cycles	Goktas et al. The co-intercalation mechanism is explained by testing the changes in electrode thickness by the method of *in situ* dilatometry. Graphite is likely the first example of SEI-free graphite anode material in SIBs	[100]
Na/Graphite	$NaPF_6$, $NaClO_4$ and NaOTf in diglyme. $NaPF_6$ in EC/DEC, DMC, THF LiPF6 in TEGDME, EC/DMC	2500 cycles	Kim et al. A discussion is made between various salts such as $NaPF_6$, $NaClO_4$ and NaOTf in diglyme and there was no clear significant effect of anions on electrochemical reactions. 10 Ag^{-1} is applied.	[101]
Na/Ordered Graphite	$NaPF_6$ and NaOTf in diglyme $NaPF_6$ in EC/DEC	400 cycles	Cabello *et al.* Coke is converted into the highly ordered graphitic structure. The capacity changes and intercalation mechanism changes are discussed. There is not much difference between $NaPF_6$ and NaOTf in electrochemical properties. Except, $NaPF_6$ has a slight higher plateau potential than NaOTf. Full cell tests are also applied.	[102]
Na/Graphite	NaI and NaOTf in diglyme	1000 cycles	Jache *et al.* Comparisons are done between the performances of NaI and NaOTf, no significant difference was found.	[81]
Na/Graphite	NaFSI in tetraglyme	Over 20 cycles	Maibach *et al.* It is proven by XPS (X-ray photoelectron spectroscopy) method that electrolyte of NaFSI in diglyme creates partial SEI formation on the surface of graphite electrode [103]. It is clear that there is an excess sodiation capacity and large irreversible capacity during the cycles and plateau potential shifts by cycle. Also, the retention during cycling is not high which is not expected.	[103]
Na/Graphite	$NaClO_4$ in diglyme LiTFSI in diglyme	Several cycles	Leifer et al. Atomic proximity of Na diglyme and Li diglyme complexes to the graphene planes are evidenced. Li-diglyme complex creates a tighter interaction with graphene sheets than Na-diglyme complex. The motion of complexes in graphite complex is discussed. The mobility of the complexes is linked to their interaction with the graphite lattice.	[104]

4. Main Aim of Thesis and Approach

The research project related to this thesis started in 2016, i.e. about two years after the initial report on the reversibility of solvent co-intercalation reactions for sodium-ion batteries. **Table 1** shows that the research field quickly developed and about 20 publications have been published specifically on graphite used in sodium ion batteries in the meanwhile. However, in general aspect, the total number of studies related to sodium ion batteries containing graphite discussion is over 200. Despite this progress, many fundamental aspects of this type of reaction needed to be studied and better understood. The main aims of this thesis were to address aspects related to clarifying the reason for the excellent reversibility of the reaction, studying the dynamics of the electrode during cycling, studying the temperature dependence of the reaction, expanding the number of possible reactions and studying possible influences of the conductive salt on the reaction. Another aim was to increase the capacity of graphite using tin. The following sections will provide some more detailed information on the methodology used to address the research questions.

Most of the related studies were done at the Friedrich-Schiller-University Jena (Research group Prof. Adelhelm) but several cooperations were established to conduct more specialized experiments. A graphical overview is shown in **Figure 5.** Online electrochemical mass spectrometry (OEMS) was conducted in cooperation with the research group of Prof. Novak (Paul Scherrer Institute, Switzerland), TEM measurements were conducted in cooperation with the research groups of Prof. Rojo (CIC EnergiGUNE, Spain) and Prof. Langenhorst (Friedrich-Schiller-University Jena), and computational studies were done by the Mollenhauer group (Justus-Liebig-University Giessen, Germany). Viscosity and conductivity measurements of liquid electrolytes were done in cooperation with the Balducci group (Friedrich-Schiller-University Jena). Further, Raman spectroscopy studies were performed in cooperation with the Komaba group (Tokyo University of Sciences, Japan) during a one-month lab stay.

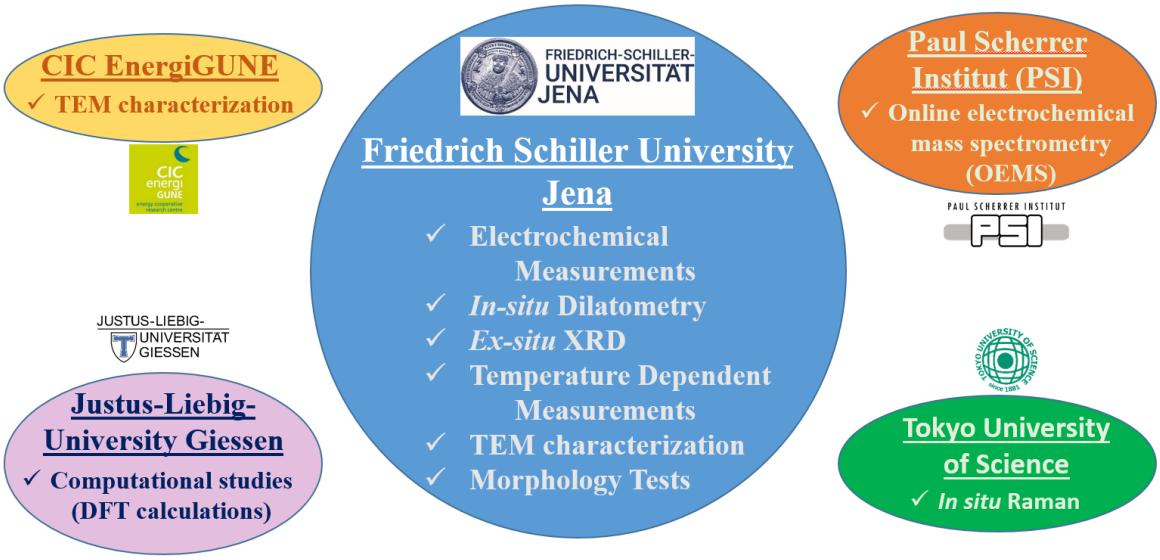

Figure 5. Important methods and collaborations.

4.1. Probing Anode Electrode Dynamics by *in situ* Electrochemical Dilatometry

This section gives an introduction into *in situ* electrochemical dilatometry (ECD) as a method for studying the dynamics of electrodes during ion insertion/deinsertion. The method allows to discuss some key questions:

* To what extent do electrodes expand/shrink during ion storage and release? Is the first cycle ("electrode activation") different from the following ones?
* How much do graphite, hard carbon, soft carbon, tin composite electrodes expand during cycling in sodium half cells? If there are differences, can we understand them?

During ion intercalation, co-intercalation or adsorption, the anode or the cathode materials undergo a volume change due to the crystal expansion. In a real application, continuous electrode expansion and shrinkage may lead to rapid electrode degradation and therefore limited cycle life. A first choice to follow changes in the electrode during cycling would be *in situ* XRD which provides information on crystalline phases. From this data, one can calculate the volume changes of the active material alone. Another approach is theory using e.g. DFT. For example, the intercalation of sodium ions into graphite by co-intercalation (**Figure 6**) leads to an increase in graphene interlayer distance from 0.335 nm to around 1.13 nm. On the other hand, one has to realize that electrodes commonly consist of many individual particles being held together by a binder. The porosity is typically in the range of 30 – 70 %, depending on how the electrodes are prepared. The important point is that the expansion/shrinkage of a crystal (as determined by XRD) will not automatically translate into the same expansion/shrinkage of the electrode. The latter can be followed by *in situ* electrochemical dilatometry (ECD) hence this method is a very useful complement. Considering practical application, determining the effective change of the electrodes during cycling is very useful for designing batteries with minimum overall volume changes. An advantage of ECD over XRD is that also the storage behavior of amorphous materials may be followed.

An *in situ* ECD system consists of a measurement cell connected to a potentiostat/galvanostat. The cell contains a capacitive sensor for recording one-dimensional displacements of the electrode (for details see ***Section 7.2***). This way, changes of the electrode thickness during galvanostatic charge and discharge (here discussed as "electrode dynamics") can be followed over several consecutive cycles, for example.

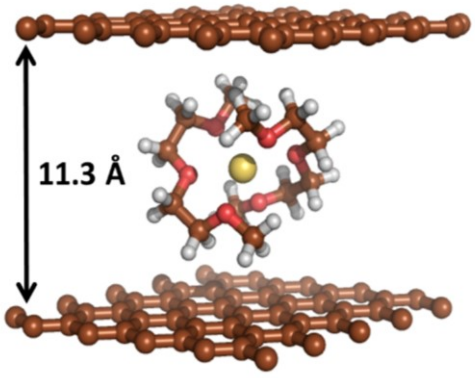

Figure 6. $Na^+(diglyme)_2$ complex intercalated into graphite calculated at PBE-D3/pw(PAW P) level of theory. Color code: carbon (brown), oxygen (red), sodium (yellow), and hydrogen (white) [100].

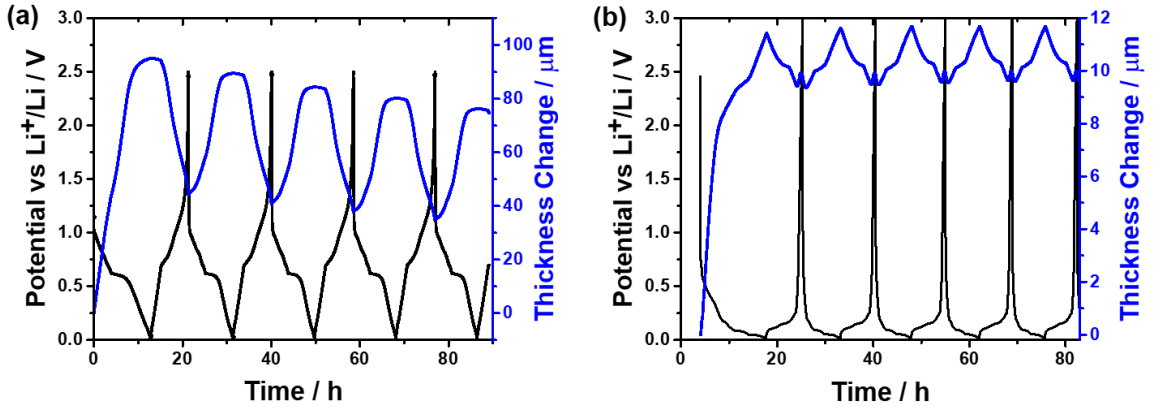

Figure 7. In situ ECD measurements on a) sodium co-intercalation into graphite from ether based electrolytes, 1M NaOTf in diglyme at C/10 (1C =110 mA g^{-1}); b) lithium intercalation into graphite from conventional carbonate based electrolytes 1M $LiPF_6$ in EC:DMC (Sigma Aldrich). Five cycles at current of C/10 (1C =372 mA g^{-1}) are shown. The initial thickness of the electrodes are about l_0=50 µm (without current collector) [100].

Typical results from the measurement are shown in **Figure 7**. **Figure 7a** shows the first 5 cycles of for a graphite electrode during the intercalation of sodium ions along with ether solvent molecules (co-intercalation). The black line shows the potential of the electrode, the blue line indicates the thickness change of the electrode. The initial thickness of the electrode is about 50 µm. As can be seen, sodiation causes a significant increase in electrode thickness, desodiation causes a significant shrinkage. Compared to the initial thickness of about 50 µm, the increase during the first sodiation is almost 200 %. The subsequent cycles show a difference of about 50 µm (100 %) between the sodiated and desodiated state, i.e. the electrode "breathes" during cycling. The changes in electrode thickness are obviously quite large for co-intercalation reactions. A measurement for conventional ion intercalation is shown in **Figure 7b**. The graph shows the result for the same graphite electrode but in this case, lithium is intercalated from carbonate based electrolytes. Comparing both graphs, one can see that the first cycle is exceptional in both cases, i.e. the thickness change is larger compared to all following cycles. The first cycle can be seen as an activation cycle which includes different phenomena such as particle restructuring, side reactions with the electrolyte, exfoliation and so on. The subsequent cycles have rather constant breathing but with a clear difference between the breathing levels. In the case of sodium, the breathing (50 µm, i.e. 100 %) is much larger compared to the case of lithium (2-3 µm, i.e. 4-6 %). The results therefore clearly show that dilatometry provides direct evidence for the kind of intercalation mechanism, i.e. co-intercalation takes place in case of sodium and solvent molecules enter the crystal structure together with the ion [81] (**Figure 6**). Therefore, the exfoliation of graphite and higher breathing in SIBs than in LIBs are expected consequences. As the expansion and shrinkage at x and y directions are negligible, the mentioned numbers can be assumed to be the volume changes. A closer comparison between both graphs also shows that the thickness change curve is more pointed for lithium and more rounded in case of sodium.

A more detailed discussion on the data is part of the publication "*Graphite as Cointercalation Electrode for Sodium-Ion Batteries: Electrode Dynamics and the Missing Solid Electrolyte Interphase (SEI)*" (shown in details in ***Section 5.1***).

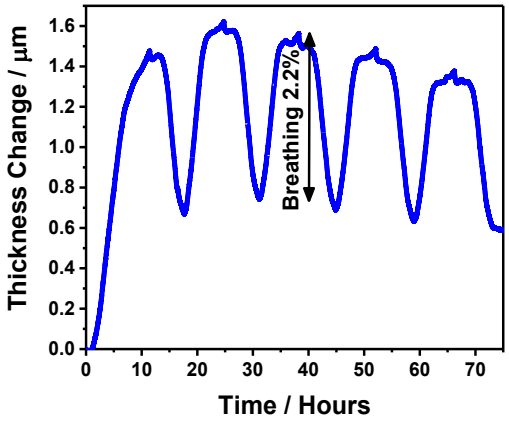

Figure 8. In situ ECD measurements at 50 mA g^{-1} over 70 hours of consecutive cycling for Hard Carbon (5 cycles) electrodes by using electrolyte of 1M $NaPF_6$ in 2G. Hard Carbon has 10 % CMC. The initial thickness of the electrodes are about l_0=37 µm (without current collector).

Apart from graphite, some other anode materials were also tested. In **Figure 8**, the breathing level of hard carbon in sodium half-cell is shown which amounts to around 2-3 %. In this experiment, the electrode was prepared using CMC as a binder and had a starting thickness is 37 µm. The cell was cycled in an electrolyte solution of 1M $NaPF_6$ in 2G. Comparing with **Figure 7a**, one can see that breathing is much smaller. This indicates that in the case of hard carbon, the insertion of sodium ions without solvent molecules takes place. Again, the dilatometry signal provides direct information on the storage mechanism. At this point, however, one has to emphasize that charge storage in hard carbon is more complex as several effects such as adsorption, pore filling and insertion are contributing. Interpretation of signals from graphite electrodes is therefore a bit more straightforward.

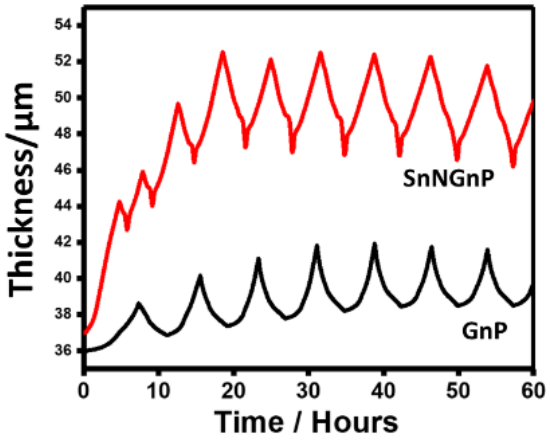

Figure 9. In situ ECD measurements at 50 mA g^{-1} over 60 hours of consecutive cycling for GnP (7 cycles) and SnNGnP (9 cycles) electrodes. Initial thicknesses for SnNGnP and GnP are 37 and 36 µm respectively [105].

Another example is shown in **Figure 9**. Here, ECD was used to follow sodium storage in electrodes made from graphene nanoplatelets (GnP) and a composite consisting of tin and GnP. GnP is a carbon-based material produced by ball milling of graphite showing a high surface area (270 m^2 g^{-1}). Comparing the result again with **Figure 7a**, one can see that there must be a change in the storage mechanism, as the breathing is much smaller for GnP (10 %) than for graphite (100 %). The difference is due to the structural loss of the graphite lattice as a result of the ball milling process (described in detail in ***Section 5.4***). In this study, the motivation to use GnP as anode material was not to use it as the active material for sodium

storage but instead as a flexible matrix to buffer volume changes of tin. Tin has a very high theoretical capacity for sodium storage ($q_{\text{theoretical}}$ = 847 mAh g^{-1}) combined with a volume expansion of 420 % (at the material level) during sodiation [106]. However, in this composite, the electrode was breathing only 14 % (58 wt % Sn). The results show that the dramatic volume change of tin on a materials level is not observed on the electrode level. The main reason for that is the porous structure of the GnP electrode which gives enough free space for tin to expand without causing too much change on the electrode level, hence minimizing the electrode breathing. As a consequence, the cycle life of this composite was found to be excellent. Details on these materials and the related experiment can be found in the related publication "*Sodium Storage and Electrode Dynamics of Tin-Carbon Composite Electrodes from Bulk Precursors for Sodium-ion Batteries*" [105] (shown in details in ***Section 5.4***).

Overall, the studies show that the ion insertion mechanism into the material affects the whole electrode dynamics. ECD allows to follow ion storage in electrodes over several cycles and provides information on the storage mechanisms. Moreover, results from ECD help to explain why composites, such as the discussed GnP-tin composite show very good cycle life despite the large volume expansion of tin on the materials level. As some comments to future projects, the effects of solvents, salts, binders, current densities, and temperature can be further studied by the ECD method.

4.2. Interface Stability vs Interphase Formation

The redox potential of anode materials is usually outside the stability limit of liquid electrolytes. This means that the interface between the electrode and the electrolyte is instable generally (but not always) leading to side reactions. These side reactions can lead to the formation of an interphase. In the ideal case, this interphase stops the side reactions leading to a "stable" electrode. Such stabilized electrodes can still work in electrochemical cells if the interphase is electronically insulating but ionically conductive. In this special case, the interphase is termed solid electrolyte interphase (SEI), after the initial concept by Peled [107]. The composition of the SEI is complex containing inorganic and polymeric parts. In the case of lithium, the inorganic compounds are thermodynamically very stable compounds such as LiF and Li_2O. As they are poor ion conductors, the SEI has to be very thin, i.e. in the range of a few tens of nm. The complex composition and the small dimension make it generally quite difficult to characterize the SEI. In this thesis, in order to better understand the interphases created on sodium and graphite electrodes, systematic studies were performed for diglyme based electrolyte solutions containing several different organic and inorganic conductive salts. The interphase properties of sodium and graphite are characterized by electrochemical impedance spectroscopy (EIS) and TEM. The stability of the electrolyte towards the electrodes during oxidation/reduction was followed by online electrochemical mass spectrometry (OEMS). Regarding the studied graphite and sodium electrodes, the thesis focused on answering the following questions:

- How "stable" are sodium and graphite electrodes in different sodium-ion conducting liquid electrolytes. Is an SEI formed or do the electrodes continuously degrade (along with gas evolution)?
- What is the influence of the conductive salt on the SEI? Can we observe differences by impedance spectroscopy?
- Is there a solid electrolyte interphase (SEI) on graphite electrodes operating with the co-intercalation mechanism?

A number of studies discussing the co-intercalation reaction of sodium with ethers into graphite has been published in the last years, see **Table 1**. The most popular electrolyte salts were NaOTf and $NaPF_6$ but also NaFSI and some others had been tested. Although the anion should not affect the reaction, the choice can be quite relevant considering the formation of the SEI, the Coulombic efficiency as well as the general stability of the electrolyte solution. This is not only relevant for the graphite electrodes targeted in this thesis, but also for sodium metal, which is the commonly used counter and reference electrode used for the experiments (as also will be discussed in ***Section 4.3***). As a first step, the stability of the electrolytes towards the sodium metal was therefore investigated.

As an example for the influence of electrolyte composition on the properties of sodium electrodes, impedance measurements on symmetrical Na|Na cells are shown in **Figure 10**. In all cases, diglyme was the electrolyte solvent. A highly resistive interphase is formed in the case of NaTFSI and NaFSI while much smaller values for areal resistance are found for NaOTf and $NaPF_6$ as salt. The results show that the areal resistance can easily change by one to two orders of magnitude, depending on the salt used.

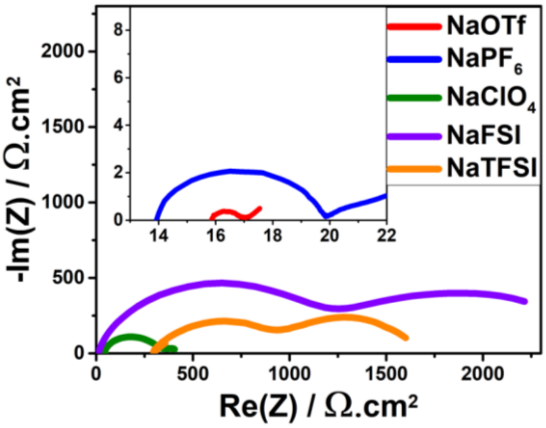

Figure 10. Impedance measurements for Na|Na symmetric cell after 48 hours of waiting at OCV.

Another method to study the stability of the electrolytes in electrochemical cells is online electrochemical mass spectrometry (OEMS). As side reactions typically lead to the release of gaseous compounds, analyzing the gas atmosphere during cell cycling can provide direct evidence for unstable interfaces. **Figure 11** shows the cumulative release of selected gases over three plating/stripping cycles from symmetrical Na|Na cells. OEMS is a very powerful tool for evidencing side reactions during cell cycling and it reveals also some dramatic differences for the different salts. For all salts, the amount of H_2 is quite similar, which is likely related to a similar level of water impurities in the electrolytes. In the case of NaFSI, NaOTf, and $NaPF_6$, the main evolution occurs directly after OCP. For NaTFSI and $NaClO_4$, the H_2 formation occurs during stripping/plating. For CH_4, by far the largest release is detected for NaTFSI. The release of CO and C_2H_4 is the largest for NaTFSI and $NaClO_4$. In contrast, the use of NaOTf and $NaPF_6$ as salts leads only to a very small gas release, hence indicating that they are most suited for using them in cells containing a sodium electrode. From these results, a qualitative order for the degree of side reactions can be gained as NaTFSI > $NaClO_4$ >> (NaFSI, NaOTf, $NaPF_6$). These results are well in line with the impedance data except $NaClO_4$ which reveals smaller resistance than NaFSI.

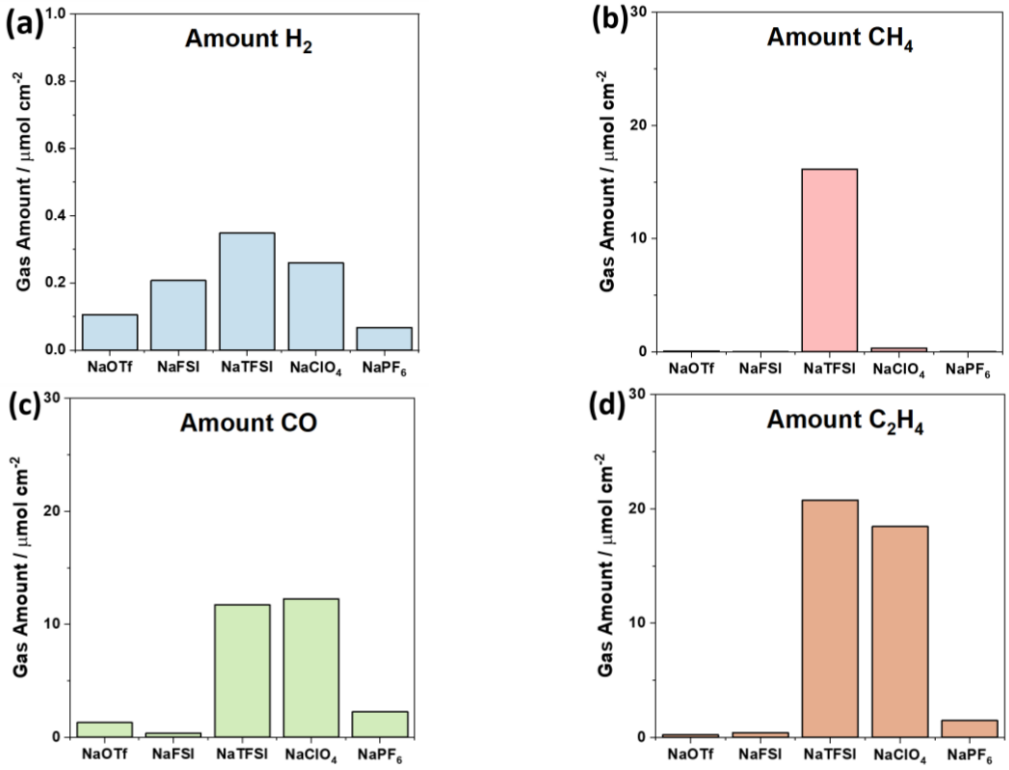

Figure 11. Total gas amount for (a) H_2, (b) CH_4, (c) CO, (d) C_2H_4 for different electrolytes during cycling in Na|Na cells. The gas amount was calculated from the first 3 plating/stripping cycles and is normalized with respect to the surface area of the copper mesh on which Na was plated.

Taking results from EIS and OEMS together, electrolytes containing NaOTf and $NaPF_6$ seem to form a thin, less resistive and stable SEI which sodium ions can easily pass. For NaTFSI and $NaClO_4$, poor passivation and continuous electrolyte decomposition occur. While EIS and OEMS provide some very clear information, they also have some limitations. In this thesis, other methods were therefore applied as well to obtain a better understanding on the electrolyte stability. IR measurements of the liquid electrolyte and XRD measurements of the sodium electrodes were done as well. For the salts leading to the strongest side reactions, XRD also showed the appearance of crystalline decomposition products, for example. In the case of NaTFSI corrosion of the sodium metal was also even visible by eye. Overall, the results clearly demonstrated that the sodium counter electrode in sodium-half cells is very sensitive to the electrolyte composition. Especially the use of NaTFSI is problematic, leading to continuous degradation of the sodium. This is quite surprising giving the fact that LiTFSI is a very popular salt used in lithium-ion battery research and is very compatible with lithium electrodes.

Similar tests were made to study whether there is any influence of the conductive salt on the graphite electrode during the co-intercalation reaction. This was especially important because the concept of co-intercalation requires in principle a SEI-free interface. **Figure 12** shows the cumulative release of different gases from Graphite|Na sodium half cells over 5 cycles. Again, the gas release is highest in the case of NaTFSI, especially for CO, CH_4, and C_2H_4. Similarly, also NaFSI leads to the substantial gas release. The least gas release was found for $NaPF_6$ and NaOTf. In another study, we found that in the case of NaOTf, the gas release is largely restricted to the first cycle only[100]. Obviously, less side reactions take place when using these salts which is well in line with the much higher Coulombic efficiency and the better cycle life obtained for these salts compared to e.g. NaTFSI or NaFSI.

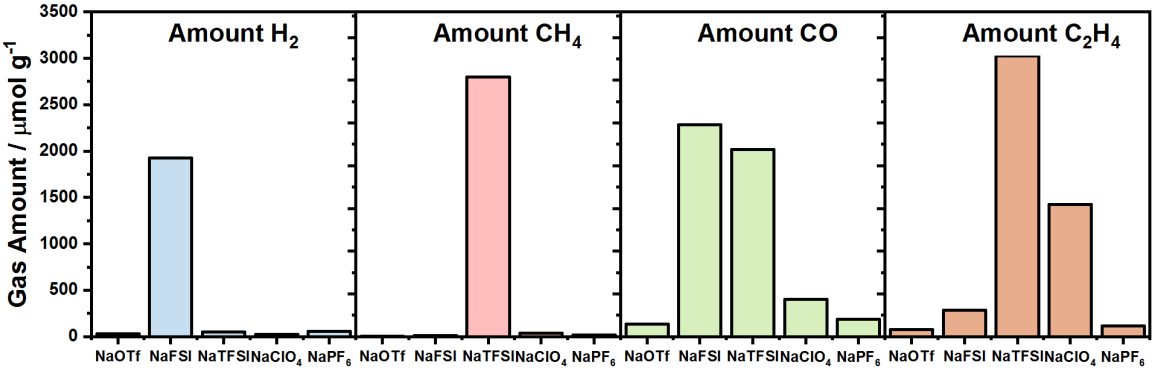

Figure 12. Total gas amounts for H_2, CH_4, CO and C_2H_4 evolution during 5 cyclovoltammetric cycles (v = 55 μVs^{-1}) with respect to the measured electrolyte solution.

TEM was used to image a possible SEI on the graphite surface. As mentioned above, the SEI is difficult to analyze and there are only few examples published in literature where an SEI is really unequivocally identified. **Figure 13a** shows a TEM image of a SEI on a graphite particle surface after lithiation by Nie *et al.* [108] The thickness of the observed SEI is in the range of 50 nm.

Considering the graphite co-intercalation reaction, published results on an SEI were contradicting In own studies[100], we found no evidence for an SEI. Several tests with TEM and reference measurements were conducted but an SEI could not be found. A typical TEM image of a graphite particle after the co-intercalation reaction is shown in **Figure 13b**. Maibach *et al.* [103], on the other hand, reported the existence of an SEI using X-ray photoelectron spectroscopy. The obvious contradiction between both findings could be clarified by the different conductive salts used in both studies. While in the own study NaOTf was used as a salt, Maibach et al. used NaFSI – which we found to lead to much more side reactions using the above-mentioned methods. Using TEM, we also found that using NaFSI leads to the enrichment of electrolyte decomposition products within the graphite electrode.

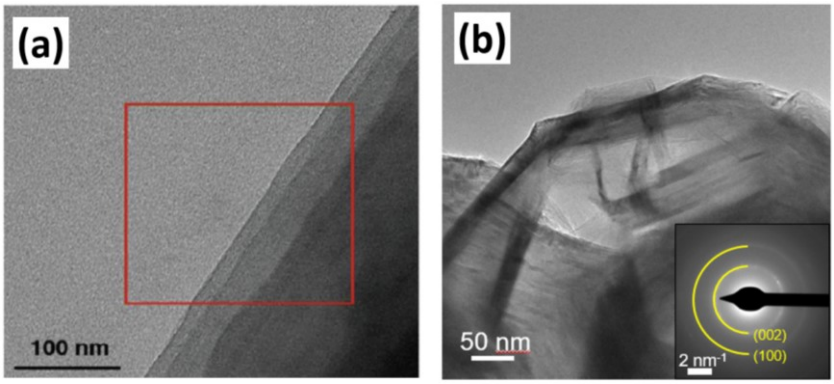

Figure 13. (a) TEM images of fresh graphite and SEI on graphite anodes cycled to four cutoff voltages in 1.2 M LiPF6/EC during first charge [108, 109], (b) TEM and HRTEM images of the graphite particles after cycling in electrolyte solutions of 1M NaOTf in diglyme (end of 5th cycle, desodiated state). Insets: SAEDs patterns for areas, the semi-circles indicate the expected positions for graphite interplanar distances.

Combining the results from electrochemistry, TEM and OEMS measurements, an important finding of this thesis was that the graphite co-intercalation reaction is likely the first example of SEI-free graphite anode in SIBs (at least in case the electrolyte is composed of diglyme

and NaOTf). Taking all results together, the suitability of the surveyed salts can be ordered as follows: (best) NaOTf≥$NaPF_6$>$NaClO_4$>NaFSI>>NaTFSI (worst).

A more detailed discussion on the electrolyte stability towards sodium and the graphite electrode can be found in the submitted manuscript "*Stable and instable diglyme-based electrolytes for batteries with sodium or graphite as electrode"* (details are in ***Section 5.3***).

4.3. Effect of Electrolyte Salts on the co-intercalation reaction

This section is closely linked to ***section 4.2*** but represents a continuation of the efforts to clarify whether the anion of the conductive salt has an influence on the co-intercalation reaction. While ***section 4.2*** was dedicated to the interphase/interface stability, this section addresses the overall electrochemical performance of the graphite electrode for electrolytes containing different salts. Moreover, *in situ* ECD was applied to test whether the different salts also have an impact on the electrode dynamics. The relevant questions addressed were

- Does the electrochemical performance of the graphite electrode depend on the type of salt anion?
- Does the salt ion have an influence on the graphite crystallinity and the electrode dynamics?

Once again, it is important to remember that the salt anion should not have any influence as it is formally not participating in the electrode reaction. However, in the previous section, we discussed the dramatic effect of the anion on the interphase/interface stability. When systematically testing the co-intercalation reaction for different salts (with diglyme as solvent), we indeed could also find a strong influence on the properties of the graphite electrode. As an example, **Figure 14a** shows galvanostatic charge/discharge curves for the co-intercalation reaction using either NaTFSI or NaOTf as salt. It is clearly seen that the discharge capacity in the case of NaTFSI is much higher compared to NaOTf but at the same time the coulombic efficiency is much lower. This is a clear sign for parasitic side reactions and is hence well in line with the results discussed in the previous section. XRD analysis of the graphite electrodes after cycling revealed that the crystallinity of the graphite particles was, depending on the salt, affected. In line with the previous findings, the first cycle leads to exfoliation of the graphite particles to smaller graphite platelets. The degree of exfoliation, however, strongly depends on the type of salt. As **Figure 14b**, the 002 reflex, representing the interlayer spacing of the graphite lattice) reduced most in case organic anions were used. The least reduction in reflex intensity was observed for the inorganic salts, in particular, $NaPF_6$. Among the organic anions, the use of NaTFSI and NaFSI clearly lead to the strongest decrease in reflex intensity which is a clear hint for faster degradation of the electrode.

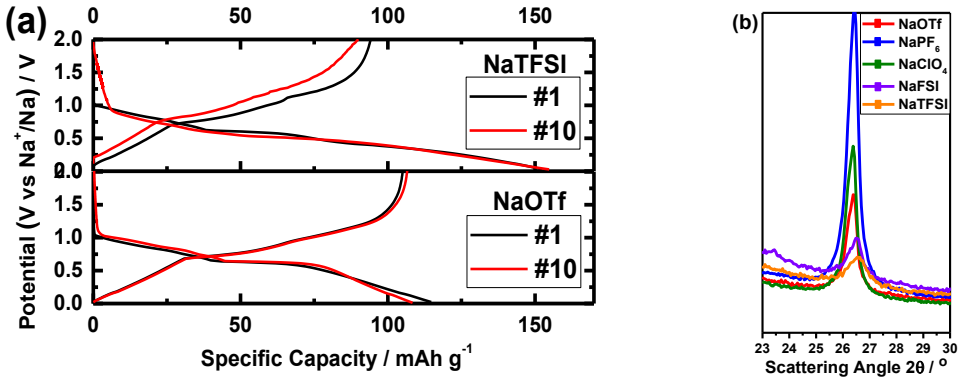

Figure 14. (a) Voltage profiles (1st and 10th cycle) of graphite-sodium cells with diglyme-based electrolytes for different electrolyte salts, (1C corresponds to 110 mA g^{-1}, $Na^{+}(diglyme)_2C_{20}-$ in the literature.[81]) (b) XRD Diffraction patterns of powder graphite after 5th desodiation for five different salt varieties at room temperature. The strong reflex at around 2θ = 26 ° indicates the graphene layer spacing of graphite (d= 3.35 Å).

Overall, the largest difference in electrode performance was detected for NaOTf (best case) and NaTFSI (worst case). Graphite electrodes from cells with these salts were further characterized in more detail using TEM, EDX, and ECD. By TEM, it was found that there is a loss in crystallinity in case of NaTFSI whereas, for NaOTf, crystalline domains can easily be detected (**Figure 14b**), being well in line with the XRD results EDX further provided some hint on that remains from the TFSI anion are somehow trapped in the graphite structure which would be in line with the larger degree in exfoliation. An interesting result was also obtained when using *in situ* ECD. **Figure 15a** shows the change in electrode thickness for five consecutive cycles. While in the case of NaOTf the change is as expected and stabilization of the electrode is achieved, the situation for NaTFSI is very different. In this case, the electrode thickness rapidly increases indicating a structural degradation and/or formation of a very thick surface layer on the graphite. The thickness of the electrode especially increases during the sodiation process which is well in line with the extra capacity observed for this salt (see **Figure 14a**). At last, **Figure 15b** shows two *in situ* ECD results for NaOTf and $NaPF_6$ in comparison. Although the capacity over several cycles is not exactly matching the similarity in the electrode dynamics is quite evident. This means that for salts that show the least side reactions the "cleanest" co-intercalation reaction, i.e. a reaction with negligible side reactions, takes place.

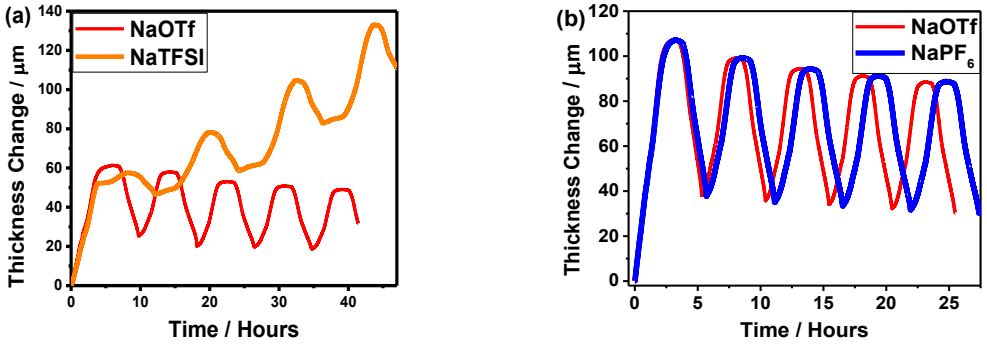

Figure 15. In-situ dilatometry measurements for a) 4 cycles of NaOTf and NaTFSI separately, b) and c) comparisons of 5 cycles of NaOTf and $NaPF_6$. For a, 45 µm of electrodes are used but for b, 50 µm of electrodes are used. The measurements are performed at C/10 =11 mA g^{-1} (1C corresponds to 110 mA g-1,$Na^{+}(diglyme)_2C_{20}^{-}$) within voltage window of 0.01V and 2.5V

A more detailed discussion on these measurements can be found in the submitted publication "*Stable and instable diglyme-based electrolytes for batteries with sodium or graphite as electrode"* (details are in ***Section 5.3***).

It goes without saying that the results are not exhaustive. Similar studies are also required for cathode materials. Finding the right electrolyte composition that performs well for both electrodes is still a challenge for assembling full cells. In the future, mixtures of salts and solvents could be tested to further optimize the performance.

4.4. Effect of Temperature and Type of Solvents on Co-intercalation Reactions

The fact that the electrolyte solvent becomes part of the electrode reaction in co-intercalation reactions leads to another degree in freedom. By changing the solvent, the redox potential can be tuned [78]. For the example of linear ethers, it has been found that the redox potentials increase with the length of the molecule [78, 94]. While several solvents (mono- to tetraglyme) had been used in literature, this thesis expands the number of solvents tested for this type of reaction. For this, pentaglyme was kindly supplied from Nippon Nyukazai Co., Ltd. Moreover, the following crown ethers, being similar to glymes, were tested as well: crown ether 4 (12-Crown-4), crown ether 5 (15-crown-5) and crown ether 6 (18-crown-6). An overview of the tested solvents is shown in **Figure 16**. Besides changing the solvents, also the temperature was varied in order to derive thermodynamic data or to overcome possible kinetic barriers. Several main questions were addressed:

* Can the number of solvents being successfully used for co-intercalation reactions be extended?
* What is the effect of temperature on co-intercalation reactions?

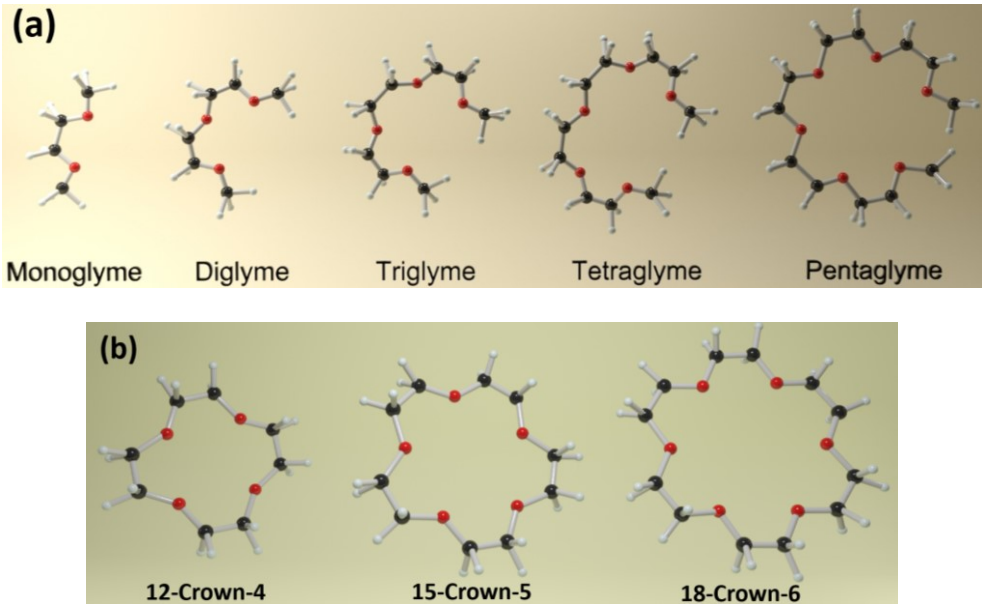

Figure 16. Ball-and-stick model of a) the glyme series and b) the different crown ethers [93].

$$(4) \qquad k = k_0 . \exp\left(\frac{-E_A}{R.T}\right)$$

$$(5) \qquad \Delta S = z.F\left(\frac{\partial E}{\partial T}\right)_P$$

Temperature was found to be a very important factor in a better understanding of the co-intercalation reaction. For example, it was previously observed that only a limited capacity was obtained when using triglyme as a solvent and the potential profile was ill-defined. Jache et al. explained this with unfavorable coordination of the sodium ion by triglyme molecules [78]. At the same time, the rate constant of a reaction is a function of temperature as shown by the Arrhenius equation (**equation 4**). So if kinetic barriers hinder the co-intercalation reaction, they might be overcome by increasing temperature. This thesis, therefore, contains a number of temperature dependent studies ranging from 20 °C and 80 °C. Moreover, considering thermodynamics, a change in temperature will lead to a change in redox potential – the change being directly linked to the entropy change of the reaction. In the case the reaction is thermodynamically controlled, temperature dependent measurements can, therefore, be used to derive thermodynamic data (**equation 5**). Results of the experiments lead to the publication entitled "*Temperature-Induced Activation of Graphite Co-intercalation Reactions for Glymes and Crown Ethers in Sodium-Ion Batteries* [93]" (in ***Section 5.2***).

Typical results from temperature dependent measurements are shown in **Figure 17**. As the temperature rises, the plateau potentials decrease with a linear slope (**Figure 17a, b**) with pentaglyme and triglyme being exceptions. For pentaglyme, the activation is required first (**Figure 17c**). After full activation is reached, it behaves similar to other glymes and plateau potential decreases with the same slope. However, the behavior of triglyme is totally different (**Figure 17d**). Although the temperature rises, the plateau potentials remain the same. The increase in capacity with temperature is a clear sign for kinetic limitations of the reaction at room temperature. In a similar way, higher capacity values could be obtained by decreasing the current density (C-rate) as shown in **Figure 17d**.

It is found that the reactions involving glymes, except triglyme, are thermodynamically controlled. Whereas, the reaction with triglyme is kinetically controlled and the effect of temperature is less compared to other glymes.

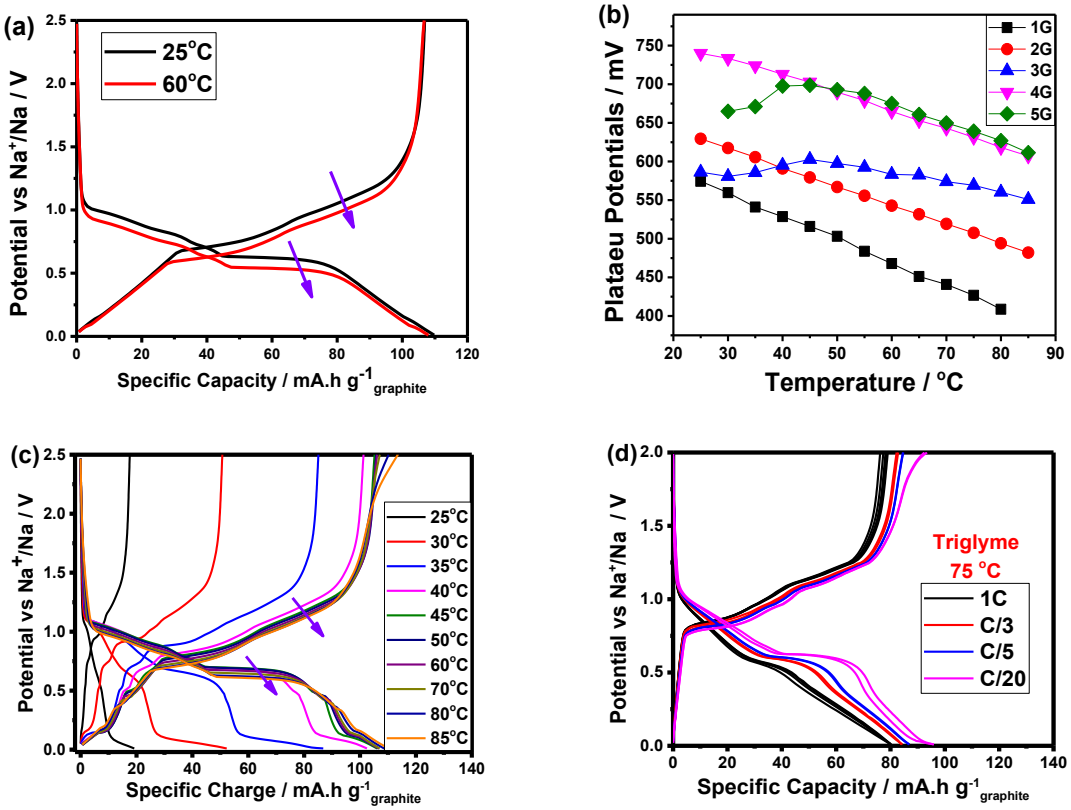

Figure 17. Potential profiles for the co-intercalation reactions with the different glymes (1G−5G) at different temperatures. (a) Glyme series. (b) Plateau potential as a function of temperature. (c) Cycling for 5G from 25 to 85 °C and (d) cycling at different current densities for 3G at 75 °C at 1C (1C corresponds to 110 mA g^{-1}, $Na^+(diglyme)_2C_{20}$ − in the literature.[81])[93]

Activation of the reaction by temperature was also found for one crown ether. While no co-intercalation could be achieved for crown ether 4 and 5 at any temperature, experiments were successful for crown ether 6 (above its melting point). The voltage profile, see **Figure 18a**, is notably different from the linear glymes and shows more distinct features indicating a more complex co-intercalation behavior. The capacity was also lower compared to the linear glymes, however, the results were the first successful example for the electrochemical formation of a t-GICs with a crown ether (6). The results on crown ethers clearly demonstrate that possibly much more *t*-GICs exist at slightly elevated temperatures.

During the time of this Ph.D. thesis, also several other solvents were tested. Selected results are shown in **Figure 18b and c**. Polyoxymethylene dimethyl ethers-POMDME (OME) solvents were tested due to their similarity to glymes with the difference of excess oxygen in the molecule. OMEs are currently highly studied as a possible synthetic substitute for gasoline and diesel to achieve less emission [110]. During electrolyte preparation, it turned out that dissolving salts in OME was the main problem. Only NaTFSI could be dissolved and created a clear electrolyte solution. But the results could not satisfy the expectations). As another solvent type, Tetramethylurea (TMU) was tested as well. While there was a clear sign for a co-intercalation reaction (yet at a low capacity of around 40 mAh/g), the electrolyte continuously decomposed during charging as can be seen from the plateau at around 0.7 V.

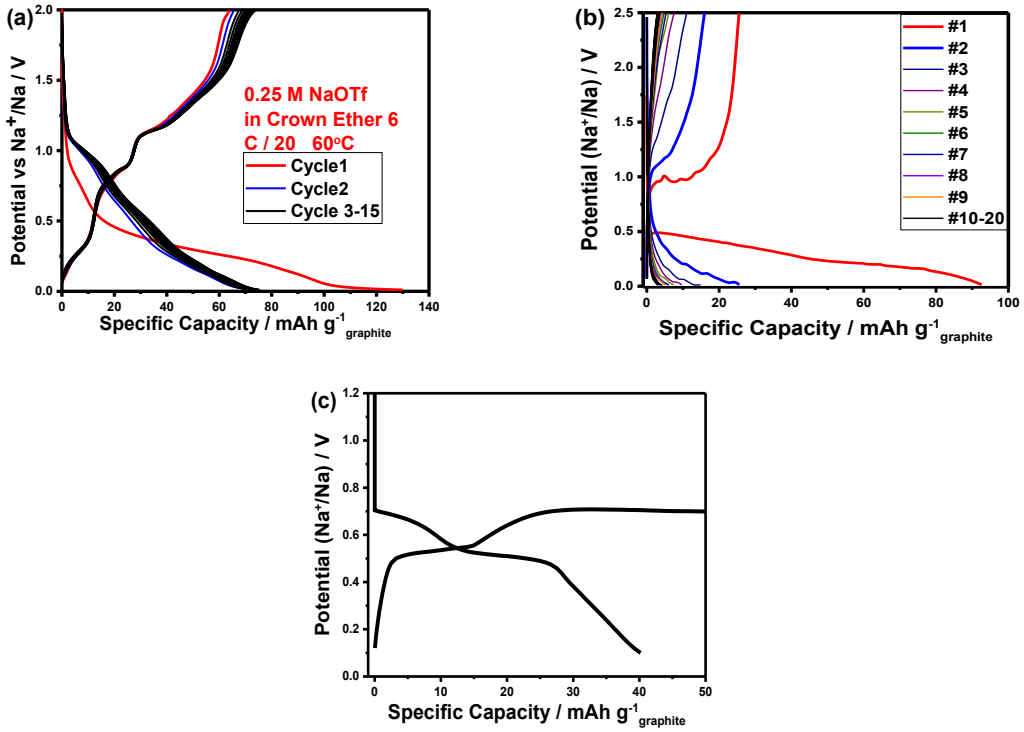

Figure 18. Potential profile for a) crown ether 6 at C/20. (1C corresponds to 110 mA g^{-1}, $Na^+(diglyme)_2C_{20}$ – in the literature.[81]), b) 1M NaTFSI in Polyoxymethylene dimethyl ethers – POMDME (OME) and c) 0.5 M NaOTf in Tetramethylurea (TMU)

Overall, this part of the thesis demonstrated that temperature can have a major influence on the co-intercalation reaction. For some solvents, kinetics are already fast enough at room temperature to classify the reactions as "thermodynamically controlled". In this case, temperature dependent measurements could be used to determine entropy changes of the reaction. For other solvents, the reaction was activated by temperature leading to full electrode utilization. Moreover, even a crown ether could be reversibly co-intercalated above its melting point. The results suggest that there are likely much more *t*-GICs than previously thought.

5. Results and Discussions - Publications

Among the many battery chemistries studied at the moment, this Ph.D. thesis was dedicated to contribute to the better understanding of co-intercalation reactions of graphite in sodium-ion batteries. For these different parameters such as solvent, salt and temperature were varied and interfaces/interphases, as well as the dynamics of the macroscopic electrode, were studied in detail. The results of this thesis are summarized in three peer-reviewed articles (2 main author, 1 co-first author) and one submitted publication. This chapter contains the publications along with brief introductions. Supporting information on the publications can be found on the website of the publishers.

5.1. Ion Insertion Mechanisms, Electrode Dynamics and the Missing Solid Electrolyte Interphase (SEI) (Publication 1)

At the beginning of this Ph.D. project, there were only several publications related to sodium ion co-intercalation into graphite. The commonly accepted idea of lithium ion intercalation into graphite through a thin SEI layer does not apply in the case of sodium. Na-rich *b*-GICs do not exist due to thermodynamic reasons. On the other hand, in 2014 sodium storage in graphite was found to be highly reversible when co-intercalating solvent molecules [81]. However, only a specific class of solvents (glymes) could be used. While this "co-intercalation reaction" was highly reversible, showed excellent kinetics and stable cycle life, the underlying mechanisms and the role of the SEI (which, if existent, should prevent any solvent co-intercalation) were poorly understood.

This first publication addressed different aspects of the reaction. Computational studies revealed that, assuming two diglyme molecules being co-intercalated, lead to an increase in graphene layer spacing rises from 0.335 to 1.13 nm, being well in line with previous XRD measurements While this change in lattice dimensions is local, the dynamics of the macroscopic electrode were followed over 30 cycles by *in situ* electrochemical dilatometry. As a surprising finding, the electrode breathes periodically by about 70-100 % during cycling yet excellent reversibility is maintained. For such a large "breathing", one would expect a fast electrode degradation Analysis by XRD and SEM showed that the graphite particles exfoliate in the first cycle ("activation") to crystalline platelets. The delamination of the platelets does not take place being an important reason for the reversibility.

Moreover, the speed at which the electrode breathes depends on the state of discharge and charge. Under 0.5 V vs. Na^+/Na, the storage behaves more like a pseudocapacitor.

OEMS gas analysis and TEM were used to better understand whether and SEI is formed and whether the electrode is stable in contact with the electrolyte. The results showed that electrolyte decomposition is largely restricted to the first cycle only and that no SEI forms. The studied reaction is therefore likely the first example of a SEI-free graphite anode.

The results of these findings were published in the Journal of *Advanced Energy Materials*.

Mustafa Goktas, Christoph Bolli, Erik J. Berg, Petr Novák, Kilian Pollok, Falko Langenhorst, M. v. Roeder, Olena Lenchuk, Doreen Mollenhauer, Philipp Adelhelm, *Graphite as Cointercalation Electrode for Sodium-Ion Batteries: Electrode Dynamics and the Missing Solid Electrolyte Interphase (SEI), Advanced Energy Materials* **2018**, 1702724.

For this paper, computational studies are performed by M. v. Roeder, Olena Lenchuk, Doreen Mollenhauer. TEM analyses are done by Kilian Pollok, Falko Langenhorst. OEMS measurements are performed by Christoph Bolli, Erik J. Berg, Petr Novák. All the measurements related to electrochemistry, ECD, XRD, SEM and also analysis of the data and further calculations are performed by the first author. AlsoThe paper is written by the first author and edited by Philipp Adelhelm. By all the comments and contributions of the authors, the paper is be published.

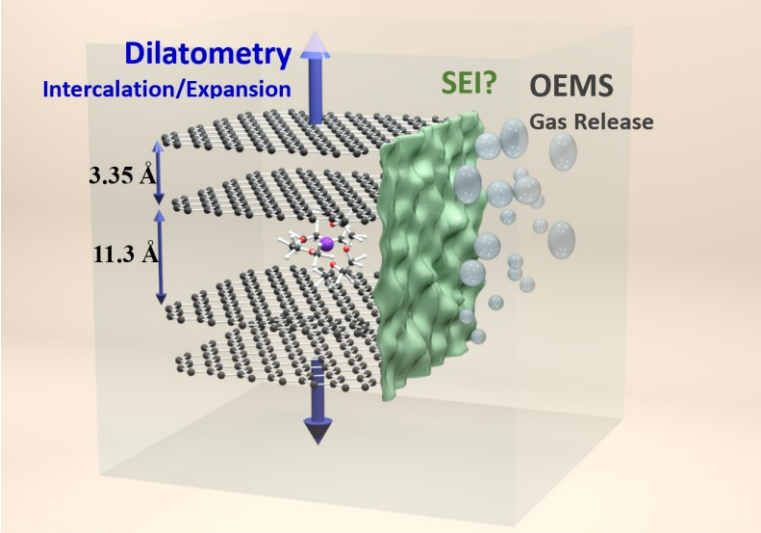

Figure 19. TOC of the 1st publication

TOC text: The reversible intercalation of solvated rather than naked ions into graphite is a peculiar electrode reaction that is currently studied for sodium-ion batteries. Charging/Discharging is accompanied by a large yet reversible electrode breathing and the charge transfer seems to occur over a kinetically stabilized interface without a solid electrolyte interphase (SEI).

ADVANCED ENERGY MATERIALS
www.advenergymat.de

Graphite as Cointercalation Electrode for Sodium-Ion Batteries: Electrode Dynamics and the Missing Solid Electrolyte Interphase (SEI)

*Mustafa Goktas, Christoph Bolli, Erik J. Berg, Petr Novák, Kilian Pollok, Falko Langenhorst, Maximilian v. Roeder, Olena Lenchuk, Doreen Mollenhauer, and Philipp Adelhelm**

The intercalation of solvated sodium ions into graphite from ether electrolytes was recently discovered to be a surprisingly reversible process. The mechanisms of this "cointercalation reaction" are poorly understood and commonly accepted design criteria for graphite intercalation electrodes do not seem to apply. The excellent reversibility despite the large volume expansion, the small polarization and the puzzling role of the solid electrolyte interphase (SEI) are particularly striking. Here, in situ electrochemical dilatometry, online electrochemical mass spectrometry (OEMS), a variety of other methods among scanning electron microscopy (SEM), transmission electron microscopy (TEM), and X-ray diffraction (XRD) as well as theory to advance the understanding of this peculiar electrode reaction are used. The electrode periodically "breathes" by about 70–100% during cycling yet excellent reversibility is maintained. This is because the graphite particles exfoliate to crystalline platelets but do not delaminate. The speed at which the electrode breathes strongly depends on the state of discharge/charge. Below 0.5 V versus Na^+/Na, the reaction behaves more pseudocapacitive than Faradaic. Despite the large volume changes, OEMS gas analysis shows that electrolyte decomposition is largely restricted to the first cycle only. Combined with TEM analysis and the electrochemical results, this suggests that the reaction is likely the first example of a SEI-free graphite anode.

1. Introduction

Meeting the global energy demand in a sustainable way is one of the most difficult challenges for human mankind. To achieve this, storing electrical energy becomes more and more important. As a power source, Li-ion batteries (LIBs) took over the lead since their introduction in the early 1990s. The most relevant advantages of LIBs are their excellent electrochemical performance especially with respect to high voltage, high energy density, and long cycle life. However, the rapidly growing battery market will put pressure on the supply chains and resources. Alternative cell chemistries based on abundant elements might therefore become important especially in case stationary energy storage reaches its market breakthrough. Here, sodium-ion batteries (SIBs) appear as an attractive alternative for the future. Research efforts on SIBs significantly increased within the last years, being mainly motivated by the large abundance of sodium and the hope to realize more cost-effective batteries.[1] Moreover, despite the often lower energy density compared to LIBs, the larger ion size of Na^+ might also enable cells with specific advantages over conventional lithium-ion technology.[1g]

In today's LIBs, graphite is the most widely used negative electrode. The electrode reaction is based on the reversible intercalation of lithium ions by forming binary graphite intercalation compounds (*b*-GIC) with the final stoichiometry of LiC_6 (q_{th} = 372 mA h g^{-1}). Unfortunately, sodium does not form sodium rich *b*-GICs and only poor storage capacities in the range of 30 mA h g^{-1} or

M. Goktas, Prof. P. Adelhelm
Institute of Technical Chemistry and Environmental Chemistry
Friedrich Schiller University Jena
Philosophenweg 7a, D-07743 Jena, Germany
E-mail: philipp.adelhelm@uni-jena.de
M. Goktas, Prof. P. Adelhelm
Center for Energy and Environmental Chemistry (CEEC Jena)
Philosophenweg 7a, D-07743 Jena, Germany

The ORCID identification number(s) for the author(s) of this article can be found under https://doi.org/10.1002/aenm.201702724.

DOI: 10.1002/aenm.201702724

Dr. C. Bolli, Dr. E. J. Berg, Prof. P. Novák
Electrochemistry Laboratory
Paul Scherrer Institute
CH-5232 Villigen PSI, Switzerland
Dr. K. Pollok, Prof. F. Langenhorst
Institute of Geosciences
Friedrich Schiller University Jena
Carl-Zeiss-Promenade 10, 07745 Jena, Germany
M. v. Roeder, Dr. O. Lenchuk, Prof. D. Mollenhauer
Institute of Physical Chemistry
Justus-Liebig-University Giessen
Heinrich-Buff-Ring 17, D-35392 Giessen, Germany

less have been experimentally found.[1a,2] As the heavier alkali metals are well known to form *b*-GICs, explaining the unusual behavior of sodium is not straightforward. We note that the family of graphite intercalation compounds is generally very large and graphite is able to host a large number of different cations and anions, such as PF_6^- or $TFSI^-$.[3]

Theoretical studies indeed suggest that the formation of sodium-rich *b*-GICs is thermodynamically not favorable.[4] For example, Nobuhara et al.[4a] relate this instability to the stretching of the C—C bond within the graphene. Liu et al.[4b] systematically compared the energy balance between ionization energies and ion–substrate interactions for a series of alkaline and alkaline earth elements. Among the alkali metals (A), only sodium shows positive formation energies for AC_6 and AC_8. More importantly, the authors found that Na as well as Mg shows the weakest binding energy to many substrates in general.

A strategy around this problem is to intercalate solvated sodium ions. The reversibility of this so-called cointercalation reaction over hundreds of cycles was first demonstrated in 2014 using diglyme as electrolyte solvent.[5] The electrode reactions based on intercalating (1) naked and (2) solvated sodium ions can be generalized as follows

$$\mathrm{Na^+(solv)}_n + x\cdot \mathrm{C} + \mathrm{e^-} \underset{\text{deintercalation}}{\overset{\text{intercalation}}{\rightleftharpoons}} \mathrm{NaC}_x + n\cdot \mathrm{solv} \quad (1)$$

$$\mathrm{Na^+(solv)}_n + x\cdot \mathrm{C} + \mathrm{e^-} \underset{\text{deintercalation}}{\overset{\text{intercalation}}{\rightleftharpoons}} \mathrm{Na(solv)}_n\,\mathrm{C}_x \quad (2)$$

NaC_x is the *b*-GIC, the solvation shell is stripped off during the charge transfer. As discussed above, this reaction is thermodynamically unfavorable. The cointercalation of (parts of) the solvation shell along with the ion leads to the formation of a ternary graphite intercalation compound (*t*-GIC) with the general formula $Na(solv)_nC_x$. The reaction for diglyme as solvent can be written as

$$\mathrm{Na^+(diglyme)}_n + x\cdot \mathrm{C} + \mathrm{e^-} \underset{\text{deintercalation}}{\overset{\text{intercalation}}{\rightleftharpoons}} \mathrm{Na(diglyme)}_n\,\mathrm{C}_x \quad n = 1 \text{ or } 2,\ x = 16-22 \quad (3)$$

A number of experimental studies on this electrode reaction has been published in the meanwhile. The exact stoichiometry, i.e., the number of solvent molecules cointercalated per ion as well as the number of carbon atoms per ion, are still under debate but experimental results and theory suggest values for $n = 1$ or 2 and $x = 16$–26.[5,6] For $x = 20$, the reaction corresponds to a theoretical specific charge of 111.7 mA h g^{-1} (graphite). Higher values of up to 150 mA h g^{-1} have been reported also, though electrodes contained also larger amount (20 wt%) of a carbon black additive.[7] The reaction proceeds over several stages below 1 V versus Na^+/Na and is accompanied by a significant increase in graphene layer spacing. Whereas the layer spacing for graphite is 3.35 Å, it increases up to about 11.3–11.9 Å during formation of the *t*-GIC. The volume expansion is in the range of 240–250%.[2d,6b,d,8] A number of (in situ) XRD [2d,5,6b,8] and Raman spectroscopy[7a,9] studies unequivocally prove that crystallinity of the electrode is preserved during subsequent cycling. Notably, also Li^+ and K^+ can be reversibly intercalated this way.[5,10]

An interesting property of cointercalation reactions is that the redox potentials can be influenced by the type of solvent. The main redox peaks in cyclic voltammograms shift by about 200 mV when changing from monoglyme to tetraglyme, for example.[2d,6b] A systematic study on the impact of different solvents on the redox potentials has been published by Jache et al.[2d] The observed rapid kinetics of the electrode reaction has been rationalized by solid-state nuclear magnetic resonance spectroscopy (NMR)[6c,11] and density functional theory (DFT)[6d] studies. Needless to say that a higher specific charge is desirable for practical applications. As the limits of this reaction type are unknown, future studies should also aim at finding cointercalation reactions with higher specific charge. For example, if enough divalent or trivalent ions could be intercalated this way, the specific charge would significantly increase. The properties of the reaction in terms of reversibility and kinetics are, however, outstanding and many of the underlying principles governing this type of reaction remain to be explored. This also includes clarifying ion–ion and ion–solvent interactions in the electrolyte solution.[12]

The experimentally observed properties of the cointercalation reaction raise two intriguing questions: (1) Why is the rechargeability excellent despite the large volume expansion? The large volume expansion should lead to rapid structural degradation and hence poor cycle life. This, however, is generally not observed and cycling for more than 1000 cycles with negligible capacity loss has been reported by different groups. (2) What about the formation of a solid electrolyte interphase (SEI)? From the general point of view, reductive decomposition of the electrolyte combined with SEI formation takes place at potentials below about 1 V versus Na^+/Na. The SEI is electronically insulating but ionically conductive therefore preventing further electrolyte decomposition but still enabling ion transfer. SEI formation is therefore generally considered an important prerequisite to render low-voltage anode materials. The SEI also prevents cointercalation of solvent molecules.[13] The concept of the SEI, however, clearly contradicts the here discussed cointercalation reaction as this type of reaction appears only feasible without a SEI. Without a SEI, however, one would expect continuous electrolyte decomposition.

In this work, we therefore study two important effects related to these so far poorly understood phenomena: (1) in situ electrochemical dilatometry (ECD) is used to study the electrode dynamics during cycling and (2) online electrochemical mass spectrometry (OEMS) is used to study the electrolyte decomposition/gas evolution during cycling. Both techniques have not been applied to cointercalation electrode reactions yet. We further use N_2 physisorption and scanning electron microscope (SEM) to study changes in particle morphology and electrode thickness, whereas transmission electron microscopy (TEM) is used to characterize the electrode/electrolyte interface.

ECD is used to measure changes in the electrode thickness during charge storage and therefore is complementary to XRD analysis, which provides information on the changes in crystal structure. The method is applied to batteries[14] as well as capacitors.[15] Phase transitions during ion insertion/deinsertion, (irreversible) reaction products such as SEI formation or degradation mechanisms can be followed, for example. In view of the drastic lattice expansion that occurs for electrode

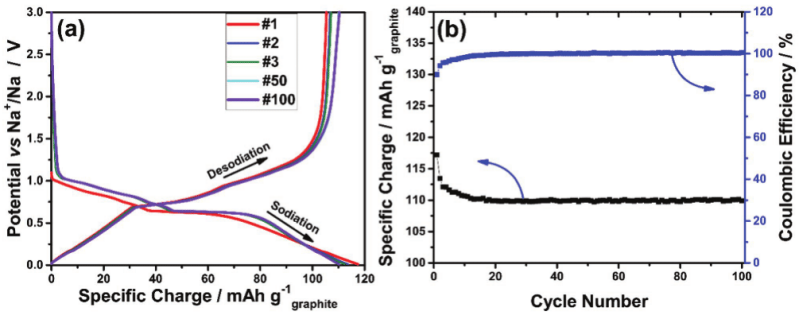

Figure 1. a) The galvanostatic sodiation (reduction) and desodiation (oxidation) potential profile of 100 cycles at C/3 = 32.7 mA g^{-1} (1 C corresponds to 110 mA g^{-1}, $Na^+(diglyme)_2C_{\bar{2}0}$ in literature [5]), b) sodiation specific charge and Coulombic efficiency profiles.

reactions based on solvent cointercalation, ECD appears especially attractive.

OEMS, also called differential electrochemical mass spectrometry, allows to monitor qualitatively and quantitatively the evolution of volatile species during the cycling of an electrochemical cell.[16] In LIBs, this technique has been applied to study, e.g., the mechanisms of the SEI formation and electrolyte decomposition on graphite negative electrodes.[17]

2. Results and Discussion

2.1. Electrode Reaction, Ion Complex, and Morphological Characterization

Electrode Reaction and Ion Complex: **Figure 1**a shows a selection of different potential profiles for graphite electrodes cycled at 32.7 mA g^{-1} in half cells with sodium metal as counter electrode and diglyme as electrolyte solvent. Electrodes contained binder (10% polyvinylidene fluoride (PVDF)) but no conductive additive in order to avoid additional ion storage effects. As reported earlier, the cointercalation reaction largely occurs at potentials below 1 V versus Na^+/Na. The profile is complex showing regions of constant and sloping potential. This indicates that the intercalation reaction is a staged process as it is also well known from conventional intercalation reactions, e.g., formation of LiC_6 over intermediates.[18] The complexity of the electrode reaction is also clearly seen from the dQ/dV plot (Figure S1, Supporting Information). Redox activity starts from 1.04 V for sodiation. The peaks at 0.6 and 0.68 V are the result of a fairly constant potential plateau contributing to about 25–30% of the total capacity. Properties of this region will be also discussed in the following subsections.

Coulombic efficiency and specific charge over hundred cycles are shown in Figure 1b. The initial Coulombic efficiency is 90%, which is typical for graphite as intercalation host and is related to side reactions and, in the common view, the formation of the SEI. Upon subsequent cycling, the Coulombic efficiency approaches 100% and a specific charge of 110 mA h g^{-1} is obtained. The excellent reversibility of the reaction is also evident from the potential profiles that are, with the exception of the first cycle, largely identical. Rate capability tests for C-rates from C/10 to 2C are shown in Figure S2 in the Supporting Information. Changes in potential and charge as a function of specific current are negligible, indicating rapid kinetics of the electrode reaction. Below about 0.5 V, the combined overpotentials for charging and discharging amount to about 12 mV (C/10) and 25 mV (2C) only. In other words, the solvated ions can easily enter the graphite lattice and rapidly diffuse despite their large size.

Properties of the solvated ion have been derived from the theoretical investigations. DFT calculations of the $Na^+(diglyme)_2$ complex based on the crystal structure of $Li(diglyme)_2ClO_4$ reveal that the solvent complex has an octahedral coordination geometry with sodium–oxygen distances of around 2.41 Å (**Figure 2**a). The $Na^+(diglyme)_2$ complex possesses a radius of 4.2–4.3 Å. It is defined as the distance between the central Na^+ ion and the outermost H atoms. The first solvation shell surrounding the Na ion is slightly aspherical with dimensions of 7.73 Å, 7.00 Å, and 6.51 Å along the [100], [010], and [001] axis, respectively. The natural population analysis (NPA) of charge distribution indicates a charge of +0.86 e for sodium and thus an ionic character of the complex with no unusual charge transfer from the solvent molecules to sodium. The charge distribution of the ether molecules exhibits the highest negative charge for the oxygen atoms (–0.56 e per atom) followed by the carbon atoms (–0.27 e per atom) at the end of the diglyme chains. All other carbon atoms carry a slightly negative charge (–0.09 e per atom) and hydrogen atoms in average a charge of +0.19 e per atom. The DFT calculations of the determined complex placed into graphite in a low concentration $[Na(diglyme)_2C_{100}]$ reveal a layer spacing of around 10.6 Å. The radius of the intercalated $Na(diglyme)_2$ in graphite remains approximately the same as of the free complex, but the solvation shell surrounding the Na^+ ion is getting even more aspherical, exhibiting the size of 7.74 Å, 8.14 Å, and 5.71 Å along the [100], [010], and [001] axis, respectively. However, placing a $Na^+(diglyme)_2$ solvation complex with slight distortion in the octahedral coordination geometry (nearly energetically degenerated and with a similar charge distribution to the descripted one) into graphite leads to a graphite layer spacing of 11.3 Å (Figure 2b) more in line with experimental findings.[2d,6b,8] This nevertheless indicates that depending on the complex geometry and position in the graphite a certain variation of graphite layer spacing is possible. On the other hand, Jung et al. reported an intercalated complex with one diglyme molecule per sodium

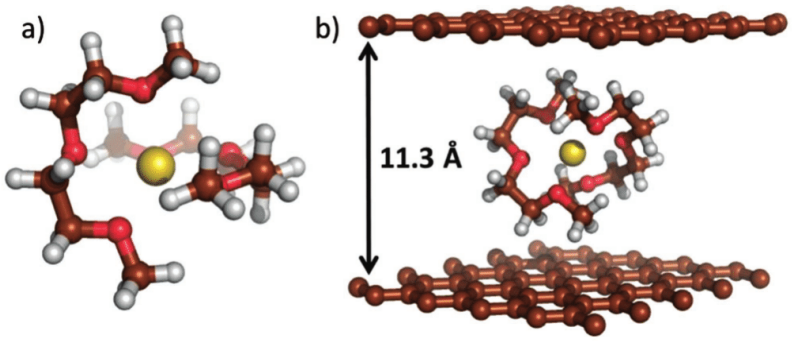

Figure 2. a) $Na^+(diglyme)_2$ complex calculated at PBE(MARI-J, COSMO)-D3/cc-pVTZ level of theory in the solvent diglyme, b) $Na^+(diglyme)_2$ complex intercalated into graphite calculated at PBE-D3/pw(PAW P) level of theory. Color code: carbon (brown), oxygen (red), sodium (yellow), and hydrogen (white).

ion in a $Na(diglyme)C_{16}$ composition showing a graphite layer spacing of 11.5 Å.[6d] Their DFT calculations were performed with a van der Waals density functional. In any case, the exact structure of the intercalated solvent complex is still a matter of debate.[5,7a] Further considerations are outside the scope of this paper. A more detailed theoretical study on the structure of the ternary GICs based on the intercalation mechanism will be due to the complexity of comprehensive calculations part of a follow-up study.

Morphological Characterization: SEM was used to study the morphology of the graphite particles before and after cycling (2nd cycle), see **Figure 3** and Figures S3 and S4 (Supporting Information). No binder was used in this case to avoid any disturbance. The pristine graphite particles show a well-defined shape with largely smooth surface. The composition of the high-purity graphite as determined by CHNS analysis was 99.70% C, 0.17% H, 0.05% N, and 0.07% S. After cycling, the particle morphology drastically changed indicating that intercalation of the solvated ions leads to exfoliation to form platelets (Figure 3b). The same morphology is observed for the particles in the sodiated state, see Figure S4 in the Supporting Information, though the high reactivity of the *t*-GICs makes it generally very difficult to study the material in the intercalated state. Noteworthy, despite exfoliation, the cycling performance was excellent and as the potential profiles remain identical during cycling, one can conclude that the platelets consist of stable, crystalline multilayers. This is also seen from the XRD results shown in Figure S5 in the Supporting Information. Very surprisingly, delamination, i.e., complete separation of the graphenes does not take place and therefore loss in crystallinity and a change in charge capacity is not observed (see comment under ref. [19] for definitions on exfoliation and delamination). Interestingly, Jung et al. suggested very recently on the basis of DFT calculations that additional van der Waals interactions between diglyme molecules and the graphene layers stabilize the structure therefore preventing delamination.[6d] This likely explains the excellent cycle life despite the large lattice expansion.

The samples were further studied by nitrogen physisorption to determine the specific surface area of the graphite before and after cycling (again, no binder and conductive additive were used). Whereas Brunauer-Emmett-Teller (BET) values of around 1 $m^2\ g^{-1}$ were found for the pristine graphite, around 15 $m^2\ g^{-1}$ were found for the graphite after cycling. Using this value, one can estimate the average thickness of the platelets to be about 30 nm (Figure S6, Supporting Information). This is in the same size regime of what can be seen by SEM and in the range of where crystallinity can be determined by XRD. Applying the Scherrer equation, a crystal size of about 30–50 nm can be estimated.

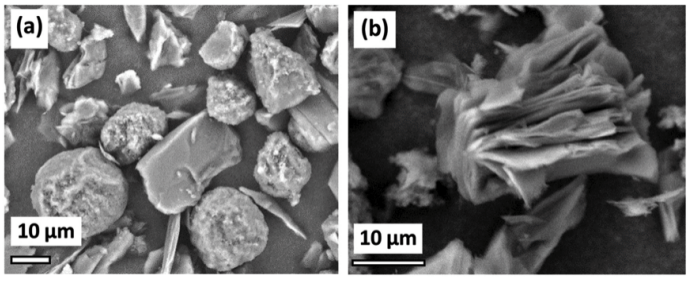

Figure 3. SEM pictures of a) the pristine graphite particles and b) graphite particles after the 2nd cycle (desodiated state). No binder or additive was used in this case to avoid disturbance.

SEM was also used to determine the thickness of the electrodes at different states of charge. **Figure 4** shows cross sections of the electrodes before sodiation, in the sodiated state, and after desodiation. The thickness of the pristine electrodes (without Cu current collector) was 56 µm as determined by a digital thickness dial gauges. Similarly, about 50 µm were found from the SEM measurements indicating that the cross section resembles the real dimensions of the electrode. After sodiation, the average electrode thickness was about 155 µm, i.e., the electrode thickness increased by about 100 µm, or 200%! This significant increase

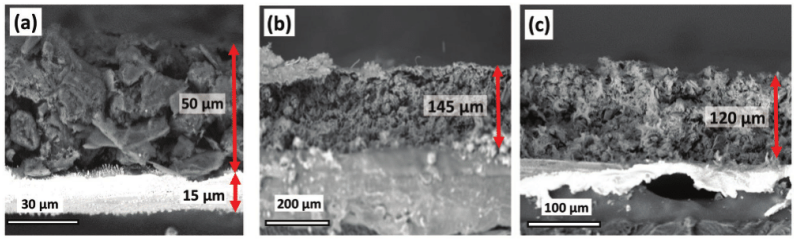

Figure 4. SEM images of graphite electrodes (with 10% PVDF), a) before sodiation, b) sodiated state (2nd cycle), c) desodiated state (end of 2nd cycle). The copper current collector has a thickness of 15 µm as determined by a digital thickness dial gauges.

in electrode thickness is clearly the result of the large increase in graphite layer spacing that occurs during sodiation (3.35 Å to about 11.1 to 11.6 Å[2d,6b,d,8]). After subsequent desodiation, the electrode shrinks to around 125 µm, i.e., an overall net increase of around 75 µm remains. We will see below that this net increase is only temporary. Such an extreme dynamic behavior of the electrode is well suited for ECD studies and is discussed in the following section.

2.2. In Situ Electrochemical Dilatometry

Given the large changes in electrode thickness during cycling, a more detailed study was conducted using an ECD setup (**Figure 5**). This way, the dynamic behavior of the electrode thickness was recorded over several consecutive cycles. Before the experiment, the cell was equilibrated for 4 h (Figure S7, Supporting Information) and the dilatation signal was set to zero as starting point. The cells were cycled galvanostatically at 110 mA g^{-1} in a climate cabinet with constant temperature (25 °C) and the change in electrode thickness was recorded. **Figure 6** shows the results for the first five cycles. The initial thickness of the electrode was $l_0 = 50$ µm.

We use two parameters to discuss the results: (1) Δt describes the change in the thickness of the graphite electrode after a full cycle referring to the initial thickness of the electrode ($l_0 = 50$ µm), i.e., $\Delta t = l_2 - l_0$. (2) Δl describes the change in electrode thickness within one cycle, i.e., the difference in electrode thickness between the sodiated and desodiated state, i.e., $\Delta l = l_1 - l_2$.

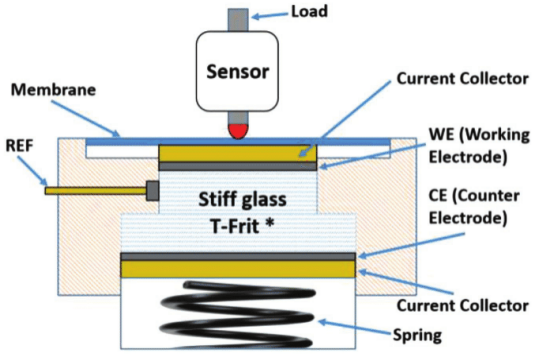

Figure 5. Sketch of the ECD setup measurement principle based on a 3-electrode geometry and an inductive sensor. *The glass frit is fixed in position, therefore only the dilatation of the WE is recorded.

We first consider the first cycle because it behaves different from the following ones. The initial sodiation of the graphite leads to a significant increase in electrode thickness by about 95 µm, i.e., ≈200%. Subsequent desodiation leads to a shrinkage by about $\Delta l = 50$ µm. After the first cycle, the electrode thickness therefore has roughly doubled from about 50 to 95 µm ($\Delta t = 45$ µm). These high values clearly indicate large structural rearrangements and a loosening of the particle network during the first cycle. This means that the porosity of the electrode increases significantly. The changes in electrode dimensions correspond well with the observations obtained by SEM. For comparison, the electrode expansion in case of lithium intercalation into graphite from conventional carbonate-based electrolytes is in the range of a few percent only see Figure S8 in the Supporting Information and ref. [14a,e,f].

The following cycles show a "breathing" of the electrode by about $\Delta l = 35$–50 µm per cycle. At the same time, the shape of the potential profiles (Figure 6a bottom) is maintained proofing that, despite the large volume changes, the crystalline nature of the graphite is preserved. Delamination to form disordered carbon would lead to a significant change in potential profiles (hard and soft carbons are well known to exhibit sloppy potential profiles). The behavior over 30 cycles (about 25 days) is shown in **Figure 7**a. Obviously, there are two different processes governing the electrode dynamics. The first process leads to a periodic breathing of the electrode and can be related to the intercalation/deintercalation process. Values for Δl slightly decrease upon cycling and fairly stabilize at a value of $\Delta l = 37$ µm after 30 cycles (Figure 7c). The other process is only temporary and relates to the increase in electrode thickness after the first cycle (Δt). The initial net increase after one cycle is about $\Delta t = 45$ µm and likely related to the exfoliation of the graphite particles. The first cycle can therefore be seen as an "activation cycle" leading to an overall thicker electrode. This change, however, is only temporary as the electrode is shrinking again during subsequent cycling 25 to 30 cycles. Values for Δt decrease from 45 µm to less 5 µm in 30 cycles. This means that the exfoliated particles rearrange during cycling. It is speculative to rationalize this relaxation behavior though the binder likely plays a key role. We note that the data drift due to the instrument is small compared to the change in Δt (Figure S7, Supporting Information).

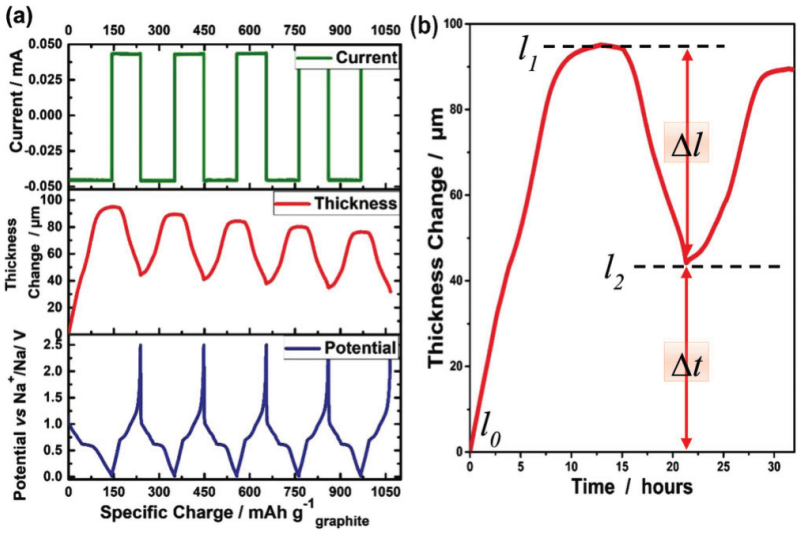

Figure 6. In situ electrochemical dilatometry measurements of first five cycles at C/10 (11 mA g^{-1}). The initial thickness of the electrode is about $l_0 = 50$ µm (without current collector).

Interestingly, the measurement signals also show that the expansion of the electrode does not linearly correlate with the amount of intercalated sodium. **Figure 8** shows the dilatation signal and its derivative ($d\Delta l/dQ$) along with the potential profile. The ($d\Delta l/dQ$)-plot shows a distinct maximum that matches with the plateau region of the potential profile at 0.6 V versus Na^+/Na. At this potential about 25–30% (nearly 40 mA h g^{-1}) of the total charge is gained but more than half of the electrode expansion takes place, see shaded area. Two minor maxima are observed before this area, which coincides with the appearance of two other smaller plateaus. The correlation can be seen more clearly from the peaks shown in dQ/dE plot Figure S1 in the Supporting Information. The results demonstrate that the staging behavior of the electrode reaction can be indirectly monitored by measuring the macroscopic dimensions of the electrode. Moreover, values for $d\Delta l/dQ$ equal nearly zero at potentials below 0.5 V versus Na^+/Na. Despite the fact that about one third of the electrode charge is obtained below this potential, almost no electrode expansion takes place anymore. This behavior can be more clearly seen from Figure 7b. This indicates that the graphene layer spacing has already reached its maximum and is large enough to incorporate further solvated ions without further dimensional changes. As the potential decreases largely linearly below 0.5 V, the electrode reactions seem to behave pseudocapacitive. This is not unreasonable considering that the graphite layer spacing is 11.3 Å. This is large enough to be considered as a pore used for capacitive storage in supercapacitor materials, for example.[20] As a result, the overpotentials in this potential regime are also the smallest (Figure S2b, Supporting Information) and hence the rate capability is very high. Notably, the negligible expansion of the electrode at the end of sodiation is opposite to what is observed for Li^+ intercalation into graphite where a much more linear correlation between electrode expansion and capacity is observed, see Figure S8 in the Supporting Information and ref. [14a].

Overall, the dilatometer studies clearly evidence that the electrode reaction is highly reversible despite the large changes in graphite layer spacing and particle morphology. The large and continuous expansion and contraction of the electrode is in strong contrast to the SEI concept. It is highly unlikely that an SEI is flexible enough to withstand such huge volume changes without cracking (and then without consuming noticeable charge for further electrolyte reduction), not to mention the additional increase in charge transfer resistance as an SEI would hamper or even prevent any solvent cointercalation. Two possibilities therefore remain: (1) The graphite electrode in ether solvents works without an SEI or (2) an SEI forms and breaks/dissolves due to the large volume expansion therefore reforming every cycle (but without significant charge consumption).

Considering (1) TEM is regularly used for high-resolution characterization of electrode/electrolyte interfaces. A number of studies has been conducted in characterizing the SEI in LIBs. The SEI thickness is typically reported to be in the range of a few up to 100 nm.[13] In our case, however we could not find any indication for the existence of a (broken) SEI. **Figure 9** and Figure S9 (Supporting Information) shows TEM images of graphite particles before and after cycling. Though analyzing several particles, we could not identify any difference between both samples. Please note that pure graphite particles without binder were used to prepare the samples in order to avoid disturbance of the measurement. SAED patterns confirm crystallinity of the samples. Considering (2), breaking/dissolving of the SEI would lead to a continuous electrolyte consumption due to its reduction, as fresh surfaces would again react with the electrolyte during cycling concomitant with the expected release of gaseous decomposition products. This phenomenon is well known for other electrode materials with large volume expansion such as alloys.[21] We will

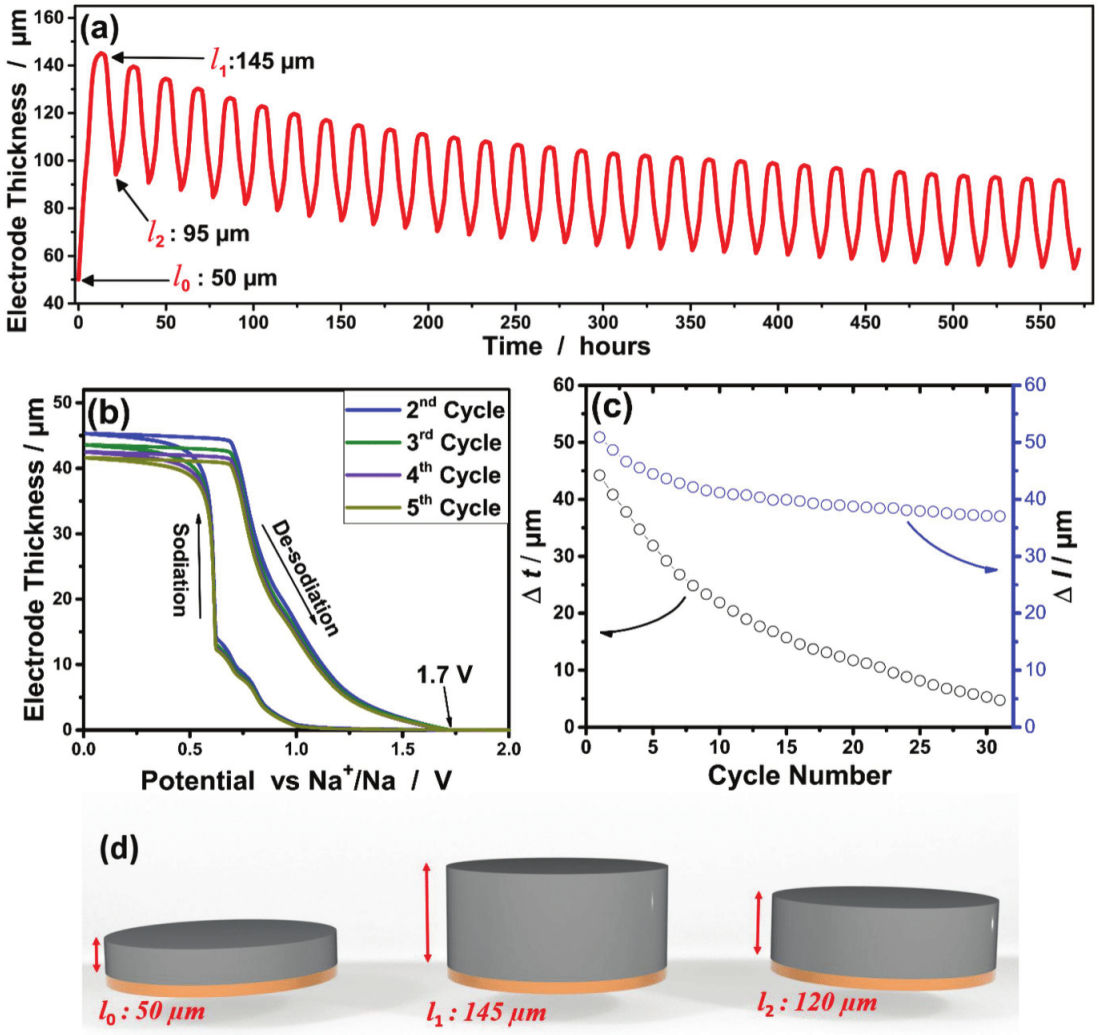

Figure 7. (a–c) ECD results: (a) Electrode thickness during cycling. (b) Change in thickness versus potential for first five cycles. (c) Change in Δt and Δl during cycling. Figure d) shows for comparision a sketch of the dimensional changes of the electrode during the first cycle based on SEM results (see Figure 6).

see in the following section, however, that electrolyte decomposition is by and large restricted to the 1st cycle only.

2.3. Online Electrochemical Mass Spectrometry

Electrolyte decomposition was studied by online OEMS. Graphite electrodes (18 mm in diameter) were sodiated/desodiated by cyclic voltammetry and decomposition of the electrolyte was followed by mass spectrometry. CO (m/z=28), CH_4 (m/z = 16), H_2 (m/z = 2), C_2H_4 (m/z = 27), and C_2H_6 (m/z = 30) were quantitatively recorded. Results are shown in **Figure 10** and Figure S10 (Supporting Information). Before cycling, the cell was equilibrated for 4 h. During this equilibration step CO could be clearly detected due to the reaction of the electrolyte with the sodium counter/reference electrodes. The parasitic contribution of the sodium electrodes to the MS signal were tested in a symmetric Na/Na cell, see Figure S11a in the Supporting Information, showing that this gassing occurs independently from the graphite electrode and is only temporary. These measurements also show that the gas release during cycling due to plating and stripping of sodium is negligible. The

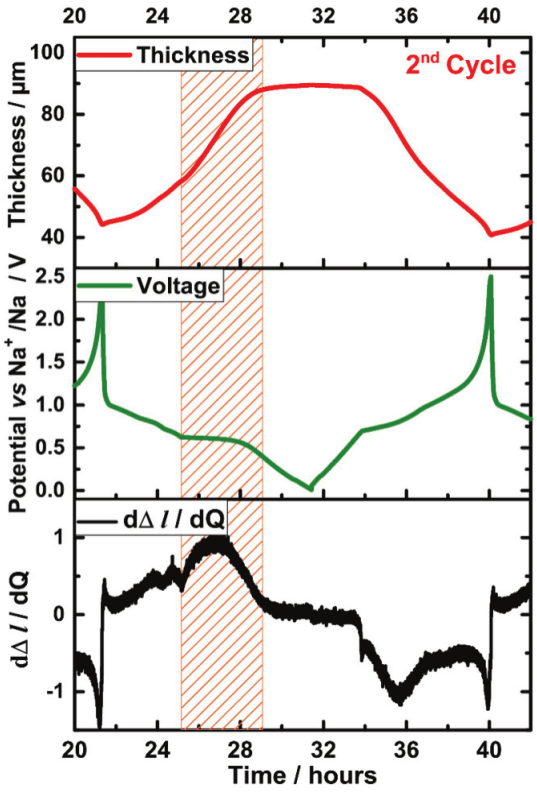

Figure 8. The thickness and voltage change by cycle number and the derivative of thickness by capacity at 2nd cycle.

sodiation of the graphite electrode starts at around 1 V versus Na^+/Na and coincides with the release of gas, especially CO and CH_4. Two maxima at around 0.4 V and at the end of reduction half-cycle are observed. During desodiation the signals are negligible. H_2, ethane, and ethylene are detected in a broader potential window with the maxima at the end of reduction. We attribute the gas release during the first sodiation to reactions between the electrolyte and the graphite surface groups (hydrogen evolution might be due to the reaction of trace amounts of water[17d]). In the classical view, an SEI has formed. As an important finding, the gas release is virtually zero in the second cycle. This means that, under the hypothesis an SEI exists and breaks due to the volume expansion, the fresh graphite surface would not further react with the electrolyte. This result therefore indeed indicates an SEI-free interface. For comparison, we studied the gas release for the intercalation of lithium into graphite using conventional carbonate based electrolytes, see Figure S11b in the Supporting Information. In this case, SEI formation is known to take place during the first cycle and indeed, we confirm that most gas release is restricted to the first cycle though the quantitative amounts are significantly larger.

Overall, results from electrochemical mass spectrometry do not provide any evidence for continuous electrolyte decomposition (at least within the sensitivity of the technique and the time of the experiments). Signals related to side reactions are largely restricted to the first cycle only. This is very surprising considering the generally accepted instability of salt and solvents and low potentials. Reductive decomposition of diglyme has been reported to occur at potentials around 0.4 V versus Li^+/Li, for example.[22] One therefore has to assume that the interface between graphite and the electrolyte is kinetically stabilized and therefore decomposition of the electrolyte is (if at all) very slow. Very recently, Maibach et al.[7b] used soft X-ray photoelectron spectroscopy to study the graphite/electrolyte interface of a cointercalation reaction. It is important to note that they used a different electrolyte composition (NaFSI in tetraglyme) and electrode (types of graphite and binder) and their cells showed much larger irreversible charge consumption. Their findings are important to our study nevertheless. Maibach et al. suggests that an SEI forms but breaks during cycling as a result of the large volume expansion. Although tetraglyme decomposition could not be ruled out completely, decomposition of the conductive salt anion (FSI^-) was identified as major degradation mechanism. To investigate this, we recorded also mass signals from possible decomposition fragments from the electrolyte anion OTf^- used in our study ($m/z = 48$ (SO_2); $m/z = 69$ (CF_3)) but also here, we could not find any evidence of continuous electrolyte decomposition. In view of that, our OEMS studies (NaOTf/diglyme electrolyte) indicate a behavior different from the one suggested by Maibach et al. for the NaFSI/tetraglyme electrolyte. We will report on the influence of the conductive salt on the reaction in a forthcoming publication.

3. Conclusions

The intercalation of solvated sodium ions into graphite was studied by different (in situ) methods. The cointercalation of solvent molecules along with the ions leads to a severe expansion in graphene layer spacing which should lead to rapid

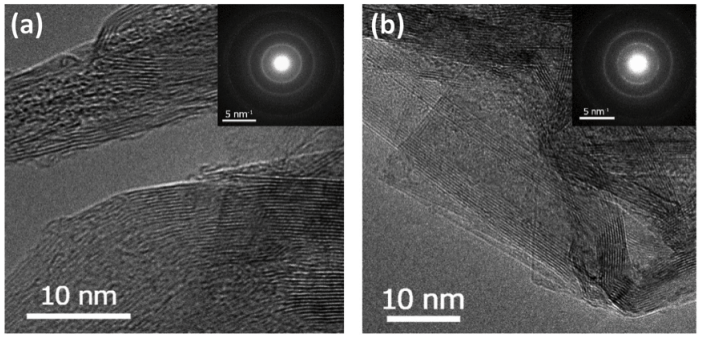

Figure 9. TEM images and SAED patterns of the graphite particles a) before cycling and b) after 2nd desodiation.

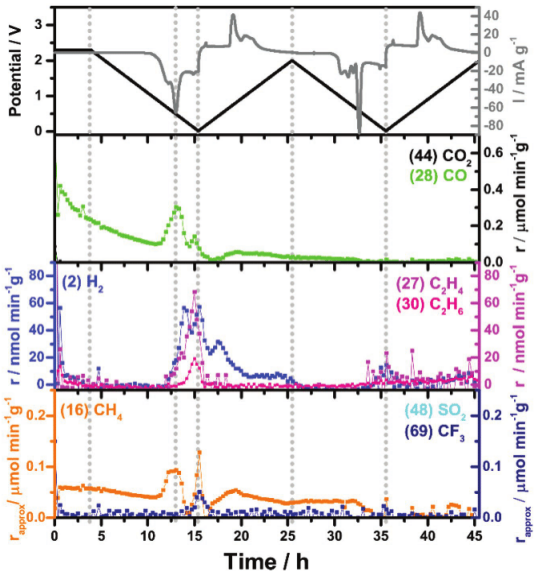

Figure 10. Cyclic voltammogram normalized by mass (with a scan-rate of 0.055 mV s^{-1}) and selected OEMS mass signals.

electrode degradation. We showed that the reaction nevertheless is highly reversible because the graphite particles only exfoliate to form crystalline platelets rather than delaminate.[19] This way, potential profiles and charge capacity remain unchanged over many cycles. By using in situ ECD, we studied the actual change in electrode dimensions during cycling and found that the electrode with an original thickness of l_0 = 50 µm breathes by around Δl = 35–50 µm within a cycle, yet excellent cycle life is achieved. In the first cycle, the electrode becomes also much thicker (Δt = 45 µm) though this effect is only temporary. The electrode shrinks again during cycling approaching the original thickness ($\Delta t \rightarrow$5 µm within 30 cycles). The dilatometry studies also showed that the intercalation reaction undergoes staging with the largest effect on the electrode thickness occurring at a voltage plateau of 0.6 V versus Na^+/Na. Below this plateau, the increase in electrode thickness is surprisingly small, which, combined with the electrochemical results, indicates a more pseudocapacitive storage mechanism in this voltage regime.

Another important finding addresses the apparently missing SEI. In the classical view, electrolyte decomposition must take place at the applied potentials and high cycle numbers can be only achieved by the formation of an SEI that prevents further decomposition as well as solvent cointercalation. Moreover, host structures with a lattice expansion as large as the one discussed here typically suffer from continuous electrolyte degradation as the SEI continuously breaks and reforms. By TEM, however, we were not able to find any sign of a SEI or fractions of it. By OEMS, we found that electrolyte decomposition is largely restricted to the first cycle only, which is likely the result of nonrecurring reactions with graphite surface groups. We therefore suggest that the decomposition products are soluble and/or volatile and that no solid SEI forms. As the gas signals quickly diminish during cycling, we can also rule out the possibility of continuous electrolyte decomposition (at least within the sensitivity of the technique and the time of the experiments). This indicates that the cointercalation reaction works without an SEI, which also would explain the excellent kinetics of the reaction that is especially visible at potentials below 0.6 V versus Na^+/Na. We therefore assume that for the studied electrode reaction, the interface between electrode and electrolyte is kinetically stabilized. Spectroscopic in situ studies by IR and Raman spectroscopy, for example, are most suited to further clarify this point although the very strong radiation absorbance of graphite is a challenge for these methods.

Overall, the studied electrode reaction behaves very different from conventional intercalation reactions of graphite. Solvated rather than naked ions insert into graphite, yet the reaction is highly reversible despite the large volume expansion. Finally, and maybe most intriguingly, the reaction is possibly the first case of an SEI-free graphite anode material. Deciphering the charge-transfer mechanism over this interface is an intriguing task for the future. The discovery of reversible electrochemical reactions based on solvent cointercalation is very recent offering a large and mostly unexplored research field.

4. Experimental Section

Experimental Details—Electrode Preparation: Electrodes contained 90% graphite (MTI Corp.) and 10% binder (Polyvinylidene fluoride 'EQ-Lib-PVDF', MTI Corp.). Slurries were mixed in *N*-methyl-2-pyrrolidone (Sigma Aldrich) and casted onto dendritic copper foil (15 µm thick). The average loading of electrodes after drying (12 h at 120 °C) was 5 mg cm^{-2}, the average electrode thickness was about 50 µm.

*Experimental Details—Electrochemical (*In Situ*) Measurements*: Cells for galvanostatic cycling, ECD, and OEMS measurements were prepared in argon-filled glove box (<0.1 ppm O_2 and H_2O) with electrodes at diameters of 12, 10, and 18 mm, respectively. For galvanostatic cycling, two-electrode coin cells (CR2032 Coin Cells by MTI Corp.) and i-shaped Swagelok cells were used. Sodium metal (BASF SE Corporation) was used as the counter and reference electrodes. As separator, Whatman glass microfiber filters (GF/A) were soaked into 100 µL electrolyte containing predried (100 °C overnight) sodium trifluoromethanesulfonate (NaOTf, purity >98.0%, Sigma Aldrich) in predried (in 4 Å porous molecular sieves, overnight) diethylene glycol dimethyl ether (diglyme, anhydrous purity >99.5%, Sigma Aldrich). The coin cells were prepared at 1000 PSI by using a crimper (TG-110). Electrochemical measurements were carried out at 25 °C by Biologic BCS battery cycler. The potential window was between 0.01 and 2.5 V versus Na^+/Na galvanostatically (at constant current–constant voltage). The C rate was calculated based on specific charge of graphite stated in literature (Q = 110 mA h g^{-1}, which forms $Na(diglyme)_2C_{20}$).[5] Therefore, 1 C represents a specific current of i = 110 mA g^{-1} and experiments were done at C/10 and C/3. In the specific design of ECD-nano cells (by EL-CELL GmbH), special ceramic porous separator was soaked by 400–500 µL of electrolyte by pre-evacuating all the gases from the pores which helped the wetting of 10 mm of electrode properly. The setup is designed in a way that only the dilatation of the working electrode (here graphite) is measured. This is done by a spring that presses the glass frit onto a metal frame. The glass frit position is therefore fixed and only the dilatation of the working electrode is recorded. For OEMS, the setup was described elsewhere[23] (see the Supporting Information). The galvanostatic and cyclic voltammetry measurements were also done simultaneously with OEMS.

Experimental Details—Analytical Methods: Morphological investigations were carried out by using a SEM (by Phenom ProX) operated at 15 kV accelerating voltage. Samples after cycling were rinsed with diglyme and dried at 25 °C under vacuum overnight. For cross section measurements, electrodes were cut by knife. Sodiated samples were air sensitive and transferring time was limited to 60 s at maximum. Electrode thickness was also determined by a digital thickness dial gauge from Käfer Messuhrenfabrik GmbH. An Autosorb iQ3 machine from Quantachrome Corporation was used for nitrogen physisorption experiments. Air contact during sample transfer was minimized by special sample holders. A vario micro cube from Elementaranalyse GmbH was used for CHNS analysis. TEM was performed by a FEI Tecnai G^2 FEG operating at 200 kV. The sample material was deposited on a copper grid with a Lacey carbon support film and directly transferred to the vacuum of the TEM.

Computational Details—Nonperiodic Calculations: DFT calculations were performed using the software package TURBOMOLE 6.6.[24] Structure optimizations were done employing the Perdew–Burke–Ernzerhof (PBE) functional[25,33] and the multipole accelerated resolution of identity approximation (MARI-J).[26] All atoms were characterized in an all electron description using the correlation consistent (cc-pVTZ) Dunning-type basis set.[27] Dispersion correction was applied in Grimme's D3 scheme with a zero-dumping.[28] Frequency calculations were performed at the PBE(MARI-J)/cc-pVTZ level of theory to confirm the presented stationary point as minimum. To include solvent effects (we assumed the pure solvent of diglyme with a dielectric constant of 7.4 [29]) the continuum solvation model (COSMO) was employed. The start structure of the $Na^+(diglyme)_2$ complex was generated based on the $Li(diglyme)_2ClO_4$ crystal structure of ref. [30]. NPA charges were calculated to investigate the charge distribution within the complex.[31]

Computational Details—Periodic Calculations: DFT calculations with periodic boundary conditions were performed using the Vienna ab initio simulation package version 5.4.1.[32] Also the generalized gradient approximation exchange-correlation functional PBE was employed[33] and the dispersion correction D3 by Grimme was added. Projector-augmented wave potentials and a plane wave basis set with an energy cutoff of 600 eV was used.[34] For the structure optimization (conjugate-gradient algorithm, convergence criteria for the total energy was 10^{-6} eV and for the forces was 10^{-2} eV $Å^{-1}$) of the bulk graphite with lattice parameters of $a = b = 12.33$ Å, a $4 \times 4 \times 2$ Monkhorst–Pack[35] *k*-point mesh was chosen.

Supporting Information

Supporting Information is available from the Wiley Online Library or from the author.

Acknowledgements

The authors thank B. Fähndrich and G. Gottschalt for technical support (physisorption measurements, elemental analysis) and BASF SE for providing high purity sodium metal. P.A., D.M., O.L., M.v.R., and M.G. thank the DFG for support within the project "Redoxchemie ternärer Graphitinterkalationsverbindungen (630743). P.A. and M.G. thank the State of Thuringia for support within the ProExzellenz program. E.J.B. acknowledges Swiss National Science Foundation (SNSF) under the "Ambizione Energy" funding scheme (Grant No. 160540). D.M., O.L., and M.v.R. thank the high performance center of the Justus-Liebig-University Giessen. F.L. is grateful for funding of SEM and TEM facilities via the Gottfried Wilhelm Leibniz programme of the DFG (LA830/14-1). The authors further thank Matthias Hahn from El-Cell and J. Breu (Bayreuth) for general advice.

Conflict of Interest

The authors declare no conflict of interest.

Keywords

cointercalation, dilatometry, graphite, sodium-ion batteries, solid electrolyte interphases

Received: September 28, 2017
Revised: December 15, 2017
Published online:

[1] a) M. D. Slater, D. Kim, E. Lee, C. S. Johnson, *Adv. Funct. Mater.* **2013**, *23*, 947; b) Y. Li, Y. Lu, C. Zhao, Y.-S. Hu, M.-M. Titirici, H. Li, X. Huang, L. Chen, *Energy Storage Mater.* **2017**, *7*, 130; c) V. Palomares, P. Serras, I. Villaluenga, K. B. Hueso, J. Carretero-González, T. Rojo, *Energy Environ. Sci.* **2012**, *5*, 5884; d) N. Yabuuchi, K. Kubota, M. Dahbi, S. Komaba, *Chem. Rev.* **2014**, *114*, 11636; e) S.-W. Kim, D.-H. Seo, X. Ma, G. Ceder, K. Kang, *Adv. Energy Mater.* **2012**, *2*, 710; f) P. Adelhelm, P. Hartmann, C. L. Bender, M. Busche, C. Eufinger, J. Janek, *Beilstein J. Nanotechnol.* **2015**, *6*, 1016; g) P. K. Nayak, L. Yang, W. Brehm, P. Adelhelm, *Angew. Chem., Int. Ed.* **2018**, *57*, 102; h) Y. Kim, K. H. Ha, S. M. Oh, K. T. Lee, *Chemistry* **2014**, *20*, 11980; i) H. Pan, Y.-S. Hu, L. Chen, *Energy Environ. Sci.* **2013**, *6*, 2338.

[2] a) S. Wenzel, T. Hara, J. Janek, P. Adelhelm, *Energy Environ. Sci.* **2011**, *4*, 3342; b) P. Ge, M. Fouletier, *Solid State Ionics* **1988**, *28–30*, 1172; c) M. Cabello, T. Chyrka, R. Klee, M. J. Aragón, X. Bai, P. Lavela, G. M. Vasylchenko, R. Alcántara, J. L. Tirado, G. F. Ortiz, *J. Power Sources* **2017**, *347*, 127; d) B. Jache, J. O. Binder, T. Abe, P. Adelhelm, *Phys. Chem. Chem. Phys.* **2016**, *18*, 14299.

[3] a) W. Märkle, N. Tran, D. Goers, M. E. Spahr, P. Novák, *Carbon* **2009**, *47*, 2727; b) G. Schmuelling, T. Placke, R. Kloepsch, O. Fromm, H.-W. Meyer, S. Passerini, M. Winter, *J. Power Sources* **2013**, *239*, 563; c) L. Fan, Q. Liu, S. Chen, Z. Xu, B. Lu, *Adv. Energy Mater.* **2017**, *7*, 1602778.

[4] a) K. Nobuhara, H. Nakayama, M. Nose, S. Nakanishi, H. Iba, *J. Power Sources* **2013**, *243*, 585; b) Y. Liu, B. V. Merinov, W. A. Goddard 3rd, *Proc. Natl. Acad. Sci.* **2016**, *113*, 3735; c) H. Moriwake, A. Kuwabara, C. A. J. Fisher, Y. Ikuhara, *RSC Adv.* **2017**, *7*, 36550.

[5] B. Jache, P. Adelhelm, *Angew. Chem., Int. Ed.* **2014**, *53*, 10169.

[6] a) A. P. Cohn, K. Share, R. Carter, L. Oakes, C. L. Pint, *Nano Lett.* **2016**, *16*, 543; b) H. Kim, J. Hong, G. Yoon, H. Kim, K.-Y. Park, M.-S. Park, W.-S. Yoon, K. Kang, *Energy Environ. Sci.* **2015**, *8*, 2963; c) K. Gotoh, H. Maruyama, T. Miyatou, M. Mizuno, K. Urita, H. Ishida, *J. Phys. Chem. C* **2016**, *120*, 28152; d) S. C. Jung, Y. J. Kang, Y. K. Han, *Nano Energy* **2017**, *34*, 456; e) G. Yoon, H. Kim, I. Park, K. Kang, *Adv. Energy Mater.* **2017**, *7*, 1601519; f) H. Kim, G. Yoon, K. Lim, K. Kang, *Chem. Commun.* **2016**, *52*, 12618.

[7] a) H. Kim, J. Hong, Y.-U. Park, J. Kim, I. Hwang, K. Kang, *Adv. Funct. Mater.* **2015**, *25*, 534; b) J. Maibach, F. Jeschull, D. Brandell, K. Edstrom, M. Valvo, *ACS Appl. Mater. Interfaces* **2017**, *9*, 12373.

[8] L. Seidl, N. Bucher, E. Chu, S. Hartung, S. Martens, O. Schneider, U. Stimming, *Energy Environ. Sci.* **2017**, *10*, 1631.

[9] a) Z. Zhu, F. Cheng, Z. Hu, Z. Niu, J. Chen, *J. Power Sources* **2015**, *293*, 626; b) Z. Guan, X. Shen, R. Yu, Z. Wang, L. Chen, *Electrochim. Acta* **2016**, *222*, 1365.

[10] A. P. Cohn, N. Muralidharan, R. Carter, K. Share, L. Oakes, C. L. Pint, *J. Mater. Chem. A* **2016**, *4*, 14954.

[11] K. Gotoh, T. Ishikawa, S. Shimadzu, N. Yabuuchi, S. Komaba, K. Takeda, A. Goto, K. Deguchi, S. Ohki, K. Hashi, T. Shimizu, H. Ishida, *J. Power Sources* **2013**, *225*, 137.

[12] a) S. Terada, H. Susa, S. Tsuzuki, T. Mandai, K. Ueno, Y. Umebayashi, K. Dokko, M. Watanabe, *J. Phys. Chem. C* **2016**, *120*, 23339; b) K. Yoshida, M. Nakamura, Y. Kazue, N. Tachikawa, S. Tsuzuki, S. Seki, K. Dokko, M. Watanabe, *J. Am. Chem. Soc.* **2011**,

133, 13121; c) J. Wahlers, K. D. Fulfer, D. P. Harding, D. G. Kuroda, R. Kumar, R. Jorn, *J. Phys. Chem. C* **2016**, *120*, 17949.

[13] S. J. An, J. Li, C. Daniel, D. Mohanty, S. Nagpure, D. L. Wood, *Carbon* **2016**, *105*, 52.

[14] a) J. L. Gómez-Cámer, C. Bünzli, M. M. Hantel, T. Poux, P. Novák, *Carbon* **2016**, *105*, 42; b) T. Kim, S. Park, S. M. Oh, *J. Electrochem. Soc.* **2007**, *154*, A1112; c) J. Kim, M. K. Chung, B. H. Ka, J. H. Ku, S. Park, J. Ryu, S. M. Oh, *J. Electrochem. Soc.* **2010**, *157*, A412; d) J. L. Gómez Cámer, J. Morales, L. Sánchez, P. Ruch, S. H. Ng, R. Kötz, P. Novák, *Electrochim. Acta* **2009**, *54*, 6713; e) M. Winter, G. H. Wrodnigg, J. O. Besenhard, W. Biberacher, P. Novák, *J. Electrochem. Soc.* **2000**, *147*, 2427; f) M. Hahn, H. Buqa, P. W. Ruch, D. Goers, M. E. Spahr, J. Ufheil, P. Novák, R. Kötz, *Electrochem. Solid-State Lett.* **2008**, *11*, A151; g) B. D. Polat, O. Keles, *J. Power Sources* **2014**, *266*, 353; h) J. B. Siegel, A. G. Stefanopoulou, P. Hagans, Y. Ding, D. Gorsich, *J. Electrochem. Soc.* **2013**, *160*, A1031; i) J. Huesker, L. Froböse, A. Kwade, M. Winter, T. Placke, *Electrochim. Acta* **2017**, *257*, 423.

[15] M. M. Hantel, V. Presser, R. Kötz, Y. Gogotsi, *Electrochem. Commun.* **2011**, *13*, 1221.

[16] F. Klein, R. Pinedo, B. B. Berkes, J. Janek, P. Adelhelm, *J. Phys. Chem. C* **2017**, *121*, 8679.

[17] a) F. La Mantia, P. Novák, *Electrochem. Solid-State Lett.* **2008**, *11*, A84; b) H. Buqa, A. Würsig, J. Vetter, M. E. Spahr, F. Krumeich, P. Novák, *J. Power Sources* **2006**, *153*, 385; c) R. Imhof, P. Novak, *J. Electrochem. Soc.* **1998**, *145*, 1081; d) R. Bernhard, M. Metzger, H. A. Gasteiger, *J. Electrochem. Soc.* **2015**, *162*, A1984; e) M. Metzger, C. Marino, J. Sicklinger, D. Haering, H. A. Gasteiger, *J. Electrochem. Soc.* **2015**, *162*, A1123.

[18] T. Ohzuku, Y. Iwakoshi, K. Sawai, *J. Electrochem. Soc.* **1993**, *140*, 2490.

[19] Comment: *The terms exfoliation and delamination are not consistently used in literature. Unfortunately, contradicting definitions exist and, in many cases, no difference between both terms is made. For our study, however, distinguishing betweeen both terms is important. Exfoliation describes the decomposition of larger particles to smaller ones. In our case, graphite particles exfoliate to form platelets. These platelets are still crystalline and therfore the XRD pattern shows the relevant diffraction lines. On the other hand, delamination would describe the separation of the graphite particles into its constituent layers (graphenes). In this case, crystallinity of the material would be lost. The meaning of the terms exfoliation and delamination is in line with the definition made by Gardolinski and Lagaly*, J. E. F. C. Gardolinski, G. Lagaly, *Clay Miner.* **2005**, *40*, 547, https://doi.org/10.1180/0009855054040191.

[20] F. Béguin, V. Presser, A. Balducci, E. Frackowiak, *Adv. Mater.* **2014**, *26*, 2219.

[21] R. Jung, M. Metzger, D. Haering, S. Solchenbach, C. Marino, N. Tsiouvaras, C. Stinner, H. A. Gasteiger, *J. Electrochem. Soc.* **2016**, *163*, A1705.

[22] S. Tobishima, H. Morimoto, M. Aoki, Y. Saito, T. Inose, T. Fukumoto, T. Kuryu, *Electrochim. Acta* **2004**, *49*, 979.

[23] M. He, L. Boulet-Roblin, P. Borel, C. Tessier, P. Novák, C. Villevieille, E. J. Berg, *J. Electrochem. Soc.* **2015**, *163*, A83.

[24] *TURBOMOLE V6.6 2014, A development of University of Karlsruhe and Forschungszentrum Karlsruhe GmbH*, **1989–2007**, TURBOMOLE, Available: http://www.turbomole.com.

[25] a) A. D. Becke, *J. Chem. Phys.* **1993**, *98*, 5648; b) A. D. Becke, *Phys. Rev. A* **1988**, *38*, 3098; c) C. Lee, W. Yang, R. G. Parr, *Phys. Rev. B* **1988**, *37*, 785; d) S. H. Vosko, L. Wilk, M. Nusair, *Can. J. Phys.* **1980**, *58*, 1200.

[26] a) M. Sierka, A. Hogekamp, R. Ahlrichs, *J. Chem. Phys.* **2003**, *118*, 9136; b) K. Eichkorn, O. Treutler, H. Öhm, M. Häser, R. Ahlrichs, *Chem. Phys. Lett.* **1995**, *240*, 283; c) K. Eichkorn, F. Weigend, O. Treutler, R. Ahlrichs, *Theor. Chem. Acc.* **1997**, *97*, 119.

[27] T. H. Dunning, *J. Chem. Phys.* **1989**, *90*, 1007.

[28] S. Grimme, J. Antony, S. Ehrlich, H. Krieg, *J. Chem. Phys.* **2010**, *132*, 154104.

[29] S. Tang, H. Zhao, *RSC Adv.* **2014**, *4*, 11251.

[30] W. A. Henderson, N. R. Brooks, W. W. Brennessel, J. Young, G. Victor, *J. Phys. Chem. A* **2004**, *108*, 225.

[31] F. Weinhold, E. D. Glendening, *NBO 6.0 Program Manual, Natural Bond Orbital Analysis Programs*, Board of Regents of the University of Wisconsin System on behalf of the Theoretical Chemistry Institute, **1996–2013**.

[32] a) G. Kresse, J. Furthmuller, *J. Pyhs. Rev. B* **1996**, *54*, 11169; b) G. Kresse, J. Hafner, *Phys. Rev. B* **1993**, *47*, 558; c) G. Kresse, J. Hafner, *Phys. Rev. B* **1994**, *49*, 14251; d) G. Kresse, J. Furthmiiller, *Comput. Mater. Sci.* **1996**, *6*, 15.

[33] a) J. P. Perdew, K. Burke, M. Ernzerhof, *Phys. Rev. Lett.* **1997**, *78*, 1396; b) J. P. Perdew, K. Burke, M. Ernzerhof, *Phys. Rev. Lett.* **1996**, *77*, 3865.

[34] a) P. E. Blöchl, *Phys. Rev. B* **1994**, *50*, 17953; b) G. Kresse, D. Joubert, *Phys. Rev. B* **1999**, *59*, 1758.

[35] H. J. Monkhorst, J. D. Pack, *Phys. Rev. B* **1976**, *13*, 5188.

5.2. Temperature Effect and Solvent Effect on Co-intercalation Reaction (Publication 2)

Although a number of publications on co-intercalation reactions have been published in the meanwhile (***Section 3.4, Table 1***) systematic studies on some key parameters were still lacking. Within previous studies, only 1G-4G were considered as solvents. In this part, pentaglyme (5G) and crown ethers and even some other solvents (OME, DTU ***Section 4.4***) were tested. None of the crown ethers as well as pentaglyme co-intercalated at room temperature. The room-temperature performance in the case of triglyme was also poor. Temperature-dependent measurements showed that this is largely due to kinetic limitation and the reactions could be activated at the higher temperatures.

Especially for pentaglyme, full activation was obtained 45 ºC, likely linked to a strong decrease in viscosity. In a similar way, also triglyme can be fully activated and the performance becomes excellent at elevated temperatures. For the other glymes, the room temperature performance was already very fast so that they could be classified as "thermodynamically controlled" reactions. This means that temperature dependent measurements provided thermodynamic information, i.e. determination of the entropy change of the reaction. Also crown ether 18c6 could be successfully used as an electrolyte solvent above its melting point. This result was the first demonstration of a t-GICs with crown ethers being synthesized by electrochemical methods. In addition, some parasitic reactions appear at elevated temperatures.

The results of this study were published in *The Journal of Physical Chemistry C*.

Mustafa Goktas, Baris Akduman, Peihua Huang, Andrea Balducci, Philipp Adelhelm, *Temperature-Induced Activation of Graphite Co-intercalation Reactions for Glymes and Crown Ethers in Sodium-Ion Batteries, The Journal of Physical Chemistry C* **2018**, *122*, 26816−26824.

For this paper, viscosity and conductivity measurements and analyses are performed by Peihua Huang and Andrea Balducci. Most of the measurements related to electrochemistry and XRD and also data analysis and further calculations are performed by the first author. Some parts of measurements and illustrative works are done by Baris Akduman. The paper is written by the first author and edited by Philipp Adelhelm. By all the comments and contributions of the authors, the paper is be published.

THE JOURNAL OF PHYSICAL CHEMISTRY C

Article

Cite This: J. Phys. Chem. C 2018, 122, 26816−26824

pubs.acs.org/JPCC

Temperature-Induced Activation of Graphite Co-intercalation Reactions for Glymes and Crown Ethers in Sodium-Ion Batteries

Mustafa Goktas,[†,‡] Baris Akduman,[§] Peihua Huang,[†,‡] Andrea Balducci,[†,‡] and Philipp Adelhelm*[,†,‡]

[†]Institute of Technical Chemistry and Environmental Chemistry and [‡]Center for Energy and Environmental Chemistry (CEEC Jena), Friedrich Schiller University Jena, Philosophenweg 7a, D-07743 Jena, Germany

[§]Department of Metallurgical and Materials Engineering, Middle East Technical University, 06800 Ankara, Turkey

Supporting Information

ABSTRACT: The intercalation of solvated ions into graphite leads to ternary graphite intercalation compounds (t-GICs). Here, we study the impact of temperature on the electrochemical activity of graphite electrodes for co-intercalation reactions between 20 and 80 °C in sodium cells. For this, a range of linear ethers (mono-, di-, tri-, and tetraglyme) are studied. For the first time, pentaglyme and several crown ethers are also investigated. We find that several solvents that appear as unsuitable for the co-intercalation reaction at room temperature provide higher capacities at elevated temperatures. The most evident example is pentaglyme. While poor performance is found at room temperature for this solvent (20 $mAhg^{-1}$ and large polarization), almost complete utilization (~110 mAh g^{-1}) and excellent rate capability are obtained at 45 °C. We find that the reactions involving mono-, di-, tetra-, and (at elevated temperatures also) pentaglyme are thermodynamically controlled, whereas the reaction with triglyme is kinetically limited. We also find that the crown ether 18c6 can be used as an electrolyte solvent above its melting point, which, for the first time, demonstrates the synthesis of t-GICs with crown ethers by electrochemical methods. Additionally, parasitic reactions are found to appear at elevated temperatures. Overall, we demonstrate that new co-intercalation reactions can be activated by temperature. The chemistry of these compounds might therefore be much richer than previously thought.

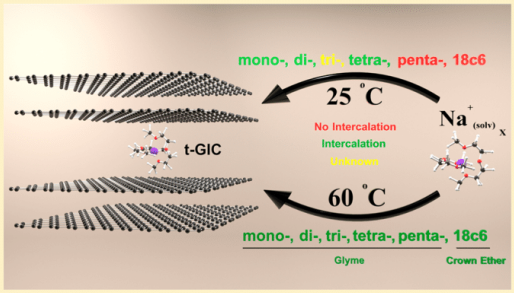

1. INTRODUCTION

Electrochemical-energy-storage technologies gain more and more relevance because of the rising markets of electric mobility, grid storage, and robotics. Because of limited resources of lithium and other valuable elements such as cobalt, researchers are seeking for alternative battery concepts to complement lithium-ion batteries (LIBs) in the future. Sodium-ion batteries (SIBs) are based on the same concept as that of LIBs, and they appear as an attractive alternative to make more cost-effective batteries that are less susceptible to resource constraints.[1−10] Changing from "lithium-ion" to "sodium-ion", however, is not always as straightforward as one may assume at first as the larger ion size of Na^+ has a strong impact on the kinetic and thermodynamic behaviors of the cell.[7]

A lot of research currently aims to find suitable materials for the negative electrode (for brevity, anode materials in the following). Carbon-based anode materials are highly preferred due to their cost-effectiveness and abundancy of carbon. The material of choice for LIBs is graphite, which forms with lithium a sequence of binary graphite intercalation compounds (b-GICs) with the final stoichiometry of LiC_6 (q_{th} = 372 mAh g^{-1}).[11,12] In the case of sodium, however, a comparable reaction hardly takes place. The current understanding is that intercalation is prevented because of thermodynamic reasons. Positive formation energies for the compounds NaC_6 and NaC_8 have been calculated, for example.[13−16] A way around this problem is to intercalate solvated sodium ions. In this case, ternary graphite intercalation compounds (t-GICs) with the general formula $Na(solv)_nC_x$ are formed. t-GICs are known for many years, but their reversible formation in electrochemical cells over many cycles was realized only recently by Jache and Adelhelm[17] and shortly after by Kim et al.[18] using diglyme as a solvent. Although the reversible intercalation of solvated ions into graphite by electrochemical methods is a poorly understood process, the electrode reaction can be generalized as follows

$$Na^+(solv)_n + xC + e^- \overset{\text{intercalation}}{\rightleftharpoons} Na(solv)_nC_x \quad n = 1 \text{ or } 2, \quad x = 16 - 22 \tag{1}$$

Received: August 14, 2018
Revised: October 30, 2018
Published: October 30, 2018

DOI: 10.1021/acs.jpcc.8b07915
J. Phys. Chem. C 2018, 122, 26816−26824

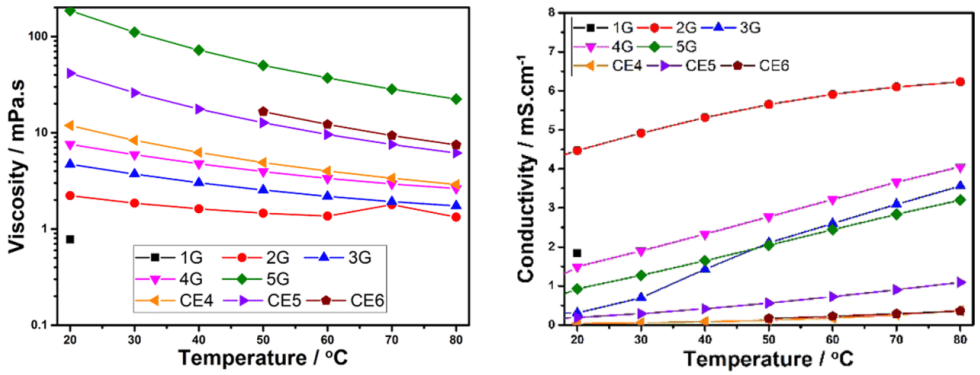

Figure 1. (a) Viscosities and (b) conductivities of glyme-based and crown-ether-based electrolytes (1 M NaOTf) at various temperatures.

The cell reaction with Na metal as a counter electrode is

$$\mathrm{Na} + x\cdot\mathrm{C} + (\mathrm{solv})_n \overset{\text{intercalation}}{\rightleftharpoons} \mathrm{Na(solv)}_n\mathrm{C}_x \qquad (2)$$

The latter equation shows that the resulting cell voltage ($E = -\Delta G/F$) will depend on the type of the solvent. This is different from the conventional Li-ion (Na-ion) concept, where the solvent does not influence the cell voltage; see, e.g., ref 7. A series of glymes (mono-, di-, tri-, and tetraglyme, abbreviated as 1G, 2G, 3G, and 4G, respectively) have been tested in the meanwhile by several groups.[19−26] Long cycle life and high currents can be generally achieved. For example, Cohn et al. reported 8000 cycles at 12 A g^{-1} with 96% capacity retention when using 2G as the solvent.[27] The concept has also been applied to potassium-ion batteries.[28] Moreover, Kim et al. achieved, for the first time, the intercalation of a Mg^{2+} ion into graphite by creating a solvation shell with glymes.[29] For all of these glymes, stage-I t-GICs are formed. 1G, 2G, and 4G show very complex yet defined discharge profile steps and cyclic voltammograms with the redox potential indeed depending on the type of glyme. Values for the specific capacity are in the range of 100−120 mAh g^{-1}. The behavior for 3G is notably different; discharge profile and cyclic voltammogram are ill defined and the capacity is generally lower (about 80 mAh g^{-1} at C/3). Steric hindrance has been suggested as a reason for this behavior, for example, ref 20, but it remains unclear whether the poorer performance with 3G is due to thermodynamics or kinetics. Notably, also t-GICs with polyethers have been recently prepared by chemical methods.[30] Overall, there is a great need in further understanding the intercalation of solvated ions in general and in particular the observed limitations in the case of 3G.

Pentaglyme (5G) extends the series of glymes, yet it has been much less studied so far. Physical properties of several electrolyte mixtures of 5G with NaTFSI were discussed by Terada et al.. Also, they tested 5G as a solvent in SIBs studying $Na_{0.44}MnO_2$ as a cathode at 30 and 60 °C, and the effect of 5G in the electrolyte is also discussed.[31] The same group again showed the applicability of 5G using cathodes of $Na_{0.44}MnO_2$ and sulfur.[32] Comparison between the rate performances of 4G and 5G is also done. Interestingly, 5G has not been tested for co-intercalation reactions into graphite so far. Within the family of ethers, the structurally related crown ethers are also of interest. Zhang et al. recently synthesized for the first time t-GICs on the basis of intercalation of complexes of Na^+ and K^+ with crown ethers using chemical methods.[33] Formation of stage-I compounds was found for crown ether 5 (15c5) and 6 (18c6), while a mixed phase was found in the case of crown ether 4 (12c4). The structure and dynamic behavior of these types of t-GICs were studied in a follow-up study by Gotoh et al. using density functional theory and NMR analysis, suggesting a bilayer intercalate structure in the case of Na^+ and a monolayer intercalate structure in the case of K^+.[34] While the chemical synthesis of these crown-ether-containing t-GICs has been demonstrated, their formation by electrochemical methods has not been successful so far.[20]

In this work, we report on the important effect of temperature on the activation of co-intercalation reactions. To accomplish and widen the research, 5G is also tested for the first time as a solvent for graphite co-intercalation reactions. While no co-intercalation takes place at room temperature (RT), we find that the reaction can be easily activated by temperature. In a similar way, the reaction with 3G is easily activated by increasing temperature, which indicates that its poor room-temperature performance is due to poor kinetics and not because of thermodynamics. Potential profiles are discussed as a function of temperature (RT to 85 °C) and as a function of the type of glyme (1G to 5G). Motivated by the recent report on the chemical synthesis of crown-ether-containing t-GICs,[33] we now report that these compounds can also be formed in electrochemical cells as long as elevated temperatures are used. Temperature therefore can be a critical effect in activating new co-intercalation reactions, and the number of possible solvents for this reaction type may be much larger as previously thought. We also comment on the side reactions that may occur at elevated temperatures or at very small currents and report data on the temperature-dependent electrolyte behavior with respect to conductivity and viscosity.

2. RESULTS AND DISCUSSION

2.1. Viscosity and Conductivity. The viscosities of different electrolyte solutions were studied between 20 and 80 °C, as shown in Figure 1. All electrolyte solutions contained 1 M NaOTf as the conductive salt. For 1G, values were determined only at 20 °C because of the high vapor pressure. For glymes, the viscosity increases with the glyme length from 0.78 mPa (1G) to 7.59 mPa (4G) at 20 °C. The viscosity for 5G locates a large gap away with 186 mPa at 20 °C, but it

DOI: 10.1021/acs.jpcc.8b07915
J. Phys. Chem. C 2018, 122, 26816−26824

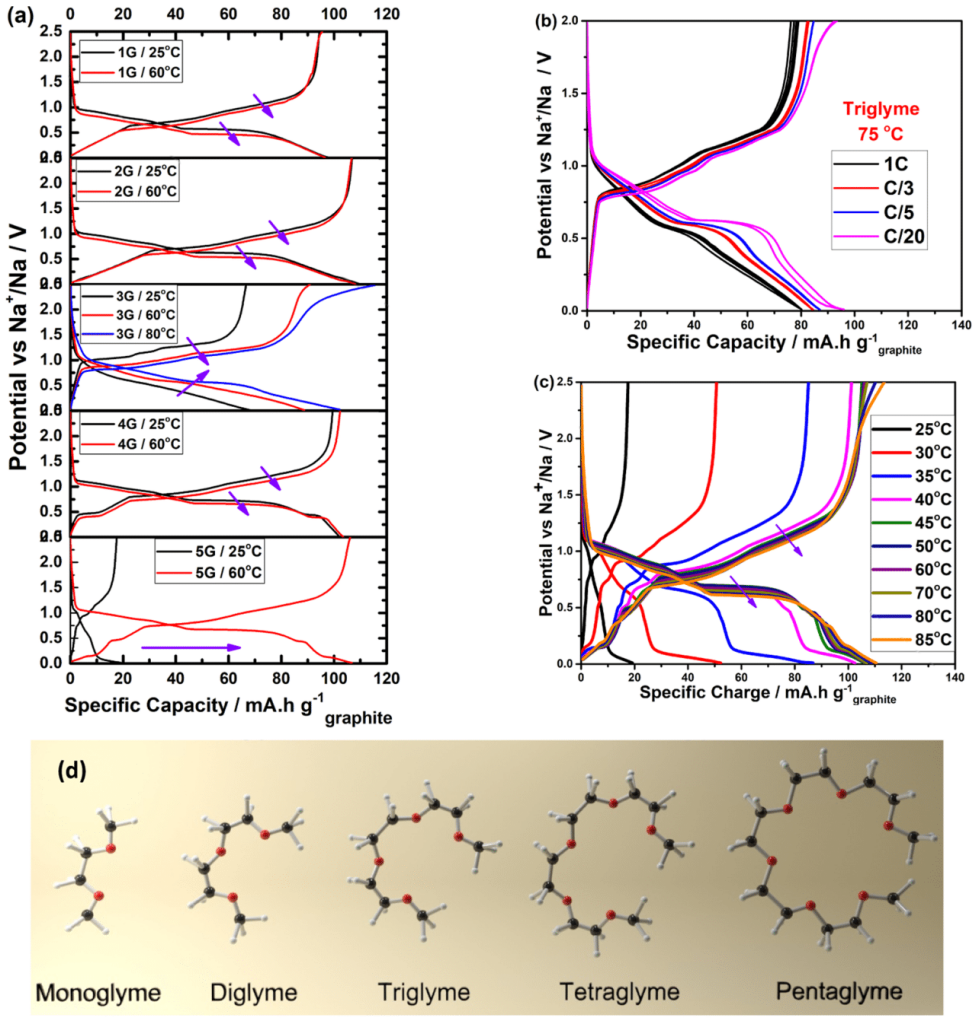

Figure 2. Potential profiles for the co-intercalation reactions with the different glymes (1G–5G) at different temperatures. (a) Glyme series. (b) Cycling at different current densities for 3G at 75 °C. (c) Cycling for 5G from 25 to 85 °C. Current is 1C (110 mA g^{-1}, which is calculated from the capacity of $Na^+(diglyme)_2C_{20}^-$, i.e., 110 mAh $g_{(graphite)}^{-1}$). (d) Ball-and-stick model of the glyme series.

decreases sharply with temperature to 72.2 mPa (50 °C) and 22.4 mPa (80 °C). Although the kinetic properties of an electrode reaction depend on many parameters, a low viscosity is generally favorable.

Figure 1b shows the conductivity evolution of the glymes and crown-ether electrolytes. The 2G-based electrolyte shows a significantly higher conductivity than that of other electrolytes with 4.47 mS cm^{-1} at 20 °C, 5.91 mS cm^{-1} at 60 °C, and 6.23 mS cm^{-1} at 80 °C. Even at −30 °C, the conductivity was as high as 1.59 mS cm^{-1}. Despite the particularly high viscosity, the conductivity of the 5G-based electrolyte at temperature above 20 °C appears to be comparable to that of the other glyme-based electrolytes, 0.926 mS cm^{-1} at 20 °C, 2.44 mS cm^{-1} at 60 °C, and 3.20 mS cm^{-1} at 80 °C. It is also noteworthy that the conductivity of the 3G-based electrolyte at 20 °C is particularly low (0.306 mS cm^{-1}). Nevertheless, its conductivity quickly increases to 2.60 mS cm^{-1} at 60 °C and 3.56 mS cm^{-1} at 80 °C. This might be related to the unfavorable coordination of Na^+ by 3G, as reported earlier.[20] Overall, the 2G electrolyte performs best with respect to viscosity and conductivity.

2.2. Glyme Series (1G → 5G). *2.2.1. Galvanostatic Cycling.* The graphite co-intercalation reaction (eq 1) was tested for different glymes as solvents as a function of temperature. Figure 1a shows the potential profiles for 25 and 60 °C in comparison (the complete data is shown in the Supporting Information; see Figures S1–S6). In the case of 1G, 2G, and 4G, the behavior is quite similar at 25 °C although the capacity in the case of 2G (109.8 mAh g^{-1}) is somehow larger as compared to when 1G (97.6 mAh g^{-1}) and 4G (102

DOI: 10.1021/acs.jpcc.8b07915
J. Phys. Chem. C 2018, 122, 26816–26824

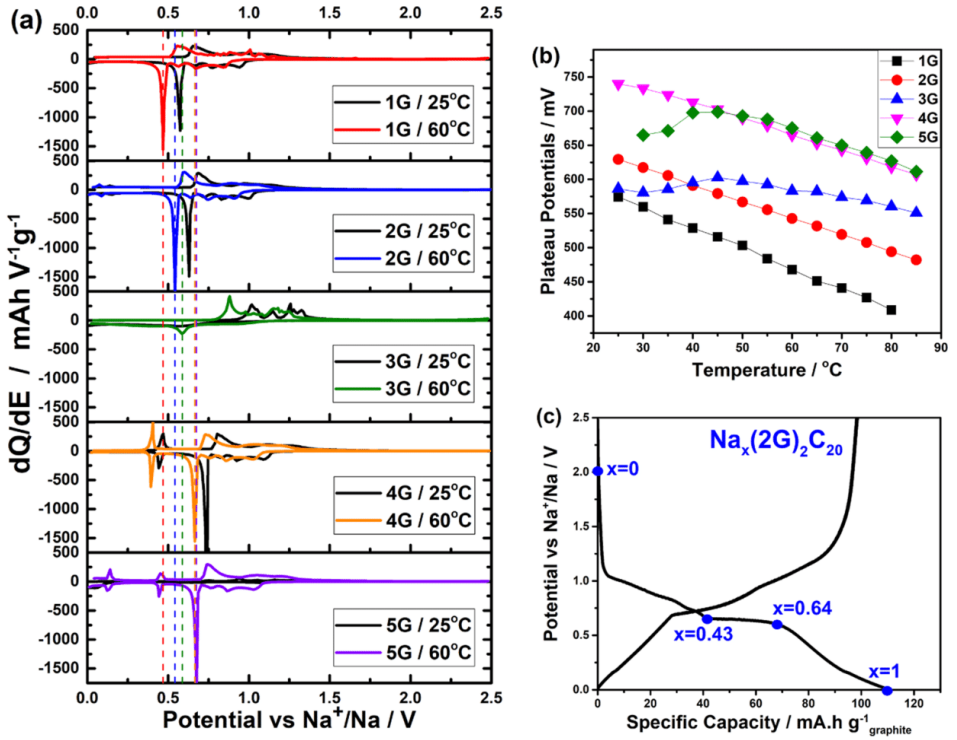

Figure 3. (a) Differential capacity plots for the different glyme electrolytes at 25 and 60 °C. (b) Plateau potential as a function of temperature. (c) Sodium content x in $Na_x(2G)_2C_{20}$.

mAh g^{-1}) are used. Overall, however, the impact of temperature on capacity and redox potential for these solvents is small. In contrast to this, temperature has a notable effect for 3G and 5G.

For 3G at room temperature, the shape of the potential profile is much less defined compared to that for 1G, 2G, and 4G. Starting from about 60 °C, however, the profile becomes more defined with the appearance of a plateau at about 0.58 V versus Na^+/Na. The length of the plateau continuously increases with temperature until 85 °C (Figure S4a), leading to a rise in capacity from about 65 mAh g^{-1} (25 °C) to 105 mAh g^{-1} (80 °C). The appearance of the plateau can be seen more clearly from the peak in the differential plots (dQ/dE vs V) shown in Figures 3a and S4b. Compared to that of the other glymes, the extent of this plateau is smaller. A capacity of 25 mAh g^{-1} is obtained at the plateau at 80 °C, which is about one-fourth of the total capacity. For the other glymes, the plateau region contributes about one-third (about 40 mAh g^{-1}) to the total capacity at all temperatures, i.e., at high temperatures, the capacity for 3G approaches the values of the other glymes. This indicates that the previously observed ill-defined behavior for 3G at room temperature is due to kinetic and not due to thermodynamic effects. The kinetic limitation for 3G is also easily seen from the fact that the voltage gap between discharge and charge curves is becoming smaller with increasing temperature. In contrast to this, for 1G, 2G, and 4G, discharge and charge curves shift toward lower potentials with increasing temperature, i.e., the reaction is thermodynamically controlled. In line with these results, reducing the current density leads to an even more defined potential profile; see Figure 2b. For 5G, the effect of temperature is even stronger. Results at room temperature were disappointing at first as capacities of only around 20 mAh g^{-1} were observed (Figure 2a,c). A slight increase in temperature, however, was enough to achieve significant improvement. Already at 45 °C, full activation was achieved reaching specific capacities of 110 mAh g^{-1} (Figure 2c). A defined discharge plateau at 0.69 V versus Na^+/Na is observed, which slightly decreases with temperature.

Overall, the reactions in the case of 5G and 3G are kinetically limited at room temperature. With increasing temperature, 5G quickly starts to behave like 1G, 2G, and 4G, i.e., the reaction becomes thermodynamically controlled. Rationalizing this behavior is difficult, but a likely reason is the viscosity of 5G, which is very high at low temperature (186 mPa at 20 °C) but rapidly drops with increasing temperature. With six oxygen atoms per molecule, 5G may also provide a favorable coordination for Na^+ (similar compared to two 2G molecules). For 3G, an increasing temperature leads to an increase in capacity but the reaction remains kinetically controlled, possibly related to the less ideal coordination. Finally, it is important to emphasize that the amount of solvent required for this reaction has to be supplied from the electrolyte. Considering eq 2, and assuming 2G, n = 2 and a capacity of 110 mAh/g, the amount of electrolyte needed is 10.7 μl/mAh or 1.18 μl/mg (graphite).

DOI: 10.1021/acs.jpcc.8b07915
J. Phys. Chem. C 2018, 122, 26816−26824

2.2.2. Thermodynamic Properties. The temperature dependence of the redox potentials can be used to calculate the reaction entropy ΔS according to

$$\Delta S = z \cdot F \left(\frac{\partial E}{\partial T} \right)_p \quad (3)$$

As the redox potential depends on the degree of sodiation and different processes are involved (ion storage through staging and pseudocapacitive effects), a comprehensive analysis is difficult and outside the scope of this article. However, one can use the plateau region to estimate the values for this particular part of the reaction (assuming that entropy values are temperature independent). Values for dE/dT can be obtained from the slope of the data shown in Figure 3b. The decrease in voltage with temperature is similar for all glymes and decreases in a largely linear fashion by about 140−175 mV, and within the studied temperature window, values for the temperature coefficient dE/dT are about -2.55 ± 0.3 mV K^{-1}. One can also see that the plateau voltage increases with the molecular weight of the glyme, which might be a result of the stronger electrostatic screening for longer glymes as suggested by Kim et al. for the series 1G, 2G, and 4G.[19] The difference between 4G and 5G, however, is surprisingly small, indicating that similar shielding takes place. This means that the structural differences among t-GICs with 4G and 5G in the plateau region should be quite small. Overall, the difference between 1G and 5G is about 200 mV. As we consider only the plateau region, the reaction equation has to be written accordingly. For example, the reaction in the case of 2G for the plateau region at 60 °C is shown in eq 4. Also, sodium ion increment in t-GICs during sodiation is represented in Figure 3c.

$$0.21\mathrm{Na} + \mathrm{Na}_{0.43}(\mathrm{solv})_n\mathrm{C}_{20} \xrightarrow[+\mathrm{solv}]{\text{intercalation}} \mathrm{Na}_{0.64}(\mathrm{solv})_n\mathrm{C}_{20} \quad (4)$$

For 2G, the temperature dependence of the plateau potential is $dE/dT = -2.45$ mV K^{-1}. The reaction entropy for the plateau region is therefore -49.6 J (mol K)$^{-1}$. Note that equilibrium conditions are required for obtaining true thermodynamic data. In our case, however, it is reasonable to assume that we are close to equilibrium, which is further supported by galvanostatic intermittent titration technique (GITT) data; see Figure S10. The exact position of the redox plateau was determined using the differential capacity plots shown in Figure 3a. In this plot, a peak corresponds to a constant redox potential. Besides the large redox plateau that was used for the discussion above, one can note that there are also several minor peaks. In particular, 2G and 5G show an additional peak below 0.5 V, which indicates an additional storage mechanism. This may be related to similar coordination effects of the sodium ion by the glyme molecules. (Note that two 2G molecules and one 5G molecule provide the identical number of coordinating oxygen atoms.) Notably, 4G and 5G also show an extra plateau at around 0.4−0.45 V. Also, only 2G and 5G represent an extra small plateau below 0.2 V, which is less visible in 2G.

2.2.3. Structural Characterization. The formation of t-GICs can be clearly proven by X-ray diffraction (XRD) measurements and is well in line with the literature; see Seidl et al., for example.[21] Figure 4 shows the result for our samples including 5G. As expected from the electrochemical measurements, first-stage t-GIC formation in the case of 5G takes place only at elevated temperatures. Sample 3G (25 °C), which reacts incompletely at low temperature, shows an additional signal at around 11−12°, indicative of some minor amount of higher-stage GIC. Overall, however, the XRD measurements clearly confirm the formation of stage-1 t-GICs, indicated by the main reflexes at $2\theta = 7.5$, 15.21, 22.91, and 30.6° with the planes of (001), (002), (003), and (004), respectively.

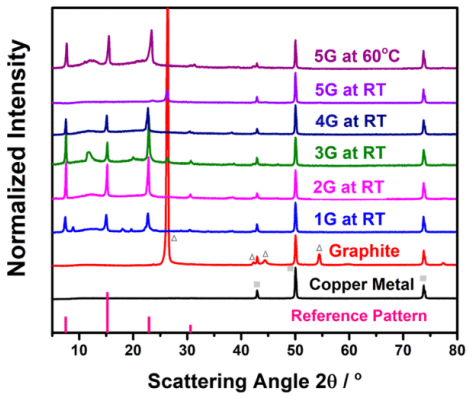

Figure 4. Diffraction patterns (recorded at room temperature) after electrochemical sodiation of powder graphite at 25 °C (RT) or 60 °C (pentaglyme) for different glymes. The squares indicate reflexes from the copper metal under the sample and the triangles indicate reflexes from the powder graphite. The strong reflex at around $2\theta = 26°$ indicates the graphene layer spacing of graphite ($d = 3.35$ Å). The diffraction pattern of the sodiated sample corresponds to a stage-1 t-GIC.

2.2.4. Side Reactions. Higher temperatures might not only benefit the electrode reaction but may also promote side reactions. For all samples, we observed some side reactions at some point starting from about 2.2 V versus Na^+/Na generally when exceeding 70−80 °C; see Figures S1−S6 (all cycles at 1C). As an example, results for 2G at the extreme temperature of 85 °C are shown in Figure 5. The shaded area indicates the region where side reactions may take place (at low currents and also at potentials close to 0 V vs Na^+/Na). It is important

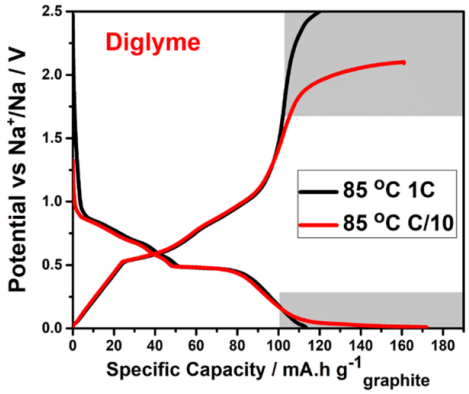

Figure 5. Potential profile for diglyme at 85 °C at 1C (black line) and C/10 (red line). The shaded area indicates side reactions that become visible for all glymes when cycled at high temperatures.

DOI: 10.1021/acs.jpcc.8b07915
J. Phys. Chem. C 2018, 122, 26816−26824

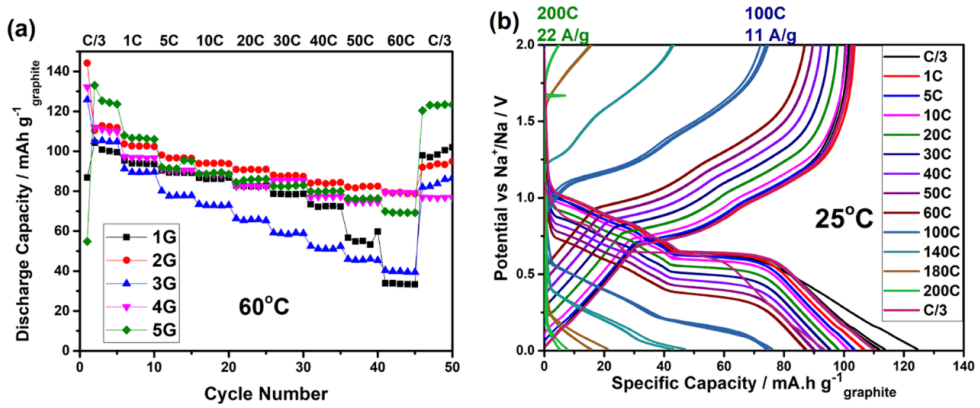

Figure 6. (a) Rate capability tests (1C = 110 mA g^{-1}) for the different glymes at 60 °C. (b) Potential profiles for 2G at 25 °C for the different C rates.

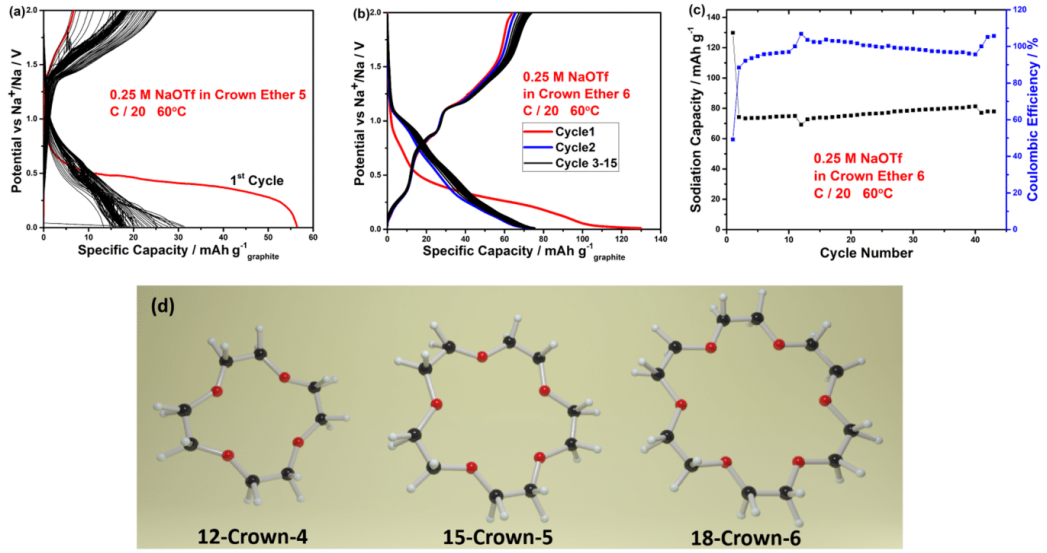

Figure 7. Galvanostatic sodiation (reduction) and desodiation (oxidation) potential profiles of (a) crown ether 5 and (b) crown ether 6 at C/20. (1C corresponds to 110 mA g^{-1}, $Na^{+}(diglyme)_2C_{20}^{-}$ in the literature.[17]) (c) Rate capability of crown ether 6. (d) Ball-and-stick model of the different crown ethers.

to note that irrespective of these parasitic processes, cycle life at elevated temperatures was still excellent for few cycles. This suggests that the electrode remains active but the electrolyte likely decomposes continuously. Cells without graphite as the electrode did not show these parasitic currents, indicating that these side reactions are at least promoted by the graphite electrode. Further studies on high-temperature aging effects are necessary to clarify the exact degradation mechanism. The results nevertheless suggest that the voltage window may need to be further optimized when operating the electrode at elevated temperatures. At room temperature, similar side reactions were never observed even at rates as low as C/50; see Figure S7c.

2.2.5. Rate Capability. The excellent rate capability of co-intercalation reactions at room temperature has been already reported by several groups[24,35] and has been rationalized by Jung et al. using theoretical calculations.[36] A diffusion coefficient of 1.1 × 10^{-8} cm^2 s^{-1} was calculated for the diffusion in Na[diglyme]C_{16} at 300 K, for example. Figure 6a shows the rate capability test for the different glymes at 60 °C between C/3 (36.7 mA g^{-1}) and 60C (6.6 mA g^{-1}). Similar tests were done at room temperature too but with lower performances (Figure S7a). All cells can be exposed to high currents without a significant structural degradation. Notably, 5G, which is inactive at room temperature (Figures S7a and S6c), shows excellent behavior. Among all glyme systems, cells with 3G perform the poorest. Potential profiles for the different

DOI: 10.1021/acs.jpcc.8b07915
J. Phys. Chem. C 2018, 122, 26816−26824

rates at room temperature are shown for 2G as the solvent in Figures 6b and S7b. Even higher currents were applied in this case. At 100 C (11 A g^{-1}), still 70 mAh g^{-1} was obtained. A further increase in current density leads to rapid capacity loss. Applying 200C or 22 A g^{-1} gave only 5 mAh g^{-1}, but full capacity was obtained when returning to lower currents afterward. This shows that the electrode is mechanically highly stable and can sustain extreme currents without deterioration.

2.3. Crown Ethers. Because of their similarity to glymes, crown ethers may be suitable solvents for co-intercalation reactions. As mentioned above, attempts using electrochemical methods were unsuccessful so far. On the other hand, Zhang et al. recently succeeded for the first time in preparing stage-1 t-GICs with sodium using crown ether 5 (15-crown-5) (15c5) and crown ether 6 (18-crown-6) (18c6).[33] These results indicate that co-intercalation reactions with crown ethers in electrochemical cells are so far limited by kinetics. In view of these results, we were interested to know whether this limitation, similarly to 3G and 5G, can be overcome by increasing temperature. We therefore conducted temperature-dependent studies on the use of 15c5 (liquid at RT) and 18c6 (solid at RT, T_m = 42 °C) as solvents. Results at 60 °C are shown in Figure 7a–c. For 15c5, the results were less successful (Figure 7a). Although improvement compared to that at RT (negligible capacity) was found, only ill-defined potential profiles and large polarization effects were observed. The first cycle shows a large irreversible capacity, and capacities of other cycles are only in the range of 15–30 mAh g^{-1}. The results are more promising for 18c6, for which a much more defined behavior is found. After the first cycle, a capacity of about 75 mAh g^{-1} was found over 45 cycles (Figure 7c), which formally corresponds to the stoichiometry of $Na(18c6)_nC_{30}$. The lower capacity compared to that of the glymes might be related to the reduced flexibility of the ring structure, which generally limits the conformational adaptability. For the same reason, the impact of molecule size (the type of crown ether and the type of glyme) on the redox activity is likely much larger for the crown ethers. We also tested 12c4, but our efforts were unsuccessful at any temperature. XRD measurements for the sample containing 18c6 revealed a very complex diffraction pattern, Figure S8, which requires further studies.

3. CONCLUSIONS

This study shows that temperature is an essential parameter for co-intercalation reactions. For this, we studied a wide range of glymes (1G to 4G and for the first time 5G) as well as several crown ethers. While the use of 3G and 5G leads to poor performance at room temperature, the reactions proceed well when temperature is elevated. The most drastic example is pentaglyme (5G). While at 25 °C only 20 mAh g^{-1} combined with large polarization is achieved, full sodiation (~110 mAh g^{-1}) and negligible polarization are found at about 45 °C. A possible reason for this behavior is viscosity, which is high at room temperature (186 mPa at 20 °C) but rapidly drops with increasing temperature. We show that for 1G, 2G, 4G (whole temperature range), and 5G (at elevated temperature), the electrode reaction is thermodynamically controlled, i.e., discharge/charge curves shift in the same direction upon temperature increase. The rate capability of 5G at elevated temperature was excellent and comparable to that of the shorter glymes 1G, 2G, and 4G. For 3G, complete sodiation can be achieved as well at a higher temperature but the reaction remains kinetically controlled. Consequently, the rate performance in the case of 3G was poor compared to that of the other glymes. We also demonstrated for the first time that t-GICs with crown ethers could be directly obtained by electrochemical methods. Crown ether 18c6, which is solid at room temperature, was successfully used as a solvent at 60 °C. A capacity of about 75 mAh g^{-1} was obtained for more than 40 cycles. Although this capacity is lower compared to that of the glymes, it is another example of activating co-intercalation reactions by temperature. We also showed the appearance of parasitic currents at about 2.2 V versus Na^+/Na and in some cases close to 0 V versus Na^+/Na when exceeding 70–80 °C. The side reactions also become more visible at low currents. Overall, our results demonstrate that the chemistry of co-intercalation reactions is likely much richer than previously thought. Solvents that may seem inappropriate at first or for which poor room-temperature performance is found may serve well at (even just slightly) increased temperature.

4. EXPERIMENTAL AND COMPUTATIONAL DETAILS

4.1. Experimental Details. *4.1.1. Electrode Preparation.* Electrodes contained 90% graphite (MTI Corp.) and 10% binder (poly(vinylidene fluoride) "EQ-Lib-PVDF", MTI Corp.). Slurries were mixed in *N*-methyl-2-pyrrolidone (Sigma-Aldrich) and cast onto a dendritic copper foil. The average loading of electrodes after drying (12 h at 120 °C) was 2–3 mg cm^{-2}.

4.1.2. Electrochemical (In Situ) Measurements. Cells for galvanostatic cycling were prepared in an argon-filled glovebox (<0.1 ppm O_2 and H_2O) with electrodes of 12 mm diameters. For galvanostatic cycling, two-electrode coin cells (CR2032 Coin Cells by MTI Corp.) and i-shaped Swagelok cells were used. Sodium metal (BASF SE) was used as the counter and reference electrodes. As a separator, Whatman glass microfiber filters (GF/A) were soaked into 100 μL of the electrolyte containing predried (100 °C overnight) sodium trifluoromethanesulfonate (NaOTf, purity > 98.0%, Sigma-Aldrich) in predried (in 4 Å porous molecular sieves, overnight) ethylene glycol dimethyl ethers. Monoglyme (1G), diglyme (2G), triglyme (3G), and tetraglyme (4G) were purchased from Sigma-Aldrich, and pentaglyme (5G) was supplied by Nippon Nyukazai Co., Ltd. 1 M NaOTf (Sigma-Aldrich) electrolyte was prepared using each glyme. Also, 0.25 M NaOTf electrolytes were prepared using crown ether 6 (18-Crown-6) (Merck KGaA Group), crown ether 4 (12-Crown-4) (Sigma-Aldrich), and crown ether 5 (15-Crown-5) (Alfa Aesar). The coin cells were prepared at 1000 PSI using a crimper (TG-110). Electrochemical measurements were carried out at different temperatures in a controlled oven (by Heraeus) by a Biologic BCS battery cycler. The potential window was between 0.01 and 2.5 V versus Na^+/Na galvanostatically (at constant current, constant voltage (CC–CV)). The C rate was calculated on the basis of specific charge of graphite stated in the literature (Q = 110 mAh g^{-1}, which forms $Na(diglyme)_2C_{20}$).[17] Therefore, 1C represents a specific current of i = 110 mA g^{-1} and experiments were done at C/3 and 1C. Temperature-dependent measurements were conducted by raising the temperature from room temperature to 85 °C in intervals of 5 °C using a lab oven. At each temperature, the cell was cycled three times. For the glyme series, data for the first discharge/charge cycle is omitted for better clarity. The first cycle includes activation of the graphite,

DOI: 10.1021/acs.jpcc.8b07915
J. Phys. Chem. C 2018, 122, 26816–26824

but the Coulombic efficiency is typically close to 90%; see ref 37.

4.1.3. Analytical Methods. Morphological investigations were carried out using X-ray diffraction (XRD) (D2 PHASER by Bruker). Before XRD measurements, instead of a graphite electrode film, powder graphite was preferred. Sodiated/desodiated graphite was placed on Cu metal inside a special XRD sample holder, which was airtight.

■ ASSOCIATED CONTENT

Supporting Information

The Supporting Information is available free of charge on the ACS Publications website at DOI: 10.1021/acs.jpcc.8b07915.

Electrochemical measurements such as rate capability tests and GITT are represented; diffraction pattern of a crown ether; melting and boiling points of the solvents are given in a plot (PDF)

■ AUTHOR INFORMATION

Corresponding Author

*E-mail: philipp.adelhelm@uni-jena.de.

ORCID

Mustafa Goktas: 0000-0002-3374-4095
Andrea Balducci: 0000-0002-2887-8312
Philipp Adelhelm: 0000-0003-2439-8802

Notes

The authors declare no competing financial interest.

■ ACKNOWLEDGMENTS

We thank BASF SE for providing high-purity sodium metal and Nippon Nyukazai Co., Ltd. for providing pentaglyme. P.A. and M.G. thank the DFG for support within the project "Redoxchemie ternärer Graphitinterkalationsverbindungen (630743)" and the State of Thuringia for support within the ProExzellenz program.

■ REFERENCES

(1) Slater, M. D.; Kim, D.; Lee, E.; Johnson, C. S. Sodium-Ion Batteries. *Adv. Funct. Mater.* **2013**, *23*, 947−958.

(2) Li, Y.; Lu, Y.; Zhao, C.; Hu, Y.-S.; Titirici, M.-M.; Li, H.; Huang, X.; Chen, L. Recent Advances of Electrode Materials for Low-Cost Sodium-Ion Batteries Towards Practical Application for Grid Energy Storage. *Energy Storage Mater.* **2017**, *7*, 130−151.

(3) Palomares, V.; Serras, P.; Villaluenga, I.; Hueso, K. B.; Carretero-González, J.; Rojo, T. Na-Ion Batteries, Recent Advances and Present Challenges to Become Low Cost Energy Storage Systems. *Energy Environ. Sci.* **2012**, *5*, 5884−5901.

(4) Yabuuchi, N.; Kubota, K.; Dahbi, M.; Komaba, S. Research Development on Sodium-Ion Batteries. *Chem. Rev.* **2014**, *114*, 11636−11682.

(5) Kim, S.-W.; Seo, D.-H.; Ma, X.; Ceder, G.; Kang, K. Electrode Materials for Rechargeable Sodium-Ion Batteries: Potential Alternatives to Current Lithium-Ion Batteries. *Adv. Energy Mater.* **2012**, *2*, 710−721.

(6) Adelhelm, P.; Hartmann, P.; Bender, C. L.; Busche, M.; Eufinger, C.; Janek, J. From Lithium to Sodium: Cell Chemistry of Room Temperature Sodium-Air and Sodium-Sulfur Batteries. *Beilstein J. Nanotechnol.* **2015**, *6*, 1016−1055.

(7) Nayak, P. K.; Yang, L.; Brehm, W.; Adelhelm, P. From Lithium-Ion to Sodium-Ion Batteries: A Materials Perspective. *Angew. Chem., Int. Ed.* **2017**, 2−21.

(8) Kim, Y.; Ha, K. H.; Oh, S. M.; Lee, K. T. High-Capacity Anode Materials for Sodium-Ion Batteries. *Chemistry* **2014**, *20*, 11980−11992.

(9) Pan, H.; Hu, Y.-S.; Chen, L. Room-Temperature Stationary Sodium-Ion Batteries for Large-Scale Electric Energy Storage. *Energy Environ. Sci.* **2013**, *6*, 2338−2360.

(10) Vaalma, C.; Buchholz, D.; Weil, M.; Passerini, S. A Cost and Resource Analysis of Sodium-Ion Batteries. *Nat. Rev. Mater.* **2018**, *3*, No. 18013.

(11) Dresselhaus, M. S.; Dresselhaus, G. Intercalation Compounds of Graphite. *Adv. Phys.* **1981**, *30*, 139−326.

(12) Schmuelling, G.; Placke, T.; Kloepsch, R.; Fromm, O.; Meyer, H.-W.; Passerini, S.; Winter, M. X-Ray Diffraction Studies of the Electrochemical Intercalation of Bis(Trifluoromethanesulfonyl)Imide Anions into Graphite For dual-Ion Cells. *J. Power Sources* **2013**, *239*, 563−571.

(13) Nobuhara, K.; Nakayama, H.; Nose, M.; Nakanishi, S.; Iba, H. First-Principles Study of Alkali Metal-Graphite Intercalation Compounds. *J. Power Sources* **2013**, *243*, 585−587.

(14) Liu, Y.; Merinov, B. V.; Goddard, W. A., 3rd Origin of Low Sodium Capacity in Graphite and Generally Weak Substrate Binding of Na and Mg among Alkali and Alkaline Earth Metals. *Proc. Natl. Acad. Sci. U.S.A.* **2016**, *113*, 3735−3539.

(15) Moriwake, H.; Kuwabara, A.; Fisher, C. A. J.; Ikuhara, Y. Why Is Sodium-Intercalated Graphite Unstable? *RSC Adv.* **2017**, *7*, 36550−36554.

(16) Xu, Z.-L.; Park, J.; Yoon, G.; Kim, H.; Kang, K. Graphitic Carbon Materials for Advanced Sodium-Ion Batteries. *Small Methods* **2018**, No. 1800227.

(17) Jache, B.; Adelhelm, P. Use of Graphite as a Highly Reversible Electrode with Superior Cycle Life for Sodium-Ion Batteries by Making Use of Co-Intercalation Phenomena. *Angew. Chem., Int. Ed.* **2014**, *53*, 10169−10173.

(18) Kim, H.; Jihyun, H.; Young-Uk, P.; Jinsoo, K.; Insang, H.; Kisuk, K. Sodium Storage Behavior in Natural Graphite Using Ether-Based Electrolyte Systems. *Adv. Funct. Mater.* **2015**, *25*, 534−541.

(19) Kim, H.; Hong, J.; Yoon, G.; Kim, H.; Park, K.-Y.; Park, M.-S.; Yoon, W.-S.; Kang, K. Sodium Intercalation Chemistry in Graphite. *Energy Environ. Sci.* **2015**, *8*, 2963−2969.

(20) Jache, B.; Binder, J. O.; Abe, T.; Adelhelm, P. A Comparative Study on the Impact of Different Glymes and Their Derivatives as Electrolyte Solvents for Graphite Co-Intercalation Electrodes in Lithium-Ion and Sodium-Ion Batteries. *Phys. Chem. Chem. Phys.* **2016**, *18*, 14299−14316.

(21) Seidl, L.; Bucher, N.; Chu, E.; Hartung, S.; Martens, S.; Schneider, O.; Stimming, U. Intercalation of Solvated Na-Ions into Graphite. *Energy Environ. Sci.* **2017**, 1631.

(22) Moon, H.; Tatara, R.; Mandai, T.; Ueno, K.; Yoshida, K.; Tachikawa, N.; Yasuda, T.; Dokko, K.; Watanabe, M. Mechanism of Li Ion Desolvation at the Interface of Graphite Electrode and Glyme−Li Salt Solvate Ionic Liquids. *J. Phys. Chem. C* **2014**, *118*, 20246−20256.

(23) Hasa, I.; Dou, X.; Buchholz, D.; Shao-Horn, Y.; Hassoun, J.; Passerini, S.; Scrosati, B. A Sodium-Ion Battery Exploiting Layered Oxide Cathode, Graphite Anode and Glyme-Based Electrolyte. *J. Power Sources* **2016**, *310*, 26−31.

(24) Kim, H.; Hong, J.; Park, Y.-U.; Kim, J.; Hwang, I.; Kang, K. Sodium Storage Behavior in Natural Graphite Using Ether-Based Electrolyte Systems. *Adv. Funct. Mater.* **2015**, *25*, 534−541.

(25) Maibach, J.; Jeschull, F.; Brandell, D.; Edstrom, K.; Valvo, M. Surface Layer Evolution on Graphite During Electrochemical Sodium-Tetraglyme Co-Intercalation. *ACS Appl. Mater. Interfaces* **2017**, *9*, 12373−12381.

(26) Jozwiak, M.; Kosiorowska, M. A.; Jozwiak, A. Enthalpy of Solvation of Monoglyme, Diglyme, Triglyme, Tetraglyme, and Pentaglyme in Mixtures of Water with N,N-Dimethylformamide at 298.15 K. *J. Chem. Eng. Data* **2010**, *55*, 5941−5945.

(27) Cohn, A. P.; Share, K.; Carter, R.; Oakes, L.; Pint, C. L. Ultrafast Solvent-Assisted Sodium Ion Intercalation into Highly Crystalline Few-Layered Graphene. *Nano Lett.* **2016**, *16*, 543−548.

(28) Cohn, A. P.; Muralidharan, N.; Carter, R.; Share, K.; Oakes, L.; Pint, C. L. Durable Potassium Ion Battery Electrodes from High-Rate

DOI: 10.1021/acs.jpcc.8b07915
J. Phys. Chem. C 2018, 122, 26816−26824

Cointercalation into Graphitic Carbons. *J. Mater. Chem. A* **2016**, *4*, 14954−14959.
(29) Kim, D.-M.; Jung, S. C.; Ha, S.; Kim, Y.; Park, Y.; Ryu, J. H.; Han, Y.-K.; Lee, K. T. Cointercalation of Mg2+ Ions into Graphite for Magnesium-Ion Batteries. *Chem. Mater.* **2018**, *30*, 3199−3203.
(30) Zhang, H.; Lerner, M. M. Preparation of Graphite Intercalation Compounds Containing Oligo and Polyethers. *Nanoscale* **2016**, *8*, 4608−4612.
(31) Terada, S.; Mandai, T.; Nozawa, R.; Yoshida, K.; Ueno, K.; Tsuzuki, S.; Dokko, K.; Watanabe, M. Physicochemical Properties of Pentaglyme-Sodium Bis(Trifluoromethanesulfonyl)Amide Solvate Ionic Liquid. *Phys. Chem. Chem. Phys.* **2014**, *16*, 11737−11746.
(32) Terada, S.; Susa, H.; Tsuzuki, S.; Mandai, T.; Ueno, K.; Umebayashi, Y.; Dokko, K.; Watanabe, M. Dissociation and Diffusion of Glyme-Sodium Bis(Trifluoromethanesulfonyl)Amide Complexes in Hydrofluoroether-Based Electrolytes for Sodium Batteries. *J. Phys. Chem. C* **2016**, *120*, 23339−23350.
(33) Zhang, H.; Lerner, M. M. Preparation of Graphite Intercalation Compounds Containing Crown Ethers. *Inorg. Chem.* **2016**, *55*, 8281−8284.
(34) Gotoh, K.; Kunimitsu, S.; Zhang, H.; Lerner, M. M.; Miyakubo, K.; Ueda, T.; Kim, H.-J.; Han, Y.-K.; Ishida, H. Structure and Dynamic Behavior of the Na−Crown Ether Complex in the Graphite Layers Studied by Dft and 1 h Nmr. *J. Phys. Chem. C* **2018**, 10963.
(35) Chen, J.; et al. Intercalation of Bi Nanoparticles into Graphite Results in an Ultra-Fast and Ultra-Stable Anode Material for Sodium-Ion Batteries. *Energy Environ. Sci.* **2018**, *11*, 1218−1225.
(36) Jung, S. C.; Kang, Y. J.; Han, Y. K. Origin of Excellent Rate and Cycle Performance of Na+-Solvent Cointercalated Graphite Vs. Poor Performance of Li+-Solvent Case. *Nano Energy* **2017**, *34*, 456−462.
(37) Goktas, M.; Bolli, C.; Berg, E. J.; Novák, P.; Pollok, K.; Langenhorst, F.; Roeder, M.; Lenchuk, O.; Mollenhauer, D.; Adelhelm, P. Graphite as Cointercalation Electrode for Sodium-Ion Batteries: Electrode Dynamics and the Missing Solid Electrolyte Interphase (SEI). *Adv. Energy Mater.* **2018**, No. 1702724.

DOI: 10.1021/acs.jpcc.8b07915
J. Phys. Chem. C 2018, 122, 26816−26824

5.3. Salt Effects on Electrolyte Stability (Submitted Manuscript 1)

Ideally, the salt anion is a "spectator" ion which has no influence on the reaction. It turned out, however, that the salt anion had a very large influence on the experimental results. Driven by some conflicting research results a systematic study was on the influence of the conductive salt on the co-intercalation reaction was done. Next to the graphite electrode, this of course also required a study of the electrolyte stability against sodium metal, being the commonly used counter and reference electrode. The study was based on diglyme as solvent and NaOTf, $NaPF_6$, $NaClO_4$, NaFSI and NaTFSI as conductive salt.

A first, the stability of the electrolyte against sodium metal was studied. A number of tests ranging from optical tests and Na|Na symmetrical cells were done. In some cases, side reactions were even noticeable by eye. Impedance spectroscopy was used to determine the "quality" of the SEI in terms of resistance. OEMS measurements were made to study the potential release of gaseous decomposition products. Overall, clear differences were observed for the different salt with NaOTf and $NaPF_6$ showing superior properties compared to the other salts. The poorest performance was found for NaTFSI.

Similar results were found for the co-intercalation reaction with the graphite electrode. While excellent performance was found in the case of NaOTf and $NaPF_6$ very poor properties were found for NaTFSI and NaFSI. XRD and TEM also evidenced that the anion has a large impact on the crystallinity of the graphite electrode. The findings could also clarify two recent conflicting findings, from Goktas *et al*. [100] and Maibach *et al*.[103], on the degree of SEI formation on graphite electrodes in SIBs.

Overall, for electrolyte solution with diglyme as a solvent, NaOTf and $NaPF_6$ are the preferred salts. Qualitatively ordering, the suitability of the salts is as (best) NaOTf≥$NaPF_6$>$NaClO_4$>NaFSI>>NaTFSI (worst)

The results of these findings were submitted to the journal *Applied Materials and Interfaces*

The authors: Mustafa Goktas, Christoph Bolli, Johannes Buchheim, Erik J. Berg, Petr Novák, Francisco Bonilla, Teófilo Rojo, Shinichi Komaba and Philipp Adelhelm.

The paper is written by the first author and edited by Philipp Adelhelm. XRD data discussions, comments, and calculations of Johannes Buchheim are considered. To observe the material in nanoscale, TEM and EDX measurement and analysis are done by Francisco Bonilla and Teófilo Rojo. FTIR data is measured in Japan by the first author within the group of Shinichi Komaba. Discussion with Shinichi Komaba and Kei Kubota is done. OEMS measurements are performed by Christoph Bolli, Erik J. Berg and Petr Novák and discussions during the progress of this work highly done with this group. All the measurements related to visual observations, all electrochemical measurements including *in situ* electrochemical dilatometry and XRD tests and also data analysis and further calculations are performed by the first author. By the comment and help of all authors, the manuscript is submitted to the journal.

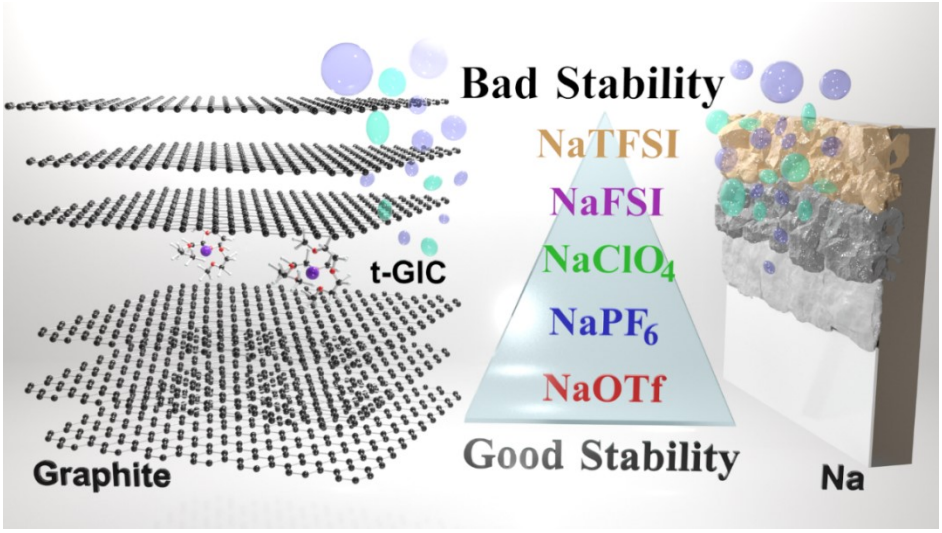

Figure 20. TOC of the submitted manuscript

TOC text: The reversible intercalation of solvated rather than naked ions into graphite is a peculiar electrode reaction that is currently studied for sodium-ion batteries. Solid electrolyte interphase (SEI) formation on the sodium surface related to the type of salt. Stability of 5 different salts. Also, gas evolution from sodium and graphite, detected by OEMS.

Stable and instable diglyme-based electrolytes for batteries with sodium or graphite as electrode

Mustafa GOKTAS[a,b], Christoph BOLLI[c*], Johannes BUCHHEIM[a,b], Erik J. BERG[d], Petr NOVÁK[c], Francisco BONILLA[e], Teófilo ROJO[e], Shinichi KOMABA[f], Kei KUBOTA[f] and Philipp ADELHELM[a,b*]

[a] Friedrich Schiller University Jena, Institute of Technical Chemistry and Environmental Chemistry, Philosophenweg 7a, D-07743 Jena, Germany
[b] Center for Energy and Environmental Chemistry (CEEC Jena), Philosophenweg 7a, D-07743 Jena, Germany
[c] Paul Scherrer Institute, Electrochemistry Laboratory, CH-5232 Villigen PSI, Switzerland
[d] Department of Chemistry, Ångström Laboratory, Uppsala University, Box 538, SE-751 21, Uppsala, Sweden
[e] CIC Energigune Parque Tecnológico C/Albert Einstein, 48, 01510 Vitoria-Gasteiz (Álava) Spain
[f] Department of Applied Chemistry, Tokyo University of Science, 1-3 Kagurazaka, Shinjuku, Tokyo 162-8061, Japan
*correspondence: Philipp.Adelhelm@uni-jena.de, Christoph.Bolli@psi.ch

Abstract

Glyme-based electrolytes are currently reconsidered for sodium-ion batteries because the often provide better compatibility with negative electrodes compared to conventional carbonate-based electrolytes. Here, we study the stability of several diglyme-based electrolytes when used in combination with sodium or graphite as electrodes. The conductive salts tested are NaOTf, $NaPF_6$, $NaClO_4$, NaFSI and NaTFSI and in some cases dramatic differences are observed. Side reactions are studied with a variety of methods including XRD, SEM, TEM, online electrochemical mass spectrometry (OEMS) and *in situ* electrochemical dilatometry. For sodium metal electrodes, we find that NaOTf and $NaPF_6$ are the preferred salts followed by $NaClO_4$ and NaFSI that lead to more side reactions and increasing impedance. By far the poorest performance is obtained for NaTFSI. A similar trend is found in case of graphite as electrode. The least side reactions and best stability are found when using NaOTf as salt, followed by $NaPF_6$. The poorest performance is found for NaTFSI leading to poor Coulombic efficiency and cycle life. Excessive side reactions also lead to an increase in electrode thickness during cycling. Overall, our results clearly show that NaOTf and $NaPF_6$ are the preferred salts for electrolyte solutions with diglyme as solvent when used in combination with graphite or sodium in Na-ion cells. They show the least side reactions compared to the other salts. In a qualitative order, the suitability is as follows $NaOTf \geq NaPF_6 > NaClO_4 > NaFSI >> NaTFSI$. Our results also explain two recent, seemingly conflicting findings on the degree of solid electrolyte interphase (SEI) formation on graphite electrodes in sodium-ion batteries (DOI: 10.1021/acsami.6b16536 and 10.1002/aenm.201702724). The different findings are due to the different conductive salts used in both studies.

1. Introduction

Sodium-ion batteries (SIBs) are currently reconsidered as energy storage devices. Aim of this technology is to provide another alternative to the rapidly growing market or rechargeable batteries [1]. Different from lithium-ion batteries (LIBs) that enable highest energy densities, sodium-ion batteries aim at lowering costs while still providing a high energy density. To really have an impact, developing SIB technology does not only include "simply" replacing lithium by sodium, but more importantly using also other abundant elements. Despite their conceptual similarity, peculiar differences can be found when comparing LIBs and SIBs (or Li/air vs. Na/air or Li/S vs. Na/S) batteries [2]. A very noticeable exception is graphite, which is the commonly used negative electrode in LIBs but is largely inactive in SIBs (when using the conventional carbonate based electrolytes). This limitation can be overcome by using solvent co-intercalation phenomena, i.e. solvated sodium-ions are intercalated. This way, graphite shows a surprisingly reversible charge storage for sodium-ions as initially shown by Jache and Adelhelm[3] and Kim *et al.* [4] using diglyme as solvent. An interesting feature of this reaction is that the redox potential of the reaction can be tuned by a few hundred mV by using different types of glymes (mono- to tetraglyme).[5] Very recently, also pentaglyme and a crown ether could be utilized by slightly increasing temperature.[6] In the same study, it was also found that for mono-, di- and tetraglyme, the reaction at room temperature thermodynamically proceeds with a temperature coefficient of about − 2.55 ± 0.3 mV K^{-1}. The high rate capability and the long cycle life (high Coulombic efficiency) are two other important characteristics of this reaction [3-5, 6-7]. For example, Cohn *et al.*[7a] reported 8,000 cycles and high rate performance up to 30 A g^{-1} and Zhu *et al*. reached up to 10 A g^{-1} for 6,000 cycles [7b]. In an own study, we achieved close to 80 mAh g^{-1} at 11 A g^{-1} corresponding to a C-rate of 100 (2−3 mg cm^{-2}) [6]. An overview on the recent literature is summarized in **Table S1**. The high rate capability has been rationalized by NMR measurements and theory. A diffusion coefficient of D_{Na+} = 1.1·10^{-8} cm^2 s^{-1} was determined by Jung *et al*. which is slightly higher than the diffusion coefficient of Li^+ in LiC_6. [8] [9]

The main conceptual question, however, considers the solid electrolyte interphase (SEI) on the graphite surface. As intercalation of the solvated ion takes place below 1.0 V vs. Na^+/Na, the common understanding is that, depending on the used solvent and salt, SEI formation needs to

take place due to the instability of liquid electrolytes at low potentials. On the other hand, an SEI would prevent the co-intercalation of solvent molecules therefore preventing any intercalation. Moreover, the large expansion/shrinkage of the electrode during cycling should lead to a continuous rupture of the SEI combined continuous electrolyte decomposition. Studies on SEI-formation are notoriously difficult, nevertheless, in a recent study we provide reasonable evidence for that the graphite/electrolyte interface is "SEI-free" and that the electrolyte is kinetically stable in contact with the graphite electrode.[10] On the other hand, Maibach *et al.* reported that SEI formation takes place.[11] It is of note, however, that different electrolytes were used in both studies. While we used sodium trifluoromethanesulfonate (triflate) in diglyme in our study, Maibach *et al.* used NaFSI dissolved in tetraglyme. As excellent cycle life has been reported for both solvents (see **Table S1**), it can be well assumed that the type of conductive salt is responsible for the different observations made. So far, a number of salts (NaOTf, NaFSI, $NaPF_6$, $NaClO_4$, NaI) has been applied for the solvent co-intercalation reaction with graphite. For example, Jache and Adelhelm[3] compared NaI and NaOTf, Kim *et al.* [4] compared $NaPF_6$, $NaClO_4$ and NaOTf, and Cabello *et al.*[12] compared $NaPF_6$ and NaOTf. Considerable differences in the electrochemical performance were not found for the tested salts, however, note that none of the studies specifically focused on the stability of the salts.

Westman *et al.* [13] provided a detailed study on the stability of $NaPF_6$/diglyme as electrolyte against hard carbon, $Na_3V_2(PO_4)_3$ and $Na_3V_2(PO_4)_2F_3$. Experimental results indicated a generally sufficient stability of the electrolyte between 0.0 V and 4.4 V vs. Na^+/Na but poor SEI formation was found in case of the hard carbon. Related to sodium metal as electrode, the same authors suggested on the basis of DFT calculations that the electrolyte is thermodynamically stable in contact with sodium metal. On the other hand, Tobishima *et al.* [14] found that reductive decomposition of diglyme (with Pt as working electrode) occurs below about 0.4 V vs. Li^+/Li. Related to Na-O_2 batteries, Lutz *et al.* [15] studied the stability of monoglyme-based electrolytes against sodium metal and found a strong influence of the conductive salt on the SEI formation. The smallest impedance was obtained for $NaPF_6$ followed by NaOTf. The worst result was found for NaTFSI. This is in line with earlier findings by Seh *et al.* [16] that identified $NaPF_6$ in diglyme as preferred electrolyte for sodium metal electrodes. Related to ionic liquids, Hosokawa *et al.* [17] found that FSI anions are preferred over TFSI anions in contact with sodium metal.

Taking these findings and the unclear role of the SEI together, there is still very limited understanding on the role of the salt anion on the stability diglyme-based electrolytes, especially with respect to intercalation electrodes. No systematic study exists so far for graphite as electrode in SIBs. A method that is particularly useful for studying the stability of electrolyte solutions is online electrochemical mass spectrometry (OEMS). For the first time, we systematically apply this method to determine which salt anion is the best and which causes detrimental side reactions with graphite and sodium.

In this study, we report on the influence of the salt anion on the stability and reversibility of solvent co-intercalation reactions with graphite in half-cells with sodium as counter electrode. Diglyme is chosen as solvent because it so far provides the best results (lowest overpotentials) among all glymes used. For the salts, we compare NaOTf, $NaPF_6$, $NaClO_4$, NaFSI and NaTFSI. The concentration of the electrolyte solution is 1M in all cases. From galvanostatic cycling, one can easily see side reactions occur for NaTFSI and NaFSI whereas much better stability is observed for the other salts. We clarify these observations by using different analytical tools and reference experiments. We first study the general stability of sodium metal in the electrolyte solutions by using Na|Na symmetrical cells to conduct plating/stripping experiments combined with electrochemical impedance spectroscopy (EIS), online electrochemical mass spectrometry (OEMS) and XRD. After this, we study side reactions between the graphite electrode and the different electrolytes in graphite-sodium half-cells. For this, we use TEM, SEM, OEMS and *in situ* electrochemical dilatometry.

2. Results and Discussion

Figure 1 and **2** shows results from galvanostatic cycling of graphite in half cells with sodium metal as counter electrode. In line with previous findings on the use of NaOTf/diglyme as electrolyte, the initial sodiation capacity and the initial Coulombic efficiency (ICE) are 114.75 mAh/g and 92.4 %. The losses in the initial cycle can be expected due to activation of the graphite electrode[10] and (if occurring) SEI formation. It is of note that an ICE value of 92.4 % is much higher compared to many hard carbons reported. The voltage profile shows a staged behavior well in line with many previous reports [3-5, 9, 18]. Cycle life and Coulombic efficiency are also excellent for this electrolyte. Considering $NaPF_6$, the ICE value is slightly lower reaching 85 %. The reversible capacity is

slightly lowered also, however, the overall stability is almost equally good as compared to when NaOTf is used. In case of $NaClO_4$, the ICE value is only 77 %, indicating more side reactions. Compared to NaOTf and $NaPF_6$, the cycle life is slightly poorer leading to a gradual decrease in capacity. The use of NaFSI and NaTFSI leads to very low ICE values and the coulombic efficiency and cycle life remain poor during cycling. As the sodiation capacity is much larger compared to the other salts, it is likely that reductive side reactions occur. These are highly detrimental to cycle life. The most drastic capacity loss is observed for NaTFSI for which the graphite becomes largely inactive after 30 – 50 cycles. Voltage profiles for over 50 cycles are shown in **Figure S1** and **Figure 2**.

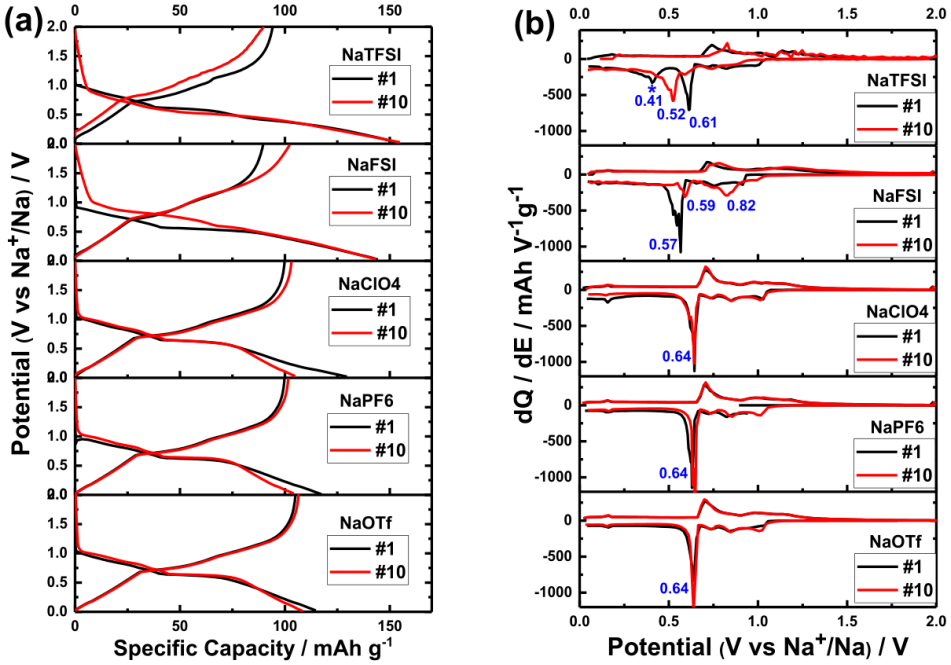

Figure 1. (a) Voltage profiles (1st and 10th cycle) of graphite-sodium cells with diglyme-based electrolytes for different electrolyte salts, (b) Differential capacity plots. The measurements are performed at C/10 =11 mA g^{-1} (1C corresponds to 110 mA g^{-1},$Na^+(diglyme)_2C_{20}^-$) within voltage window of 0.01V and 2.5V

For NaTFSI, the voltage profile for desodiation is very unsteady indicative for a very unstable electrode reaction. The derivative plots emphasize the clear difference for the different salts. Maxima in this plot indicate voltage plateaus, i.e. redox activity at a defined redox potential. While plots for the 1st and 10th cycle largely match in case of NaOTf, $NaPF_6$ and $NaClO_4$, the behavior is different for NaFSI and NaTFSI. For NaFSI, the first maximum during sodiation is less defined

and shifted to slightly lower values, peaking at 0.57 V vs. Na^+/Na. The peak maximum for desodiation is also much broader. During cycling, a new reductive peak at 0.82 V vs. Na^+/Na appears. The clear deviations compared to the much more defined behavior for NaOTf, $NaPF_6$ and $NaClO_4$ can be taken as signs for side reactions. Peak shifting and broadening is also observed for NaTFSI. Here, one can also notice an increase in overpotentials over cycling. One can also notice an additional maximum at around 0.41 V (marked with an asterisk) that is not visible for the other salts. This also indicates a reductive instability of the electrolyte.

In the following sections, we take a closer look at where side reactions occur for the different electrolytes. For this, we need to separately consider the compatibility of the electrolyte against the graphite electrode and against the sodium metal counter electrode.

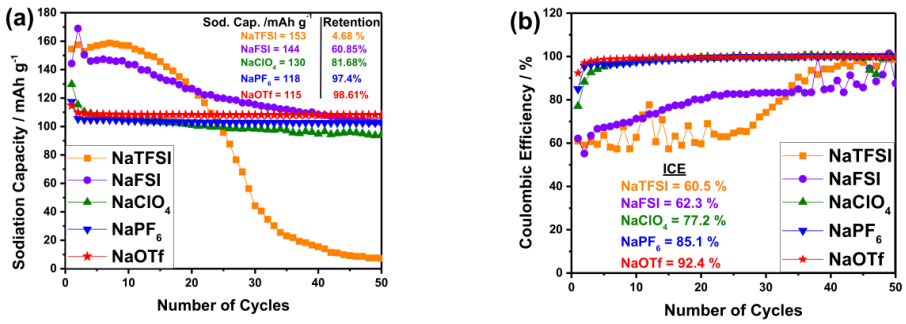

Figure 2. (a) Cycle life of graphite-sodium cells with diglyme-based electrolytes for different electrolyte salts, (b) coulombic efficiency. The measurements are performed at C/10 =11 mA g^{-1} (1C corresponds to 110 mA g^{-1},$Na^+(diglyme)_2C_{20}^-$) within voltage window of 0.01V and 2.5V

2.1.Side reactions with sodium metal

Sodium metal was exposed to the different electrolyte solutions (and to pure diglyme as reference) for several days. The metallic nature of sodium was preserved in most cases with NaTFSI being the exception. Rapid degradation of the sodium metal along with a color change took place. Images can be found in the supporting information **(Figures S2** and **S3).** A slight color change was also observed in case of $NaClO_4$. Similar observations have been reported in literature [15, 17] though the obvious chemical instability is still surprising considering the frequent use of LiTFSI as salt in lithium-ion cells. We therefore also tested the stability of 1M LiTFSI/diglyme electrolyte in contact with sodium metal and lithium metal. The comparison is shown in **Figure S4**. While a

good stability was found for Li/LiTFSI, corrosion still took place case of Na/LiTFSI. This shows that the instability seems intrinsic to the combination of sodium metal with $TFSI^-$ and does not depend on e.g. impurities (note that only lithium salts are commercially available in "battery grade"). While these results easily point on issues related to NaTFSI as salt, it does not mean that the other salts are stable during plating/stripping in an electrochemical cell. We therefore assembled symmetrical Na|Na cells and conducted galvanostatic plating/stripping experiments. Results are shown in **Figure 3a-c**. The applied current densities were ± 0.9 µA cm^{-2} and ± 9 µA cm^{-2}. Each current pulse was applied for 120 min (@ ± 9 µA cm^{-2} corresponding to plating/stripping of a 0.16 µm thick layer of sodium). Clear differences between the different salts can be seen. The largest overpotentials are found for NaFSI with about 1.5 mV at ± 0.9 µA cm^{-2} and about 13 mV at ± 9 µA cm^{-2}. This value remains constant upon cycling indicating a stable but compared to the other salts more resistive SEI. The smallest polarization is found for NaOTf followed by $NaPF_6$. Consecutive cycling does not lead to any increase in resistance indicating a rather stable and low-resistive SEI. For NaTFSI and $NaClO_4$, the situation is different. Starting with relatively low polarization, the plating/stripping overpotential increases during cycling which is a clear sign for poor passivation and continuous electrolyte decomposition.

A more quantitative analysis was done by using electrochemical impedance spectroscopy in the frequency range from 1 MHz to 10 mHz. The data can be interpreted by making use of a simple equilibrium circuit model which is commonly accepted for analogue Li batteries [19] (**Model 1**). Usually, this model consists out of two parallel R/CPE units corresponding to interfacial processes, precisely charge transfer through the electrochemical double layer (R_{CT}/CPE_{dl}) and surface layer impedance (R_{SEI}/CPE_{SEI}). A single resistance in series (R_{El}) largely represents the bulk electrolyte, whereas possible diffusion limitations at low frequencies are described by a Warburg-element (W).

$$R_{el} + {R_{SEI}}/{CPE_{SEI}} + {R_{ct}}/{CPE_{dl}} + W \qquad \textbf{Model 1}$$

Figure 3c displays the impedance spectra for symmetric cells obtained for the different salts. Data was recorded 48 h after cell assembly. At this point the measured impedance was fairly stable. According to Zhao *et al.* [20] we attribute the higher frequency response to surface layer impedance and lower frequency response to charge transfer kinetics. Note that given values in text refer to areal resistance.

Results reveal a major impact of the salt anion on the electrode/electrolyte interface (**Figure 3c, S5**). Electrolytes with NaOTf, $NaPF_6$ and NaFSI show good ionic conductivity, however, choosing NaFSI leads to a rapid buildup of a highly resistive interface (R_{SEI} = 1094 Ω·cm^2, R_{ct} = 1567 Ω·cm^2). Much smaller values were recorded for NaOTf and $NaPF_6$, 0.95 and 5.87 Ω·cm^2 for R_{SEI}, and 0.29 and 6.45 Ω·cm^2 for R_{ct}, respectively. Therefore, these electrolytes seem to form a thin, less resistive passivation layer which sodium ions can easily pass. Results for $NaPF_6$ electrolytes are in accordance with the study of Westman *et al.* [13], i.e. the spectra depicts a similar semicircle with small resistances. For NaTFSI, the interface properties were also quite poor ($R_{SEI} \approx R_{ct} \approx$ 690 Ω·cm^2), but more importantly, a continuous increase of electrolyte resistance up to 287 Ω·cm^2 emerged indicating that strong side reactions are affecting the bulk phase liquid electrolyte. This indicates a very unstable situation due to continuous corrosion. An intermediate behavior was found in case of $NaClO_4$, i.e. the situation was better compared to NaTFSI and NaFSI but still much worse than in case of NaOTf and $NaPF_6$. It is of note, however, that the poor behavior for NaTFSI can be partly mitigated by adding $NaPF_6$ as co-salt, see **Figure S7a**. For a 1:1 mixture, the sum over all interfacial resistances ($R_{SEI} + R_{ct}$) after 24 hours was only 28 Ω·cm^2. This is only slightly higher compared to using $NaPF_6$ alone (12 Ω·cm^2) but much smaller compared to NaTFSI (1378 Ω·cm^2). While mixing conductive salts may be an effective strategy for improving the poor situation for NaTFSI, a more detailed analysis on this has to be part of future studies.

An immediate question is how these findings compare to electrolyte solutions based on the much more common carbonate solvents. **Figure S7 b and c** show time resolved impedance data for electrolytes based on EC/DMC and PC (using $NaPF_6$ as salt). Results were in the range of several thousand Ohms being more than two orders of magnitude higher compared to $NaPF_6$ or NaOTf in diglyme. The high values for carbonate based electrolytes are well in line with a former study by Iermakova *et al.* who investigated the influence of different carbonate combinations on Li/electrolyte- and Na/electrolyte interfaces [19]. Overall, this clearly shows the favorable properties of diglyme as electrolyte solvent in contact with sodium metal (unless using NaFSI or NaTFSI as salts).

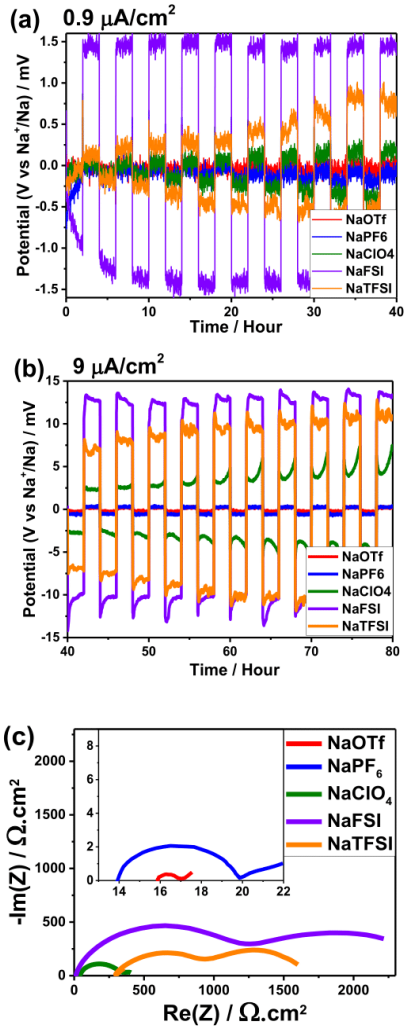

Figure 3. Sodium plating measurements in sodium – sodium dual electrode cells in different electrolytes by applying (a) 0.9 μA cm^{-2} and (b) 9 μA cm^{-2} current. (c) Time dependent impedance measurements for Na|Na symmetric cell at OCV.

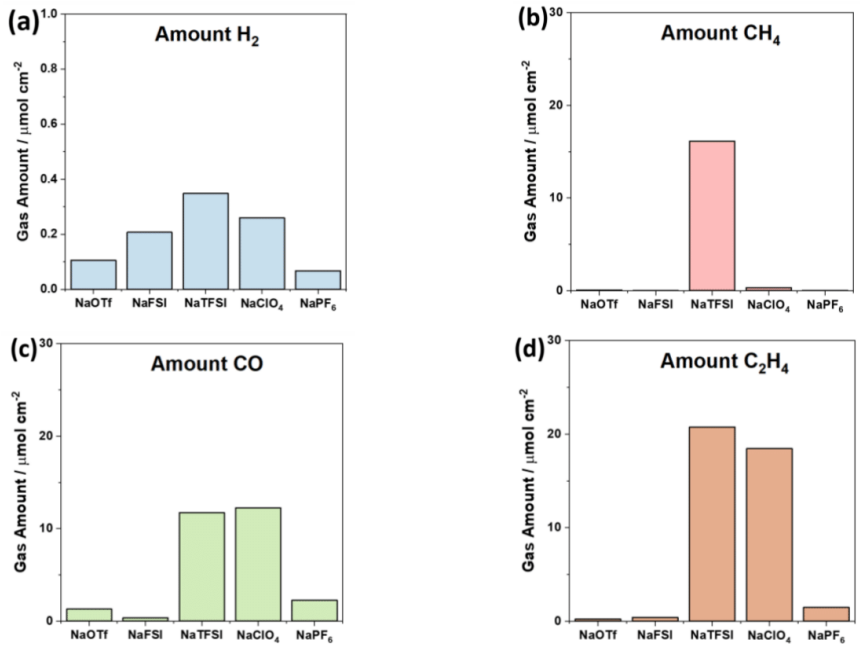

Figure 4. Total gas amount for (a) H_2, (b) CH_4, (c) CO, (d) C_2H_4 for different electrolytes during cycling in Na|Na cells. The gas amount was calculated from the first 3 plating/stripping cycles and is normalized with respect to the surface area of the copper mesh on which Na was plated.

Side reactions between the different electrolyte solutions and sodium metal were also followed using online electrochemical mass spectrometry (OEMS). Again, symmetrical Na|Na cells were used for this purpose and plating/stripping was done for 3 consecutive cycles at a current density of 110 µA cm^{-2} with intervals of 9.5 h. The ion currents for fragments m/z = 2 (H_2), 16 (CH_4), 28 (CO), 30 (C_2H_6), were recorded without calibration and converted into approximate gas evolution rates that allow direct semi-quantitative comparison between the evolution of these fragments from one data set to another. The ion currents for fragments m/z = 27 (C_2H_4) was calibrated and the data allow quantitative comparison. Details are provided in the supporting information. **Figures 4a-d** shows the total amount of released gas during plating/stripping over 3 cycles for H_2, CH_4, CO and C_2H_4. In all cases H_2 is released, but the differences between the samples are rather small. In case of NaFSI, NaOTf and $NaPF_6$ the main evolution occurs directly after OCP (**Figure S11**) and beginning of polarization and is likely due reduction of residual water impurities. For NaTFSI and $NaClO_4$, the H_2 formation occurs during stripping/plating and is therefore related to electrolyte

side reactions. For methane, the by far largest release is detected for NaTFSI which amounts to about 16.1 µmol cm^{-2}. The release of CO and C_2H_4 is largest for NaTFSI and $NaClO_4$. Taking these results, a qualitative sequence for the degree of side reactions would be NaTFSI > $NaClO_4$ >> (NaFSI, NaOTf, $NaPF_6$). The larger the gas release the poorer the stability of the electrolyte solution under stripping/plating conditions. These results are well in line with the plating/stripping experiments shown in **Figure 3a-c** that show a gradual increase in resistance over time. In case of NaTFSI, the side reactions come along with the formation of larger amounts of methane. For NaFSI, the gas release is moderate considering the large overpotentials required for plating and stripping. This indicates a thin, but highly resistive SEI.

Although OEMS is a very powerful tool for evidencing side reactions during cell cycling and it reveals dramatic differences between the different salts, it is important to remember that it does not detect solid and soluble decomposition products. These are, however, much more difficult to determine as their detection requires disassembling of the cell (*post mortem* analysis) which easily could cause secondary side reactions. Moreover, the SEI is very thin and the total amount of electrolyte is very small so that the total amounts of decomposition products are very small which complicates the analysis. We nevertheless applied FTIR spectroscopy and recorded several spectra of a NaTFSI electrolyte that was exposed to sodium metal up to 21 days. Results are shown in **Figure 5**.

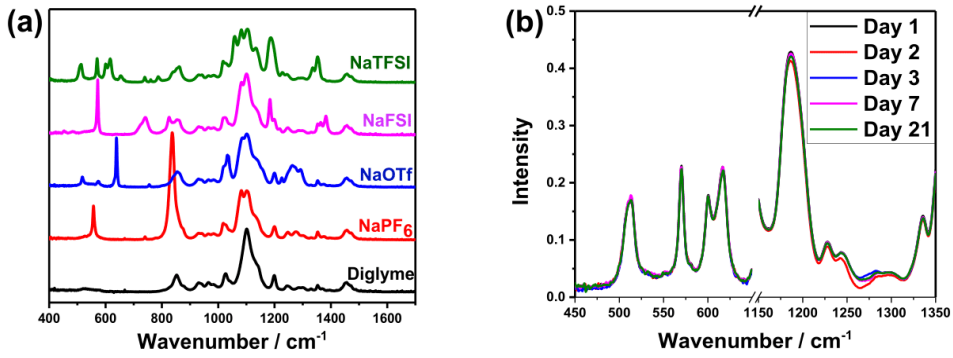

Figure 5. a) FTIR measurements for diglyme and for the different electrolyte solutions, b) Spectra of the electrolyte 1M NaTFSI in 2G after different times of exposure to Na metal.

The results show that the spectra are dominated by diglyme which shows intense bands in the range between 800 – 1500 cm^{-1}. Clear differences between the samples are found at lower wave numbers, where, depending on the salt, some characteristic bands appear. In case of NaTFSI, these are especially notable in the range of 450 – 650 cm^{-1}. Although electrolyte degradation was clearly visible by eye (see images **Figure S3**), the time dependent measurements did not provide any indication for decomposition of the solvent or the salt. Overall, the results show that, for the above-mentioned reasons, the use of FTIR spectroscopy in our study is less straight-forward for studying the stability of the electrolyte in contact with sodium metal.

In order to detect possible crystalline decomposition products, XRD measurements of the sodium electrodes were done after exposing them for 3 weeks to the different electrolyte solutions (**Figure 6**). The sodium metal pieces were placed on a Cu foil as internal reference. No crystalline side products could be detected in case of NaOTf, NaFSI and $NaPF_6$. In case of $NaClO_4$, weak signals of Na_2O and NaCl were found. In case of NaTFSI, a clear signal due to NaF could be observed. Again, this is a strong hint that the use of NaTFSI leads to strong side reactions. From OEMS and XRD data, the major decomposition products are CH_4 and NaF, showing that both the solvent as well as the salt are decomposing.

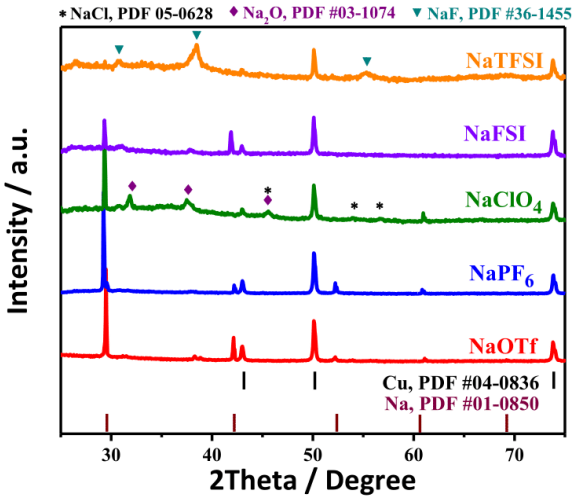

Figure 6. Diffraction patterns of sodium metal after storage in different electrolyte solutions for 3 weeks. Copper was added as reference compound to correct for possible data shift. Stars, squares and downward triangles represent NaCl, Na_2O and NaF respectively.

2.2. Side reactions with graphite

As initial characterization, we recorded XRD patterns of the graphite electrodes after the 5th cycle, i.e. the electrode in its desodiated state. The XRD pattern provides an easy access to the crystallite dimensions of the graphite that are often expressed using L_c, describing the stack height of the graphenes (direction perpendicular to the basal plane of graphite, *00l* diffraction lines) and the layer size L_a, describing the size of the graphene layers (*hk0* diffraction lines). Results are shown in **Figure 7**. Next the (002) reflex of graphite at around 2θ = 26 °, the diffraction pattern also shows signals from the copper current collector. The graphite *hk0* diffraction lines are hardly visible due to preferential orientation of the graphite particles. In our earlier study (using NaOTf in diglyme as electrolyte solution)[10], we showed that the (002) reflex at around 26 ° decreases significantly due to an activation process that largely occurs in the 1st cycle only. This activation includes exfoliation of larger graphite crystallites to smaller ones in the nm range. It is important to note that delamination, i.e. separation or the graphenes along with complete loss in crystallinity, is not observed. The exfoliated graphite still remains crystalline which is one of the important reasons for the excellent cycle life observed for this type of reaction.

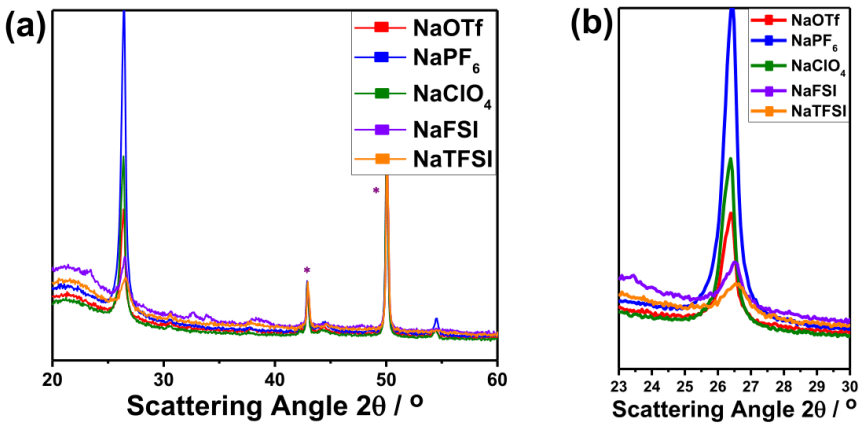

Figure 7. XRD Diffraction patterns of powder graphite after 5th desodiation for five different salt varieties at room temperature. Stars indicate reflexes from the copper metal under the sample at 43.1° and 50.1°. The strong reflex of graphite is at around 2θ = 26 ° indicates the graphene layer spacing of graphite (d= 3.35 Å). The diffraction pattern of the sodiated sample corresponds to a Stage 1 t-GIC.

It is therefore expected that the reflex at 26° is weaker compared to bulk graphite, see **Figure 7b**. The loss in intensity, however, depends on the salt. The intensity of the (002) reflex after cycling is strongest for $NaPF_6$, followed by $NaClO_4$ and NaOTf indicating different degrees in exfoliation with $NaPF_6$ maintaining the largest stack height L_c. An even stronger decrease in intensity if found for NaFSI and NaTFSI, but here, also the reflex position shifts to slightly larger values. Next to exfoliation, this also indicates a loss in crystalline order (or even delamination) which might be the result of continuous side reactions of NaFSI or NaTFSI containing electrolyte solutions with the graphite. The full width at half maximum (FWHM) and an estimate for the L_c values (using the Scherrer equation) is given in the supporting information, **Table S3**. After activation, the crystallite size is about 36 nm in case of NaOTf whereas it is about 24 nm for NaTFSI, i.e. exfoliation is more severe in case of NaTFSI. A long term study was done for the NaOTf electrolyte, see **Figure S8**. The capacity retention of 95.6 % over 2,000 cycles combined with a very stable voltage profile clearly underline the excellent structural stability, i.e. the material maintains its 3D graphite lattice. Loss of 3D crystallinity, e.g. induced by high energy ball milling, would prevent the solvent co-intercalation reaction, leading to a different voltage profile resembling that of soft carbon, see ref. [21]. However, the average crystallite dimensions seem to slowly further decrease gradually, i.e. exfoliation continues at a very small rate, see **Figure S8c**.

Applying the Scherrer equation, a crystal size of about 30–50 nm can be estimated.

For further analysis by SEM and TEM/ED, we largely restrict our comparison to the salts with the best (NaOTf) and worst (NaTFSI) performance. SEM cross sections of the electrodes after 5 cycles are shown in **Figure 8**. Before cycling, the electrode thickness was about 45 µm in both cases. After cycling, the electrode thickness increased to 65 µm (NaOTf) and 145 µm (NaTFSI). An increase in thickness compared to the starting value was expected based on our previous findings [10]. The increase for NaTFSI is, however, much more extreme which is another strong hint on structural degradation (or delamination) of the graphite when using this salt. A more detailed discussion on the thickness change is given below along with *in situ* electrochemical dilatometry.

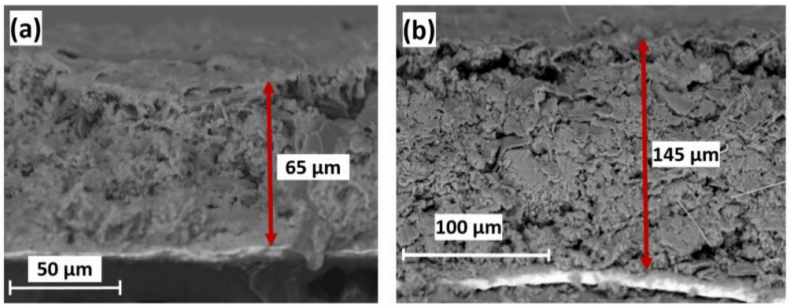

Figure 8. SEM images of graphite electrodes (with 10% PVDF) after cycling in electrolyte solutions of a) 1M NaOTf in diglyme and b) 1M NaTFSI in diglyme (end of 5th cycle, desodiated state). The copper current collector on the bottom has a thickness of 15 µm.

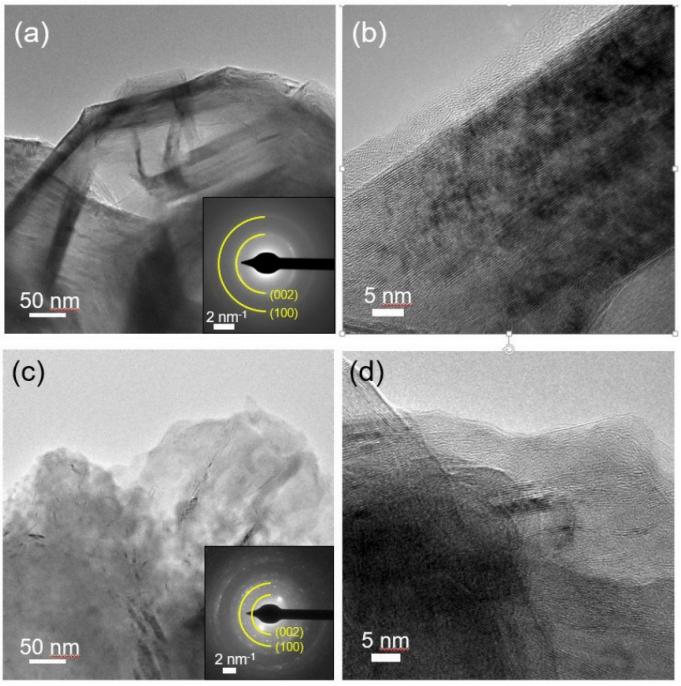

Figure 9. TEM and HRTEM images of the graphite particles after cycling in electrolyte solutions of a-b) 1M NaOTf in diglyme and c-d) 1M NaTFSI in diglyme (end of 5th cycle, desodiated state). Insets: SAEDs patterns for areas in a) and b), the semi-circles indicate the expected positions for graphite interplanar distances.

For TEM/SAED measurements, graphite powders instead of graphite electrodes were used to ease the sampling and to avoid artefacts from the binder. Results for NaOTf and NaTFSI are compared in **Figure 9**. Overall, it was much easier to detect ordered graphite domains for the sample cycled with NaOTf. Rings in the SAEDs of NaOTf could be indexed with the graphite crystal structure.

In contrast, the use of NaTFSI leads to more disorder in the structure along with several other crystalline decomposition products. Note that the quality of the SAED pattern was not sufficient to resolve the nature of the decomposition products.

It is of note that also for NaTFSI, a "classical SEI" could not be directly detected indicating that the side reactions do not lead to a thin surface film. EDX analysis showed that the samples cycled with NaTFSI contained larger amounts elements stemming from the salt. Signals for Na, S, F and O were much larger compared to the when NaOTf was used, see **Figure S10**. This indicates irreversible trapping of these elements within the disordered carbon structure as a result of side reactions.

We further applied *in situ* electrochemical dilatometry to compare the dynamic behavior of the graphite electrodes during cycling in either NaOTf or NaTFSI containing electrolyte solutions, see **Figure 10a, b**. Results for NaOTf were again in line with our previous findings, i.e. after the activation cycle, the thickness change of the electrode upon sodium insertion and removal is very constant. The "breathing" amounts to about 31 µm along with a slight shrinkage of the electrode upon cycling. In case of NaTFSI, the behavior is notably different. The shrinkage during desodiation is always much smaller compared to the increase during sodiation. The thickness of the electrode continuously increases threefold within a few cycles reaching about 150 µm (desodiated state). This is well in line with the SEM results on the electrode cross sections shown in **Figure 8**. The 4th cycle is magnified in **Figure 10b**. Although the shrinkage in electrode thickness during desodiation is similar for both salts, the electrode expansion during sodiation is much larger in case of NaTFSI. This points on an insufficient reductive stability of this electrolyte. The poor performance for the NaTFSI electrolyte is therefore directly reflected by a poor structural stability of the electrode. Finally, **Figure 10c** shows the results for the two best performing salts (NaOTf and $NaPF_6$) in comparison. The breathing behavior is nearly identical, indicating that both salts are much more suitable (the shift in capacity is due to intrinsic limitations of the dilatometer cell which sometimes leads to slightly non-ideal utilization of the electrode). Note that dilatometry was recently also applied by Karimi *et al.* [22] who studied the influence of the type of glyme (with NaOTf as salt) on the electrode dynamics of the same reaction. Compared to their results, one can see that the salt can have an even stronger influence on the electrode dynamics than the type of glyme.

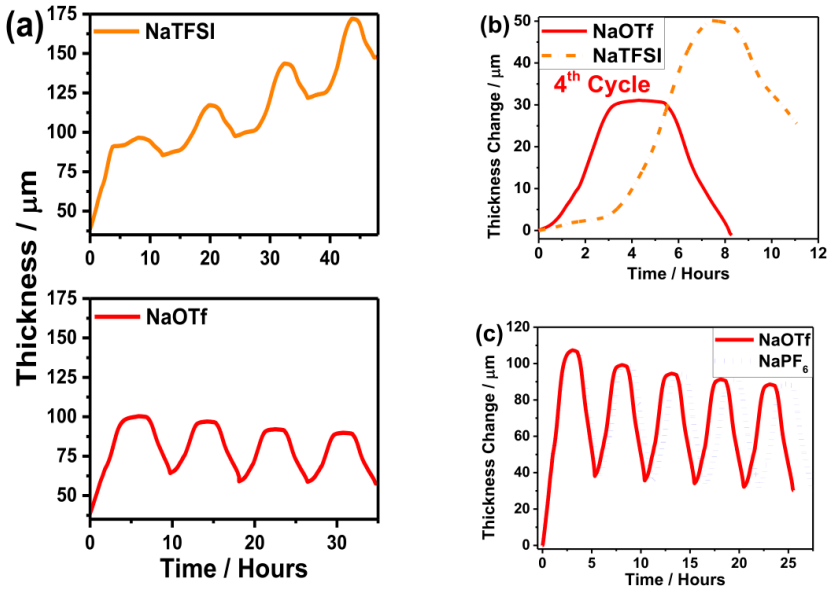

Figure 10. Results from in situ electrochemical dilatometry measurements using NaOTf or NaTFSI as conductive salt a) Thickness of the electrodes over the first four cycles, b) comparison of the 4th cycle. c) shows a comparison over five cycles for NaOTf and $NaPF_6$. The measurements were performed at C/10 =11 mA g^{-1} between 0.01V and 2.5V vs. Na^+/Na. The initial electrode thickness was around 45 µm.

Finally, we applied OEMS in graphite-sodium half cells to monitor the gas release online. **Figure 11** shows the evolution of H_2, CH_4, CO and C_2H_4 for the different salts during 5 consecutive cyclic voltammetric cylces, the cumulative amounts can be found in **Figure 12**. The evolution profile and the integrated gas amount for H_2 show a very strong gas formation for the NaFSI system, the total amount of H_2 released is over 30 times larger than for the other electrolytes. Two gas releasing processes can be easily distinguished: The first one occurs already during the constant potential step (green area in **Figure 10**) before the cell is cycled is observed as evolution peak at t = 0 h which afterwards decays exponentially. As the graphite is unsodiated at this stage, this gas evolution peak indicates a side reaction of the electrolyte or impurities on the Na side of the cell. Note that this behavior was not observed for Na/Na cells, indicating that the graphite electrode could be somehow involved (e.g. by residual impurities). As the potential of the cell is lowered, further H_2 peaks are observed on top of the decaying evolution profile. The most significant sets

on below 0.8 V and can be observed for each cycle. In parallel a strong CO evolution is observed below 0.8 V as well as slighter evolution of C_2H_4 and CH_4, indicating the decomposition of the solvent on the graphite side of the cell. H_2, CO and C_2H_4 evolution, even though at reduced rate, are observed also in the following cycles and are indicating a continuous decomposition of the electrolyte.

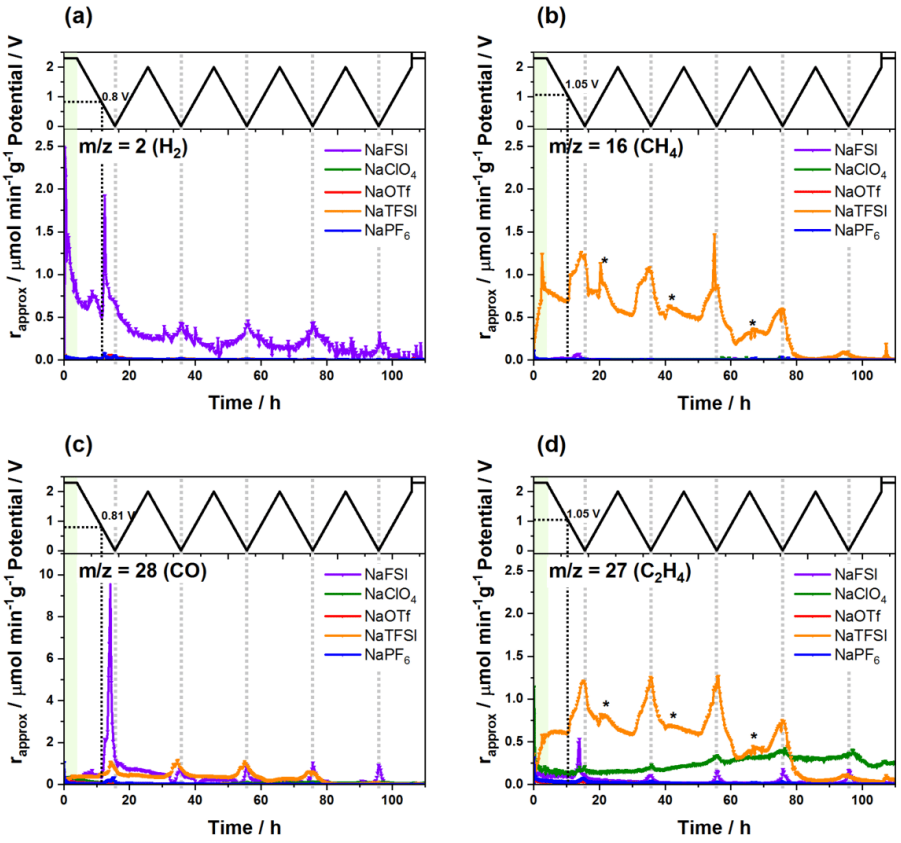

Figure 11. (a) H_2, (b) CH_4, (c) CO and (d) C_2H_4 evolution for Na/graphite cells during 5 cyclovoltammetric cycles (v = 55 µV) with respect to the measured electrolyte. Before the CV cycling the potential of all cells was hold at 2.2 V for 4h (green area).

Significant CO evolution can also be observed at potentials below 0.8 V for the NaTFSI system. In addition, strong evolutions for CH_4 and C_2H_4 are observed. For all gases, several processes can be identified: All three gases are clearly observed during the constant potential phases, which is agreement with the observations from the Na|Na cells and shows the instability of this electrolyte towards Na metal. When during the first cycle the potential is lowered below 1.05 V further

evolution of CH_4 and C_2H_4 sets on, which is accompanied by slight CO evolution, altogether indicating decomposition of the solvent on the sodiated graphite. A further contribution to the gas release can be observed during the potential sweep to higher potential when the graphite electrode is desodiated and fresh Na is plated on the Na side of the cell. Here further evolution CH_4 and C_2H_4 evolution peaks (marked with an asterisk (*) in **Figure 11** (b) and (d)) can be observed.

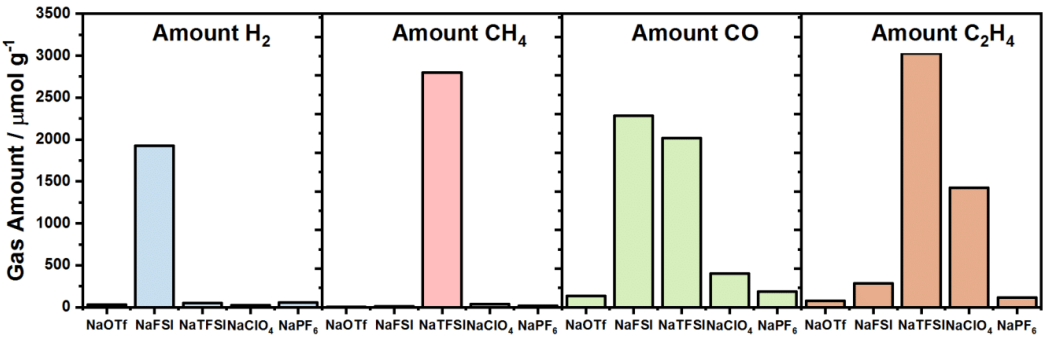

Figure 12. Total gas amounts for H_2, CH_4, CO and C_2H_4 evolution during 5 cyclovoltammetric cycles (v = 55 μVs^{-1}) with respect to the measured electrolyte solution.

For the $NaClO_4$ system, the evolution of H_2, CH_4 and CO is significantly lower than for NaFSI and NaTFSI. The only remarkable gas evolution is observed for C_2H_4 for which a more or less constant evolution is observed from the constant potential step all over the five CV cycles, which indicates constant solvent decomposition, probably on the Na side of the cell. On top of that, small peaks are observed close to the potential minimum, most likely from the sodiated graphite.

In contrast to this three salts, $NaPF_6$ and NaOTf show significant less gas release, most of which occurs during the first cycle as shown in our previous study[10]. As these electrolytes are also showing the best electrochemical cycling, there exists be a clear link between the (electro)chemical stability of these electrolytes and their performance.

3. Summary and conclusion

The stability of diglyme based electrolytes with different conductive salts has been studied with respect to graphite (solvent co-intercalation reaction) and sodium metal (plating/stripping processes). While the solvent co-intercalation is a highly reversible process for e.g. NaOTf, cycle life is poor in case of NaTFSI and NaFSI. Several analytical tools were used to study the stability of the different electrolytes. Side reactions were determined and analyzed using XRD, SEM, TEM,

in situ electrochemical dilatometry and online electrochemical mass spectrometry. Overall, the following conclusions can be made:

Sodium electrode: Plating/Stripping tests in symmetrical Na/Na cells show the highest resistance for NaFSI and the lowest for NaOTf followed by $NaPF_6$. For these salts, the polarization remains constant over consecutive plating/stripping indicating a fairly stable interface. For NaTFSI and $NaClO_4$, the resistance increases over cycling indicating an instable interface / growing SEI. At least in case of NaTFSI, this is already visible by the bare eye when exposing sodium metal to the electrolyte solution. XRD evidences NaF as a major decomposition product in case of NaTFSI and Na_2O in case of $NaClO_4$. OEMS shows that for NaTFSI, different from all other salts, larger amounts of CH_4 are released. Among the different salt, the formation of C_2H_4 and CO was also notably higher in case of $NaClO_4$ and NaTFSI. Minor amounts of H_2 were detected for all salts (which may also be due to water impurities). Overall, the total gas release was smallest for NaOTf, NaFSI and $NaPF_6$.

Graphite electrode: Galvanostatic cycling indicates that the intercalation of solvated ions into graphite (graphite reduction) is accompanied by large irreversible reactions in case of NaTFSI and NaFSI are used as conductive salt. XRD shows that the height of the graphite stacks, L_c, significantly decreases as a result of the co-intercalation reaction. However, the degree of exfoliation depends on the salt. Exfoliation is smallest for $NaPF_6$ and by far largest for NaFSI and NaTFSI. For the latter even delamination and complete structural loss may take place. This is further corroborated by TEM measurements which show a loss in crystallinity in case of NaTFSI while crystalline domains are easily detectable for NaOTf. Decomposition products within the carbon structure and trapping of electrolyte salt remains were found in case of NaTFSI. SEM cross section measurements show an excessive growth in electrode thickness in case of NaTFSI. These observations are clearly supported by *in situ* electrochemical dilatometry which indicates a continuous growth of the electrode due to side reactions. This might be due to delamination of the graphite particles combined with accumulation of decomposition products. OEMS shows that for NaFSI and NaTFSI electrolyte gas evolution on the sodiated graphite electrode occurs once the potential drops below a certain threshold (1.05 V for NaTFSI, 0.8 V for NaFSI) contributing to the further decomposition of these electrolytes. The release of different gases for the two electrolytes also indicates different decomposition mechanisms for the organic solvent.

Overall, our results clearly show that NaTFSI (as well as NaFSI) lead to severe side reactions when used in Na/Na or Graphite/Na cells. Considering graphite, we cannot exclude a cross-talk effect from the sodium counter electrode but as the electrochemical studies show side reactions with the graphite electrode starting from the very beginning, it is quite safe to assume that these salts are unsuitable for graphite electrodes in sodium-ion batteries. Based on our analysis, we can rank the suitability of the different salts in the following order: NaOTf (most suitable) ≥$NaPF_6$>$NaClO_4$>NaFSI>>NaTFSI (least suitable). Our results also explain the only seeming contradiction between the results from Goktas *et al.* that found no SEI on the graphite surface (using NaOTf as salt) and Maibach *et al.* that found an SEI (using NaFSI as salt). From our point of view, NaOTf and $NaPF_6$ are the preferred salts for achieving long cycle life for solvent co-intercalation reactions with graphite in sodium-ion batteries. It remains, however, an intriguing question why NaTFSI is obviously so incompatible with sodium metal electrodes while the combination of LiTFSI and lithium does not show any apparent problems.

4. Experimental

Electrode preparation: Electrodes contained 90% graphite (MTI Corp.) and 10% binder (Polyvinylidene fluoride 'EQ-Lib-PVDF', MTI Corp.). Slurries were mixed in N-methyl-2-pyrrolidone (NMP, Sigma Aldrich) and casted onto dendritic copper foil. The average loading of electrodes after drying (12 hours at 120 ºC) was 2-3 $mg \cdot cm^{-2}$.

Electrochemical (in situ) measurements: Cells for galvanostatic cycling were prepared in argon-filled glove box (<0.1 ppm O_2 and H_2O) with electrodes at diameters of 12 mm respectively. For galvanostatic cycling, two-electrode coin cells (CR2032 Coin Cells by MTI Corp.) and i-shaped Swagelok cells were used. Sodium metal (BASF SE) was used as the counter and reference electrodes. As separator, Whatman glass microfiber filters (GF/A) were soaked into 100 µL electrolyte containing pre-dried (100ºC overnight) sodium trifluoromethanesulfonate (NaOTf, purity > 98.0%, Sigma Aldrich), Sodium hexafluorophosphate ($NaPF_6$, purity > 99+%, Alfa Aesar), Sodium perchlorate, ($NaClO_4$, purity > 97+%, Alfa Aesar), Sodium(I) Bis(trifluoromethanesulfonyl)imide (NaTFSI, purity 99.5%, Solvionic), Sodium(I) bis(fluorosulfonyl)imide (NaFSI, purity 99.7%, Solvionic), in pre-dried (in 4 Å porous molecular sieves, overnight) ethylene glycol dimethyl ether purchased from Sigma Aldrich. 1M NaOTf (Sigma Aldrich) electrolyte was prepared by diglyme. The coin cells were prepared at 1000 PSI

by using a crimper (TG-110). Electrochemical measurements were carried out at room temperatures by Biologic BCS battery cycler. The potential window was between 0.01 V and 2.5 V vs Na^+/Na galvanostatically (at constant current-constant voltage (CC-CV)). The C rate was calculated based on specific charge of graphite stated in literature (Q = 110 mAh g^{-1}, which forms $Na(diglyme)_2C_{20}$ [3]). Therefore, 1 C represents a specific current of i = 110 mA g^{-1} and experiments were done at C/3 and C/10. Electrochemical impedance spectroscopy (EIS) analysis were performed to understand SEI formation on sodium metals.

For OEMS, the setup was described elsewhere [23] (See the Supporting Information). The galvanostatic and cyclic voltammetry measurements were also done simultaneously with OEMS.

Analytical methods: Morphological investigations were carried out by using X-ray diffraction (XRD) (Bruker Phaser D2 diffractometer with Cu-Kα radiation (λ = 1.54056 Å)). Before XRD measurements, instead of graphite electrode film, powder graphite is preferred. Sodiated/desodiated graphite is placed on Cu metal inside special sample holder (Bruker A100-B111-X6) was used to avoid decomposition of air-sensitive phases.

TEM imaging and SAEDs were carried out by a FEI Tecnai G2 FEG operating at 200 kV. The samples were deposited on a copper grid with a holey carbon support film and then transferred to the microscope. Samples were prepared and mounted in the TEM holder into the glove box under argon atmosphere.

Acknowledgements

P.A. and M.G. thank the DFG for support within the project “Redoxchemie ternärer Graphitinterkalationsverbindungen (630743). P.A., T.R. and S.K. thank the BMBF (01DR18003), MINECO and JST for support within the LIBRA project funded over the EIG Concert Japan initiative. High purity sodium was kindly provided by BASF SE. Lukas Medenbach is acknowledged for his support with the impedance data analysis. We further thank Mr. Horoo Onuma for his assistance with the FTIR measurements.

References

[1] aP. K. Nayak, L. Yang, W. Brehm, P. Adelhelm, *Angewandte Chemie International Edition* **2017**; bG. Åvall, J. Mindemark, D. Brandell, P. Johansson, *Advanced Energy Materials* **2018**, *8*, 1703036; cD. Kundu, E. Talaie, V. Duffort, L. F. Nazar, *Angew Chem Int Ed Engl* **2015**, *54*, 3431-3448; dH. Pan, Y.-S. Hu, L. Chen, *Energy & Environmental Science* **2013**, *6*, 2338-2360; eK.

Kubota, S. Komaba, *Journal of The Electrochemical Society,* **2015**, *162*, A2538-A2550; fM. Á. Muñoz-Márquez, D. Saurel, J. L. Gómez-Cámer, M. Casas-Cabanas, E. Castillo-Martínez, T. Rojo, *Advanced Energy Materials* **2017**, *7*, 1700463; gN. Yabuuchi, K. Kubota, M. Dahbi, S. Komaba, *Chemical Reviews* **2014**, *114*, 11636-11682; hH. Kim, H. Kim, Z. Ding, M. H. Lee, K. Lim, G. Yoon, K. Kang, *Advanced Energy Materials* **2016**, *6*, 1600943.

[2] aP. K. Nayak, L. T. Yang, W. Brehm, P. Adelhelm, *Angewandte Chemie-International Edition* **2018**, *57*, 102-120; bL. Medenbach, P. Adelhelm, *Topics in Current Chemistry* **2017**, *375*; cP. Adelhelm, P. Hartmann, C. L. Bender, M. Busche, C. Eufinger, J. Janek, *Beilstein Journal of Nanotechnology* **2015**, *6*, 1016-1055.

[3] B. Jache, P. Adelhelm, *Angewandte Chemie International Edition* **2014**, *53*, 10169-10173.

[4] H. Kim, J. Hong, Y.-U. Park, J. Kim, I. Hwang, K. Kang, *Advanced Functional Materials* **2015**, *25*, 534-541.

[5] aB. Jache, J. O. Binder, T. Abe, P. Adelhelm, *Physical Chemistry Chemical Physics* **2016**, *18*, 14299-14316; bH. Kim, J. Hong, G. Yoon, H. Kim, K.-Y. Park, M.-S. Park, W.-S. Yoon, K. Kang, *Energy Environ. Sci.* **2015**, *8*, 2963-2969.

[6] M. Goktas, B. Akduman, P. Huang, A. Balducci, P. Adelhelm, *The Journal of Physical Chemistry C* **2018**, *122*, 26816−26824.

[7] aA. P. Cohn, K. Share, R. Carter, L. Oakes, C. L. Pint, *Nano Letters* **2016**, *16*, 543-548; bZ. Zhu, F. Cheng, Z. Hu, Z. Niu, J. Chen, *Journal of Power Sources* **2015**, *293*, 626-634; cI. Hasa, X. Dou, D. Buchholz, Y. Shao-Horn, J. Hassoun, S. Passerini, B. Scrosati, *Journal of Power Sources* **2016**, *310*, 26-31.

[8] aK. Gotoh, H. Maruyama, T. Miyatou, M. Mizuno, K. Urita, H. Ishida, *Journal of Physical Chemistry C* **2016**, *120*, 28152−28156; bN. Leifer, M. F. Greenstein, A. Mor, D. Aurbach, G. Goobes, *The Journal of Physical Chemistry C* **2018**, *122*, 21172-21184.

[9] S. C. Jung, Y. J. Kang, Y. K. Han, *Nano Energy* **2017**, *34*, 456-462.

[10] M. Goktas, C. Bolli, E. J. Berg, P. Novák, K. Pollok, F. Langenhorst, M. v. Roeder, O. Lenchuk, D. Mollenhauer, P. Adelhelm, *Advanced Energy Materials* **2018**, 1702724.

[11] J. Maibach, F. Jeschull, D. Brandell, K. Edstrom, M. Valvo, *ACS Appl Mater Interfaces* **2017**, *9*, 12373-12381.

[12] M. Cabello, T. Chyrka, R. Klee, M. J. Aragón, X. Bai, P. Lavela, G. M. Vasylchenko, R. Alcántara, J. L. Tirado, G. F. Ortiz, *Journal of Power Sources* **2017**, *347*, 127-135.

[13] K. Westman, R. Dugas, P. Jankowski, W. Wieczorek, G. Gachot, M. Morcrette, E. Irisarri, A. Ponrouch, M. R. Palacín, J. M. Tarascon, P. Johansson, *ACS Applied Energy Materials* **2018**, *1*, 2671-2680.

[14] S. Tobishima, H. Morimoto, M. Aoki, Y. Saito, T. Inose, T. Fukumoto, T. Kuryu, *Electrochimica Acta* **2004**, *49*, 979-987.

[15] L. Lutz, D. Alves Dalla Corte, M. Tang, E. Salager, M. Deschamps, A. Grimaud, L. Johnson, P. G. Bruce, J.-M. Tarascon, *Chemistry of Materials* **2017**, *29*, 6066-6075.

[16] Z. W. Seh, J. Sun, Y. Sun, Y. Cui, *ACS Cent Sci* **2015**, *1*, 449-455.

[17] T. Hosokawa, K. Matsumoto, T. Nohira, R. Hagiwara, A. Fukunaga, S. Sakai, K. Nitta, *The Journal of Physical Chemistry C* **2016**, *120*, 9628-9636.

[18] aH. Kim, G. Yoon, K. Lim, K. Kang, *Chem Commun (Camb)* **2016**, *52*, 12618-12621; bG. Yoon, H. Kim, I. Park, K. Kang, *Advanced Energy Materials* **2016**, 1601519; cZ.-L. Xu, J. Park, G. Yoon, H. Kim, K. Kang, *Small Methods* **2018**, 1800227.

[19] D. I. Iermakova, R. Dugas, M. R. Palacın, A. Ponrouch, *Journal of The Electrochemical Society* **2015**, *162*, A7060-A7066.

[20] Y. Zhao, L. V. Goncharova, A. Lushington, Q. Sun, H. Yadegari, B. Wang, W. Xiao, R. Li, X. Sun, *Adv Mater* **2017**, *29*.

[21] T. Palaniselvam, M. Goktas, B. Anothumakkool, Y.-N. Sun, R. Schmuch, L. Zhao, B.-H. Han, M. Winter, P. Adelhelm, *Advanced Functional Materials* **2019**, 1900790.
[22] N. Karimi, A. Varzi, S. Passerini, *Electrochemica Acta* **2019**, *304*, 474-486.
[23] M. He, (Eidgenössische Technische Hochschule (ETH) Zürich), **2016**.

5.4. From Co-intercalation in Graphite to insertion in graphene/Sn Composites (Publication 3)

In a related project of the thesis, anode materials with higher capacity were sought for. Tin (Sn) is an attractive electrode material for sodium-ion batteries but it suffers from large volume expansion of about 420 % on the materials level. A suitable matrix buffering these volume changes is therefore required. In this project, graphene nanoplatelets (GnP), prepared by ball milling of graphite were used for this purpose. The resulting GnP-Sn composite (combined with some N-doping of the carbon) was then studied as anode material. Ball-milling of graphite leads to a decrease in crystallinity finally leading to a soft "non-graphitic" carbon. It was found that the ion storage mechanism changes from co-intercalation to conventional intercalation and hence the electrode dynamics were found to be very different. While the breathing of graphite was normally 70-100 % in our previous study [100], the breathing was only around 10 % for the GnP. In a similar way, it was found for the GnP-Sn composite that the electrode breathing (around 14 %) is much smaller as compared to what would be expected from the 420 % during sodiation of tin. This shows that the GnP matrix effectively can buffer the volume expansion hence excellent cycle life (1000 cycles) could be achieved.

The results of these findings were published in the Journal of *Advanced Functional Materials*.

Thangavelu Palaniselvam, Mustafa Goktas, Bihag Anothumakkool, Ya-Nan Sun, Richard Schmuch, Li Zhao, Bao-Hang Han, Martin Winter, Philipp Adelhelm, *Sodium Storage and Electrode Dynamics of Tin–Carbon Composite Electrodes from Bulk Precursors for Sodium-Ion Batteries, Advanced Functional Materials* **2019**, 1900790.

The paper is written by the first author Thangavelu Palaniselvam and edited by Philipp Adelhelm. TEM images are done by Ya-Nan Sun, Li Zhao and Bao-Hang Han. *In situ* XRD measurements and XPS analysis are performed by Bihag Anothumakkool, Richard Schmuch, and Martin Winter. All the measurements related to electrochemistry, XRD and also analysis of the data and further calculations are performed by the first author. Some parts of electrochemical data analysis, overall interpretation, and discussions, also *in situ* electrochemical dilatometry measurements and 3D model drawings are performed by Mustafa Goktas. By all the comments and contributions of the authors, the paper is be published.

ADVANCED FUNCTIONAL MATERIALS
www.afm-journal.de

Sodium Storage and Electrode Dynamics of Tin–Carbon Composite Electrodes from Bulk Precursors for Sodium-Ion Batteries

Thangavelu Palaniselvam, Mustafa Goktas, Bihag Anothumakkool, Ya-Nan Sun, Richard Schmuch, Li Zhao, Bao-Hang Han, Martin Winter, and Philipp Adelhelm**

Here, a Sn–C composite material prepared from bulk precursors (tin metal, graphite, and melamine) using ball milling and annealing is reported. The composite (58 wt% Sn and 42 wt% N-doped carbon) shows a capacity up to 445 mAh g_{Sn+C}^{-1} and an excellent cycle life (1000 cycles). For the graphite, the ball milling leads to graphene nanoplatelets (GnP) for which the storage mechanism changes from solvent co-intercalation to conventional intercalation. The final composite (Sn at nitrogen-doped graphite nanoplatelets (SnNGnP)) is obtained by combining the GnPs with Sn and melamine as the nitrogen source. Rate-dependent measurements and in situ X-ray diffraction are used to study the asymmetric storage behavior of Sn, which shows a more sloping potential profile during sodiation and more defined steps during desodiation. The disappearance of two redox plateaus during desodiation is linked to the preceding sodiation current density (memory effect). The asymmetric behavior is also found by in situ electrochemical dilatometry. This method also shows that the effective electrode expansion during sodiation is much smaller (about +14%) compared to what is expected from Sn (+420%), which gives a reasonable explanation for the excellent cycle life for the SnNGnP (and likely other nanocomposites in general). Next to the advantages, challenges, which result from the nanocomposite approach, are also discussed.

1. Introduction

The success of portable electronics as well as, more recently, the rise of electromobility and grid storage is almost exclusively based on lithium-ion batteries (LIBs).[1] High cell voltage, high energy density, long cycle life, and low costs per operational life are the major advantages of this technology. However, the price fluctuations of Li and concerns about its future costs and availability combined with its uneven geographical distribution recently evoked interest in alternative, Li-free battery concepts.[2] Thanks to the abundance of sodium and the technological similarity to LIBs, sodium-ion batteries (SIBs) are considered as attractive alternative, especially for grid storage.[3] While many attractive cathode materials have been identified, anode materials that combine high storage capacity, suitable redox potential, and sufficient cycling stability are still lacking.

Graphites are used as the state-of-the-art anode in LIBs due to their attractive cost, low redox potential (mostly <0.15 V vs Li^+/Li), high theoretical and practical specific capacities as well as charge density (372 mAh g^{-1} or 818 Ah L^{-1}) and unrivalled overall performance. The storage mechanism is based on the formation of LiC_6, a binary graphite intercalation compound (*b*-GIC).[4,5] Unfortunately, the same reaction does not occur in case of sodium. Reversible storage of Na^+ in graphite has been only successful by solvent co-intercalation, i.e., solvated sodium ions are intercalated to form a ternary graphite intercalation compound (*t*-GIC). In this case, ether-based electrolytes are needed.[6] By this co-intercalation reaction, a storage capacity of about 110 mAh g^{-1} with an outstanding rate capability and stability over more than 1000 cycles are found.[6–8] Regrettably, the limited capacity and the large volume expansion so far limit the practical use of this approach. Apart from graphite, many anode materials have been proposed including hard carbons,[9] carbon nanofiber,[10] and graphene with and without heteroatom doping,[11] transition metals and their intermetallic phases (alloys),[12] metal oxides and their composites with carbon structures.[13a] In the present scenario, hard carbons

Dr. T. Palaniselvam, M. Goktas, Prof. P. Adelhelm
Institute of Technical Chemistry and Environmental Chemistry
Friedrich Schiller University Jena
Philosophenweg 7a, D-07743 Jena, Germany
E-mail: t.palaniselvam@uni-jena.de; philipp.adelhelm@uni-jena.de
Dr. T. Palaniselvam, M. Goktas, Prof. P. Adelhelm
Center for Energy and Environmental Chemistry Jena (CEEC Jena)
Friedrich-Schiller-University Jena
Philosophenweg 7a, D-07743 Jena, Germany
Dr. B. Anothumakkool, Dr. R. Schmuch, Prof. M. Winter
MEET Battery Research Center
University of Muenster
Corrensstr. 46, D-48149 Muenster, Germany
Y.-N. Sun, Prof. L. Zhao, Prof. B.-H. Han
CAS Key Laboratory of Nanosystem and Hierarchical Fabrication
CAS Center for Excellence in Nanoscience
National Center for Nanoscience and Technology
Beijing 100190, China
The ORCID identification number(s) for the author(s) of this article can be found under https://doi.org/10.1002/adfm.201900790.

DOI: 10.1002/adfm.201900790

appear currently most promising for SIBs, though they have been presently outruled for use in LIBs due to safety concerns at high guest uptake.[13b] Typically, capacities in the range of 250–350 mAh g^{-1} are obtained; recently even 400 mAh g^{-1} has been reported.[13c] However, much of the capacity is obtained on a plateau very close to 0 V versus Na^+/Na, which could lead to dendrite formation and hence causes safety issues.

Elements such as Sn, Sb, and Bi can deliver a high Na^+ storage capacity due to the formation of Na-rich alloys.[14] Among them, Sn was identified as promising due to its high theoretical capacity of 847 mAh g^{-1} (formation of $Na_{3.75}Sn$) and low charge/discharge potential.[15] However, the large volume change of Sn (about 420%)[16] during sodiation and desodiation that are even higher than for lithiation[17] causes particle cracking and hence fast electrode degradation.[11] At the same time, the continuous pulverization of the electrode leads to ongoing solid electrolyte interphase (SEI)[18] formation as reported for Li.[19] In addition, Sn is a relatively expensive material[20] and tends to dissolve in the electrolyte.[21] To overcome these limitations, many active/inactive composite materials based on nanosized Sn combined with carbon (nanostructures) have been studied for SIBs (Table S1, Supporting Information). The Sn/carbon nanocomposite usually provides higher specific capacity and improved cycling stability by maintaining electrode integrity.[22] A disadvantage of this approach is that nanocomposites typically exhibit a low packing density thus reducing the practical charge density. Moreover, the high surface area of many nanostructured composites results in excessive SEI formation, which causes a large irreversible capacity in the first cycle.

The sodiation mechanism of Sn was recently studied by in situ X-ray diffraction (XRD)[4,23] (by cycling at 50 mA g^{-1}). The reaction involves the formation of several intermediate intermetallic Na–Sn phases but has not been fully clarified yet. It has been also found that in LIB, the commonly used mixed carbonate based electrolytes carbonate-based electrolytes[24] appear less suitable in conjunction with Sn, as Sn acts as the catalyst for electrolyte decomposition leading to thick SEI formation.[25] On the other hand, glyme-based electrolytes are increasingly studied for SIBs[26,27] because of their better stability at low redox potentials, though they show also limited oxidation stability. Zhang et al. have successfully demonstrated the use of ether-based electrolytes for tin/carbon (Sn/C) electrodes, and long cycle life was achieved.[25] Nevertheless, considering the large volume expansion during sodiation of Sn, there is a lack of understanding on why such electrodes can be cycled over hundreds of cycles.

Here, we describe a simple method for the preparation of a composite (SnNGnP) consisting of Sn supported by nitrogen-doped graphite nanoplatelets (NGnP) and study its behavior as anode for SIBs. The composite is prepared by ball milling bulk precursors (graphite, Sn, and melamine) followed by annealing in inert atmosphere. High-resolution transmission electron microscopy (HRTEM), X-ray photoelectron spectroscopy (XPS), and XRD are used to study the structural and chemical properties of the material. Concerning the electrochemical properties, we first show how ball milling affects the storage mechanism of graphite, i.e., solvent co-intercalation mechanism versus conventional insertion. Second, the composite (i.e., SnNGnP) is studied and in situ XRD is used to determine the phase evolution of the Sn phase at different currents. Finally, in situ electrochemical dilatometry (ECD) is used to study the change in electrode thickness during cycling.

2. Results and Discussion

2.1. Synthesis and Structural Characterization

Scheme 1 illustrates the synthesis route of the SnNGnP composite and its storage characteristics. In more details, the graphite powder was ball-milled with Sn powder and melamine (i.e., nitrogen precursor) followed by annealing at 1100 °C in

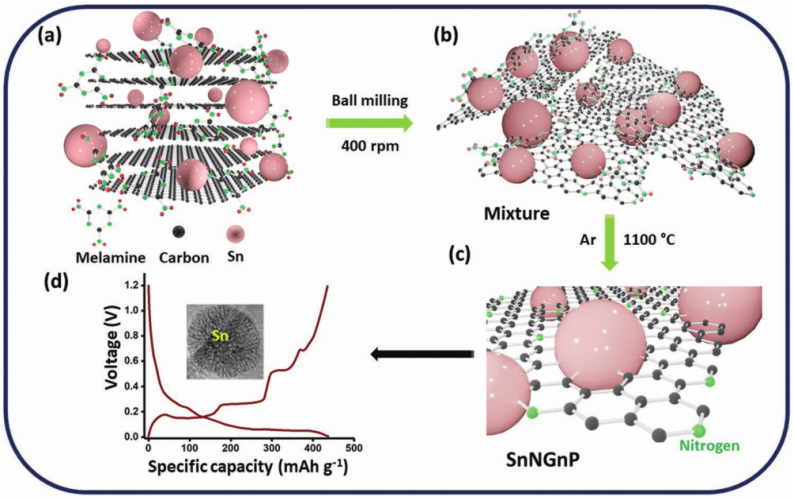

Scheme 1. a–c). Synthesis steps for SnNGnP composite and d) the process of (de)sodiation in SnNGnP composite.

Ar atmosphere. The detailed preparation procedure is provided in the Supporting Information. To determine the properties of the carbon material, we first studied the effect of ball milling on graphite and found that the treatment leads to small domains, hereafter called graphene nanoplatelets.

Figure 1 shows the transmission electron microscopy (TEM) images of graphite before and after ball milling. The TEM images (Figure 1a,b) of the graphite show that the sample consists of larger particles with a highly ordered microstructure. On the other hand, ball milling significantly reduced the particle size to the nanometer regime (Figure 1c), and the structure of the sheets is nearly similar to the what is generally described as few-layered graphene sheets (Figure 1d).[28,29] This confirms the effective transformation of graphite into graphene nanoplatelets (GnP) via ball milling. The higher magnification image of GnP shows that the graphene sheets are wrinkled, similar to the curled graphene sheets in hard carbon.[30] However, as we will show in the following section, the Na storage mechanism in GnP is not only different from graphite, but also different from hard carbon.[30]

Figure 2 represents the TEM images of SnNGnP composite. The TEM and high angle annular dark-field scanning transmission electron microscopy (HAADF/STEM) images (Figure 2a,b) reveal a fine distribution of Sn nanoparticles on the carbon matrix. The structure of carbon is similar to what has been found for the GnP in Figure 1 and Figure S1 (Supporting Information). The particle size of Sn has reduced significantly down to about 5–50 nm. The Sn particles are still crystalline. For the Sn particle in Figure 2d, a *d*-spacing (inset Figure 2d) of 0.29 nm was found, corresponding to the (200) plane. This result is in line with the XRD measurements evidencing that crystalline Sn nanoparticles are existing in GnP matrix. Scanning electron microscopy (SEM) images (Figure S2, Supporting Information) show that the SnNGnP composite also contains larger Sn particles in the micrometer range. Uniform nitrogen doping of the GnP was confirmed by energy dispersive X-ray analysis (EDAX) combined with TEM; see Figure S3 in the Supporting Information. A total nitrogen content of 0.62 wt% was determined by CHNS elemental analysis (Table S2, Supporting Information). The total weight content of Sn in the composite was 58 wt% (i.e., 12 mol%) as determined using thermogravimetric analysis (TGA) analysis

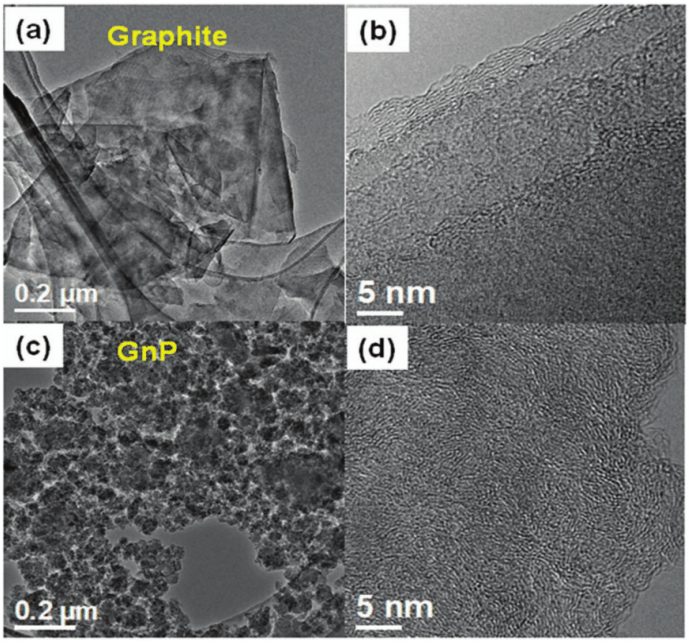

Figure 1. TEM images of a,b) graphite and c,d) GnP at different magnifications.

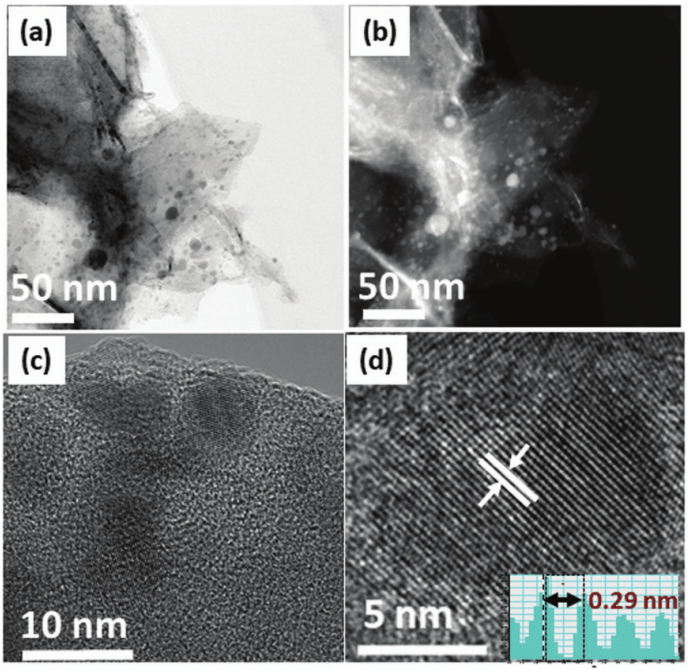

Figure 2. a) TEM image of SnNGnP and b) its corresponding HAADF/STEM image measured at dark field. c,d) HRTEM images of SnNGnP at different magnifications.

(Figure S4, Supporting Information) and is well supported by CHNS elemental analysis. This is slightly less than the expected ≈66% (Sn:C ratio of 2:1) but can be well understood. Annealing of melamine with Sn causes the catalytic decomposition of melamine and produces some pyrolytic carbon which slightly decreases the Sn/C ratio.[31] More information can be found in the supporting information.

The samples were also characterized by XRD; see **Figure 3**a. The graphite powder exhibits the expected strong diffraction reflection at $2\theta = 26.3°$ due to the (002) planes. Ball milling reduces the intensity and the reflection becomes much broader, indicating exfoliation of graphite into few-layered graphene sheets for the samples GnP and SnNGnP. The average Sn crystallite size was estimated using the Scherrer equation.[32] The calculated value for Sn in SnNGnP is 54 nm while it is 80 nm for a Sn powder reference. Overall, the XRD and microscopic analysis show that ball milling and pyrolysis of the composite mixture result in crystalline Sn with reduced particle/crystallite size. Further, the elemental composition of the SnNGnP was examined by XPS analysis. The survey spectrum of XPS is displayed in Figure 3b, which shows signals related to C, N, O, and Sn (see Table S3 in the Supporting Information). The Sn content was only 1.0 at %. As XPS only probes a few nanometers of a surface, this indicates that the smaller Sn particles are well embedded in NGnP (or the surface of large Sn particles is covered by NGnP).

The deconvoluted Sn 3d spectra (Figure 3c) show two major peaks at 487.4 and 495.8 eV, which correspond to Sn^{4+}—O.[33] Meanwhile, no indication for Sn^{2+}—O is found at 486.5 eV,[34a] which indicates that the surface is composed of an oxide, i.e., SnO_2. As XRD provides evidence for highly crystalline Sn (Figure 3a) as bulk phase, the presence of SnO_2 is likely the result of surface oxidation upon air contact. The weak signal at 485.5 eV indicates the existence of Sn_3N_4,[34b] which can be ascribed to the nitrogen doping. The deconvoluted N 1s spectra are shown in Figure 3d. The total nitrogen content was estimated to around 5.1 wt% by EDAX analysis (Figure S5, Supporting Information). From the deconvoluted spectra, three different nitrogen species could be observed. The peak at 398.5 eV corresponds to pyridinic nitrogen, while the other two peaks at 401.2 and 403.8 eV are corresponding to graphitic nitrogen and nitrogen bound with oxygen functional groups, respectively.[35–37] Over all, the successful nitrogen doping in GnP was confirmed from N 1s spectra, and their importance was identified from the electrochemical studies. Finally, the specific surface area of the materials was determined by nitrogen physisorption using the Brunauer–Emmett–Teller (BET) method. The graphite has a BET specific surface area of around 1 $m^2\ g^{-1}$,[38] When graphite converts to GnP or SnNGnP, the BET specific surface area values increase to about 270 $m^2\ g^{-1}$ and 60 $m^2\ g^{-1}$, respectively (see Figure S6, Supporting Information).

2.2. Electrochemical Characterization of GnP and Graphite

The sodium storage behavior of GnP was evaluated by galvanostatic discharge/charge experiments and compared to graphite.

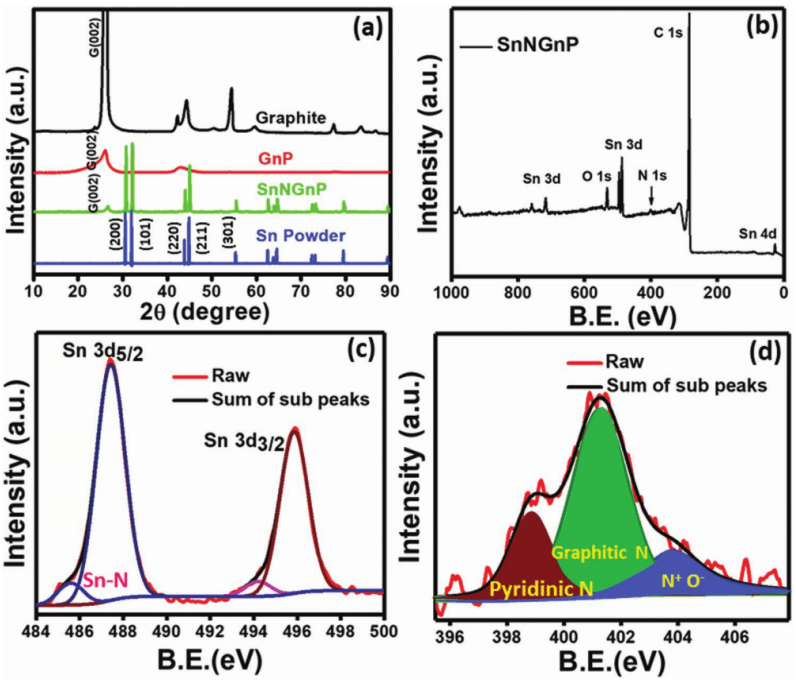

Figure 3. a) XRD patterns of SnNGnP, Sn powder, GnP, and Graphite. b) Long-range XPS spectrum of SnNGnP, c) Sn 3d spectra of SnNGnP, and d) N 1s spectra of SnNGnP.

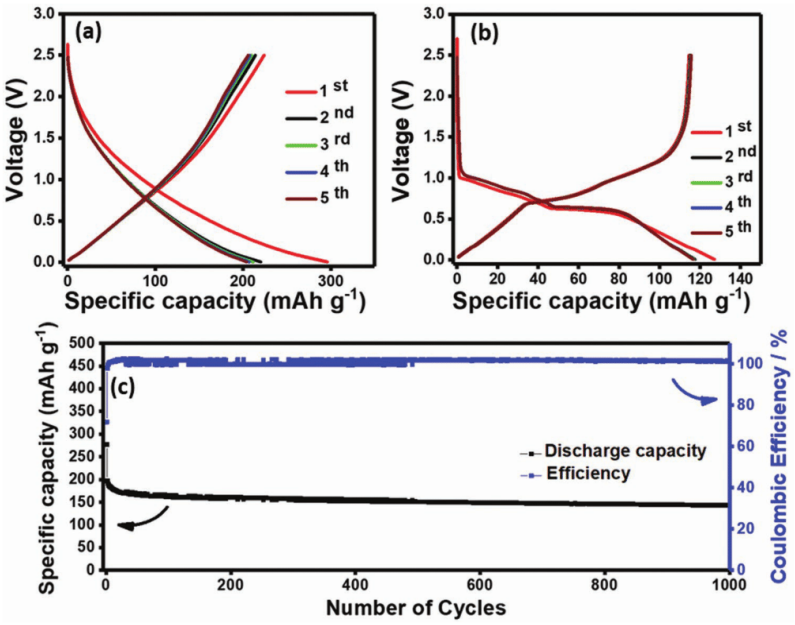

Figure 4. a) Charge–discharge curves of GnP and b) charge–discharge curves of graphite, recorded at a current density of 50 mA g^{-1}. c) Cycling stability of GnP electrode evaluated with charge/discharge rates of 500 mA g^{-1} for 1000 cycles. All measurements were conducted in two-electrode geometry with Na metal as counter electrode.

A solution of $NaPF_6$ in diglyme was used as electrolyte; see **Figure 4**. In line with other literature reports (see Table S4 in the Supporting Information), we limited the upper threshold voltage to 2.5 V. GnP delivers first discharge and charge capacities of around 297 and 223 mAh g^{-1}, respectively, with a resulting initial Coulombic efficiency (ICE) of 75.1%. Interestingly, this ICE value is in the same range as for hard carbon anodes,[39] albeit the much higher surface area of GnP. This indicates irreversible trapping of Na^+ rather than excessive electrolyte decomposition/SEI formation.

The specific capacity in the second cycle is 220 mAh g^{-1}, which quickly stabilizes upon further cycling. Complementary measurements with a more common carbonate electrolyte ($NaPF_6$ in ethylene carbonate(EC)/propylene carbonate (PC)) are shown in Figure S7 (Supporting Information). It is important to note that although the reversible capacities are the same for both electrolytes, the ICE value was higher for the diglyme electrolyte (75.1% vs 52.2%). Higher values are desired, the results nevertheless show that the use of diglyme can partly mitigate the excessive SEI formation frequently observed for high surface area materials. The better performance is likely related to the generally better electrochemical stability of ethers over carbonates at low potentials.[38,40] The obtained specific capacity for GnP is significantly higher than that of graphite (120 mAh g^{-1}) and many other graphene-based materials existing in the literature (Table S4, Supporting Information). We note that with a surface area of 270 m^2 g^{-1}, the capacitve contribution to the total charge storage is still negligible.[41]

Comparing Figure 4a (GnP) and Figure 4b (graphite), one can observe a clear difference not only in capacity but also in the voltage profiles. It is worth noting that the shape of the voltage profile is a direct indicator for the storage mechanism. Graphite and GnP can be clearly distinguished. While defined plateaus are found for graphite (formation of t-GICs via solvent co-intercalation[38]), a very sloping profile over the whole voltage window is found for GnP. Such a sloping behavior is typical for so-called nongraphitic carbons, which do possess no far-reaching order/crystallinity. The redox behavior therefore becomes much more ill-defined for the latter. Overall, the structural deformation from graphite to GnP by the ball milling process changes the storage mechanism from co-intercalation to intercalation. The loss of the co-intercalation mechanism can also be corroborated from the fact that the potential profile and the reversible capacity of GnP is nearly the same for both ether- and carbonate-based electrolytes. Only the former would allow reversible solvent co-intercalation along with defined redox potentials. Moreover, GnP does not show the low-voltage redox plateau typical for hard carbons, which finally classifies GnP more as a "soft carbon."[42,43]

Further, the rate performance of GnP was investigated by charging and discharging at different current densities ranging from 0.05 to 2 A g^{-1} (Figure S8, Supporting Information). With gradually increased current densities, the GnP displays capacities of 220, 197, 190, 178, 171, and 159 mAh g^{-1} at 0.05, 0.1, 0.2, 0.5, 1.0, and 2.0 A g^{-1}, respectively. When setting the current density back to 0.05 A g^{-1}, the specific capacity recovers to 190 mAh g^{-1}, demonstrating excellent rate performance and stability. Subsequently, the long-term cycling of GnP was

studied over 1000 cycles at 0.5 A g^{-1} (Figure 4c). Starting from 196 mAh g^{-1} (second cycle) the reversible capacity remains at 150 mAh g^{-1} after 1000 cycles, i.e., 77% of retention in capacity.

2.3. Electrochemical Characterization of SnNGnP

Electrochemical results on SnNGnP are shown in **Figure 5**. In line with the previous measurements, 1 M $NaPF_6$ in diglyme was used as electrolyte. Note that the voltage window had to be limited to an upper threshold of 1.2 V as a higher limit leads to poor cycle life for Sn-based electrodes.[44] The initial discharge capacity is 517 mAh $g_{(Sn+C)}^{-1}$ with an ICE of 76.2% indicating some side reactions (the index Sn+C indicates that the capacity is normalized on the mass of Sn and nitrogen doped carbon (NGnP)). In the second cycle, the capacity amounts to 445 mAh $g_{(Sn+C)}^{-1}$ with 99.9% Coulombic efficiency. The same values were obtained for the following cycles indicating a fast stabilization of the electrode. As the NGnP (obtained by removal of Sn) has a capacity of 78 mAh g_C^{-1} (see Figure S9 in the Supporting Information), its contribution to the capacity is 17%, i.e., most of the capacity is due to Sn. Indeed, with the Sn content of 58 wt%, Sn in the composite reaches 85% (from the second cycle) of its theoretical capacity of 847 mAh g_{Sn}^{-1}, which implies a high utilization degree.[45] Full utilization of Sn in the composite would lead to a capacity of 524 mAh $g_{(Sn+C)}^{-1}$. (Detailed calculations are given in the Supporting Information). Without doubt, further improvement in performance is possible. Results for increasing Sn contents are shown in Figure S10 (Supporting Information). This, however, generally leads to a decrease in cycle life, so a careful balance and further tuning of the preparation process are needed.

The fact that Sn dominates the storage capacity can be also seen from the voltage profiles, which show several defined redox plateaus. These result from the subsequent formation of several binary Na_xSn phases during sodiation ($Sn + xNa^+ + xe^- \rightarrow Na_xSn$, $x \leq 3.75$)[4,46] or desodiation, respectively. During charging, subsequent formation of $Na_{15}Sn_4$, Na_9Sn_4, α-NaSn, and $NaSn_5$ has been found by in situ XRD.[47] The plateaus can be more clearly seen from the dQ/dV plot shown in Figure S11 (Supporting Information). Remarkably, no obvious fading in capacity was observed in the subsequent cycles, elucidating the high reversible storage behavior and stability of SnNGnP.

Further, the rate performance of SnNGnP was investigated by charging and discharging at different current densities ranging from 0.05 to 2 A g^{-1} (Figure 5b). By increasing the current densities, SnNGnP showed capacities of 452, 437, 429, 405, 384, and 253 mAh g_{Sn+C}^{-1} at 0.05, 0.1, 0.2, 0.5, 1.0, and 2.0 A g^{-1}, respectively. When the current density was reduced to 0.05 A g^{-1}, the reversible capacity again reached to 449 mAh g_{Sn+C}^{-1}, showing the outstanding rate performance characteristics of SnNGnP. Further, excellent cycle life was found when cycling is over 1000 cycles at a high current of 1 A g^{-1}. Figure 5c shows that SnNGnP exhibited an excellent long-term cycling with only minor capacity fading. The obtained reversible capacities at the end of 20, 100, 200, 300, 400, 500, 600, 700, and 1000 cycles were 345, 320, 311, 303, 304, 305, 304, 294, and 290 mAh g^{-1}, respectively. Despite the large volume expansion of the alloying reaction, SnNGnP maintained 290 mAh g_{Sn+C}^{-1} after 1000 cycles at 1 A g^{-1} (i.e., 82.6% retention

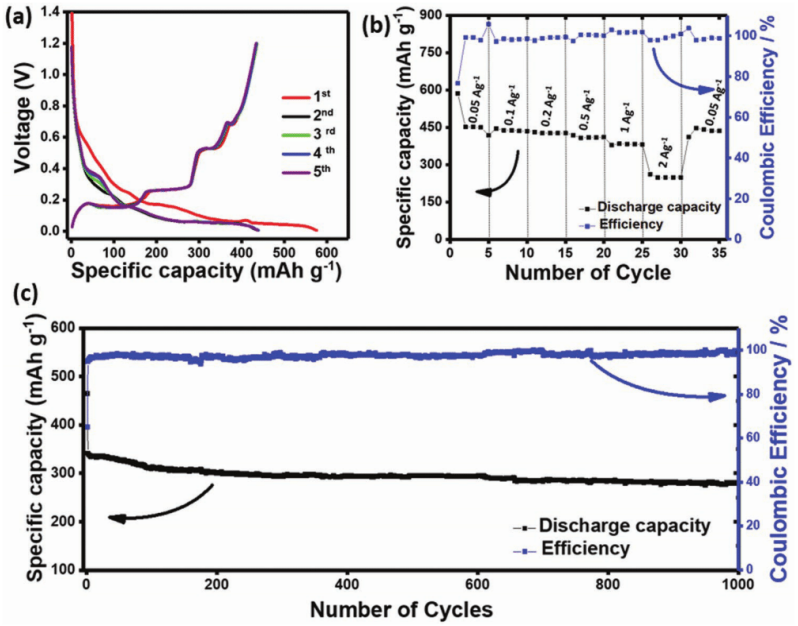

Figure 5. a) Galvanostatic charge–discharge curves of SnNGnP, recorded at a current density of 50 mA g^{-1}. b) Rate capability of SnNGnP electrode measured from 50 to 2000 mA g^{-1}. c) Cycle life of the SnNGnP electrode recorded at 1000 mA g^{-1} for 1000 cycles. All measurements were conducted in two-electrode geometry with Na metal as counter electrode.

in capacity referring to the second cycle (350 mAh g_{Sn+C}^{-1}). Even at 1 A g^{-1}, the loss over 1000 cycles is small (0.06 mAh g^{-1} per cycle).[48] We note that the nitrogen doping seems an important reason for this excellent cycle life. A comparison with a non-N-doped composite is shown in Figure S12 (Supporting Information). The beneficial impact of nitrogen doping of carbon materials has been reported many times although the explanations are less straightforward. Indeed, nitrogen doping can increase the electronic conductivity of the electrode materials, and the structural defects provide additional storage sites for Na^+ and/or stronger interaction with Sn. Better wettability and improved SEI formation have also been discussed.[49]

2.4. Postmortem Analysis of SnNGnP

SnNGnP electrodes after cycling were characterized by TEM and XPS. TEM images after 50 cycles at 500 mA g^{-1} are shown in Figure S13 (Supporting Information). The nanosized Sn particles showed cracks throughout the whole volume because of the repeated expansion/contraction during cycling. A thin amorphous layer observed on the particle edges (Figure S14, Supporting Information) suggests the formation of a thin and fragmented SEI layer. At the same time, the cycle life was excellent, meaning that the Sn particles remained well connected to the carbon, and the mechanical stability of the electrode was therefore maintained. A more detailed discussion on the mechanical stability is provided in the "In Situ Electrochemical Dilatometry" section.

SEI formation was further studied by XPS. For this purpose, SnNGnP electrodes before and after cycling were compared. The deconvoluted spectra of C 1s, O 1s, F 1s, and Sn 3d spectra are displayed in the Supporting Information. The C 1s spectra of SnNGnP (Figure S15a, Supporting Information) exhibit the major peak at 284.9 eV corresponding to sp^2-hybridised carbon of GnP, while the other peaks at 285.1 and 286.0 eV correspond to sp^3-hybridized carbon and C=N, respectively.[50] After cycling, however, two additional peaks were observed at 283.9 and 288.0 eV as shown in Figure S15b (Supporting Information). The peak at 283.9 eV corresponds to the C−Sn bond,[51] while the other peak at 288.0 eV corresponds to a carbon−oxygen bond (C−ONa).[25] While the O 1s spectrum (Figure S16, Supporting Information) shows a corresponding peak at 535.9 eV (C−O) both are indicating the existence of RCH_2ONa, which is the main reduction product of diglyme.[25] The O 1s spectrum also exhibits a minor signal at 529.7 eV corresponding to Na−O (Figure S16b, Supporting Information).[51] In addition, a dominating peak at 686.6 eV could be observed in Figure S17 (Supporting Information) and corresponds to P−F, which is due to residual Na_xPF_y and $Na_xPO_yF_z$ species in the SEI.[52] Overall, the XPS analysis concludes the formation of SEI consisting of both organic and inorganic species such as RCH_2ONa, NaF, and $Na_xPO_yF_z$.[52]

2.5. Rate Dependence of Na–Sn Phase Behavior

It is interesting to note that the number of plateaus in the voltage profile during charging depends on the current density; see Figure S18a–e in the Supporting Information (50–500 mA g^{-1}). Four plateaus (at 0.15, 0.26, 0.53, and 0.68 V) can be clearly distinguished when charging at 50 and 100 mA g^{-1}. At currents of 200 mAg^{-1} and higher (i.e. at 500 mAg^{-1} and 1000 mAg^{-1}) however, the plateaus at 0.15 and 0.26 V disappear and a single, while larger plateau at 0.21 V occurs (Figure S18f, Supporting Information). The effect of current density on the voltage profile at around 0.68 V versus Na^+/Na has been mentioned by Zhang et al.[25] However, the more noticeable change occurs at around 0.2 V. Obviously, the phase formation mechanism depends on the current density. To gain more insight into it, we conducted in situ XRD at three different current densities (50, 250, and 500 mA g^{-1}).

Figure 6 and Figure S19 (Supporting Information) show the in situ measurement results at 50 mA g^{-1}. The obtained voltage

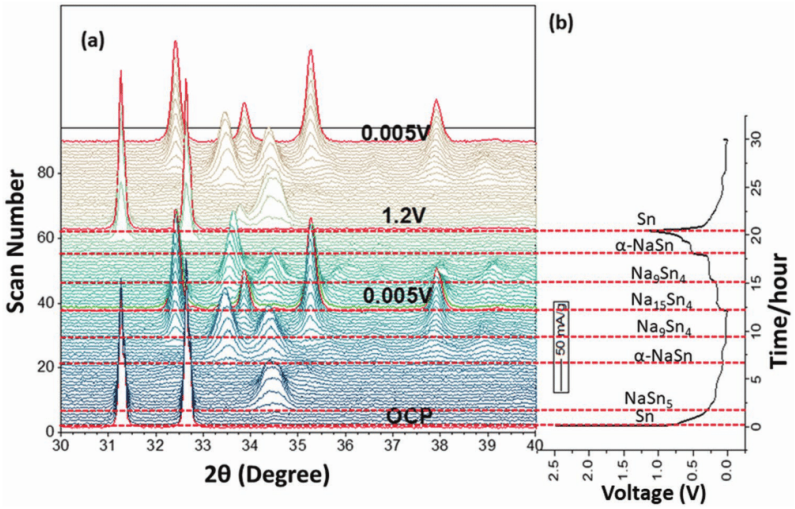

Figure 6. a) In situ XRD data and b) the corresponding voltage curves. The indicated phases are the ones expected from the binary phase diagram.

profile (Figure 6b) of SnNGnP, during in situ XRD measurement, is nearly matching with the voltage profile measured with coin cells (Figure 5a; Figure S20, Supporting Information). The in situ XRD data show that several intermediates are formed during sodiation. Discharging leads to a gradual disappearance of the Sn reflection combined with the appearance of new reflection. These reflections are broad, indicating only a limited degree in crystallinity. At the end of discharge, the XRD pattern shows a good match with the $Na_{15}Sn_4$ phase, which is the theoretical discharge product of the reaction. It is important to note, however, that none of the intermediate phases matches with the phases that one would expect from the phase diagram; see Figure S21 in the Supporting Information. This is in line with the results obtained from Obrovac and co-workers.[4] During charging, again several intermediates appear and finally Sn forms, indicating reversibility of the electrode reaction. The number of unknown intermediates, however, differs between discharging and charging (Figure S19, Supporting Information) so that the reaction mechanism within one cycle is asymmetric with respect to the phase behavior. Besides, the sodiation in the second cycle (Figure 6) exactly matches with the first sodiation profile, which shows the consistency of sodiation in Sn with respect to the cycle numbers. Basically, our results at low current density are consistent with the former findings. As observed earlier, the asymmetric behavior in Figures 5a and 6b is due to kinetic limitations and/or the presence of nonequilibrium phases. To gain more insight, we performed galvanostatic intermittent titration technique (GITT) measurements to test the equilibrium states (Figure S22, Supporting Information).[53] GITT measurements show that the number of plateaus becomes more symmetric. This means the asymmetric behavior is due to kinetic effects.

Next, the specific (de)sodiation current was increased to 250 and 500 mA g^{-1}. The diffraction patterns for discharge and charge are shown in Figures S23 and 24 (Supporting Information). Compared to the low-current measurements, the signals become even less defined, and the positions of the reflexes change. This can be more clearly seen in **Figure 7** that shows the results after complete discharge, i.e., after reaching 0.005 V. At higher currents, no evidence for $Na_{15}Sn_4$ is found whereas the appearing reflexes do not match with any other of the previous phases either (Figure S25, Supporting Information). The new reflections are possibly due to an overlap of reflections of Na–Sn phases in Sn due to incomplete charging or unknown (metastable) Na–Sn phase formation. While a deeper structural analysis is desirable, the poor signal intensity prevents any further analysis at this point. In any case, the phase behavior during discharge seems to depend on the current density.

Figure S26a,b in the supporting information compare voltage profiles for cycling at rates of 50 and 500 mA g^{-1}. The number of plateaus, particularly visible during desodiation, depends on the current density. 4 and 3 plateaus are found at 50 and 500 mAh g^{-1}, respectively.

Following on this, we changed the current density within a cycle, i.e. sodiation and desodiation were done at different rates. Results are shown in Figure 26c,d. Briefly, the results show that the number of plateaus appearing during desodiation depends on the sodiation current. For small sodiation currents always four plateaus appear during desodiation. Only three plateaus appear when the sodiation current is high; however, the obtained results indicate that the rate of sodiation determines the desodiation pathway for the Na–Sn alloy at potentials below 0.3 V versus Na^+/Na. This can be interpreted as a kind of memory effect.[54] The underlying reasons for the asymmetric behavior, the structure of the new phases, as well as the memory effect require further studies. It is worth noting that the overshooting of the potential at around 0.68 V versus Na^+/Na during desodiation only depends on the desodiation current. This means that no memory effect takes place in this case, and the reaction is kinetically limited as also suggested by Zhang et al.[25] Finally, the plateau at 0.5 V versus Na^+/Na during desodiation is clearly visible at all tested current densities and conditions, indicating that it is a very fast two-phase reaction.

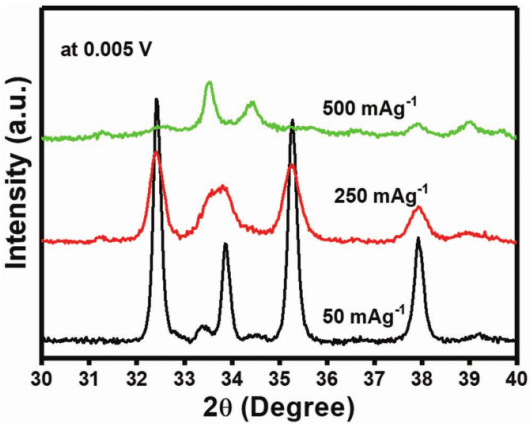

Figure 7. In situ XRD patterns of SnNGnP measured at 0.005 V (i.e., complete sodiation) with different current densities. The figure represents the changes in the formation of Na–Sn intermetallic phases with respect to applied current.

2.6. In Situ Electrochemical Dilatometry

The volume expansion of 420% (at the material level) during cycling of Sn electrodes is obviously a key issue, which can limit cycle life. On the other hand, stable cycling of Sn/carbon composites has been reported and our study also confirms an excellent cycling stability. In order to understand that, herein, the effective change in electrode thickness during cycling is followed using in situ ECD. Results for GnP and SnNGnP are compared in **Figure 8**. The starting thickness for both electrodes is very similar (36 and 37 µm). Consecutive sodiation/desodiation leads to periodic expansion/contraction of the electrodes.

In both cases, a few cycles are necessary for obtaining a stable condition. The larger initial increase for the SnNGnP electrode might be related to a stronger SEI formation due to the catalytic effect of Sn. Despite the large volume expansion of Sn, it is quite evident that the volume change at the electrode

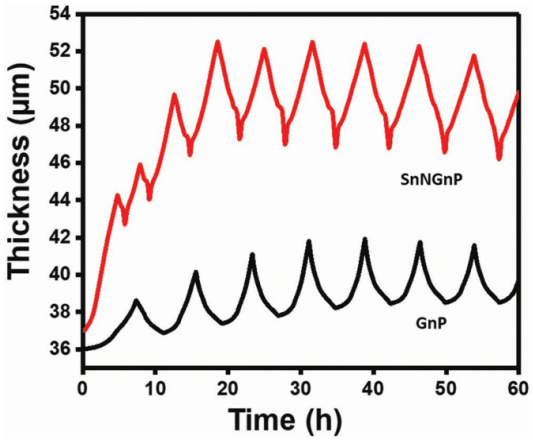

Figure 8. In situ ECD measurements at 50 mA g^{-1} over 60 h of consecutive cycling for GnP (seven cycle) and SnNGnP (nine cycle) electrodes.

level is much smaller. For GnP, the difference between the sodiated and desodiated states is about 3.5–4.5 µm corresponding to a change of about 10% referring to the initial electrode thickness. For SnNGnP, the change is slightly larger in the range of 4.8–5.5 µm, which corresponds to about 14% increase. The results clearly show that the dramatic volume expansion of tin is not effective at the total electrode level, which is the result of the porous structure of the nanocomposite leaving enough free space.

A close-up of the fourth cycle is shown in Figure S27 (Supporting Information). While the GnP electrode shows a more or less symmetrical and pointed behavior during sodiation/desodiation, the situation is different for the Sn-containing electrode. In line with the asymmetric voltage profile of SnNGnP, i.e., more sloping during sodiation and more plateaus during desodiation (see, e.g., Figure 5a), the change in electrode thickness is also slightly asymmetric. In particular, at the end of charging starting at about 1.0 V versus Na^+/Na, the electrode change first becomes smaller and then suddenly larger. The differences become more apparent in the derivative plot; see Figure S27a in the Supporting Information. Overall, this shows that the sodiation/desodiation of GnP occurs more gradually, whereas the numerous phase transitions in case of tin lead to a more stepwise behavior. The degree of electrode expansion for GnP (about 10%) also proves that the solvent co-intercalation mechanism is absent as much higher values would be expected in this case.[30] In the case of SnNGnP (Figure S28, Supporting Information), the increase in electrode density during sodiation is also a good sign for the negligible volume expansion of the Sn-based electrode (detailed discussion is given in the Supporting Information). Overall, the only moderate change in electrode thickness during cycling is likely one of the reasons for the excellent cycle life found for many nanostructured metal/carbon-based nanocomposites. Thanks to the loose and opened structure of these nanocomposites, enough free volume (filled with electrolyte during cell cycling) exists that allows tin to easily expand within the electrode. Large electrode expansion, which more easily would lead to electrode degradation, is effectively prevented.

2.7. Challenges

Although the approach of making (nano)structured composites is attractive and we found comparatively high capacity and long cycle life, it is also important to mention challenges of this approach that are often neglected in literature. Although the areal capacity of the electrodes is reasonable (about 1.5 mAh cm^{-2} compared to about 1–3 mAh cm^{-2} for LIB technology), the loose structure of the composite creates extra free volume in the electrode. This leads to a penalty with respect to volumetric capacity as well as gravimetric capacity (the latter because the excess electrolyte will increase the weight of the electrode). For example, for our SnNGnP electrode, we calculate a porosity of about 80% and a volumetric capacity of about 253 mAh cm^{-3}. These values are still lower compared to conventional graphite electrodes in LIBs that are additionally compressed by calendaring to increase volumetric capacity (about 540 mAh cm^{-3} can be estimated assuming a theoretical capacity of 818 mAh cm^{-3} for graphite and allowing 1/3 of porosity).[55] While the study presented here still addresses fundamental aspects of (nano)composites for SIBs, future studies aiming at application of such materials should also aim at achieving electrodes with higher effective volumetric capacity. Increasing the effective capacity by increasing loading and packing density seems more a technical challenge; however, it is a critical task for putting the advantages of (nano)composites into practice.

3. Conclusion

Structural and electrochemical properties of a composite containing tin- and nitrogen-doped carbon (graphene nanoplatelets) were studied. We show that ball milling of graphite leads to the formation of GnP along with a change from co-intercalation storage mechanism (110 mAh g^{-1}) to insertion (220 mAh g^{-1}). For the tin-containing composites (58 wt% Sn, $q_{lth} = 558$ mAh g_{Sn+C}^{-1}), we find a high utilization of tin (85% from the second cycle) and excellent cycle life (1000 cycles). The voltage profiles of tin during sodiation and desodiation show an asymmetric behavior, i.e., the sodiation profile appears more sloping while defined potential/voltage plateaus are found during desodiation. The potential profiles of the investigated anode material are much more favorable than hard carbon, as low potentials, and thus the risk of possible sodium plating, can be easily avoided. By applying different currents during sodiation and desodiation in one cycle, we find that the number of redox plateaus during desodiation depends on the preceding sodiation current (memory effect). At currents exceeding 200 mA g^{-1}, two plateaus at 0.15 and 0.26 V are replaced by one intermediate plateau (at 0.21 V). In situ XRD shows that at high currents, a new phase forms replacing the ideal discharge product $Na_{3.75}Sn$. The asymmetric shape of the voltage profile is also noticeable in the in situ ECD measurement. Finally, ECD also shows that the change in electrode thickness for the

SnNGnP composite during cycling is just 14% and therefore much smaller compared to what one would expect from the 420% that arise from $Na_{3.75}Sn$. This is the direct evidence for that the carbon matrix effectively buffers the volume change of the Sn during cycling. The small change in electrode thickness is likely the key factor enabling the excellent cycle life.

4. Experimental Section

Preparation of SnNGnP: The SnNGnP was synthesized by a simple high-energy ball milling method (HEBM) in argon (Ar) atmosphere. In brief, commercially available Sn and graphite (2:1) were placed in zirconium oxide–based ball milling jar with zirconium oxide balls (ZrO_2) (12 numbers). Further, 4 g of melamine was added into the jar and closed. The entire process was done in an Ar-saturated glove box. The jar was then fixed in the planetary ball milling and allowed for mechanical milling with 400 rpm for 48 h. The resulting mixture was collected and placed in an alumina boat. Subsequently, the solid mixture containing boat was kept in the middle of the quartz tube. Then the quartz tube was placed into the tubular furnace and saturated with Ar atmosphere. The temperature of the furnace was increased from room temperature to 1100 °C with the rate of 2 °C min^{-1} and was maintained at same temperature for 3 h. After pyrolysis, the resulting product was washed with ethanol to remove organic residues present in the mixture. The final product was collected and preserved for further analysis. In order to study the role of nitrogen doping in GnP, the undoped sample, i.e., SnGnP was prepared under similar experimental conditions without addition of melamine during ball milling and annealing at high temperature. In order to study the effect of Sn content in the composite, the Sn content was increased by increasing the ratio of Sn:graphite such as 1:1, 2:1, 3:1, and 4:1 and the resulting samples were denoted as SnNGNP 1:1, SnNGNP 2:1, SnNGNP 3:1, and SnNGNP 4:1. On the other hand, for the effective comparison, Sn was removed from the composite, i.e., SnNGnP by the acid leaching method. In brief, active composite was dispersed in 1 M HCl and allowed for mechanical rotation at 90 °C for 12 h. The final material was separated by simple filtration and washed with water for many times. The resulting material was termed as NGnP and preserved for further studies. Also, graphitic nanoplatelets were prepared by adopting the same method for the preparation of SnNGnP. Herein, the preparation of GnP was achieved without addition of Sn, melamine, and without doing pyrolysis. In brief, the 3 g of graphite was placed in a ZrO_2-based ball milling jar and the jar was allowed for the mechanical milling for 48 h with 400 rpm. The resulting product was treated with 1 M HCl at 90 °C for 24 h to remove impurities if any.

Material Characterizations: XRD measurements were done using a Bruker Phaser 2 diffractometer. X-rays were generated by a Cu Kα source at 20 kV operating voltage. Morphological investigations were carried out by using a SEM (Phenom ProX) operated at 15 kV accelerating voltage. TEM images were measured on a Tecnai G2 20 S-TWIN microscope (FEI, USA). For the TEM measurement, the material to be measured was dispersed in *N*-methyl pyrrolidone (NMP) well and then applied on the holey/lacey formvar carbon-coated grid. When the solvent evaporates completely, the carbon-coated grid can be put into the microscope. XPS measurement was taken on an ESCALab220i-XL electron spectrometer (VG Scientific Ltd., UK) by using Al Kα radiation at 300 W. An Autosorb iQ3 machine from Quantachrome Corporation was used for BET surface area measurements through the nitrogen physisorption method. Prior to the experiment, the sample was activated at room temperature (for 12 h) and at 150 °C (for 12 h) under ultrahigh vacuum (10^8 mbar). About 100 mg of the sample was loaded for gas adsorption, and the weight of the sample was recorded before and after outgassing to verify the complete removal of all guest molecules including the coordinated H_2O in SnNGnP. A vario microcube from Elementaranalyse GmbH was used for CHNS analysis. Values were averaged over four measurements. The electrode thickness was measured by digital thickness dial gauge from Käfer Messuhrenfabrik GmbH. TGA measurements were conducted with a Netzsch STA 449 F3 Jupiter.

Electrochemical Measurements: The SnNGnP anode material was fabricated by making a slurry of SnNGnP with carboxymethyl cellulose (CMC) and conducting carbon with the mass ratio of 8.5:1.0:0.5, respectively. Water was used as the blending solvent for the mixture. The slurry was then allowed for mechanical rotation for 12 h to get uniform mixing. Then the slurry was coated on carbon-coated Cu foil and dried for 12 h under vacuum at 110 °C. The SnNGnP-coated film was cut into small pieces equivalent to 12 mm in area. The active mass loading was in the range of 2.5–3 mg cm^{-2}. The coin-type cells (CR2032 Coin Cells by MTI Corp.) were assembled using SnNGnP as an active anode material and sodium metal (BASF SE Corporation) as the counter and reference electrode in the argon-filled glove box (<0.1 ppm O_2 and H_2O). The 1 M sodium hexafluorophosphate ($NaPF_6$) (predried 60 °C overnight) in predried (in 4 Å porous molecular sieves, overnight) diethylene glycol dimethyl ether (diglyme, anhydrous purity > 99.5%, Sigma Aldrich) was employed as the electrolyte. As a separator, Whatman glass microfiber filters (GF/A) were soaked with 150 µL electrolyte for coin cell measurements. The coin cells were prepared at 1000 PSI by using a crimper (TG-110). For effective comparison, 1 M $NaPF_6$ in ethylene carbonate/propylene carbonate was also used as a reference system. The cells were measured using in Biologic BCS cycler at 25 °C. The cells were galvanostatically charged and discharged at various current densities from 50 mA g^{-1} to 2 A g^{-1} in the voltage range 0.005 to 1.2 V versus Na^+/Na. In the case of graphite and GnP, the potential window was maintained at 0.005–2.5 V. GITT was measured by applying a pulse constant current (20 mA g^{-1}) with duration 15 min, followed by 1 h relaxation to reach an equilibrium voltage.

Electrochemical Measurements—Electrochemical (In Situ) Measurements: Cells for ECD measurements were prepared in an argon-filled glove box (<0.1 ppm O_2 and H_2O) with electrodes at diameters of 10 mm. In the special design of ECD nanocells (by EL-CELL GmbH), a special ceramic porous separator named T-frit was soaked by 400–500 µL of electrolyte by pre-evacuating all the gases from the pores which helped the wetting of 10 mm of electrode properly. Measurements were conducted at 50 mA g^{-1} in a climate cabinet at 25 °C.

Electrochemical Measurements—In Situ XRD measurements: A Bruker D8 Advance diffractometer was used to perform in situ XRD using a home-made airtight cell. SnNGnP electrode slurry was prepared in 1-methylpyrrolidine by mixing with 10 wt% Super C65 and 10 wt% polyvinylidene fluoride (PVDF) and casted over a beryllium current collector and dried under vacuum at 120 °C overnight. Na metal was used as counter and reference electrode, and separated from working electrode using a Whatman glass fiber separator. The cell assembly was carried out in a moisture-free glove box (H_2O < 0.5 ppm, O_2 < 0.3 ppm), and 1 M $NaPF_6$ in diglyme was used as the electrolyte. The electrode was continuously scanned in Bragg Brentano geometry between 2θ = 25° and 81° during the charge and discharge at 0.05 A g^{-1}; one scan lasts for 20 min in both cases. For a higher current density of 0.25 A g^{-1}, a relaxation step for 15 min was used in each 100 mV step during the entire charge–discharge for to achieve enough number of scans.

Supporting Information

Supporting Information is available from the Wiley Online Library or from the author.

Acknowledgements

T.P. and M.G. contributed equally to this work. T.P. acknowledges Alexander von Humboldt Foundation, Germany, for the financial support. P.A. and L.Z. acknowledge support over the Sino-German Center (325774457) within the project "Sodium-Ion Storage in Carbon

Nanomaterials". The authors thank Gottschalt, Fähndrich, and Wermann (Robl group) for N_2 physisorption, TGA and elemental analysis.

Conflict of Interest

The authors declare no conflict of interest.

Keywords

anode, nitrogen-doped carbon, sodium-ion battery, tin composite, volume expansion

Received: January 24, 2019
Revised: February 18, 2019
Published online:

[1] a) M. Armand, J. M. Tarascon, *Nature* **2008**, *451*, 652; b) P. G. Bruce, B. Scrosati, J. M. Tarascon, *Angew. Chem., Int. Ed.* **2008**, *47*, 2930; c) Y. Wang, H. C. Zeng, J. Y. Lee, *Adv. Mater.* **2006**, *18*, 645; d) S. Chen, Y. Zhao, B. Sun, Z. Ao, X. Xie, Y. Wie, G. Wang, *ACS Appl. Mater. Interfaces* **2015**, *7*, 3306; e) S. Chen, P. Bao, X. Huang, B. Sun, G. Wang, *Nano Res.* **2014**, *7*, 85; f) S. Chen, P. Bao, G. Wang, *Nano Energy* **2013**, *2*, 425; g) R. Schmuch, R. Wagner, G. Hörpel, T. Placke, M. Winter, *Nat. Energy* **2018**, *3*, 267; h) R. Wagner, N. Preschitschek, S. Passerini, J. Leker, M. Winter, *J. Appl. Electrochem.* **2013**, *43*, 481.

[2] a) L. Suo, Y. S. Hu, H. Li, M. Armand, L. Chen, *Nat. Commun.* **2013**, *4*, 1481; b) H. L. Pan, Y. S. Hu, L. Q. Chen, *Energy Environ. Sci.* **2013**, *6*, 2338.

[3] a) P. K. Nayak, L. Yang, W. Brehm, P. Adelhelm, *Angew. Chem., Int. Ed.* **2018**, *57*, 102; b) C. Vaalma, D. Buchholz, M. Weil, S. Passerini, *Nat. Rev. Mater.* **2018**, *3*, 18013; c) N. Yabuuchi, K. Kubota, M. Dahbi, S. Komaba, *Chem. Rev.* **2014**, *114*, 11636; d) M. H. Han, E. Gonzalo, G. Singh, T. Rojo, *Energy Environ. Sci.* **2015**, *8*, 81.

[4] a) L. D. Ellis, T. D. Hatchard, M. N. Obrovac, *J. Electrochem. Soc.* **2012**, *159*, A1801; b) M. Winter, J. O. Besenhard in *Handbook of Battery Materials* (Ed: J. O. Besenhard), Vol. *3*, Wiley-VCH, Weinheim **1999**, p. 383.

[5] M. Winter, J. O. Besenhard, M. E. Spahr, P. Novak, *Adv. Mater.* **1998**, *10*, 725.

[6] B. Jache, P. Adelhelm, *Angew. Chem., Int. Ed.* **2014**, *53*, 10169.

[7] H. Kim, J. Hong, Y. U. Park, J. Kim, I. Hwang, K. Kang, *Adv. Funct. Mater.* **2015**, *25*, 534.

[8] M. Goktas, B. Akduman, P. Huang, A. Balducci, P. Adelhelm, *J. Phys. Chem. C* **2018**, *122*, 26816.

[9] a) Z. Li, Z. Jian, X. Wang, I. A. R. Perez, C. Bommier, X. Ji, *Chem. Commun.* **2017**, *53*, 2610; b) K. Wang, Y. Jin, S. Sun, Y. Huang, J. Peng, J. Luo, Q. Zhang, Y. Qiu, C. Fang, J. Han, *ACS Omega* **2017**, *2*, 1687; c) V. Simone, A. Boulineau, A. de Geyer, D. Rouchon, L. Simonin, S. Martinet, *J. Energy Chem.* **2016**, *25*, 761.

[10] W. Li, M. Li, K. R. Adair, X. Sun, Y. Yu, *J. Mater. Chem. A* **2017**, *5*, 13882.

[11] S. Wun, R. Ge, M. Lu, R. Xu, Z. Zhang, *Nano Energy* **2015**, *15*, 379.

[12] W. Luo, F. Shen, C. Bommier, H. Zhu, X. Ji, L. Hu, *Acc. Chem. Res.* **2016**, *49*, 231.

[13] a) C. Bommier, X. Ji, *Isr. J. Chem.* **2015**, *55*, 486; b) M. Winter, K. C. Moeller, J. O. Besenhard, in *Lithium Batteries: Science and Technology* (Eds. G. A. Nazri, G. Pistoia), Kluwer Academic Publishers, New York, NY **2004**, pp. 144–194; c) C. Zhao, Q. Wang, Y. Lu, B. Li, L. Chen, Y. S. Hu, *Sci. Bull.* **2018**, *63*, 1125.

[14] a) M. Lao, Y. Zhang, W. Luo, Q. Yan, W. Sun, S. X. Dou, *Adv. Mater.* **2017**, *29*, 1700622; b) Y. Kim, K. H. Ha, S. M. Oh, K. T. Lee, *Chem. - Eur. J.* **2014**, *20*, 11980; c) A. Darwiche, C. Marino, M. T. Sougrati, B. Fraisse, L. Stievano, L. Monconduit, *J. Am. Chem. Soc.* **2012**, *134*, 20805.

[15] a) H. Ying, W. Q. Han, *Adv. Sci.* **2017**, *4*, 1700298; b) H. Zhu, Z. Jia, Y. Chen, N. Weadock, J. Wan, O. Vaaland, X. Han, T. Li, L. Hu, *Nano Lett.* **2013**, *13*, 3093.

[16] a) J. W. Wang, X. H. Liu, S. X. Mao, J. Y. Huang, *Nano Lett.* **2012**, *12*, 5897; b) M. K. Datta, R. Epur, P. Saha, K. Kadakia, S. K. Park, P. N. Kumta, *J. Power Sources* **2013**, *225*, 316.

[17] M. Winter, J. O. Besenhard, J. H. Albering, J. Yang, M. Wachtler, *Prog. Batteries Battery Mater.* **1998**, *17*, 208.

[18] M. Winter, *Z. Phys. Chem.* **2009**, *223*, 1395.

[19] M. Winter, W. K. Appel, B. Evers, T. Hodal, K. C. Moeller, I. Schneider, M. Wachtler, M. R. Wagner, G. H. Wrodnigg, J. O. Besenhard, *Monatsh. Chem.* **2001**, *132*, 473.

[20] P. Meister, H. Jia, J. Li, R. Kloepsch, M. Winter, T. Placke, *Chem. Mater.* **2016**, *28*, 7203.

[21] H. Jia, R. Kloepsch, X. He, M. Evertz, S. Nowak, J. Li, M. Winter, T. Placke, *Acta Chim. Slov.* **2016**, *63*, 470.

[22] a) C. Kim, K. Y. Lee, I. Kim, J. Park, G. Cho, K. W. Kim, J. H. Ahn, H. J. Ahn, *J. Power Sources* **2016**, *317*, 153; b) C. Kim, I. Kim, H. Kim, M. K. Sadan, H. Yeo, G. Cho, J. Ahn, J. Ahn, H. Ahn, *J. Mater. Chem. A* **2018**, *6*, 22809.

[23] L. Baggetto, P. Ganesh, R. P. Meisner, R. R. Unocic, J. C. Jumas, C. A. Bridges, G. M. Veith, *J. Power Sources* **2013**, *234*, 48.

[24] a) R. W. Schmitz, P. Murmann, R. Schmitz, R. Mueller, L. Kraemer, P. Isken, P. Niehoff, S. Nowak, G.-V. Roeschenthaler, N. Ignatiev, P. Sartori, S. Passerini, M. Kunze, A. Lex-Balducci, C. Schreiner, I. Cekic-Laskovic, M. Winter, *Prog. Solid State Chem.* **2014**, *42*, 65; b) I. Cekic-Laskovic, N. von Aspern, L. Imholt, S. Kaymakziz, K. Oldiges, B. R. Rad, M. Winter, *Top. Curr. Chem.* **2017**, *375*, 37.

[25] B. Zhang, G. Rousse, D. Foix, R. Dugas, D. A. D. Corte, J. M. Tarascon, *Adv. Mater.* **2016**, *28*, 9824.

[26] a) C. L. Bender, B. Jache, P. Adelhelm, J. Janek, *J. Mater. Chem. A* **2015**, *3*, 20633; b) H. Kim, J. Hong, G. Yoon, H. Kim, K. Park, M. Park, W. Yoon, K. Kang, *Energy Environ. Sci.* **2015**, *8*, 2963.

[27] a) K. Gotoh, H. Maruyama, T. Miyatou, M. Mizuno, K. Urita, H. Ishida, *J. Phys. Chem. C* **2016**, *120*, 28152; b) J. Zhang, D. W. Wang, W. Lv, S. Zhang, Q. Liang, D. Zheng, F. Kang, Q. H. Yang, *Energy Environ. Sci.* **2017**, *10*, 370.

[28] a) T. Palaniselvam, M. O. Valappil, R. Illathvalappil, S. Kurungot, *Energy Environ. Sci.* **2014**, *7*, 1059; b) T. Palaniselvam, H. B. Aiyappa, S. Kurungot, *J. Mater. Chem.* **2012**, *22*, 23799.

[29] a) D. W. Chang, E. K. Lee, E. Y. Park, H. Yu, H. J. Choi, I. Y. Jeon, G. J. Sohn, D. Shin, N. Park, J. H. Oh, L. Dai, J. B. Baek, *J. Am. Chem. Soc.* **2013**, *135*, 8981; b) S. Wang, D. Yu, L. Dai, D. W. Chang, J. B. Baek, *ACS Nano* **2011**, *5*, 6202; c) L. Qu, Y. Liu, J. B. Baek, L. Dai, *ACS Nano* **2010**, *4*, 1321; d) I. Y. Jeon, H. J. Choi, M. J. Ju, I. T. Choi, K. Lim, J. Ko, H. K. Kim, J. C. Kim, J. J. Lee, D. Shin, S. M. Jung, J. M. Seo, M. J. Kim, N. Park, L. Dai, J. B. Baek, *Sci. Rep.* **2013**, *3*, 2260.

[30] Z. Li, C. Bommier, Z. S. Chong, Z. Jian, T. W. Surta, X. Wang, Z. Xing, J. C. Neuefeind, W. F. Stickle, M. Dolgos, P. A. Greaney, X. Ji, *Adv. Energy Mater.* **2017**, *7*, 1602894.

[31] T. Yang, G. Han, *Int. J. Electrochem. Sci.* **2012**, *7*, 10884.

[32] L. Alexander, H. P. Klug, *J. Appl. Phys.* **1950**, *21*, 137.

[33] F. Lu, X. Ji, Y. Yang, W. Deng, C. E. Banks, *RSC Adv.* **2013**, *3*, 18791.

[34] a) X. T. Chen, K. X. Wang, Y. B. Zhai, H. J. Zhang, X. Y. Wu, X. Wie, J. S. Chen, *Dalton Trans.* **2014**, *43*, 3137; b) S. S. Pan, S. Wang, Y. X. Zhang, Y. Y. Luo, F. Y. Kong, S. C. Xu, J. M. Xu, G. H. Li, *Appl. Phys. A* **2012**, *109*, 267.

[35] T. Palaniselvam, V. Kashyap, S. N. Bhange, J. B. Baek, S. Kurungot, *Adv. Funct. Mater.* **2016**, *26*, 2150.
[36] a) X. Zhou, J. Bao, Z. Dai, Y. G. Guo, *J. Phys. Chem. C* **2013**, *117*, 25367; b) M. Sha, H. Zhang, Y. Nie, K. Nie, X. Lv, N. Sun, X. Xie, Y. Ma, X. Sun, *J. Mater. Chem. A* **2017**, *5*, 6277.
[37] D. Das, S. Kim, K. R. Lee, A. K. Singh, *Phys. Chem. Chem. Phys.* **2013**, *15*, 15128.
[38] M. Goktas, C. Bolli, E. J. Berg, P. Novák, K. Pollok, F. Langenhorst, M. v. Roeder, O. Lenchuk, D. Mollenhauer, P. Adelhelm, *Adv. Energy Mater.* **2018**, *8*, 1702724.
[39] K. Westman, R. Dugas, P. Jankowski, W. Wieczorek, G. Gachot, M. Morcrette, E. Irisarri, A. Ponrouch, M. R. Palacín, J. M. Tarascon, P. Johansson, *ACS Appl. Energy Mater.* **2018**, *1*, 2671.
[40] D. Aurbach, D. E. Eli, *J. Electrochem. Soc.* **1995**, *142*, 1746.
[41] B. Lobato, L. Suarez, L. Guardia, T. A. Centeno, *Carbon* **2017**, *122*, 434.
[42] B. Cao, H. Liu, B. Xu, Y. Lei, X. Chen, H. Song, *J. Mater. Chem. A* **2016**, *4*, 6472.
[43] P. Adelhelm, P. E. Jongh, *J. Mater. Chem.* **2011**, *21*, 2417.
[44] R. Mogensen, J. Maibach, A. J. Naylor, R. Younesi, *Dalton Trans.* **2018**, *47*, 10752.
[45] Y. Liu, N. Zhang, L. Jiao, J. Chen, *Adv. Mater.* **2015**, *27*, 6702.
[46] L. Wu, X. Hu, J. Qian, F. Pei, F. Wu, R. Mao, X. Ai, H. Yang, Y. Cao, *Energy Environ. Sci.* **2014**, *7*, 323.
[47] V. L. Chevrier, G. Ceder, *J. Electrochem. Soc.* **2011**, *158*, A1011.
[48] Y. Liu, N. Zhang, L. Jiao, Z. Tao, J. Chen, *Adv. Funct. Mater.* **2015**, *25*, 214.
[49] a) Y. Qiao, M. Ma, Y. Liu, S. Li, Z. Lu, H. Yue, H. Dong, Z. Cao, Y. Yin, S. Yang, *J. Mater. Chem. A* **2016**, *4*, 15565; b) J. Xu, M. Wang, N. P. Wickramaratne, M. Jaroniec, S. Dou, L. Dai, *Adv. Mater.* **2015**, *27*, 2042; c) Y. Liu, Z. Gao, *ChemElectroChem* **2017**, *4*, 1.
[50] Y. S. Ye, Y. N. Chen, J. S. Wang, J. Rick, Y. J. Huang, F. C. Chang, B. J. Hwang, *Chem. Mater.* **2012**, *24*, 2987.
[51] H. Xue, J. Zhao, J. Tang, H. Gong, P. He, H. Zhou, Y. Yamauchi, J. He, *Chem. - Eur. J.* **2016**, *22*, 4915.
[52] Z. W. Seh, J. Sun, Y. Sun, Y. Cui, *ACS Cent. Sci.* **2015**, *1*, 449.
[53] Y. Xu, Y. Zhu, Y. Liu, C. Wang, *Adv. Energy Mater.* **2013**, *3*, 128.
[54] a) T. Sasaki, Y. Ukyo, P. Novák, *Nat. Mater.* **2013**, *12*, 569; b) M. Winter, J. O. Besenhard, *Chem. Unserer Zeit* **1999**, *33*, 252.
[55] J. Kim, C. Oh, C. Chae, D. H. Yeom, J. Choi, N. Kim, E. S. Oh, J. K. Lee, *J. Mater. Chem. A* **2015**, *3*, 18684.

6. Conclusion and Outlook

The main aim of this Ph.D. project was to better understand the hardly understood electrochemical co-intercalation mechanism of sodium ions into graphite. For this, selected parameters were varied (the type of salt, solvent, temperature) and a variety of analytical methods were used. Comprehensive information on the reaction was obtained by applying also *in situ* methods. Online electrochemical mass spectrometry (OEMS, in cooperation) was used to evidence undesired side reactions. *In situ* electrochemical dilatometry (ECD) was extensively applied to study the dynamics of the electrode on a macroscopic level. Besides many electrochemical measurements, analyses was also done using methods such as XRD, TEM, and SEM.

The major conclusions from this thesis are as follows:

* The co-intercalation reaction is likely the first example of a SEI-free graphite anode. A SEI-free graphite anode is against the classical concept of using alkali-ion GICs in rechargeable batteries but explains well the excellent kinetics found for this type of reaction. At the same time, this means that the electrolyte solution (NaOTf in diglyme) is likely kinetically stabilized. $NaPF_6$ seems a suitable salt also. In case other salts are used, the situation may be different. Especially the use of NaTFSI as salt leads to a surprisingly bad behavior, i.e. continuous electrolyte decomposition along with a severe growth in electrode thickness are found. Also NaFSI leads to side reactions which explain another literature report showing SEI formation.

* TEM and OEMS measurements of graphite further help to understand that whether or not SEI formation on graphite takes place is heavily affected by the selection of salt. Our studies help to clarify the conflict between the findings from Maibach *et al*. [103] (used NaFSI in 2G) and ours (used NaOTf in 2G) [100].

* The reversibility of the reaction is excellent despite the large volume expansion. *In situ* ECD results showed that the "breathing" of the electrode is in the range of 100 % yet more than 1,000 cycles can be obtained without significant capacity loss.

* ECD, OEMS, XRD, and SEM show that the graphite electrode undergoes an activation cycle which includes exfoliation of larger graphite particles to smaller (yet crystalline) graphite platelets along with the gas release and a severe increase in electrode thickness. After this activation, the stability is excellent. Delamination of the graphite platelets, which would lead to electrode degradation, does not take place.

* Compared to graphite "breathing" level (70-100 %) in SIBs, lithium intercalation into graphite leads to a much smaller change (around 5 %). This represents the difference between intercalation and co-intercalation. On the other hand, the charge storage mechanism in hard carbon is more complex as more mechanisms such as adsorption, pore filling and insertion are contributing. Similarly, a change in the storage mechanism from co-intercalation to insertion can be clearly seen in ball milled graphite which becomes graphene nanoplatelets (GnP). This change directly is visible by dilatometry showing an electrode "breathing" of only 10 %.

* Temperature was found to have a dramatic effect on some co-intercalation reactions. For the first time, crown ether and pentaglyme could be successfully used as solvents for electrochemically driven co-intercalation reactions suggesting that many more compounds exist at elevated temperature. Temperature-dependent measurements also provided thermodynamic information on the entropy change of the reaction. Temperature rise did also affect the co-intercalation for triglyme as a solvent. While the storage is incomplete and ill-defined at room temperature, the capacity increases with temperature yet remains kinetically controlled. Consequently, changing the current density also had an impact on capacity. The peculiar behavior of triglyme for this reaction might be related to the less ideal coordination of the Na-ion.

* On the laboratory level, sodium metal is frequently used as the counter and the reference electrode. The stability of the interface/interphase in contact with different liquid electrolytes revealed that the use of NaTFSI leads to rapid corrosion reactions. This might limit the applicability of electrolyte solutions using this salt in cells containing sodium metal.

* The use of NaTFSI and NaFSI for the co-intercalation reaction leads to side reactions with the results of ion trapping in the electrode as well as in the case of NaTFSI excessive growth of the electrode. XRD measurements showed that the strongest decrease in reflex intensity and hence the fastest lattice degradation occurs for these salts. In contrast, NaOTf and $NaPF_6$ show the least side reaction, i.e. the “cleanest” co-intercalation reaction with negligible side reaction.

* Combining all results from OEMS, XRD, ECD, TEM, and the electrochemical measurements leads to a ranking on the suitability of the tested salts: (best) NaOTf≥$NaPF_6$>$NaClO_4$>NaFSI>>NaTFSI (worst).

The results of this Ph.D. thesis help to unravel some of the questions and contradictions found in sodium ion intercalation in graphite in SIBs, although some problems remain unsolved. Still, there are many major challenges waiting to be solved and fundamental understanding is needed to be advanced in this field of research. Important questions, which are needed to be addressed in the future, can be summarized as follows:

* The electrode thickness change of graphite is discussed in detail only for one binder and random initial thicknesses. What are the correlations between the thickness change and binder type, binder percentage, additives, initial thickness, etc.? As the co-intercalation is dominated thermodynamically and kinetically, can these effects be seen on micro scale?
* In order to make graphite ready for the industry, the loading onto the electrode should be increased further. Will the loading change the cycling performance due to diffusion limitation? What kind of effect can be seen if the electrodes are pressed?
* For industrial purposes, full cell measurements are necessary. Graphite is aimed to be used as an anode. What kind of cathode materials and electrolytes should be used in a full cell? What is the electrochemical performance of a full cell?

- The discussion on SEI continues further. To conclude this conflict, *in situ* TEM measurements might be effective. Also, more studies of XPS are required to understand the surface layers on the graphite after cycling.
- At high temperatures, the cell performances are tested. As the melting temperatures of solvents are so low and diffusion is rapid, can these systems be used at low temperatures below zero degrees?
- In many studies, it is assumed that two diglyme and one sodium ion co-intercalate into graphite. Is it really true? What might be given as proof to specify the number of diglyme used during the reaction? What is the number of molecules co-intercalating into graphite, while using other types of glymes?

All in all, graphite is a really special electrode example for efficient and high rate performance in SIBs. As an assumption, if a special SEI former solvent and/or co-intercalating solvent is found, graphite can show a higher capacity in SIBs. Till that time, the addition of different materials into graphite or carbon types will be helpful to further improve the performance of SIBs.

7. Experimental Methods and Characterization Techniques

7.1. Electrochemical Measurements

Electrode and Electrolyte Preparation:

In an electrochemical cell; anode, cathode, electrolyte, and reference are the main components. As anode, graphite, hard carbon and tin electrodes are taken into consideration. Sodium (BASF SE Corporation) and lithium (Rockwood Lithium, 99.8 %) are used as counter, and reference electrodes. As electrolyte, carbonates and ethers are tested related to the type of measurements.

In the case of graphite (MTI Corp.) electrodes, only 10 % of binder is applied. The rest of the electrode film contains active material which is graphite. For hard carbon or tin electrodes, as extra, 5-10 % carbon black (MTI Corp.) is included to slurry in order to increase the electrical conductivity of the active material. The types of binders (10 %) used in electrode are PVDF (Polyvinylidene fluoride 'EQ-Lib-PVDF', MTI Corp.) or CMC (carboxymethyl cellulose). Slurries are mixed in N-methyl-2- pyrrolidone (Sigma Aldrich) if PVDF is preferred as the binder and in water, if CMC is preferred as the binder. The slurries are casted onto carbon-coated copper or dendritic copper foil (15 μm thick). The average loading of electrodes after drying (12 h at 120 °C) is 2-5 mg cm^{-2}. The average electrode thickness is about 50 μm. Cells for galvanostatic cycling, ECD, and OEMS measurements are prepared in an argon-filled glove box (<0.1 ppm O_2 and H_2O) with electrodes at diameters of 12, 10, and 18 mm, respectively.

Electrolyte contains:

- ✓ *Pre-dried (100°C overnight) salts:*

  Sodium trifluoromethanesulfonate (**NaOTf**, purity > 98.0 %, Sigma Aldrich),
  Sodium hexafluorophosphate (**$NaPF_6$**, purity > 99+%, Alfa Aesar),
  Sodium perchlorate, (**$NaClO_4$**, purity > 97+%, Alfa Aesar),
  Sodium(I) Bis(trifluoromethanesulfonyl)imide (**NaTFSI**, purity 99.5 %, Solvionic),
  Sodium(I) bis(fluorosulfonyl)imide (**NaFSI**, purity 99.7 %, Solvionic),
  Lithium hexafluorophosphate (**$LiPF_6$**, purity 98.0 %, Sigma Aldrich)

- ✓ *Pre-dried (in 4 Å porous molecular sieves, overnight) solvents:*

  - Linear / Symmetric ethers: Ethylene glycol dimethyl ethers. Monoglyme (**1G**), diglyme (**2G**), triglyme (**3G**) and tetraglyme (**4G**) are purchased from Sigma Aldrich and pentaglyme (**5G**) is supplied by Nippon Nyukazai Co., Ltd.

  - Cyclic polyether types: Crown ether 6 (**18-Crown-6**) (Merck KGaA Group) and crown ether 4 (**12-Crown-4**) (Sigma Aldrich) and crown ether 5 (**15-crown-5**) (Alfa Aesar).

  - Carbonates: EC, DMC and PC are purchased from Sigma Aldrich.

Galvanostatic; Charge and discharge measurements

- ✓ Cyclic Voltammetry: It is one of the most versatile electrochemical techniques. The current developing in a cell is measured. And the voltage is in excess of that predicted by the Nernst equation. In this technique, the sweep rate is an important parameter.

✓ For galvanostatic cycling: Under a constant current for both charge and discharge and with potential limitations, cycling is performed. By this method, the total ion storage of the material can be measured. Depending on the current, performance can be tested. By galvanostatic intermittent titration technique (GITT), the equilibrium state of the ion storage mechanism can be understood. Also, diffusion of the ions can be estimated with this method.

Cell assembly details: For two-electrode systems, coin cells (CR2032 Coin Cells by MTI Corp.) and i-shaped Swagelok cells are used. For three-electrode systems, t-shaped Swagelok cells are preferred. Sodium metal (BASF SE Corporation) is used as the counter and reference electrodes. The coin cells were prepared at 1000 PSI by using a crimper (TG-110). Electrochemical measurements were carried out at 25 °C by Biologic BCS battery cycler. The potential window was between 0.01 and 2.5 V versus Na+/Na galvanostatically (at constant current–constant voltage). The C rate was calculated based on the specific charge of graphite stated in literature (Q = 110 mA h g^{-1}, which forms $Na(diglyme)_2C_{20}$)[81]. Therefore, 1 C represents a specific current of i = 110 mA g^{-1} and experiments were done at C/10 and C/3.

7.2. *In situ* Measurements

In situ Electrochemical Dilatometry

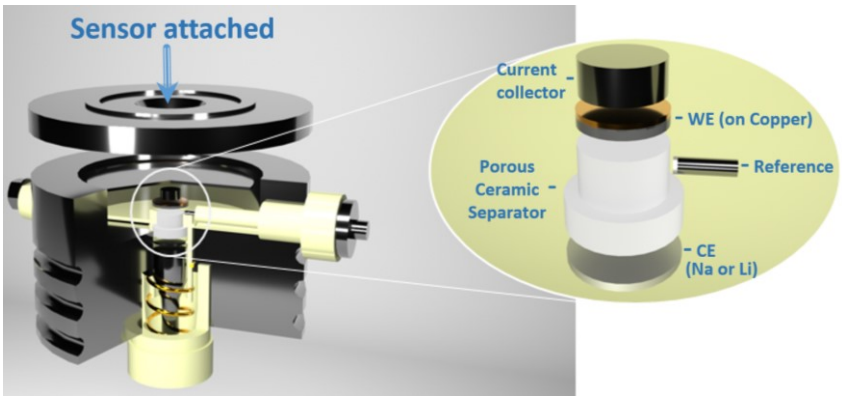

Figure 21. Sketch of the ECD setup measurement principle based on a 3-electrode geometry and an inductive sensor.

In the specific design of ECD-nano cells (by EL-CELL GmbH), the special ceramic porous separator was soaked by 400–500 µL of the electrolyte by pre-evacuating all the gases from the pores which helped the wetting of 10 mm of electrode properly. By the help of spring, the ceramic porous separator is pressed onto a metal frame in z-direction. The glass frit position is therefore fixed and only the dilatation of the working electrode is recorded.

As protection from inner gas pressure, the valve is slightly loosened. In case, the valve is turned more, the gases from the air may leak inside and this causes the sodium and other components to be oxidized and so conductivity loss and cell failure are possible.

In situ DEMS/OEMS

For OEMS, the setup was described elsewhere [111]. The galvanostatic and cyclic voltammetry measurements were also done simultaneously with OEMS. The gas releases of material in a specific cell are monitored during cycling depending on time, current density and temperature.

7.3. Characterization Methods

XRD

Morphological investigations were carried out by using X-ray diffraction (XRD) (D2 PHASER by Bruker). Before XRD measurements, instead of graphite electrode film, powder graphite is preferred. Sodiated/desodiated graphite is placed on Cu metal inside a special XRD sample holder which is airtight.

SEM, TEM, BET

- ✓ *Scanning electron microscopy (SEM)*

This is a high magnification imaging technique. Morphological investigations are carried out by using a SEM (by Phenom ProX) operated at 15 kV accelerating voltage. In order not to make a wrong interpretation, the measurements are performed with and without binder and before and after cycling separately. All the samples are placed onto adhesive carbon films. Before cycling, tests are easier to apply, as air contact does not create any side reaction. The cells after cycling are disassembled in an argon-filled glove box to avoid chemical reaction in the air atmosphere. Samples taken from cells were rinsed with diglyme, as it is the electrolyte solvent and dried at 25 °C under vacuum overnight. To avoid further exfoliation or side reactions of the electrode, the drying temperature was not risen. For cross section measurements, electrodes are cut by a knife. Sodiated samples are air sensitive and transferring time is limited to 60 s at maximum. Electrode thickness is also determined by a digital thickness dial gauge from Käfer Messuhrenfabrik GmbH.

- ✓ *Transmission electron microscopy (TEM)*

Another morphological technique is TEM. TEM is a very powerful technique for high-resolution imaging used in a broad range of scientific fields. TEM provides direct evidence in the irregularities at the atomic level of the material and in the local structure. By this technique, the size, shape, arrangement of atoms in the nanoparticles can be determined. Actually, the working principle of TEM is similar to a light microscope while employing electron instead of light. Once the electron beam is directed onto a sample, the electrons are either scattered or remain unaffected. Therefore, there will be a non-uniform appearance of electrons on the surface. This appearance can be converted into an image. By this technique, the diffraction pattern of the sample can be gained and the discussion about microstructure, defects, and crystallography can be done. TEM is performed by a FEI Tecnai G2 FEG operating at 200 kV. The sample material is deposited on a copper grid with a Lacey carbon support film and directly transferred to the vacuum of the TEM.

- ✓ *Brunauer–Emmett–Teller (BET)*

An Autosorb iQ3 machine from Quantachrome Corporation is used for nitrogen physisorption experiments. Air contact during sample transfer is minimized by special sample holders. The sample holders for electrochemically treated samples are prepared in a glovebox by using air-tight cap. The measurements are performed with and without these special caps.

8. Appendix

8.1. Supporting information on Publication 1

Supporting Information

for *Adv. Energy Mater.,* DOI: 10.1002/aenm.201702724

Graphite as Cointercalation Electrode for Sodium-Ion Batteries: Electrode Dynamics and the Missing Solid Electrolyte Interphase (SEI)

*Mustafa Goktas, Christoph Bolli, Erik J. Berg, Petr Novák, Kilian Pollok, Falko Langenhorst, Maximilian v. Roeder, Olena Lenchuk, Doreen Mollenhauer, and Philipp Adelhelm**

Supporting Information on

Graphite as co-intercalation electrode for sodium-ion batteries: Electrode dynamics and the missing solid electrolyte interphase (SEI)

Mustafa GOKTAS[a,b], Christoph BOLLI[c], Erik J. BERG[c], Petr NOVÁK[c], Kilian POLLOK[d], Falko LANGENHORST[d], Maximilian v. ROEDER[e], Olena LENCHUK[e], Doreen MOLLENHAUER[e], and Philipp ADELHELM[a,b*]

[a] Friedrich Schiller University Jena, Institute of Technical Chemistry and Environmental Chemistry, Philosophenweg 7a, D-07743 Jena, Germany
[b] Center for Energy and Environmental Chemistry (CEEC Jena), Philosophenweg 7a, D-07743 Jena, Germany
[c] Paul Scherrer Institute, Electrochemistry Laboratory, CH-5232 Villigen PSI, Switzerland
[d] Friedrich Schiller University Jena, Institute of Geosciences, Carl-Zeiss-Promenade 10, 07745 Jena
[e] Justus Liebig University Giessen, Institute of Physical Chemistry, Heinrich-Buff-Ring 17, D-35392 Giessen, Germany

*correspondence: philipp.adelhelm@uni-jena.de

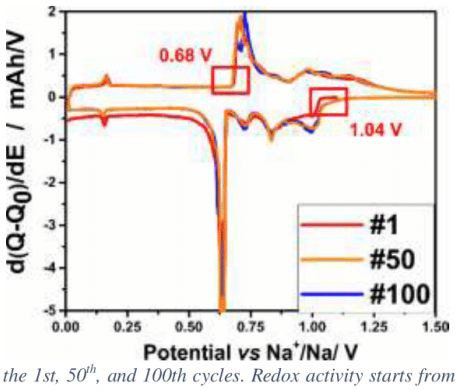

S 1. Differential charge plots for the 1st, 50th, and 100th cycles. Redox activity starts from 1.04 V for reduction (sodiation). Until 0.6 V several small deeps show the stages of sodium co-intercalation by small plateaus in galvanostatic plots. At around 0.6 V, the biggest deep shows the biggest plateau which is about one third of the total charge.

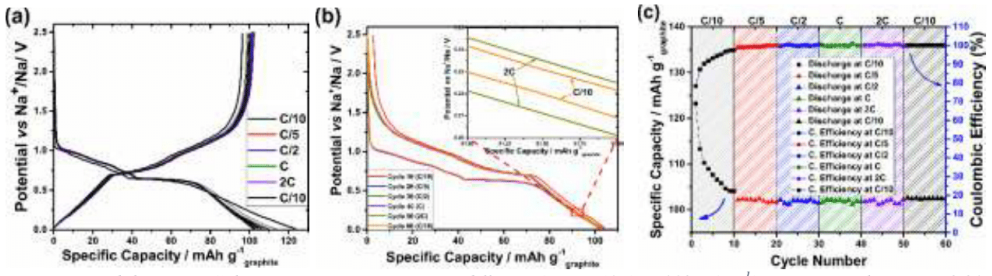

S 2.Rate capability tests: Galvanostatic measurements at different C rates (1 C = 110 mA g^{-1}) in a potential range = 0.01-2.50 V vs Na^+/Na. The C-rate was changed every 10 cycles. (a) and (b) show the same data, i.e. potential profiles at different currents. # indicates the cycle number. The combined overpotentials can be discerned from (b). (c) shows the specific charge during the rate test.

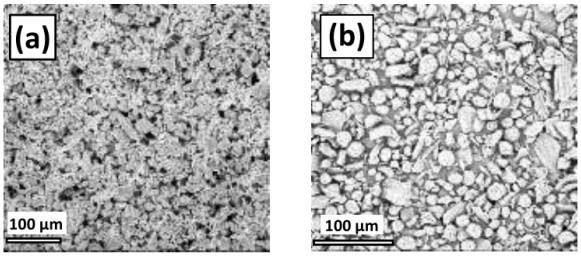

S 3. SEM pictures of (a) the pristine graphite electrode containing 10 % PVDF, (b) graphite powder.

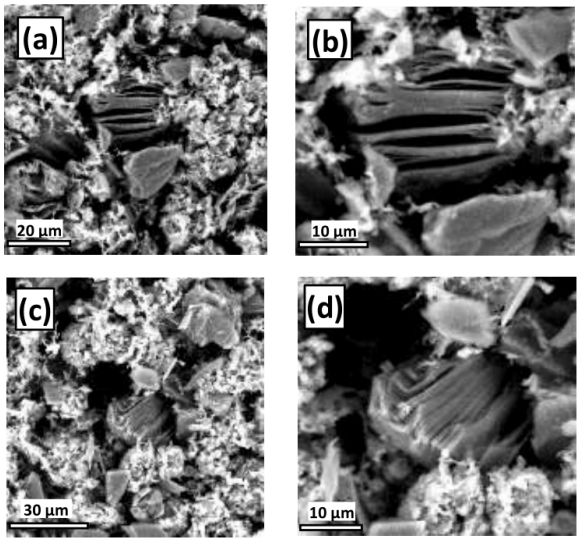

S 4. SEM pictures of graphite electrode (with 10% PVDF) after 2nd reduction (sodiation) at C/10 (1 C = 110 mA g^{-1}). We note that the intercalated graphite is highly reactive and we found it to readily react upon air exposure. Characterizing the intercalated graphite post mortem is therefore challenging. Air exposure time was therefore minimized during sample transfer. The sample shown in the SEM image was exposed to air for 60 seconds at maximum.

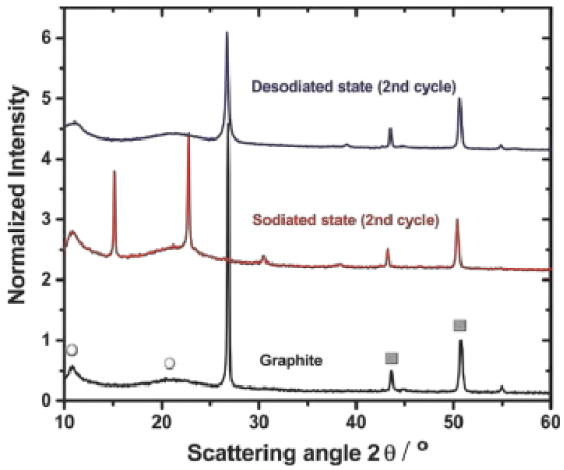

S 5. Diffraction patterns of graphite electrodes before sodiation (black), after sodiation (red) and after desodiation (blue). Circles indicate background noise from the air-tight sample holder, squares indicate reflexes from the copper current collector. The strong reflex at around 2θ = 26 ° indicates the graphene layer spacing of graphite (d= 3.35 Å). The diffraction pattern of the sodiated sample corresponds to a Stage 1 t-GIC. [1, 2]

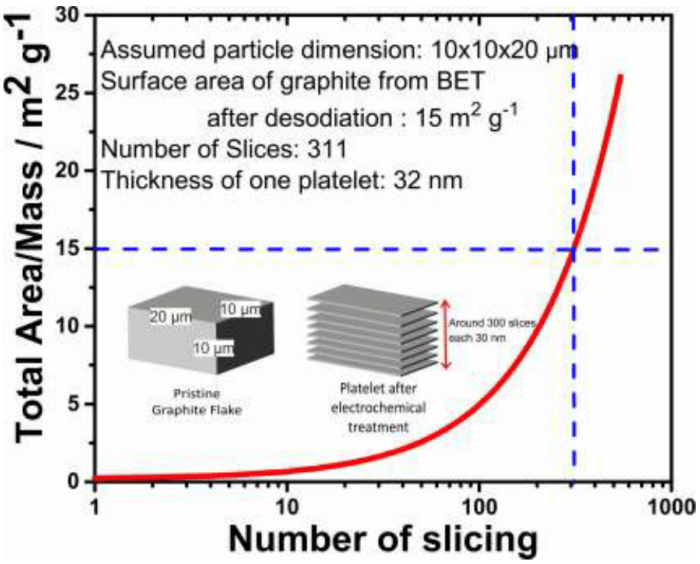

S 6. Estimate of the size of the graphite platelets that form as a result of particle exfoliation. The dimensions of the starting graphite particle were defined as 10x10x20 µm. The surface area of 15 m^2/g was taken from the BET measurements. Although this is calculation is a rough estimate and only provides an average value, it shows that the results agree reasonably well with the SEM images showing the exfoliated platelets. Crystalline platelets of this size can be also detected by XRD. A crystal size of about 30 – 50 nm can be estimated applying the Scherrer equation to the main reflex (002) of the XRD pattern shown in Figure S5.

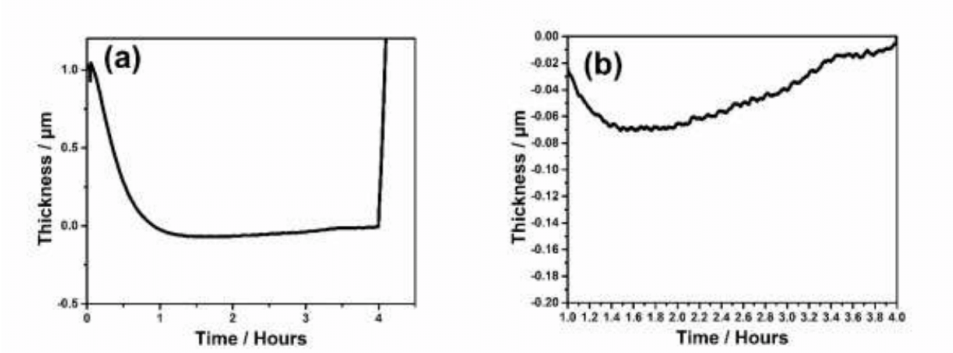

S 7. Dilatometer signal of the ECD over 4 hours. It can be seen that the signal stabilizes after one hour. However, a minor drift in data can occur over the 500 hours experiment. In a worst case scenario (taking a shift of 0.023 µm per hour as calculated from the magnified illustration on the right), the signal would drift by a maximum value of 11.5 µm. In other test, we found the drift to be smaller. Anyway, the potential impact of the drift is still much lower than the total change in Δt over 500 hours.

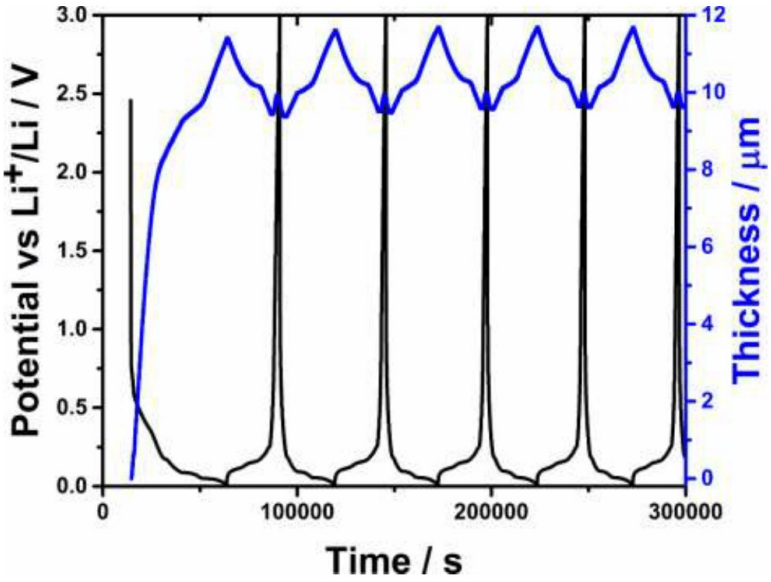

S 8 In situ ECD measurements on lithium intercalation into graphite from conventional carbonate based electrolytes 1M $LiPF_6$ in EC:DMC (Sigma Aldrich). Five cycles at current of C/10 (1C =372 mA g^{-1}) are shown. The initial thickness of the electrode is about l_0=50 µm (without current collector). The behavior is well in line with previous reports [3,4,5]. The differences to the sodium co-intercalation reaction are clearly visible: (a) Intercalation of Li^+ into graphite leads to a much smaller electrode expansion, (b) the correlation between electrode expansion and storage capacity is much more linear.

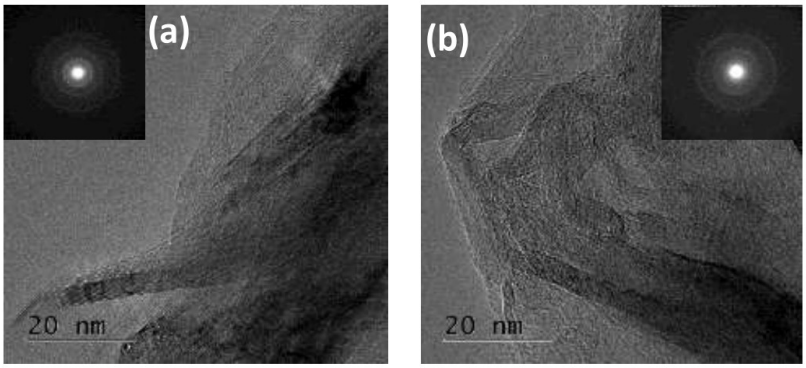

S 9. TEM images of the graphite particles (a) before and (b) after two cycles

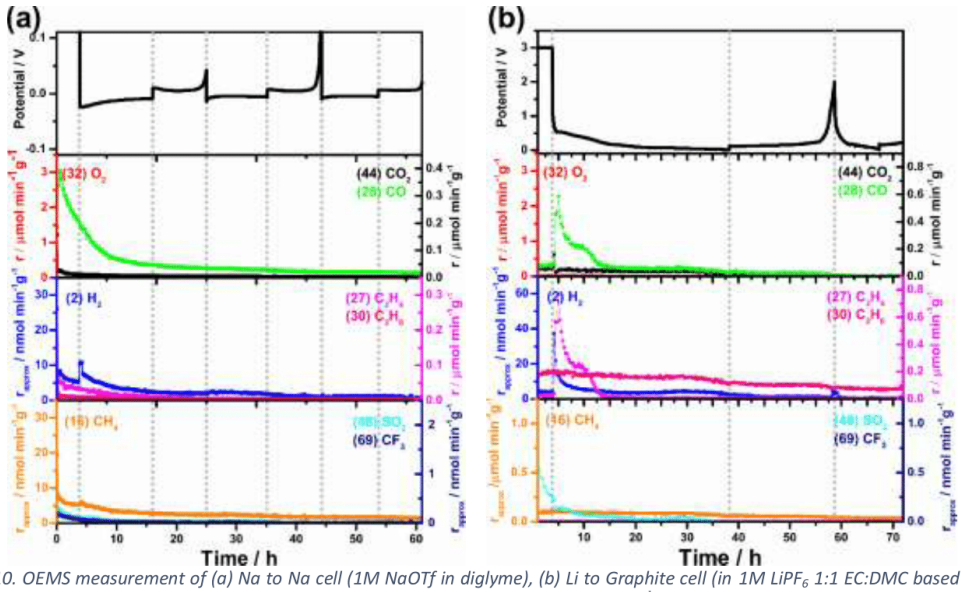

S 10. OEMS measurement of (a) Na to Na cell (1M NaOTf in diglyme), (b) Li to Graphite cell (in 1M $LiPF_6$ 1:1 EC:DMC based electrolyte). All these measurements are done at C/10 (1 C corresponds to 110 mA g^{-1})

Experimental Details of OEMS

The OEMS setup was described elsewhere [6] and operates with a quadrupole mass spectrometer (QMS 200, Pfeiffer) for partial pressure measurements, a pressure transducer (PAA-33X, Keller Druck AG) for total cell pressure, temperature, and internal volume determination, stainless steel gas pipes and Swagelok fittings (3 mm compression tube fittings, Swagelok, OH, US) to connect the OEMS cell, a set of solenoid valves (2-way magnetic valve, Series 99, silver-plated nickel seal, Parker) and a scroll pump (nXDS15i, EDWARDS GmbH) for efficient flushing. The magnetic valves are electronically controlled with a Solid State Relay Module (NI 9485 measurement System, National Instruments) connected to a computer with a LabView Software (NI Labview 2013, National Instruments). For partial pressure and gas evolution rate analysis 1.3 mL of gas are extracted from the headspace (~ 4 mL) of the cell and replaced by pure Ar (quality 5.0). Calibration gas bottles were utilized to relate the MS ion-current signals at m/z = 2, 27, 32 and 44 to known concentrations of H_2, C_2H_4, O_2 and CO_2 (1000 ppm of C_2H_4, O_2 and CO_2 in Ar, respectively, and 1% of H_2 in Ar), before and after the measurement.

The ion currents for fragments m/z = 16 (CH_4), 28 (CO), 30 (C_2H_6), 48 (SO_2), and 69 (CF_3) were recorded without calibration and converted into approximate gas evolution rates that allow direct semi-quantitative comparison between the evolution of these fragments from one data set to another. The indicated m/z channels were deliberately selected for monitoring the described molecular species because they provided the strongest and least obscured signals.

References

1. L. Seidl, N. Bucher, E. Chu, S. Hartung, S. Martens, O. Schneider and U. Stimming, *Energy Environ. Sci.*, 2017, DOI: 10.1039/c7ee00546f.

2. H. Kim, J. Hong, G. Yoon, H. Kim, K.-Y. Park, M.-S. Park, W.-S. Yoon and K. Kang, *Energy Environ. Sci.*, 2015, **8**, 2963-2969.
3. J. L. Gómez-Cámer, C. Bünzli, M. M. Hantel, T. Poux and P. Novák, *Carbon*, 2016, **105**, 42-51.
4. M. Winter, G. H. Wrodnigg, J. O. Besenhard, W. Biberacher and P. Novák, *Journal of The Electrochemical Society*, 2000, **147**, 2427-2431.
5. M. Hahn, H. Buqa, P. W. Ruch, D. Goers, M. E. Spahr, J. Ufheil, P. Novák and R. Kötz, *Electrochemical and Solid-State Letters*, 2008, **11**, A151.
6. M. He, L. Boulet-Roblin, P. Borel, C. Tessier, P. Novák, C. Villevieille and E. J. Berg, *Journal of The Electrochemical Society*, 2015, **163**, A83-A89.

8.2. Supporting information on Publication 2

Supporting Information

Temperature Induced Activation of Graphite Co-intercalation Reactions for Glymes and Crown Ethers in Sodium-ion Batteries

Mustafa GOKTAS[a,b], Baris AKDUMAN[c], Peihua HUANG[a,b], Andrea BALDUCCI[a,b], Philipp ADELHELM[a,b*]

[a] Friedrich Schiller University Jena, Institute of Technical Chemistry and Environmental Chemistry, Philosophenweg 7a, D-07743 Jena, Germany
[b] Center for Energy and Environmental Chemistry (CEEC Jena), Philosophenweg 7a, D-07743 Jena, Germany
[c] Department of Metallurgical and Materials Engineering, Middle East Technical University, 06800 Ankara, Turkey
* Correspondence: philipp.adelhelm@uni-jena.de

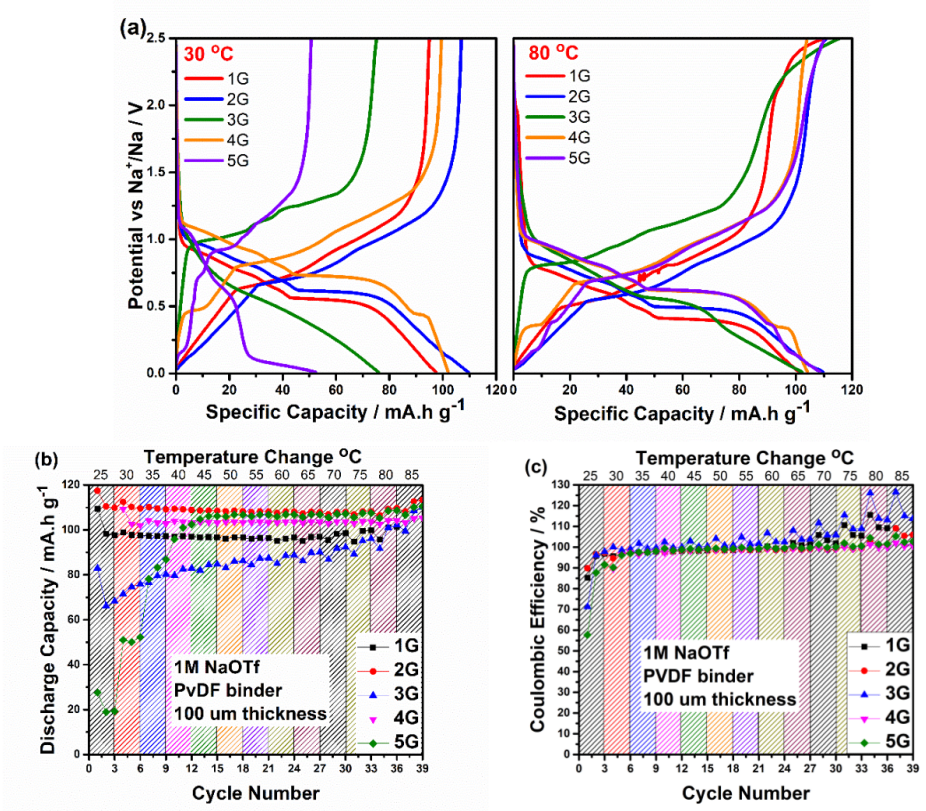

S 1. (a) The galvanostatic sodiation (reduction) and de-sodiation (oxidation) potential profile of glyme series at different temperatures, at 1C= 110 mA g^{-1}. (b) Sodiation specific capacity at different temperatures and at 1C (c) coulombic efficiency profiles at different temperatures and at 1C.

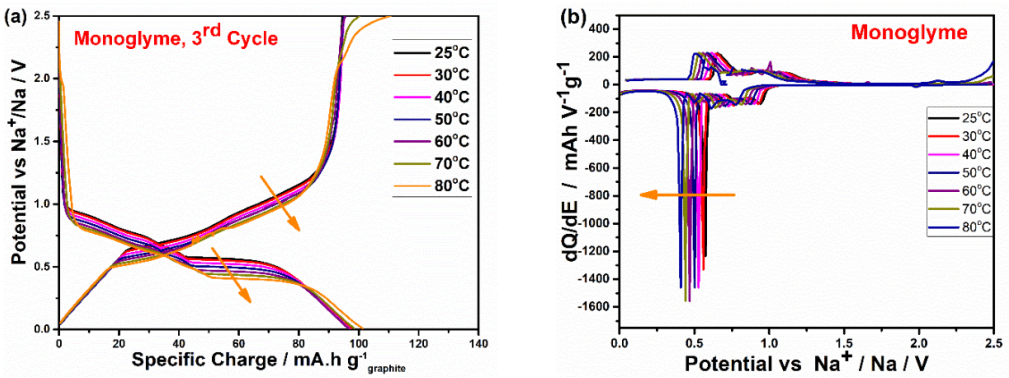

S 2. (a) Galvanostatic discharge/charge profiles for monoglyme at different temperatures. (b) Differential plots obtained from (a).

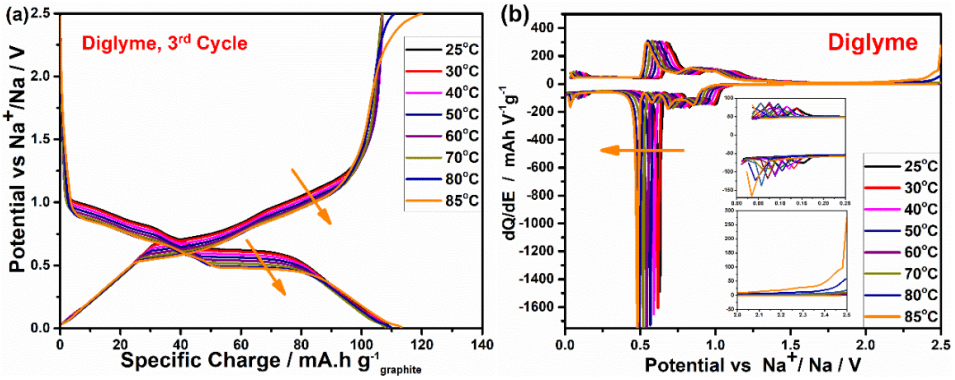

S 3. (a) Galvanostatic discharge/charge profiles for diglyme at different temperatures. (b) Differential plots obtained from (a).

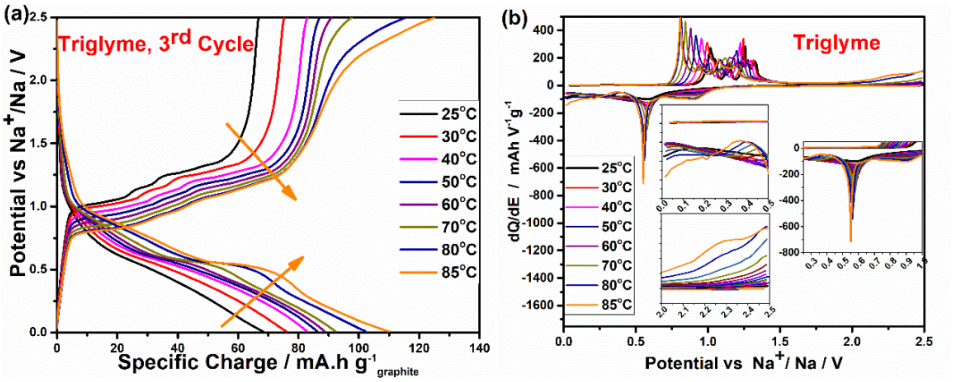

S 4. (a) Galvanostatic discharge/charge profiles for triglyme at different temperatures. (b) Differential plots obtained from (a).

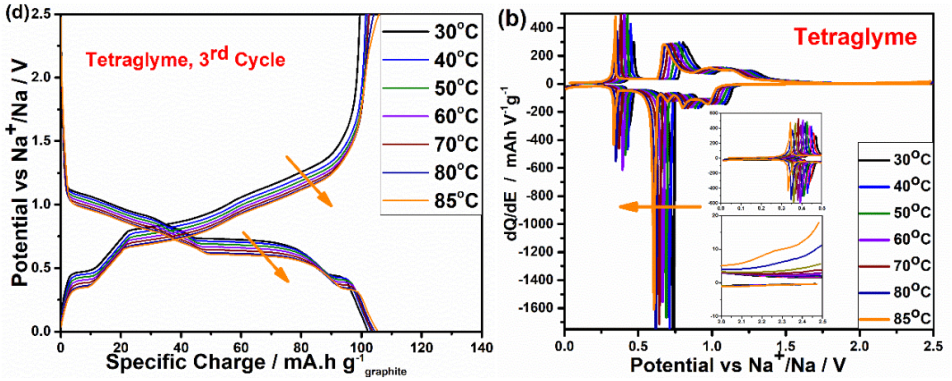

S 5. (a) Galvanostatic discharge/charge profiles for tetraglyme at different temperatures. (b) Differential plots obtained from (a).

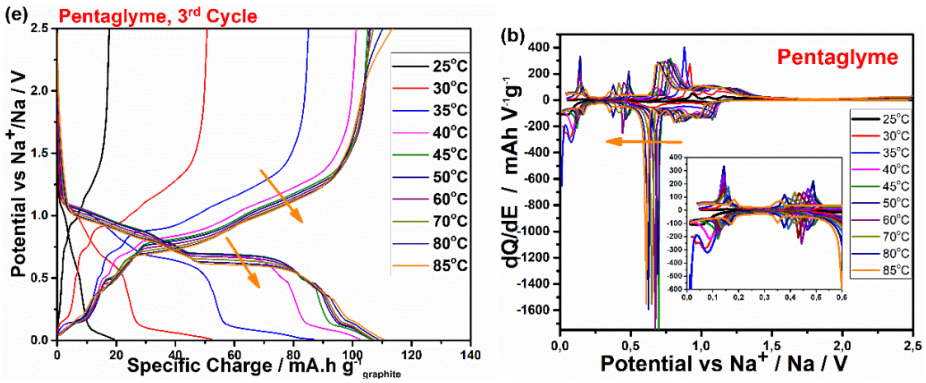

S 6. (a) Galvanostatic discharge/charge profiles for pentaglyme at different temperatures. (b) Differential plots obtained from (a).

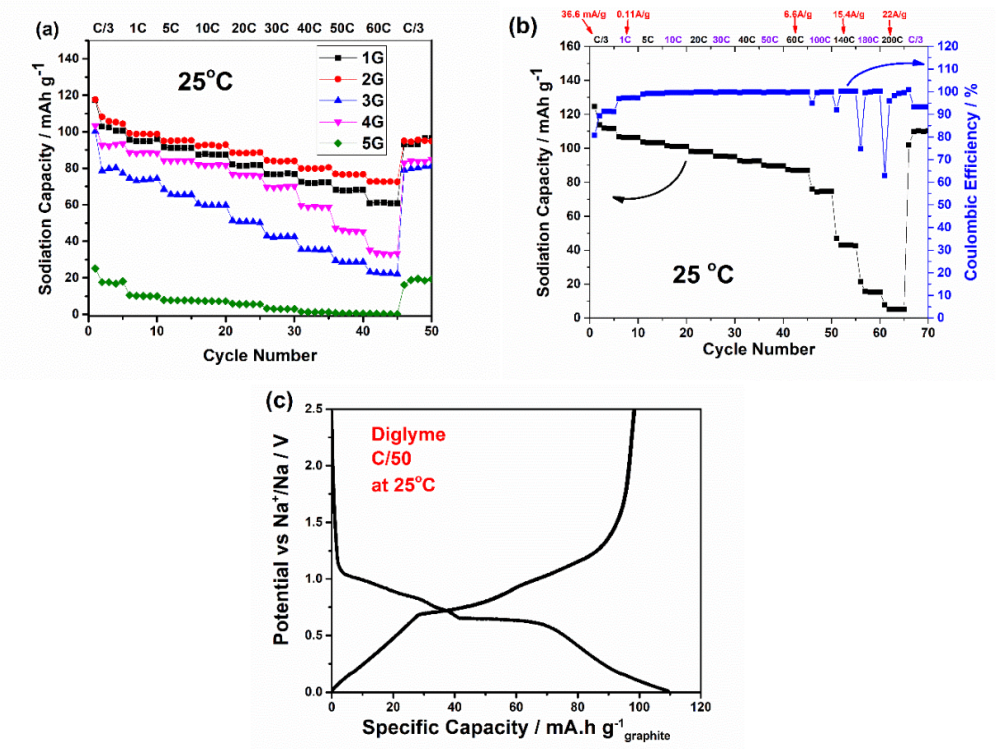

S 7. (a) Rate Capability tests (1C = 110 mA g^{-1}) for different glymes at 25°C (b) Rate Capability tests (1C = 110 mA g-1) for diglyme at 25°C, (c)Potential profile for diglyme at 25 °C at C/50 (2nd cycle). Parasitic capacity at low and high voltage is not observed.

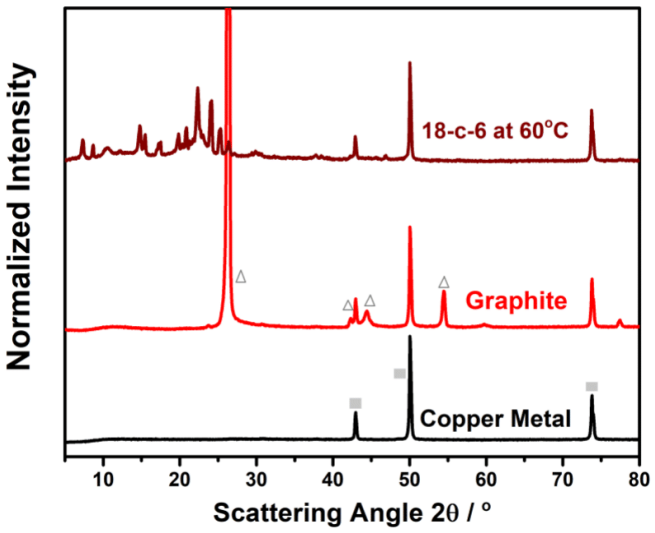

S 8. Diffraction patterns (recorded at room temperature) for copper metal (current collector), graphite powder and after electrochemical sodiation of graphite at 60 °C using 18-c-6 as solvent. Squares indicate reflexes from the copper metal under the sample, triangles indicate the minor reflexes from graphite. The strong reflex at around 2θ = 26 ° is due to the graphene interlayer spacing (d= 3.35 Å).

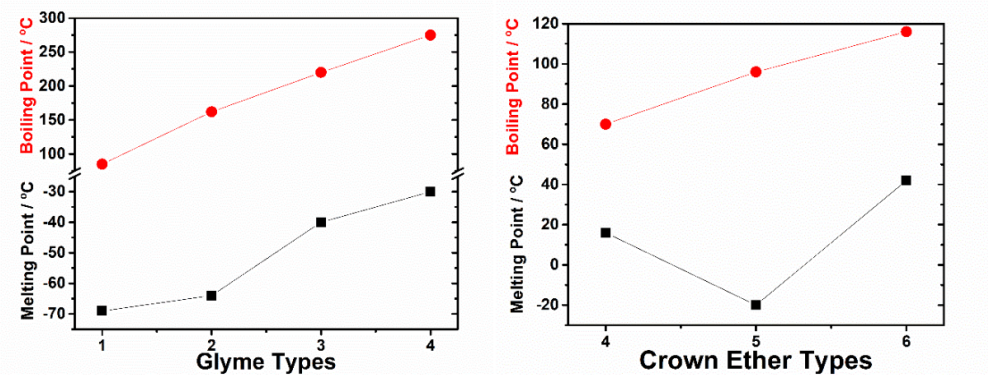

S 9. Melting and boiling point of glymes and crown ethers [1-2]

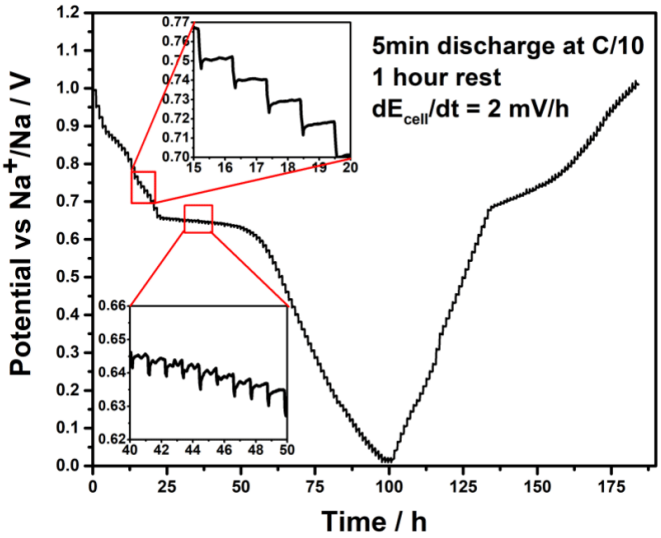

S 10. Results using Galvanostatic Intermittent Titration Technique (GITT) using a 2G based electrolyte. The data shows that the electrode reaction is close to equilibrium at a current rate of C/10 (11 mA g^{-1}).

References

(1) Tang, S.; Zhao, H., Glymes as Versatile Solvents for Chemical Reactions and Processes: From the Laboratory to Industry. *R. Soc. Chem. Adv.* **2014**, *4*, 11251-11287.

(2) Tobishima, S.; Morimoto, H.; Aoki, M.; Saito, Y.; Inose, T.; Fukumoto, T.; Kuryu, T., Glyme-Based Nonaqueous Electrolytes for Rechargeable Lithium Cells. *Electrochim. Acta* **2004**, *49*, 979-987.

8.3. Supporting information on Submitted Manuscript 1

Supporting Information

Stable and instable diglyme-based electrolytes for batteries with sodium or graphite as electrode

Mustafa GOKTAS[a,b], Christoph BOLLI[c*], Johannes BUCHHEIM[a,b], Erik J. BERG[d], Petr NOVÁK[c], Francisco BONILLA[e], Teófilo ROJO[e], Shinichi KOMABA[f], Kei KUBOTA[f] and Philipp ADELHELM[a,b*]

[a] Friedrich Schiller University Jena, Institute of Technical Chemistry and Environmental Chemistry, Philosophenweg 7a, D-07743 Jena, Germany
[b] Center for Energy and Environmental Chemistry (CEEC Jena), Philosophenweg 7a, D-07743 Jena, Germany
[c] Paul Scherrer Institute, Electrochemistry Laboratory, CH-5232 Villigen PSI, Switzerland
[d] Department of Chemistry, Ångström Laboratory, Uppsala University, Box 538, SE-751 21, Uppsala, Sweden
[e] CIC Energigune Parque Tecnológico C/Albert Einstein, 48, 01510 Vitoria-Gasteiz (Álava) Spain
[f] Department of Applied Chemistry, Tokyo University of Science, 1-3 Kagurazaka, Shinjuku, Tokyo 162-8061, Japan
*correspondence: Philipp.Adelhelm@uni-jena.de, Christoph.Bolli@psi.ch

Table S1. Overview on different experimental studies on solvent co-intercalations with graphite, their used electrolyte solutions and main findings

Cell type	Salt and Solvent	Cycle Number	Comments / Main findings	Ref.
Na/Graphite	NaOTf or LiOTf in Diglyme, $NaPF_6$ or $LiPF_6$ in EC/DMC	1000 cycles	Jache *et al.*; The first time, in 2014; Graphite can have 110 mAh g-1 of capacity	[1]
Na/Graphite	NaOTf or LiOTf in Monoglyme, Diglyme, Triglyme, Tetraglyme, Bis(methoxypropyl)ether (DPGDME), Bis(2-butoxyethyl)ether (Butyl-2G), 1,5-Dimethoxy-pentane (1,5-DMP), tetrahydrofuran (THF). $NaPF_6$ or $LiPF_6$ in EC/DMC.	50 cycles	Jache *et al.*; Some electrochemical properties such as capacity, retention, efficiency and over potential are compared. It is found that diglyme is electrochemically performing well within glyme series.	[2]
Na/Graphite	$NaClO_4$ in Monoglyme, Diglyme, Triglyme, Tetraglyme. $NaClO_4$ in EC/DMC	20 cycles	Seidl *et al*; Crystal structure changes and phase formations of graphite during cycling with glyme series. The crystal structure change of graphite depends on the type of glymes used during sodiation. But overpotential is slightly increasing during these cycles.	[3]
Na/Graphite	$NaPF_6$ in Monoglyme, Diglyme and Tetraglyme	200 cycles	Kim *et al*. A comparative study of several glymes by experimental and computational methods in order to understand the intercalation mechanisms. There are two layers of ions together with glymes going in between graphene layers while forming stage 1 compound.	[4]
Na/Graphite	NaOTf in Monoglyme, Diglyme, Triglyme, Tetraglyme, Pentaglyme, Crown Ether 4, Crown Ether 5, Crown Ether 6.	50 cycles	Goktas *et al*. Electrochemical properties of glymes from monoglyme to pentaglyme are examined. Kinetic and thermodynamic properties of the reaction are discussed as a function of temperature. The first time, crown ethers are used for electrochemical co-intercalation of sodium ions into graphite by giving 75 mAh g^{-1} capacity.	[5]
Na/Graphite	$NaPF_6$ in Diglyme	8000 cycles	Cohn *et al*. The superior performances of graphite in SIBs is tried to be underlined. High rate capabilities up to 30 A g^{-1} and high cycle life of 8000 cycles are gained.	[6]
Na/Graphite	$NaCF_3SO_3$ in Tetraglyme	6000 cycles	Zhu *et al.* A study was done by using $NaCF_3SO_3$ in tetraglyme and they reached up to 10 A g^{-1} for 6000 cycles. For the first time, graphite in used in full cell in SIBs	[7]
Na/Graphite	$NaClO_4$ in Tetraglyme, EC/DMC, EC/DEC	500 cycles for half cell, 100 cycles for full cell.	Hasa *et al*. Trial of graphite with a cathode to make a full cell. High rate as high as 10C is applied to the full cell.	[8]
Na/Graphite	Sodium−diglyme-d_{14}−GIC was prepared by a solution-phase reaction.	-	Gotoh *et al.* NMR study to prove t-GICs. The formation of t-GICs with a stoichiometry $C_{22-26}(diglyme)_{1.8-2.2}Na_{1.0}$ is proven by NMR studies.	[9]
Na/Graphite	-	-	Jung *et al*. Study for modelling Due to co-intercalation mechanism, diglyme can easily create Van Der Waals interactions and diffuses fast	[10]

			through the graphite lattice. Diffusion is faster compared to the case of lithium.	
Na/Graphite	$NaPF_6$ in tetraglyme, diglyme, monoglyme, THF, DOL, DMC, DEC, EC, PC.	-	Yoon *et al*. The computational studies are performed for the electrolytes of $NaPF_6$ salt in carbonate solvents such as EC/DMC, DMC, DEC, PC and ethers such as THF, DOL, DME, DEGDME, TEGDME. And they concluded that for the reversible co-intercalation the high solvation energy of Na and chemical stability of Na-solvent complexes are important parameters.	[11]
Na, Li, K / Graphite	MCF_3SO_3 M= Na, Li or K in tetraglyme	60 cycles	Kim *et al.* Comparisons of Li, K and Na are done by using tetraglyme based electrolyte. Current density is applied up to 3 A g^{-1}.	[12]
Na/Graphite	NaOTf in diglyme	100 cycles	Goktas et al. Co-intercalation mechanism is explained by testing the changes in electrode thickness by the method of in situ dilatometry. Graphite is likely the first example of SEI-free graphite anode material in SIBs	[13]
Na/Graphite	$NaPF_6$, $NaClO_4$ and NaOTf in diglyme. $NaPF_6$ in EC/DEC, DMC, THF LiPF6 in TEGDME, EC/DMC	2500 cycles	Kim et al. A discussion is made between various salts such as $NaPF_6$, $NaClO_4$ and NaOTf in diglyme and there was no clear significant effect of anions on electrochemical reactions. 10 Ag^{-1} is applied.	[14]
Na/Ordered Graphite	$NaPF_6$ and NaOTf in diglyme $NaPF_6$ in EC/DEC	400 cycles	Cabello *et al.* Coke is converted into highly ordered graphitic structure. The capacity changes and intercalation mechanism changes are discussed. There is not much difference between $NaPF_6$ and NaOTf in electrochemical properties. Except, $NaPF_6$ has slight higher plateau potential than NaOTf. Full cell tests are also applied.	[15]
Na/Graphite	NaI and NaOTf in diglyme	1000 cycles	Jache *et al.* Comparisons are done between the performances of NaI and NaOTf, no significant difference was found.	[1]
Na/Graphite	NaFSI in tetraglyme	Over 20 cycles	Maibach *et al.* It is proven by XPS (X-ray photoelectron spectroscopy) method that electrolyte of NaFSI in diglyme creates partial SEI formation on the surface of graphite electrode [16]. It is clear that there is an excess sodiation capacity and large irreversible capacity during the cycles and plateau potential shifts by cycle. Also, the retention during cycling is not high which is not expected.	[16]
Na/Graphite	$NaClO_4$ in diglyme LiTFSI in diglyme	Several cycles	Leifer et al. Atomic proximity of Na diglyme and Li diglyme complexes to the graphene planes are evidenced. Li-diglyme complex creates a tighter interaction with graphene sheets than Na-diglyme complex. Motion of complexes in graphite complex is discussed. The mobility of the complexes is linked to their interaction with the graphite lattice.	[17]

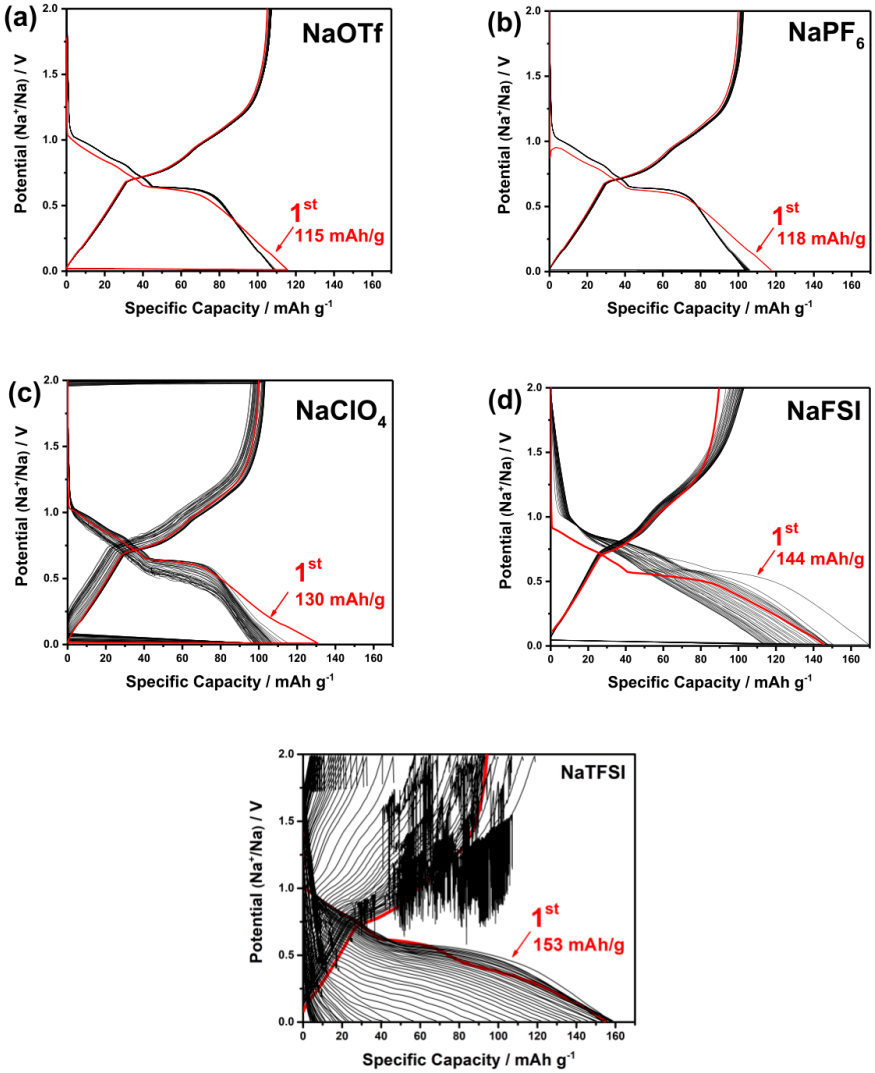

S 1. Galvanostatic cyclings for of graphite half-cells for 100 cycles for different salt systems which are NaOTf, NaPF6, NaClO4, NaTFSI and NaFSI.

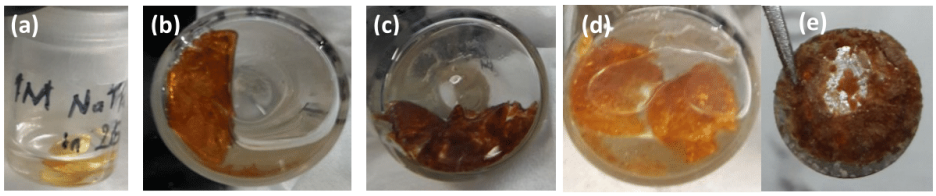

S 2. Time dependent measurement for sodium metal in 1M NaTFSI electrolyte in diglyme (a) Day 3, (b) Week 1, (c) Month 1 and (d) sodium metal in 1M LiTFSI electrolyte in digylme after 7 days. Also, (e) electrochemically cycled sodium metal from coin cell.

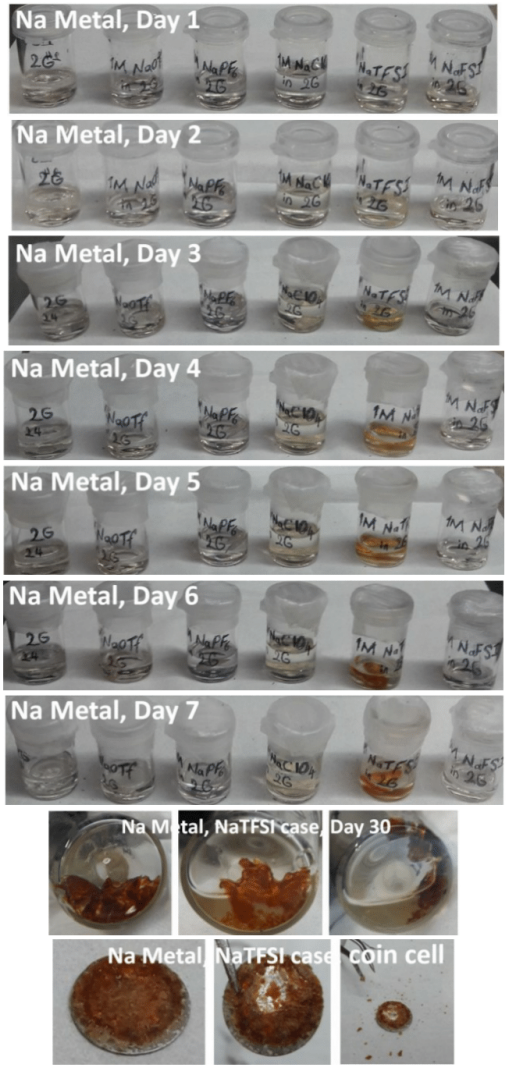

S 3. Time dependent measurement for sodium metal in 1M electrolytes in diglyme. Day 1-7 and day 30, Sodium metal after cycling in coin cell.

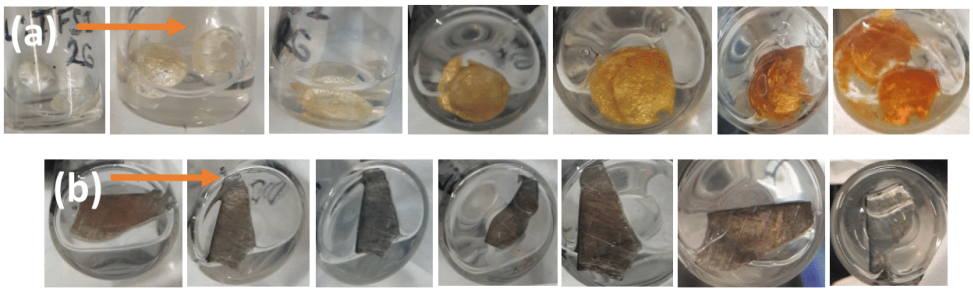

S 4. Time dependent measurement in 1M LiTFSI in diglyme for (a) sodium metal and (b) lithium metal from day 1 to 7

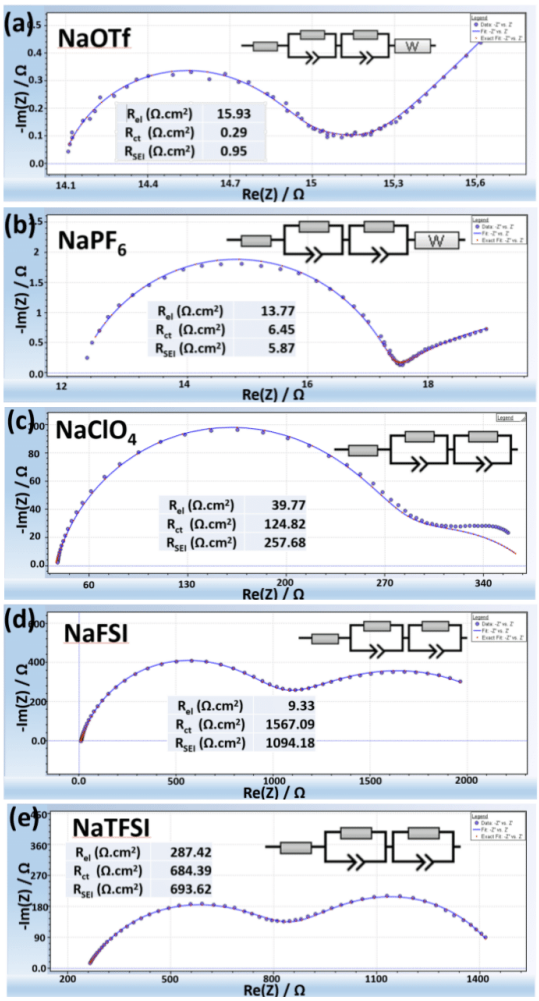

S 5. Analysis of Impedance measurements for Na | Na symmetrical cell at OCV for different salts after 48 hours. Resistance values of electrolyte, charge transfer and SEI layer for each electrolyte containing different salts in the frequency range of 10 mHz to 1 MHz.

Table S 2. Resistance and capacitance values derived from constant phase element for NaOTf and NaTFSI cases.

Salt Types	R_{SEI} (Ω.cm²)	CPE_{SEI}(mF)	R_{ct} (Ω.cm²)	CPE_{dl}(mF)
NaOTf	0.95	0.5182	0.29	181.2
NaTFSI	694	0.407	684	0.0113

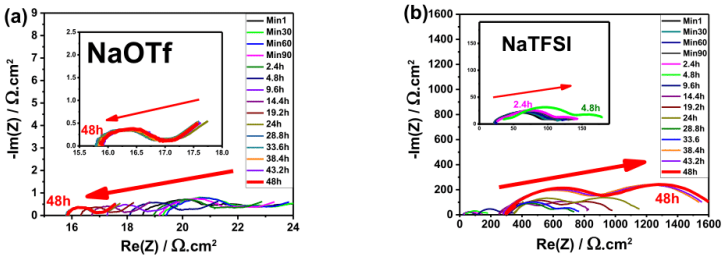

S 6. Time dependent impedance measurements of (a) 1M NaOTf) in 2G and (b) 1M NaTFSI in 2G in Na | Na symmetrical cell. SEI layer is stabilized at 48 hours.

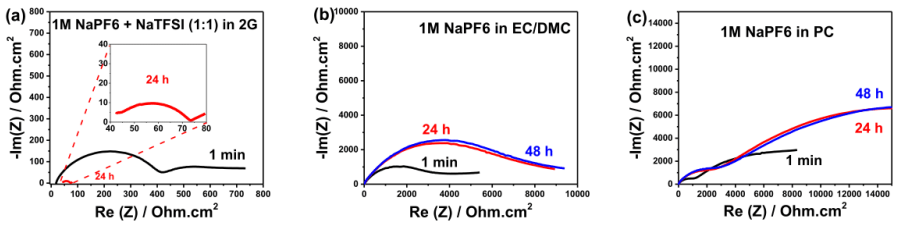

S 7. Time dependent impedance measurements of (a) 1M $NaPF_6$ + NaTFSI (1:1) in 2G and (b) 1M $NaPF_6$ in EC/DMC (c) 1M $NaPF_6$ in PC in Na | Na symmetrical cell. SEI layer is stabilized after 24 to 48 hours.

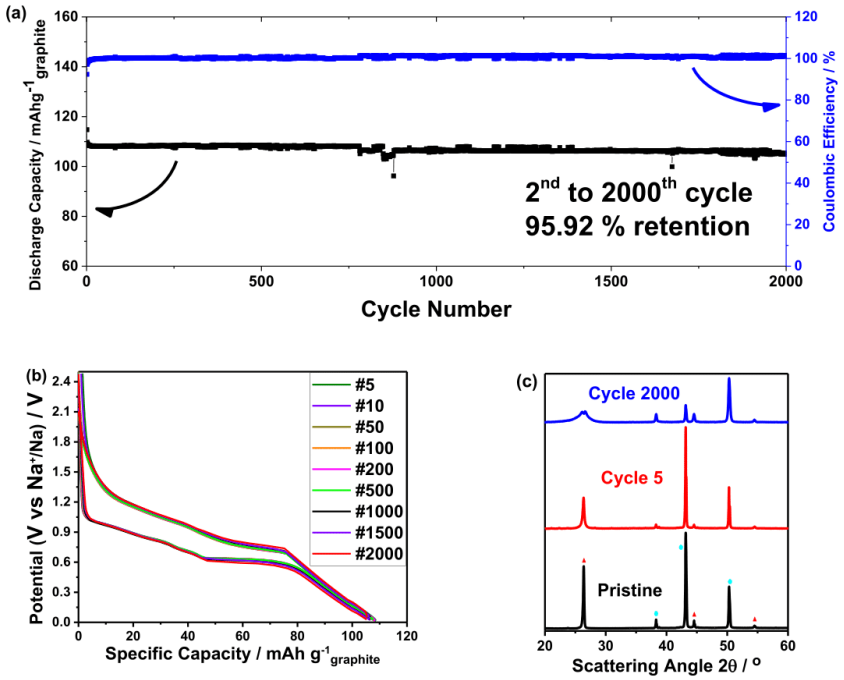

S 8. a) Cycle life of graphite-sodium cells within 1M NaOTf in 2G, b) Voltage profiles from initial cycles to 2,000th cycle. c) XRD Diffraction patterns of powder graphite and after the 5th and 2000th cycle (desodiated state) d. Rounds indicate reflexes from the copper current collector, triangles indicate reflexes from the powder graphite. The strong reflex at around 2θ = 26 ° indicates the graphene layer spacing of graphite (d= 3.35 Å). The diffraction pattern of the sodiated sample corresponds to a Stage 1 t-GIC

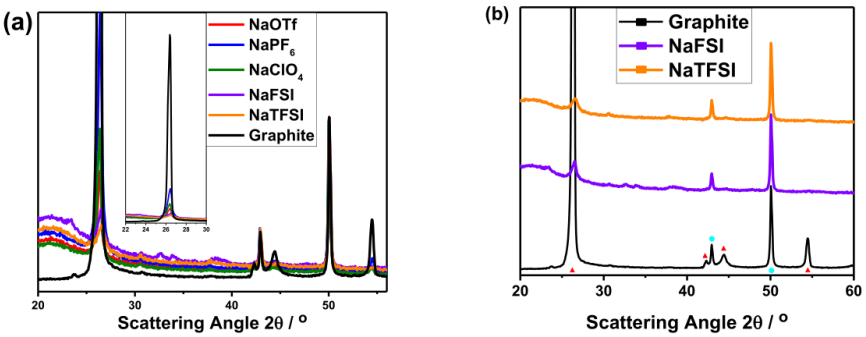

S 9. Diffraction patterns of sodium metal after resting them in different electrolytes for 3 weeks. Squares indicate reflexes from the sodium metal which are at reflexes at 2θ = 29.44, 42.12, 52.22, 61.09, 69.25°. Rounds indicate reflexes from the copper metal under the sample. Downward and upward triangles represent NaF and Na_2O. Also star shows NaCl.

Table S 3. Results from XRD measurements obtained for the graphite samples at the end of the 5th cycle (desodiated state, see Figure 5) using diglyme-based electrolytes with different salts. L_c was estimated using the Scherrer equation (Scherrer constant: 0.94 and λ (Å):1.54178).

Sample	*d*-spacing [Å]	2*θ* position [°]	FWHM	L_c / nm
$NaClO_4$	3.3735	26.42	0.4997	36
NaFSI	3.3177	26.48	0.6211	29
NaOTf	3.4988	26.39	0.4953	36
$NaPF_6$	3.3998	26.43	0.5358	33
NaTFSI	3.3507	26.54	0.7864	24

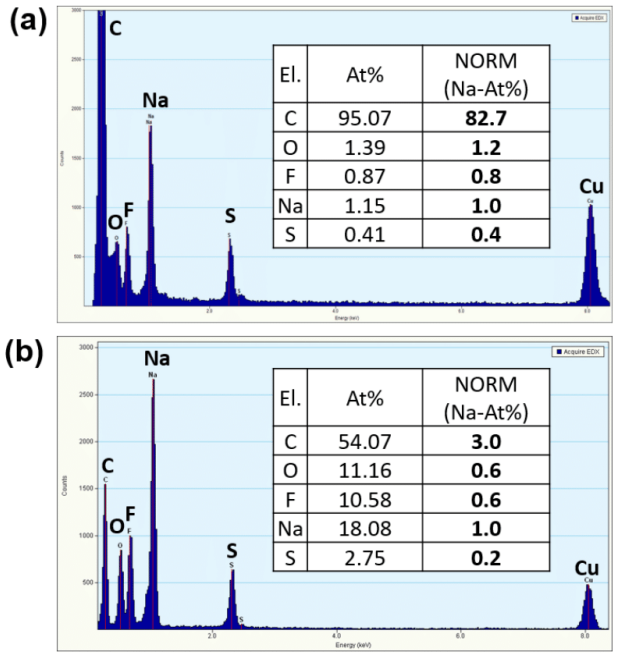

S 10. EDX analysis on the surface of graphite after cycling bythe salt systems of (a) NaOTf and (b) NaTFSI. Insets: tables with the EDX quantifications, At% were normalized with respect to the Na At% in order to compare NaOTf and NaTSI

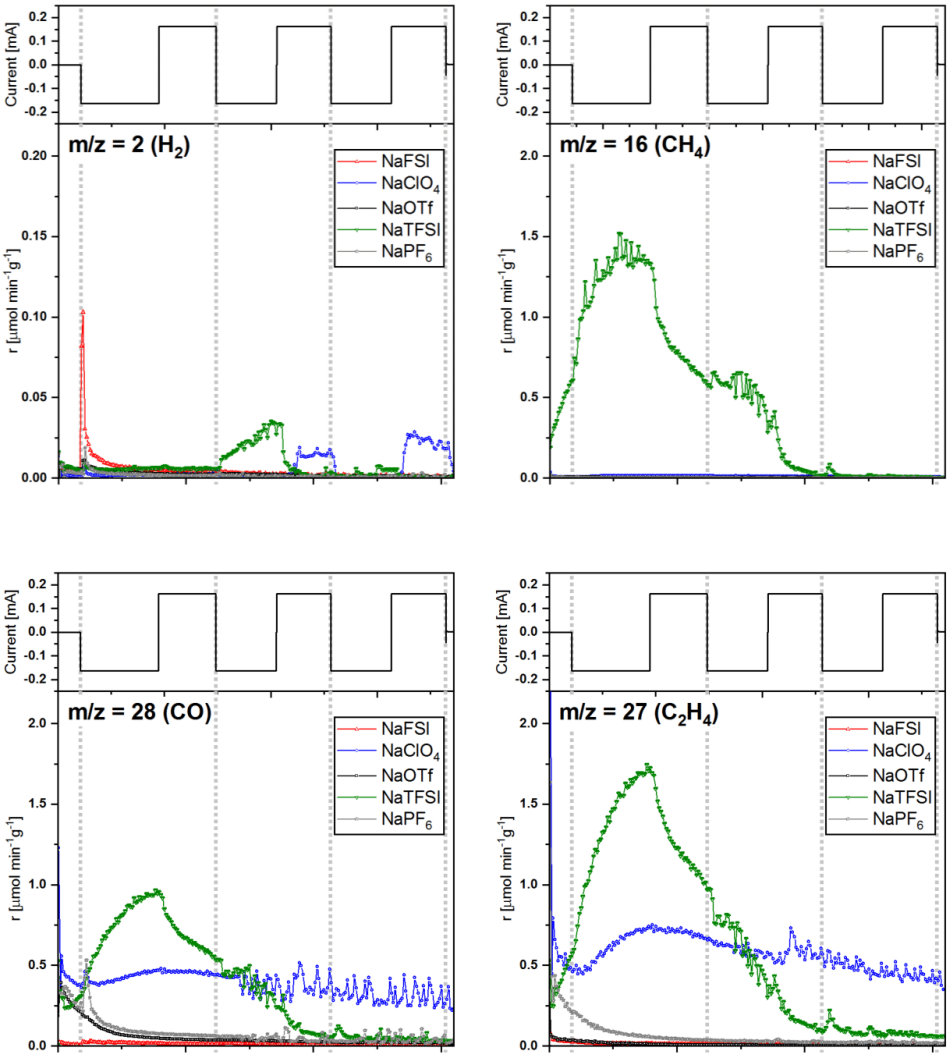

S 11. H_2, CH_4, CO and C_2H_4 evolution for Na|Na cells with respect to the measured electrolyte.

Experimental Details of OEMS

The OEMS setup was described elsewhere [18] and operates with a quadrupole mass spectrometer (QMS 200, Pfeiffer) for partial pressure measurements, a pressure transducer (PAA-33X, Keller Druck AG) for total cell pressure, temperature, and internal volume determination, stainless steel gas pipes and Swagelok fittings (3 mm compression tube fittings, Swagelok, OH, US) to connect the OEMS cell, a set of solenoid valves (2-way magnetic valve, Series 99, silver-plated nickel seal, Parker) and a scroll pump (nXDS15i, EDWARDS GmbH) for efficient flushing. The magnetic valves are electronically controlled with a Solid State Relay Module (NI 9485 measurement System, National Instruments) connected to a computer with a LabView Software (NI Labview 2013, National Instruments). For partial pressure and gas evolution rate analysis 1.3 mL of gas are extracted from the headspace (~ 4 mL) of the cell and replaced by pure Ar (quality 5.0). Calibration gas bottles were utilized to relate the MS ion-current signals at m/z = 2, 27, 32 and 44 to known concentrations of H_2, C_2H_4, O_2 and CO_2 (1000 ppm of C_2H_4, O_2 and CO_2 in Ar, respectively, and 1% of H_2 in Ar), before and after the measurement.

The ion currents for fragments m/z = 16 (CH_4), 28 (CO), 30 (C_2H_6), 48 (SO_2), and 69 (CF_3) were recorded without calibration and converted into approximate gas evolution rates that allow direct semi-quantitative comparison between the evolution of these fragments from one data set to another. The indicated m/z channels were deliberately selected for monitoring the described molecular species because they provided the strongest and least obscured signals.

References

[1] B. Jache, P. Adelhelm, *Angewandte Chemie International Edition* **2014**, *53*, 10169-10173.

[2] B. Jache, J. O. Binder, T. Abe, P. Adelhelm, *Physical Chemistry Chemical Physics* **2016**, *18*, 14299-14316.

[3] L. Seidl, N. Bucher, E. Chu, S. Hartung, S. Martens, O. Schneider, U. Stimming, *Energy Environ. Sci.* **2017**.

[4] H. Kim, J. Hong, G. Yoon, H. Kim, K.-Y. Park, M.-S. Park, W.-S. Yoon, K. Kang, *Energy & Environmental Science* **2015**, *8*, 2963-2969.

[5] M. Goktas, B. Akduman, P. Huang, A. Balducci, P. Adelhelm, *The Journal of Physical Chemistry C* **2018**, *122*, 26816−26824.

[6] A. P. Cohn, K. Share, R. Carter, L. Oakes, C. L. Pint, *Nano Letters* **2016**, *16*, 543-548.

[7] Z. Zhu, F. Cheng, Z. Hu, Z. Niu, J. Chen, *Journal of Power Sources* **2015**, *293*, 626-634.

[8] I. Hasa, X. Dou, D. Buchholz, Y. Shao-Horn, J. Hassoun, S. Passerini, B. Scrosati, *Journal of Power Sources* **2016**, *310*, 26-31.

[9] K. Gotoh, H. Maruyama, T. Miyatou, M. Mizuno, K. Urita, H. Ishida, *Journal of Physical Chemistry C* **2016**, *120*, 28152−28156.

[10] S. C. Jung, Y. J. Kang, Y. K. Han, *Nano Energy* **2017**, *34*, 456-462.

[11] G. Yoon, H. Kim, I. Park, K. Kang, *Advanced Energy Materials* **2016**, 1601519.

[12] H. Kim, G. Yoon, K. Lim, K. Kang, *Chem Commun (Camb)* **2016**, *52*, 12618-12621.

[13] M. Goktas, C. Bolli, E. J. Berg, P. Novák, K. Pollok, F. Langenhorst, M. v. Roeder, O. Lenchuk, D. Mollenhauer, P. Adelhelm, *Advanced Energy Materials* **2018**, 1702724.

[14] H. Kim, J. Hong, Y.-U. Park, J. Kim, I. Hwang, K. Kang, *Advanced Functional Materials* **2015**, *25*, 534-541.

[15] M. Cabello, T. Chyrka, R. Klee, M. J. Aragón, X. Bai, P. Lavela, G. M. Vasylchenko, R. Alcántara, J. L. Tirado, G. F. Ortiz, *Journal of Power Sources* **2017**, *347*, 127-135.
[16] J. Maibach, F. Jeschull, D. Brandell, K. Edstrom, M. Valvo, *ACS Appl Mater Interfaces* **2017**, *9*, 12373-12381.
[17] N. Leifer, M. F. Greenstein, A. Mor, D. Aurbach, G. Goobes, *The Journal of Physical Chemistry C* **2018**, *122*, 21172-21184.
[18] M. He, (Eidgenössische Technische Hochschule (ETH) Zürich), **2016**.

8.4. Supporting information on Publication 3

Supporting Information

for *Adv. Funct. Mater.,* DOI: 10.1002/adfm.201900790

Sodium Storage and Electrode Dynamics of Tin–Carbon Composite Electrodes from Bulk Precursors for Sodium-Ion Batteries

Thangavelu Palaniselvam, Mustafa Goktas, Bihag Anothumakkool, Ya-Nan Sun, Richard Schmuch, Li Zhao, Bao-Hang Han, Martin Winter, and Philipp Adelhelm**

WILEY-VCH

Supporting Information on

Sodium Storage and Electrode Dynamics of Tin-Carbon Composite Electrodes from Bulk Precursors for Sodium-ion Batteries

Thangavelu Palaniselvam[a,b]†, Mustafa Goktas[ab†], Bihag Anothumakkool,[c] Ya-Nan Sun,[d] Richard Schmuch,[c] Li Zhao[d], Bao-Hang Han,[d] Martin Winter[c] and Philipp Adelhelm[a,b]**

Table S1. *A summary of specific discharge capacity of Sn with carbon based composites for sodium ion batteries.*

Electrode	Electrolyte	Potential range (V *vs* Na^+/Na)	Current Densities (mAg^{-1})	Charge capacities ($mAhg^{-1}$)	Stability	Ref.
Sn with graphene	1M $NaClO_4$ in EC/DEC	0.01-2.0	0.5C	615	after 30 cycles at 0.5 C	S1
Self-supported Sn on graphene films	1 M $NaClO_4$ in EC:PC:FEC	0.01-0.75	50	□350	324 $mAhg^{-1}$ at 50 mAg^{-1} after 30 cycles	S2
Sn nano particles encapsulated in graphene	1 M $NaClO_4$ in EC:PC	0.01-2.0	100	434	413 $mAhg^{-1}$ at 100 mAg^{-1} after 100 cycles	S3
Sn with conductive carbon	1 M $NaPF_6$ in Diglyme	0.01-1.0	-	-	768 after 100 cycles at 250 mAg^{-1}_{Sn}	S4
Sn ball milled with graphite	1 M $NaClO_4$ in EC:DMC	0.01-1.2	50	420	□350 $mAhg^{-1}$ at 50 mAg^{-1} after 20 cycles	S5
Sn-polyacrylate	1 M $NaClO_4$ in PC:FEC(2%)	0.0-0.8	-	-	□500 $mAhg^{-1}$ at 50 mAg^{-1} after 20 cycles	S6
Sn@woodfiber	1 M $NaPF_6$ in EC:DEC	0.0-1.5	84	□260	145 $mAhg^{-1}$ at 84 mAg^{-1} after 100 cycles	S7
Sn/porous carbon	1 M $NaClO_4$ in PC:DMC	0.02-1.5	-	-	200 $mAhg^{-1}$ at 20 mAg^{-1} after 15 cycles	S8
Sn/C	1 M $NaClO_4$ in EC:DEC	0.01-2.0	200	493	415 $mAhg^{-1}$ at 1000 mA g^{-1} after 500 cycles	S9
Sn with nitrogen doped graphene nano platelets	1 M $NaPF_6$ in Diglyme	0.005-1.2	50	445	290 mAh g^{-1} at 1000 mAg^{-1} after 1000 cycles	Present work

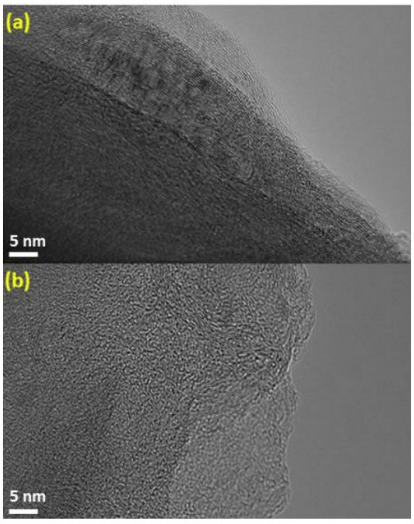

Figure S1. *HRTEM of SnNGnP show the higher graphitic nature of GnP sheets.*

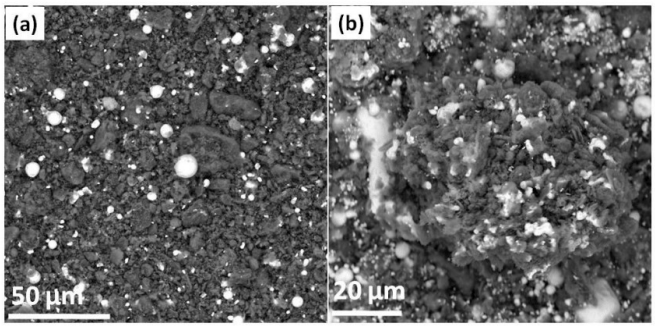

Figure S2. *SEM images of SnNGnP in different magnifications.*

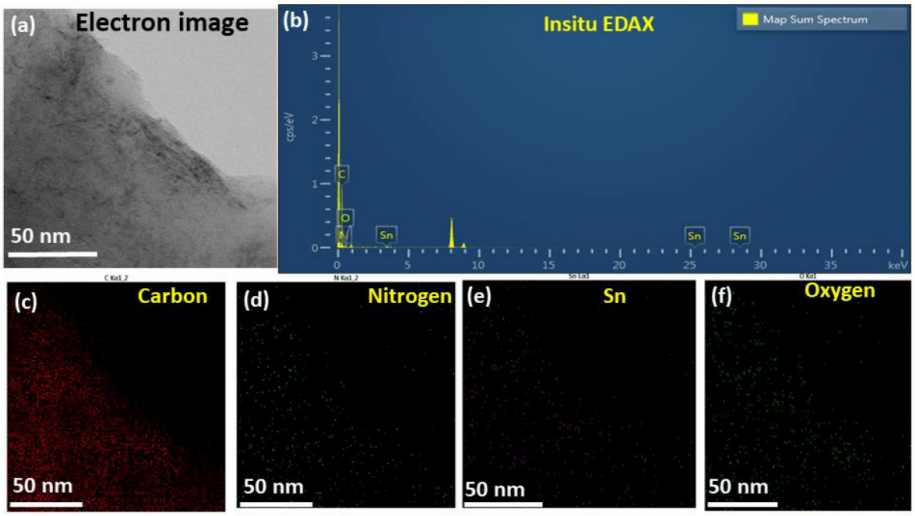

***Figure S3**. TEM image of SnNGnP and EDAX spectra with corresponding elemental mapping of C, N, Sn and O.*

***Table S2**. Summary of elemental percentage of SnNGnP, SnGnP, and NGnP as derived from CHNS analysis.*

S.No	*Name*	*N (%)*	*C (%)*	*H (%)*	*S (%)*
1.	*SnNGnP*	*0.6*	*41.2*	*0.1*	*0.01*
2	*SnGnP*	*0.1*	*31.2*	*0.7*	*0.0*
3	*NGnP*	*0.2*	*98.4*	*0.2*	*0.01*

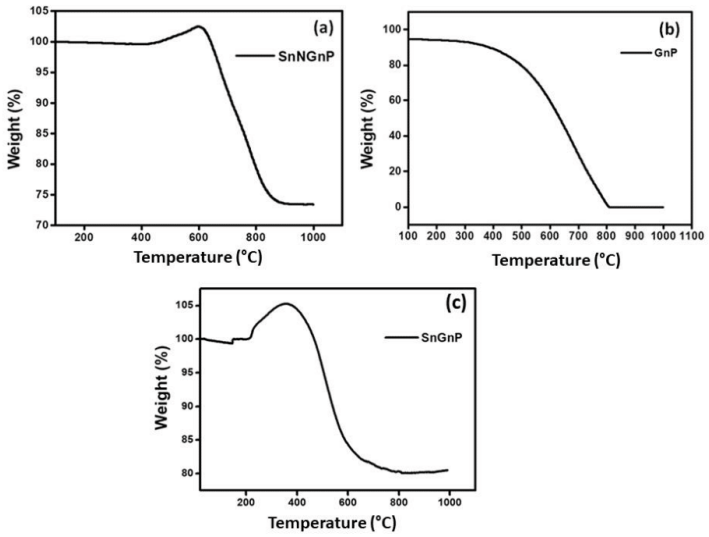

***Figure S4**. Thermogravimetric analysis of (a) SnNGnP (b) GnP and (c) SnGnP.*

Calculation of weight percentage of Sn

The TGA was carried out in air atmosphere. The existing Sn was expected to convert as SnO_2 at 1000 °C. Thus, it is meaningfull to measure the Sn content by using the following method. In the case of SnNGnP:

$$\text{Sn (wt\%)} = 100 \text{ X } \frac{\text{Molecular weight of Sn}}{\text{Molecular weight of } SnO_2} \text{ X } \frac{\text{Final weight}}{\text{Initial weight}}$$

$$\text{Sn (wt\%)} = 100 \text{ X } \frac{118.7 \text{ g/mol}}{150.71 \text{ g/mol}} \text{ X } \frac{73.43}{100}$$

$$= 57.49$$

In the case of SnGnP:

$$\text{Sn (wt\%)} = 100 \text{ X } \frac{\text{Molecular weight of Sn}}{\text{Molecular weight of } SnO_2} \text{ X } \frac{\text{Final weight}}{\text{Initial weight}}$$

$$\text{Sn (wt\%)} = 100 \text{ X } \frac{118.7 \text{ g/mol}}{150.71 \text{ g/mol}} \text{ X } \frac{80.5}{100}$$

$$= 63.4$$

Overall weight gain of carbon by annealing of Sn with Melamine is □ 8 %

The annealing of Sn with melamine in argon atmosphere resulting the strong nitrogen-doping in carbon. It also produces some pyrolytic carbon which was identified from CHNS analysis (Table S2). In SnNGnP, the expected carbon content is 33.3 %. The obtianed carbon content is 41.2 %. Therefore, the weight gain was estimated as 8%. The controlled experiment for the preparation of SnGnP ensures that there is no weight gain of carbon which is due to the absence of annealing with melamine at high temperature.

Calculation of theoretical capacity of SnNGnP

The theoretical capacity of SnNGnP was calculated by using following equation[S10]

$C_{SnNGnP} = C_{Sn\ x\ wt\%\ Sn} + C_{GnPxwt\%\ GnP}$

The theoretical capacity of Sn is 847 $mAhg^{-1}$. The specific capacity delivered by GnP is 78 $mAhg^{-1}$ at 50 mAg^{-1} (as shown in Figure. 4b), the weight percentage of Sn and GnP is found as 42 and 58, respectively (Figure S4).

$$C_{SnNGnP} = (847 \times 58\%) + (78 \times 42\%)$$
$$C_{SnNGnP} = 491.2 + 32.7$$

Therefore, the calculated theoretical capacity of SnNGnP is 524 $mAhg^{-1}$.

Active material utilization in first cycle = (524-517)/524 X 100
= 98.7 %

Active material utilization from second cycle = (524-445)/524 X 100
= 85%

Table S3. *Elemental composition of SnNGnP as derived from XPS.*

Name	*Atomic %*
C 1s	*92.5*
N1s	*2.4*
Sn3d	*1.0*
O1s	*4.2*

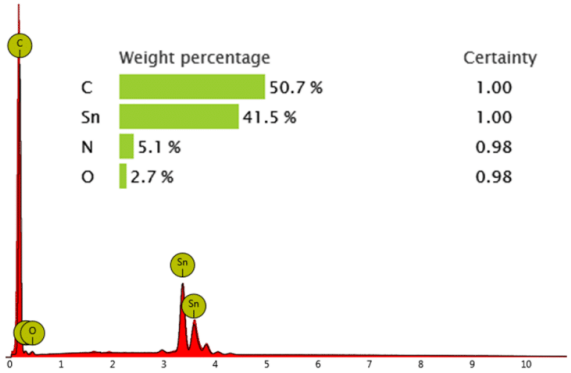

Figure S5. *EDAX spectra of SnNGnP.*

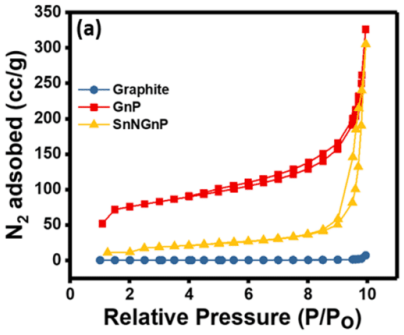

(b)

Sample	BET surface area (m^2/g)
Graphite	1
GnP	270
SnNGnP	60

Figure S6. *N_2 adsoprtion-desoprtion profile used for BET surface measurement for Graphite, GnP and SnNGnP (b) Summary of surface area of Graphite, GnP and SnNGnP.*

Table S4. *A summary of specific discharge capacity of graphene based materials for sodium ion batteries.*

Type of carbon	Electrolyte	Potential range (V *vs* Na^+/Na)	Current Densities (mAg^{-1})	Charge capacities ($mAhg^{-1}$)	Surface area (m^2g^{-1})	Additional information	Ref.
r-GO	1 M $NaClO_4$ in EC:PC:FEC	0.005-3.0	50	272	198	Sn induced GO reduction (RT)	S11
Graphene nanosheets	1 M $NaClO_4$ in EC:DEC	0.01-2.0	30	220	-	GO prepared by modified Staudenmaier method and reduced at 300 °C in Argon	S12
Expanded graphite	1 M $NaClO_4$ in PC	0.0-2.0	20	284	34.7	Heat treatment based reduction (600 °C)	S13
Reduced graphene oxide (free standing paper electrode)	-	0.0-2.5	100	140	-	Heat treatment based reduction.	S14
Crumpled graphene sheet	1 M $NaClO_4$ in PC	0.005-2.5	100	183	47.4	Thionyl chloride used as reducing agent followed by heat treatment at 600 C in Argon	S15
Reduced graphene oxide	1 M $NaClO_4$ in PC	0.01-2.0	40	174	330.9	RGOs prepared by heat treatment (450 °C) followed by annealing in N_2 atmosphere at 750 °C	S16
Expanded graphitic material	1 M $NaPF_6$ in EC:DEC	0.003-2.0	37	150	30	Heat treatment based reduction (300 °C)	S17
Graphite	1m NaOTf in Diglyme	0.005-2.5	32.7	115	5	Commercial material	S18
Graphite nano plateletes	1 M $NaPF_6$ in Diglyme	0.005-2.5	50	220	190	Ball milling of graphite	Present work

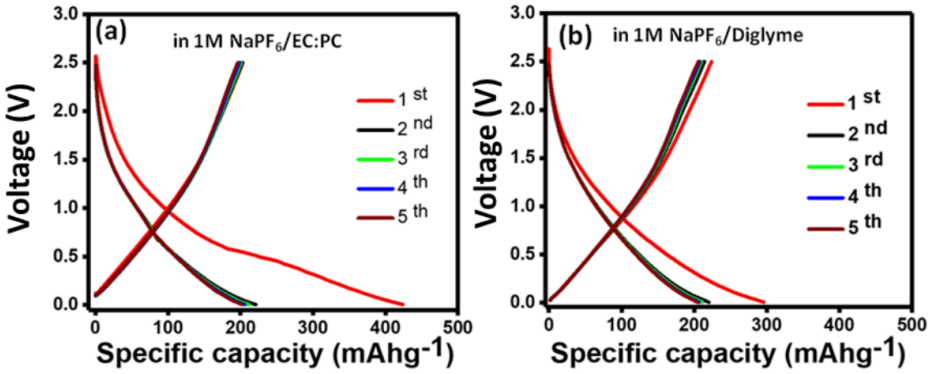

Figure S7. *Charge-discharge curves of GnP measured with 1M NaPF6 in (a) EC: PC and (b) Diglyme electrolyte recorded at current density of 50 mAg^{-1}.*

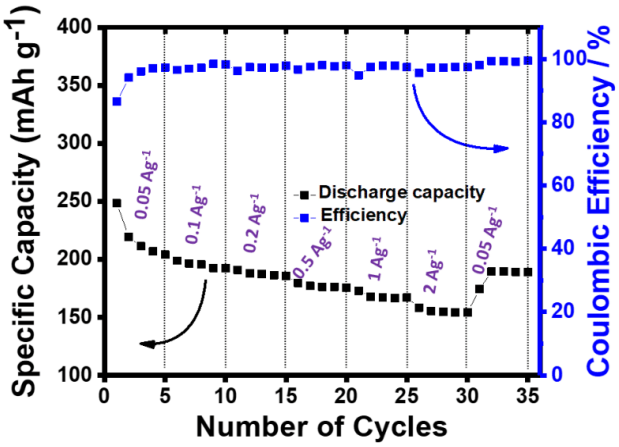

Figure S8. *Rate capability of GnP electrode measured from 50-2000 mA g^{-1}.*

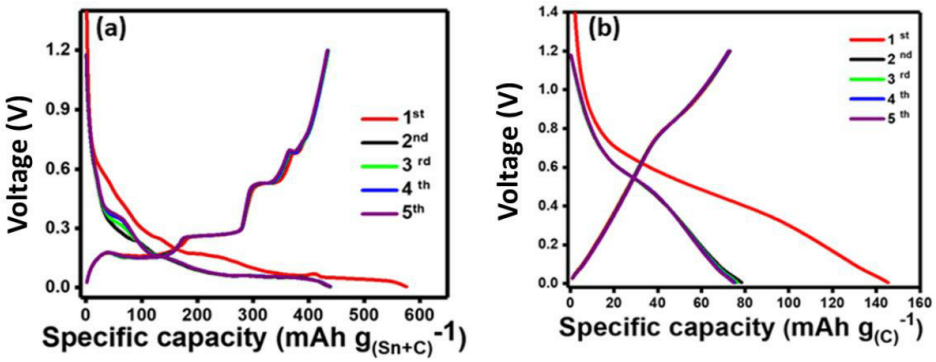

Figure S9. *Charge-discharge curves of SnNGnP and NGnP (i.e. after removal of Sn) recorded with 1M $NaPF_6$ in diglyme at 50 mAg^{-1}.*

The composite *i.e.* SnNGnP exhibit the specific capacity around 450 m Ah $g_{(Sn+C)}^{-1}$. While the NGnP, *i.e.* after removal of Sn from the composite delivers the specific capacity around 78 $mAhg_{(C)}^{-1}$. The percentage of contribution of C in the composite was estimated as 17 % which is negligible. Thus, the overall specific capacity for the composite was normalised with resepect to Sn in the main text.

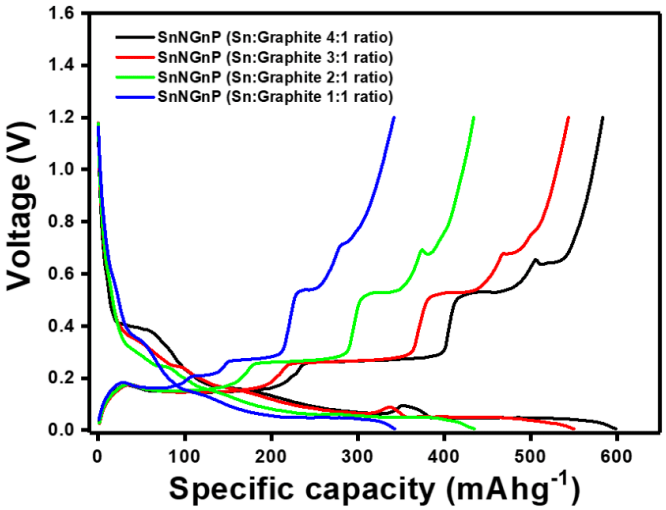

Figure S10. *Galvanostatic charge-discharge curves of SnNGnP with different Sn: Graphite ratio, recorded at a current density of 50 mA g^{-1}.*

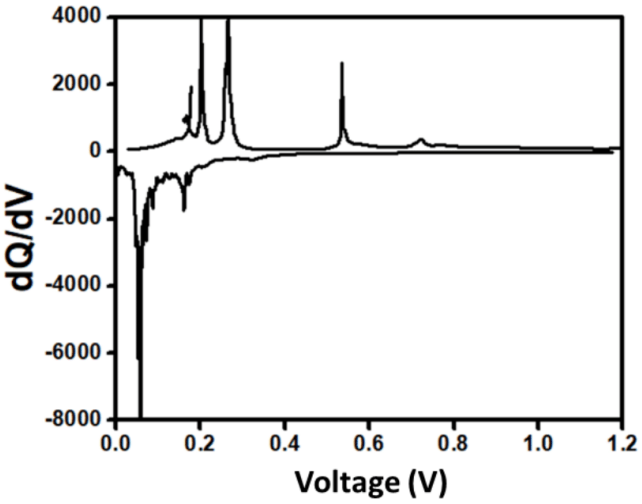

Figure S11. *Differential charge plots for the SnNGnP at 50 mA h g^{-1} (10 th cycle).*

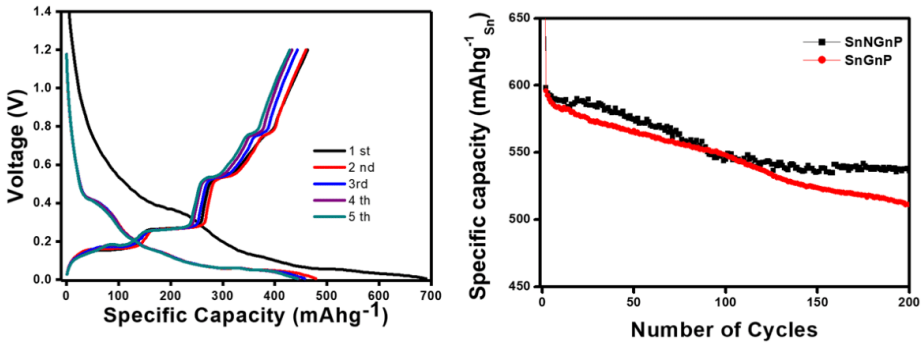

Figure S12. *(a) Galvanostatic charge-discharge curves of SnGnP recorded at a current density of 50 mA g^{-1}.* (b) *Cycle life of the SnNGnP and SnGnP electrodes recorded at 1000 mA g^{-1} for 200 cycles (the specific capacity relates to per gram of Sn). The retention in capacity (from 2nd cycle to 200 cycle) for SnNGnP is 90.1% whereas for SnGnP is 85.8 %.*

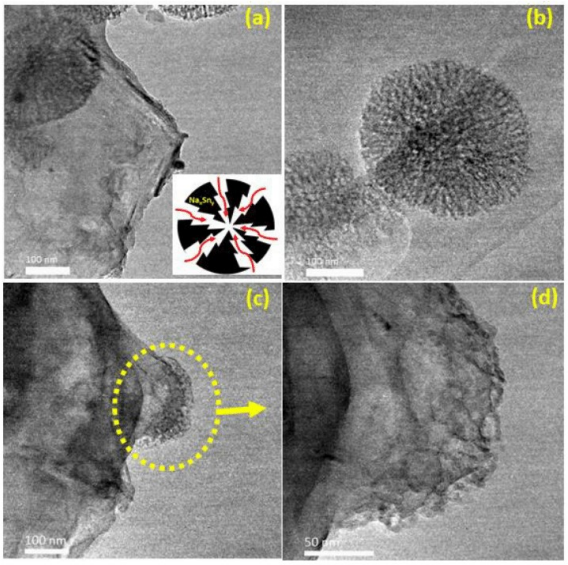

Figure S13. *TEM images of SnNGnP after cycling (SnNGnPac) at 500 mAg^{-1} for 50 cycles.*

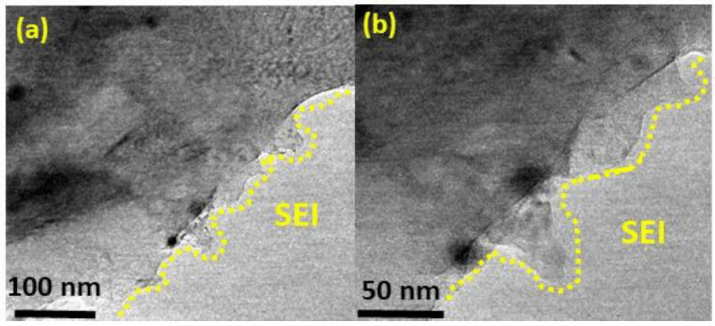

Figure S14. *TEM images of SnNGnP after cycling for 50 cycles at 500 mAg^{-1}.*

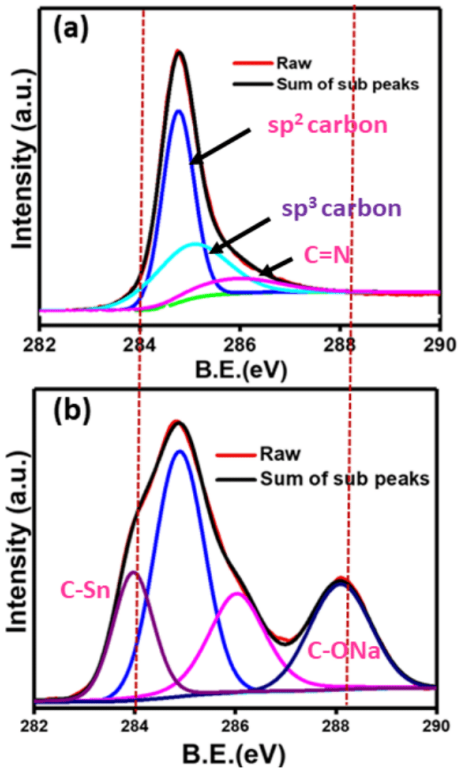

Figure S15. *Comparison of C 1s spectra of SnNGnP before and after cycling.*

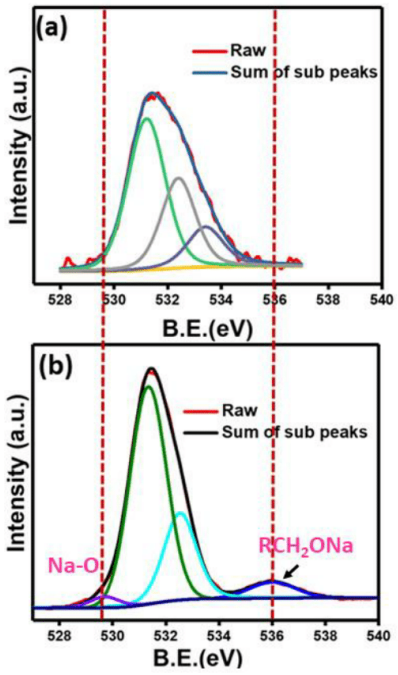

Figure S16. *Comparison of O1s spectra of SnNGnP before and after cycling.*

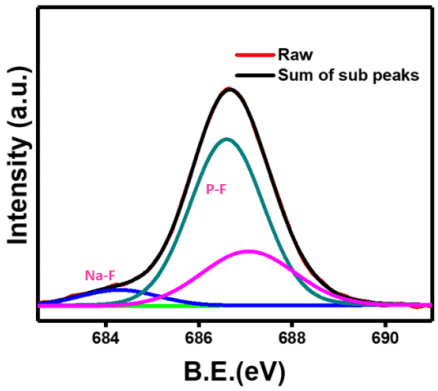

Figure S17. *F 1s spectra of SnNGnP after cycling.*

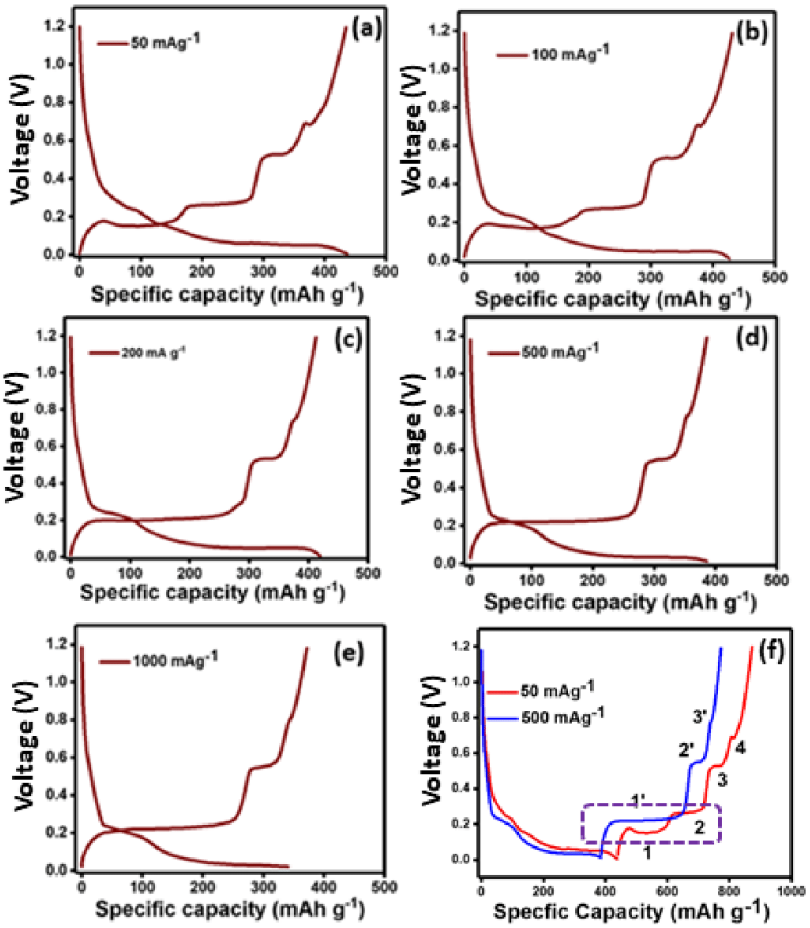

Figure S18*.(a-e) Charge-Discharge curves of SnNGnP, recorded at different current densities. (f) Comparison of charge-discharge curves of SnNGnP, recorded at 50 and 500 mAg^{-1} (the dotted rectangle represent the disappearance of two plateaus at 0.15 and 0.26 V and appearance of the single while large plateau at 0.21 V measured at 500 mAg^{-1}).*

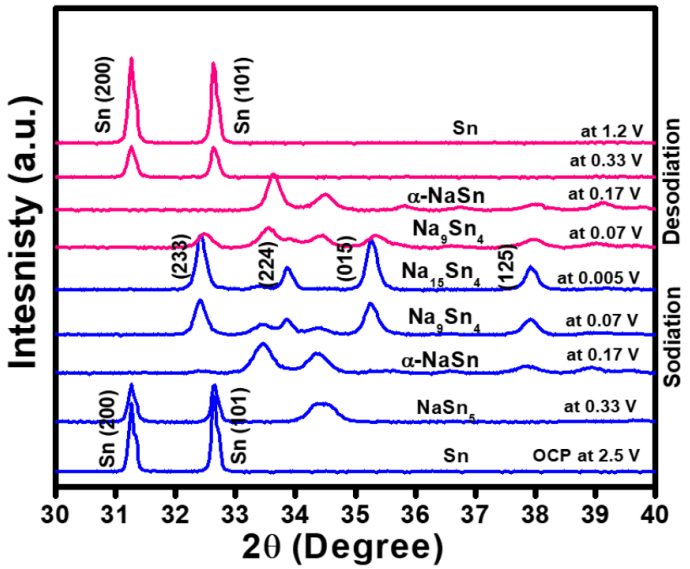

Figure S19. *In situ XRD pattern for SnNGnP recorded at 50 mAg^{-1}. (The indicated phases are the ones expected from the binary phase diagram).*

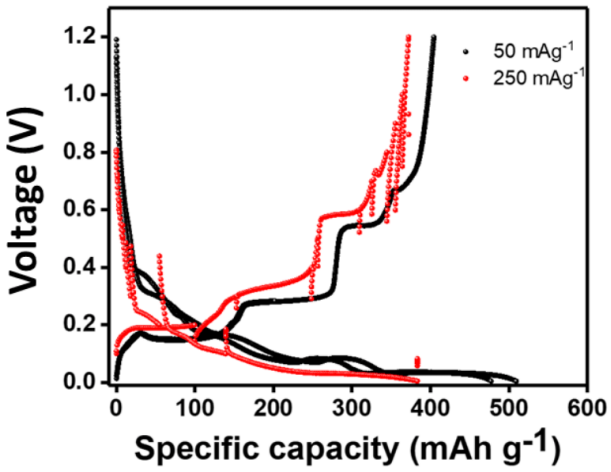

Figure S20. *Galvanostatic charge-discharge curves of SnNGnP, recorded with in situ XRD measurements. (at 250 mAg^{-1}, the noise signals are observed which is due to relaxation time).*

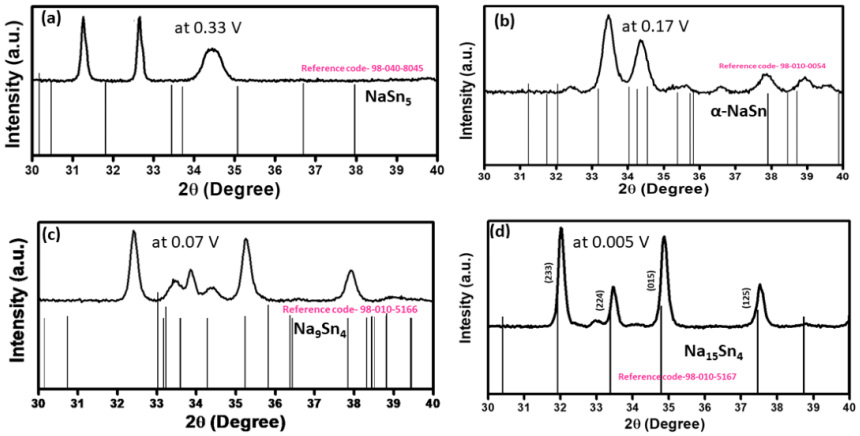

Figure S21. *XRD patterns obtained in situ at 50 mAg^{-1} during discharge at potentials of 0.33, 0.17, 0.07 and 0.005 V vs Na^{+}/Na. The graphs also show the reference pattern from the phases that would be expected from the equilibrium phase diagram. Obviously, only for the fully sodiated state, the expected phase $Na_{15}Sn_4$ is found. All other phases remain unknown.*

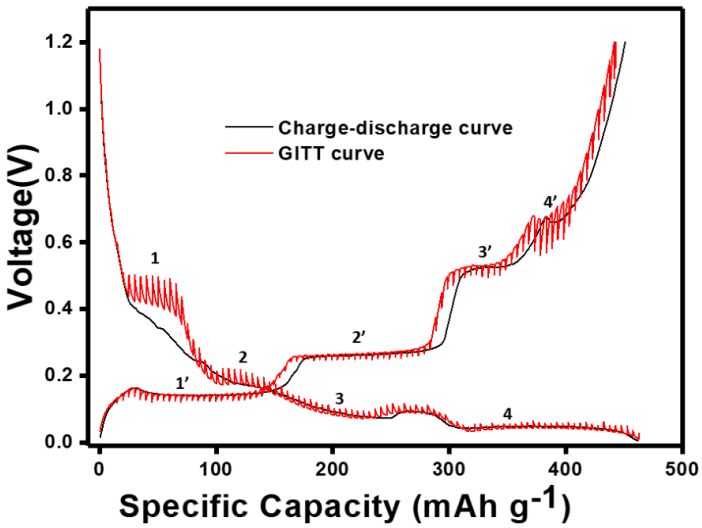

Figure S22. *GITT measurement on SnNGnP electrode and overlay with a galvanostatic discharge curve recorded at a current density of 20 mA g^{-1}.*

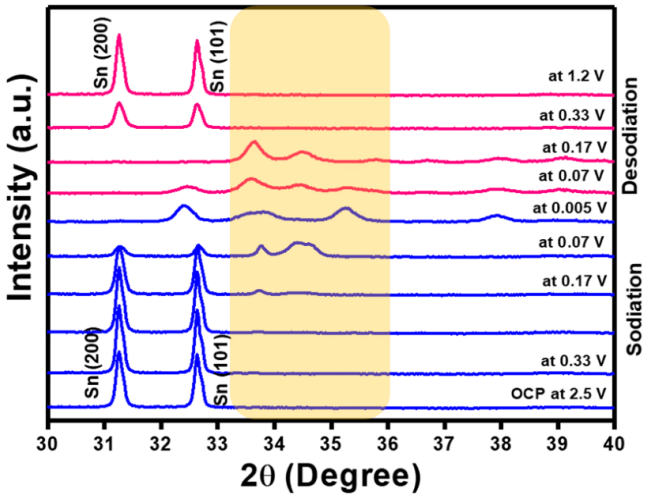

Figure S23. *In situ XRD pattern for SnNGnP recorded at 250 mAg^{-1}. (The yellow part indicates the appearance and disappearance of Na-Sn phase at different potential)*

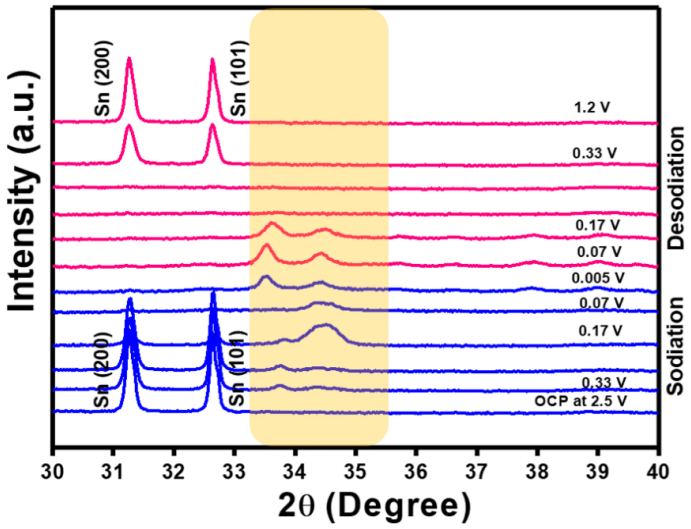

Figure S24. *In situ XRD pattern for SnNGnP recorded at 500 mAg^{-1}. (The yellow part indicates the appearance and disappearance of Na-Sn phase at different potential)*

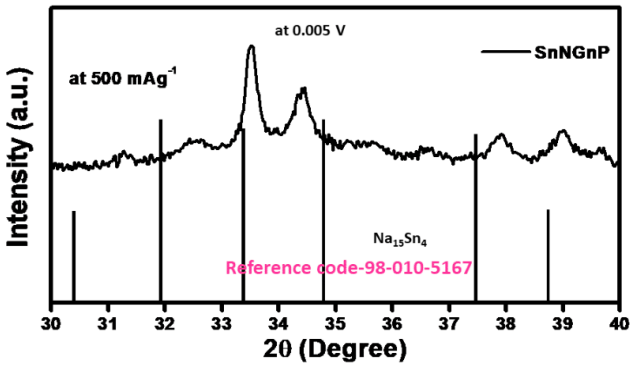

Figure S25. *In situ XRD pattern of the sodiated tin phase formed at 0.005 V vs. Na^+/Na ($Na_{15}Sn_4$ phase). (Galvanostatic charge-discharge curves of SnNGnP, recorded at current density of 500 mAg^{-1})*

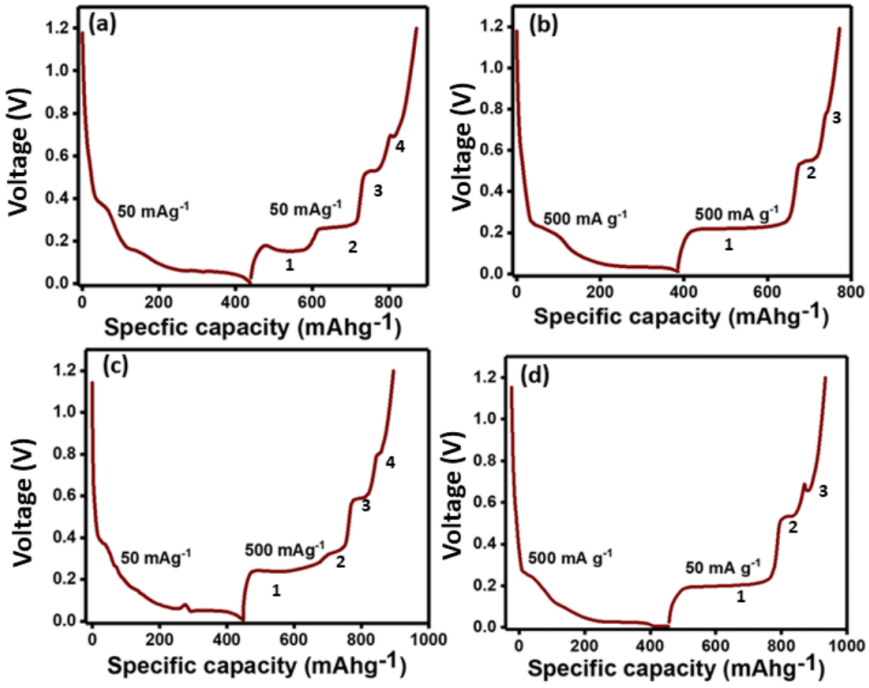

Figure S26. *Charge-discharge curves of SnNGnP, recorded at current density of 50 mAg^{-1}(4 plateaus are observed during charging process). (b) Charge-discharge curves of SnNGnP, recorded at current density of 500 mAg^{-1}(3 plateaus are observed during charging process). (c) Charge-discharge curves of SnNGnP, the discharging process recorded at 50 mAg^{-1} and the charging process recorded at 500 mAg^{-1} (during charging process, 3 plateaus are expected to appear, instead 4 were observed). (d) Charge-discharge curves of SnNGnP, the discharging process recorded at 500 mAg^{-1} and the charging process recorded at 50 mAg^{-1} (during charging process, 4 plateaus are expected to appear, instead 3 were observed).*

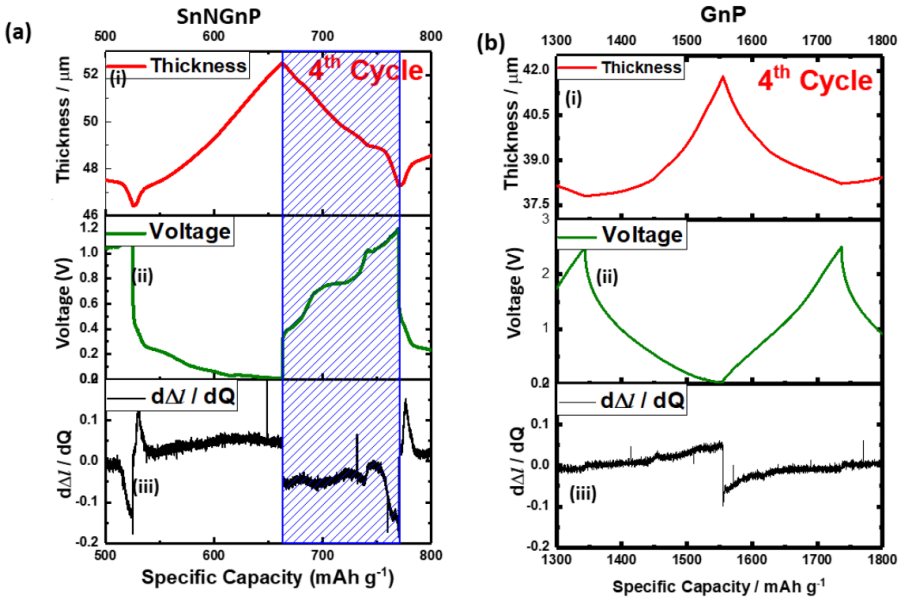

Figure S27. *The thickness and voltage change by cycle number and the derivative of thickness by capacity at 4th cycle in (a) SnNGnP and (b) GnP.*

Using the data from the dilatometer measurements, the starting values (initial thickness, loading) as well as the obtained capacity, the volume and density of the electrode can be calculated.

During sodiation, there are generally two competing effects related to mass, volume and density. (a) electrode expansion leads to an increase in volume and hence decrease in density, and (b) sodiation leads to an increase in mass and hence higher density. The opposite effects take place during desodiation.

Results are shown in Figure S28 for the 4th cycle (from this cycle on, the changes upon cycling are fairly periodic). The volume of the electrode at V_1 is 0.00364 cm^3 (Figure S28b and Table S5) increases to 0.00412 cm^3 due to sodiation (at V_2). After desodiation (at V_3), the volume is reduced to 0.00371 cm^3. Likewise, the density of the electrode also changes after sodiation (at D_1 and D_2 in Figure S28b). It is of note that, at D_2, the density and volume of the electrode become larger compared at D_1. This means that the increased mass due to sodium outweighs the volume expansion of the electrode hence leading to a higher density. This behavior is due to the opened structure of the nanocomposite which provides free volume to accommodate the expansion of tin in its interior.

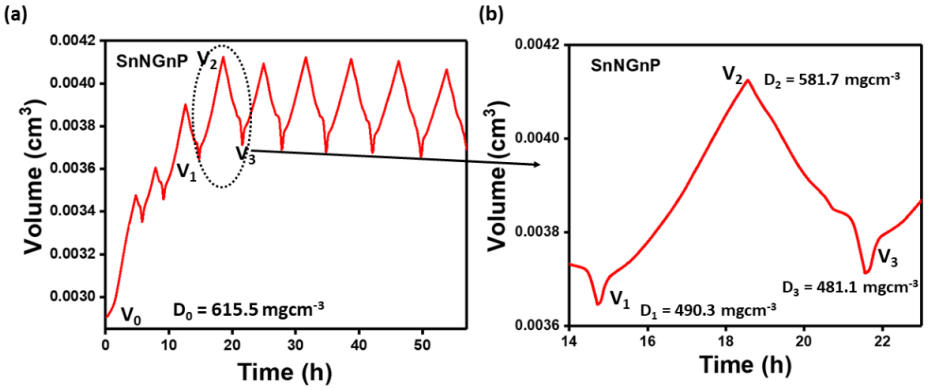

Figure S28. (a) *Volume changes of SnNGnP electrode with respect to time*. (b) *Representation of volume changes in the 4th cycle in SnNGnP electrode.*

Table S5. Specifications of SnNGnP electrode for the calculation of density changes from the *in situ* dilatometry study.

Specifications	**SnNGnP**
Initial active mass of electrode [mg] M_1	1.785
Thickness of electrode in *z* direction (without Cu current collector) [µm]	37
Radius of the electrode [cm]	0.5
Initial Volume [cm^3] V_0	0.0029
Volume [cm^3] during 4th cycle (before sodiation) V_1	0.00364
Volume [cm^3] during 4th cycle (sodiated) V_2	0.00412
Volume [cm^3] after 4th cycle (desodiated) V_3	0.00371
Active mass [mg] after sodiation M_2 (including Na)	2.397
Initial electrode density [mg/cm^3] D_0	615.5
Density during 4th cycle (before sodiation) [mg/cm^3] D_1	490.3
Density during 4th cycle (sodiated) [mg/cm^3] D_2	581.7
Density after 4th cycle (desodiated) [mg/cm^3] D_3	481.1

* mass of electrolyte and binder are neglected.

References

[S1] Y. Jeon, X. Han, K. Fu, J. Dai, J. H. Kim, L. Hu, T. Song and U. Paik, *J. Mater. Chem. A*, **2016**, *4*, 18306.

[S2] F. Pan, W. Zhang, J. Ma, N. Yao, L. Xu, Y. S. He, X. Yang, Z. F. Ma, *Electrochim. Acta,* **2016***, 196*, 572.

[S3] B. Luo, T. Qiu, D. Ye, L. Wang, L. Zhi, *Nano Energy*., **2016**, ***22,*** 232.

[S4] B. Zhang, G. Rousse, D. Foix, R. Dugas, D. A. D. Corte, J. M. Tarascon, *Adv. Mater.* **2016**, *28*, 9824.

[S5] M. K. Datta, R. Epur, P. Saha, K. Kadakia, S. K. Park, P. N. Kumta, *J .Power Sources*, **2013**, *225*, 316.

[S6] S. Komaba, Y. Matsuura, T. Ishikawa, N. Yabuuchi, W. Mutata, S. Kuze, *Electrochem. Commun*., **2012**, *21*, 65.

[S7] H. Zhu, Z. Jia, Y. Chen, N. Weadock, J. Wan, O. Vaaland, X. Han, T. Li, L. Hu, *Nano Lett*. **2013**, *13,* 3093.

[S8] Y. H. Xu, Y. J. Zhu, Y. H. Liu, C. S. Wang, *Adv. Energy Mater.***2013**, *3,* 128.

[S9] Y. Liu , N. Zhang , L. Jiao, Z. Tao, J. Chen, *Adv. Funct. Mater*. **2015**, *25*, 214.

[S10] Y. Liu, N. Zhang, L. Jiao, J. Chen, *Adv. Mater*., **2015**, *27*, 6702.

[S11] N. A. Kumar, R. R. Gaddam, S. R. Varanasi, D. Yang, S. K. Bhatia, X. S. Zhao, *Electrochim. Acta*., **2016**, *214*, 319.

[S12] F. Luo, C. H. Yang, Y. Y. Peng, N. W. Pu, M. D. Ger, C. T. Hsieh, J. K. Chang, *J. Mater. Chem. A*., **2015**, *3*, 10320.

[S13] Y. Wen, K. He, Y. Zhu, F. Han, Y. Xu, I. Matsuda, Y. Ishii, J. Cumings, C. Wang, *Nat. Commun*, **2014**, *5*, 4033.

[S14] L. David, G. Singh, *J. Phys. Chem. C*., **2014**, *118*, 28401.

[S15] Y.S. Yun, Y. U. Park, S. J. Chang, B. H. Kim, J. Choi, J. Wang, D. Zhang, P.V. Braun, H. J. Jin, K. Kang, *Carbon*, **2016**, *99*, 658.

[S16] Y. X. Wang, S. L. Chou, H. K. Liu, S. X. Dou, *Carbon*, **2013**, *57*, 202.

[S17] A. Ramos, I. Camean, N. Cuesta, C. Antuna, A.B. Garcia, *Electrochim. Acta*., **2016**, *187*, 496.

[S18] M. Goktas, C. Bolli, E. J. Berg, P. Novák, K. Pollok, F. Langenhorst, M. v. Roeder, O. Lenchuk, D. Mollenhauer, P. Adelhelm, *Adv. Energy Mater*. **2018**, 1702724.

9. References

1. D. Larcher and J. M. Tarascon, *Nat Chem*, 2015, **7**, 19-29.
2. N. S. Lewis, *MRS Bulletin*, 2007, **32**, 808-820.
3. K. Rademaekers, M. Smith, J. Yearwood, Y. Saheb, J. Moerenhout, K. Pollier, N. Debrosses, T. Badouard, A. Peffen, H. Pollitt, S. Heald and M. Altman, *Study on Energy Prices, Costs and Subsidies and their Impact on Industry and Households* European Commission, Trimonics, Netherlands 2018.
4. https://www.danskenergi.dk/nyheder/danmark-saetter-ny-rekord-vind).
5. B. Kaźmierczak, M. Żygadło, J. Kotowski, J. Oko, M. Kutyłowska, K. Piekarska and P. Jadwiszczak, *E3S Web of Conferences*, 2018, **44**, 00202.
6. B. Dunn, H. Kamath and J.-M. Tarascon, *Science*, 2011, **334**, 928-935.
7. M. A. Rosen, *Journal of Power and Energy Engineering*, 2015, **03**, 470-474.
8. A. Azzunia and C. Breyer, *Energy Procedia*, 2018, **155**, 237-258.
9. X. Luo, J. Wang, M. Dooner and J. Clarke, *Applied Energy*, 2015, **137**, 511-536.
10. Energy Storage https://www.dob-academy.nl/news/types-of-energy-storage-facilities/, DOI: https://www.dob-academy.nl/news/types-of-energy-storage-facilities/).
11. A. Sharma, V. V. Tyagi, C. R. Chen and D. Buddhi, *Renewable and Sustainable Energy Reviews*, 2009, **13**, 318-345.
12. R. A. Guidotti and P. Masset, *Journal of Power Sources*, 2006, **161**, 1443-1449.
13. J. Antonanzas, E. Jimenez, J. Blanco and F. Antonanzas-Torres, *Renewable and Sustainable Energy Reviews*, 2014, **37**, 36-46.
14. W. Buckles and W. V. Hassenzahl, *IEEE Power Engineering Review* 2000, **20**, 16-20.
15. S. Westerlund and L. Ekstam, *IEEE Transactions on Dielectrics and Electrical Insulation* 1994, **1**, 826-839.
16. P. Simon, Y. Gogotsi and B. Dunn, *Science*, 2014, **343**, 1210-1211.
17. B. E. Conway, *Kluwer Academic/Plenum Publishers, New-York*, 1999.
18. Y. Wang, Z. Shi, Y. Huang, Y. Ma, C. Wang, M. Chen and Y. Chen, *The Journal of Physical Chemistry C* 2009, **113**, 13103–13107.
19. T. Brousse, D. Belanger and J. W. Longd, *Journal of The Electrochemical Society*, 2015, **162**, A5185-A5189.
20. M. S. Halper and J. C. Ellenbogen, *Supercapacitors: A Brief Overview*, MITRE Nanosystems Group, The MITRE Corporation, McLean, Virginia, USA, 2006.
21. G. Fuchs, B. Lunz, M. Leuthold and D. U. Sauer, *Smart Energy for Europe Platform GmbH (SEFEP)*, 2012.
22. S. BASU, *Recent Trends in Fuel Cell Science and Technology* Springer, 2007.
23. J. Larminie and A. Dicks, *Fuel Cell Systems Explained*, Wiley, 2003.
24. T. B. Reddy, *Linden's Handbook of Batteries*, McGraw-Hill Education, Fourth Edition edn., 2011.
25. J. David, *Journal of Power Sources*, 1995, **57**, 71-73.
26. A. Taniguchi, N. Fujioka, M. Ikoma and A. Ohta, *Journal of Power Sources*, 2001, **100**, 117-124.
27. A. Manthiram and X. Yu, *Small*, 2015, **11**, 2108-2114.
28. C.-H. Dustmann, *Journal of Power Sources*, 2004, **127**, 85-92.
29. L. Medenbach, I. Escher, N. Kowitsch, M. Armbruster, L. Zedler, B. Dietzek and P. Adelhelm, *Angew Chem Int Ed Engl*, 2018, **57**, 13666-13670.
30. L. Medenbach and P. Adelhelm, *Top Curr Chem (Cham)*, 2017, **375**, 81.
31. F. Cheng and J. Chen, *Chem Soc Rev*, 2012, **41**, 2172-2192.
32. X. Zhang, X.-G. Wang, Z. Xie and Z. Zhou, *Green Energy & Environment*, 2016, **1**, 4-17.
33. T. Nagaura, presented in part at the in: Proc. 5th Intern. Seminar on Lithium Battery Technology and Applications, Deerfield Beach, FI, March 5-7, 1990.
34. *JEC Battery Newsletter, Sony Corporation Battery Group and Sony Energytec*, July-August, 1993, p. 19.

35. K. Brandt, *Solid State Ionics*, 1994, **69**, 173-183.
36. C. Pillot, *The Rechargeable Battery Market and Main Trends 2016-2025*, Avicenne Energy, AABC Europe, 2017.
37. F.-I. f. s.-u. I. ISI, *Energiespeicher-Roadmap (Update 2017) Hochenergie-Batterien 2030+ und Perspektiven zukünftiger Batterietechnologien*, FRAUNHOFER ISI, 2017.
38. M. Salvatore, G. Carotenuto, S. De Nicola, C. Camerlingo, V. Ambrogi and C. Carfagna, *Nanoscale Res Lett*, 2017, **12**, 167.
39. W. Rüdorff, *Advances in Inorganic Chemistry and Radiochemistry*, 1959, **1**, 223-266.
40. R. YAZAMI and P. TOUZAIN, *Journal of Power Sources*, 1983, **9**, 365-371.
41. C. Schafhäutl, *J Prakt Chem*, 1840, **21**, 129–157.
42. B. Brodie, *Ann Chem Physique* 1855, **45**, 351–352.
43. 1979.
44. K. Mizushima, P. C. Jones, P. J. Wiseman and J. B. Goodenough, *Mat. Res. Bull.* , 1980, **15**, 783-789.
45. W. S. Harris, July 17, 1958.
46. A. N. Dey, *Journal of Electrochemical Society*, 1971, **118**, 1547-1549.
47. M. Winter, B. Barnett and K. Xu, *Chem Rev*, 2018, **118**, 11433-11456.
48. M. L. B. Rao and K. R. Hill, *U. S. Army TR no. 2 (Contract no. DA-44-009-AMC-1537-T)*, 1967.
49. A. Yoshino, *Angew Chem Int Ed Engl*, 2012, **51**, 5798-5800.
50. 1985.
51. 1985.
52. G. E. Blomgren, *Journal of The Electrochemical Society*, 2017, **164**, A5019-A5025.
53. A. N. Dey and B. P. Sullivan, *J. Electrochem. Soc*, 1970, **117**, 222-224.
54. R. Fong, U. y. Sacken and J. R. Dahn, *Journal of The Electrochemical Society*, 1990, **137**, 2009-2013.
55. E. Peled, *This Journal*, 1979, **126**, 2047.
56. E. Peled, D. Golodnitsky and G. Ardel, *Journal of Electrochemical Society*, 1997 **144**, L208-L210.
57. E. Peled and S. Menkin, *Journal of The Electrochemical Society*, 2017, **164**, A1703-A1719.
58. N. Yabuuchi, K. Kubota, M. Dahbi and S. Komaba, *Chemical Reviews*, 2014, **114**, 11636-11682.
59. M. S. Dresselhaus and G. Dresselhaus, *Advances in Physics*, 1981, **30**, 139-326.
60. G. Schmuelling, T. Placke, R. Kloepsch, O. Fromm, H.-W. Meyer, S. Passerini and M. Winter, *Journal of Power Sources*, 2013, **239**, 563-571.
61. M. Wakihara and O. Yamamoto, *Lithium Ion Batteries: Fundamentals and Performance*, WILEY-VCH Verlag GmbH, Weinheim, 2008.
62. T. Ohzuku, Y. Iwakoshi and K. Sawai, *Journal of Electrochemical Society*, 1993, **140**, 2490-2498.
63. A. CHARLIER, M. F. CHARLIER and D. FRISTOT, *Journal of Physics and Chemistry of Solids* 1989, **50**, 987-996.
64. K. Nobuhara, H. Nakayama, M. Nose, S. Nakanishi and H. Iba, *Journal of Power Sources*, 2013, **243**, 585-587.
65. M. D. Slater, D. Kim, E. Lee and C. S. Johnson, *Advanced Functional Materials*, 2013, **23**, 947-958.
66. Y. Li, Y. Lu, C. Zhao, Y.-S. Hu, M.-M. Titirici, H. Li, X. Huang, L. Chen and *Energy Storage Materials*, 2017, **7**, 130-151.
67. V. Palomares, P. Serras, I. Villaluenga, K. B. Hueso, J. Carretero-González and T. Rojo, *Energy & Environmental Science*, 2012, **5**, 5884-5901.
68. S.-W. Kim, D.-H. Seo, X. Ma, G. Ceder and K. Kang, *Advanced Energy Materials*, 2012, **2**, 710-721.
69. P. Adelhelm, P. Hartmann, C. L. Bender, M. Busche, C. Eufinger and J. Janek, *Beilstein Journal of Nanotechnology*, 2015, **6**, 1016-1055.

70. P. K. Nayak, L. Yang, W. Brehm and P. Adelhelm, *Angewandte Chemie International Edition* 2017, DOI: 10.1002/anie.201703772.
71. Y. Kim, K. H. Ha, S. M. Oh and K. T. Lee, *Chemistry*, 2014, **20**, 11980-11992.
72. H. Pan, Y.-S. Hu and L. Chen, *Energy & Environmental Science*, 2013, **6**, 2338-2360.
73. P. Adelhelm, P. Hartmann, C. L. Bender, M. Busche, C. Eufinger and J. Janek, *Beilstein Journal of Nanotechnology*, 2015, **6**, 1016-1055.
74. D. A. Stevens and J. R. Dahn, *Journal of The Electrochemical Society*, 2000, **147**, 1271-1273.
75. S. Wenzel, T. Hara, J. Janek and P. Adelhelm, *Energy & Environmental Science*, 2011, **4**, 3342.
76. P. GE and M. FOULETIER, *Solid State Ionics*, 1988, **28-30**, 1172-1175.
77. M. Cabello, T. Chyrka, R. Klee, M. J. Aragón, X. Bai, P. Lavela, G. M. Vasylchenko, A. R., T. J. L. and O. G. F., *J Power Sources*, 2017, **347**, 127-135.
78. B. Jache, J. O. Binder, T. Abe and P. Adelhelm, *Physical Chemistry Chemical Physics*, 2016, **18**, 14299-14316.
79. Y. Liu, B. V. Merinov and W. A. Goddard, 3rd, *Proceedings of the National Academy of Sciences* 2016, **113**, 3735-3539.
80. H. Moriwake, A. Kuwabara, C. A. J. Fisher and Y. Ikuhara, *RSC Advances*, 2017, **7**, 36550-36554.
81. B. Jache and P. Adelhelm, *Angewandte Chemie International Edition*, 2014, **53**, 10169-10173.
82. S. A. Solin and H. Zabel, *Advances in Physics*, 1988, **37**, 87-254.
83. H. Zabel and S. Solin, *Graphite Intercalation Compounds I, Structure and Dynamics* Springer Series in Materials Science, 1990.
84. P. Lagrange, A. Bendriss-Rerhrhaye and J. F. M. A. E. Mcrae, *Synthetic Metals*, 1985, **12**, 201-206.
85. A. P. Cohn, K. Share, R. Carter, L. Oakes and C. L. Pint, *Nano Lett*, 2016, **16**, 543-548.
86. H. Kim, J. Hong, G. Yoon, H. Kim, K.-Y. Park, M.-S. Park, W.-S. Yoon and K. Kang, *Energy Environ. Sci.*, 2015, **8**, 2963-2969.
87. K. Gotoh, H. Maruyama, T. Miyatou, M. Mizuno, K. Urita and H. Ishida, *The Journal of Physical Chemistry C*, 2016, **120**, 28152-28156.
88. S. C. Jung, Y. J. Kang and Y. K. Han, *Nano Energy*, 2017, **34**, 456-462.
89. G. Yoon, H. Kim, I. Park and K. Kang, *Advanced Energy Materials*, 2016, DOI: 10.1002/aenm.201601519, 1601519.
90. H. Kim, G. Yoon, K. Lim and K. Kang, *Chemical Communiations*, 2016, **52**, 12618-12621.
91. L. Seidl, N. Bucher, E. Chu, S. Hartung, S. Martens, O. Schneider and U. Stimming, *Energy Environ. Sci.*, 2017, DOI: 10.1039/c7ee00546f.
92. A. P. Cohn, K. Share, R. Carter, L. Oakes and C. L. Pint, *Nano Letters*, 2016, **16**, 543-548.
93. M. Goktas, B. Akduman, P. Huang, A. Balducci and P. Adelhelm, *The Journal of Physical Chemistry C*, 2018, **122**, 26816−26824.
94. H. Kim, J. Hong, G. Yoon, H. Kim, K.-Y. Park, M.-S. Park, W.-S. Yoon and K. Kang, *Energy & Environmental Science*, 2015, **8**, 2963-2969.
95. Z. Zhu, F. Cheng, Z. Hu, Z. Niu and J. Chen, *Journal of Power Sources*, 2015, **293**, 626-634.
96. I. Hasa, X. Dou, D. Buchholz, Y. Shao-Horn, J. Hassoun, S. Passerini and B. Scrosati, *Journal of Power Sources*, 2016, **310**, 26-31.
97. K. Gotoh, H. Maruyama, T. Miyatou, M. Mizuno, K. Urita and H. Ishida, *Journal of Physical Chemistry C*, 2016, **120**, 28152−28156.
98. S. C. Jung, Y.-J. Kang and Y.-K. Han, *Nano Energy*, 2017, **34**, 456-462.
99. H. Kim, G. Yoon, K. Lim and K. Kang, *Chem Commun (Camb)*, 2016, **52**, 12618-12621.
100. M. Goktas, C. Bolli, E. J. Berg, P. Novák, K. Pollok, F. Langenhorst, M. v. Roeder, O. Lenchuk, D. Mollenhauer and P. Adelhelm, *Advanced Energy Materials*, 2018, DOI: 10.1002/aenm.201702724, 1702724.
101. H. Kim, J. Hong, Y.-U. Park, J. Kim, I. Hwang and K. Kang, *Advanced Functional Materials*, 2015, **25**, 534-541.

102. M. Cabello, T. Chyrka, R. Klee, M. J. Aragón, X. Bai, P. Lavela, G. M. Vasylchenko, R. Alcántara, J. L. Tirado and G. F. Ortiz, *Journal of Power Sources*, 2017, **347**, 127-135.
103. J. Maibach, F. Jeschull, D. Brandell, K. Edstrom and M. Valvo, *ACS Appl Mater Interfaces*, 2017, **9**, 12373-12381.
104. N. Leifer, M. F. Greenstein, A. Mor, D. Aurbach and G. Goobes, *The Journal of Physical Chemistry C*, 2018, **122**, 21172-21184.
105. T. Palaniselvam, M. Goktas, B. Anothumakkool, Y.-N. Sun, R. Schmuch, L. Zhao, B.-H. Han, M. Winter and P. Adelhelm, *Advanced Functional Materials*, 2019, DOI: 10.1002/adfm.201900790, 1900790.
106. J. W. Wang, X. H. Liu, S. X. Mao and J. Y. Huang, *Nano Lett*, 2012, **12**, 5897-5902.
107. E. Paled, *Journal of The Electrochemical Society*, December 1979, 2047-2051.
108. M. Nie, D. Chalasani, D. P. Abraham, Y. Chen, A. Bose and B. L. Lucht, *The Journal of Physical Chemistry C*, 2013, **117**, 1257-1267.
109. S. J. An, J. Li, C. Daniel, D. Mohanty, S. Nagpure and D. L. Wood, *Carbon*, 2016, **105**, 52-76.
110. M. Arvidson, M. E. Fakley and M. S. Spencer, *Journal of Molecular Catalysis*, 1987, **41**, 391-393.
111. M. He, Doctoral dissertation, 2016.

10.List of Contributions

List of Publication

1. Mustafa Goktas, Christoph Bolli, Erik J. Berg, Petr Novák, Kilian Pollok, Falko Langenhorst, M. v. Roeder, Olena Lenchuk, Doreen Mollenhauer, Philipp Adelhelm, *Graphite as Cointercalation Electrode for Sodium-Ion Batteries: Electrode Dynamics and the Missing Solid Electrolyte Interphase (SEI), Advanced Energy Materials* **2018**, 1702724.

2. Mustafa Goktas, Baris Akduman, Peihua Huang, Andrea Balducci, Philipp Adelhelm, *Temperature-Induced Activation of Graphite Co-intercalation Reactions for Glymes and Crown Ethers in Sodium-Ion Batteries, The Journal of Physical Chemistry C* **2018**, *122*, 26816−26824.

3. Mustafa Goktas, Christoph Bolli, Johannes Buchheim, Erik J. Berg, Petr Novák, Francisco Bonilla, Teófilo Rojo, Shinichi Komaba, Kei Kubota, Philipp Adelhelm, *Stable and instable diglyme-based electrolytes for batteries with sodium or graphite as electrode, (Submitted Manuscript)*.

4. Thangavelu Palaniselvam*****, Mustafa Goktas *****, Bihag Anothumakkool, Ya-Nan Sun, Richard Schmuch, Li Zhao, Bao-Hang Han, Martin Winter, Philipp Adelhelm, *Sodium Storage and Electrode Dynamics of Tin–Carbon Composite Electrodes from Bulk Precursors for Sodium-Ion Batteries, Advanced Functional Materials* **2019**, 1900790. (***** shared first authorship)

5. Timo Stettner, Peihua Huang, Mustafa Goktas, Philipp Adelhelm, and Andrea Balducci, *Mixtures of glyme and aprotic-protic ionic liquids as electrolytes for energy storage devices*, The Journal of Chemical Physics, **2018**, 148, 193825.

List of Conference

2016 German Israeli Battery School 2016 in Munich / Germany (Workshop) – Poster Presentation

2016 GDCH (Gesellschaft Deutscher Chemiker) (Society of German Chemists) 'Chemie and Energie 2016' in Jena / Germany – Poster Presentation '*Sodium-Ion storage in Carbon Structures*'

2017 GDCH (Gesellschaft Deutscher Chemiker) (Society of German Chemists) 'Wissenschaftsforum chemie' in September 2016 in Berlin / Germany – Poster Presentation '*Electrode Dynamics of Graphite Electrodes for Sodium Ion Batteries: An in situ Study by Electrochemical Dilatometry'*

2018 The World Conference on Carbon in July 2018 in Madrid / Spain – Oral Presentation '*Graphite as Co-intercalation Electrode for Sodium-ion Batteries: Electrode Dynamics and the Missing Solid Electrolyte Interphase (SEI)*'

2018 Na-ion battery workshop – Jena, in Jena / Germany – Oral Presentation '*Graphite as Co-intercalation Electrode for Sodium-Ion Batteries*'

2018 Material Research Society (MRS) Fall Meeting and Exhibit 2018 in Boston / USA – Poster Presentation '*Graphite as Co-intercalation Electrode For Sodium-ion Batteries: Electrode Dynamics and Temperature Induced Activation of Graphite Reactions'*